

---

**Damage Mechanics**

**Applied to**

**Structural Impact**

---

**Marcílio Alves**



**THE UNIVERSITY**  
*of* **LIVERPOOL**

---

# Damage Mechanics

## Applied to

# Structural Impact

---

LIVERPOOL  
UNIVERSITY  
LIBRARY

Thesis submitted in accordance with the requirements of the

**University of Liverpool** for the degree of  
**Doctor in Philosophy**

by **Marcílio Alves**

May 1996



THE UNIVERSITY  
*of* LIVERPOOL

---

*to Isabel and Taís*

---

## Acknowledgments

The completion of the present study has been an immense privilege, made possible by the sponsorship of the Brazilian agency CAPES.

I thank Dr. C.C. Tu, from the University of São Paulo, Brazil, for his encouragement and constant attention. I am highly indebted to the staff of the University of Liverpool for their dedication. In particular, Mrs. M. White, Mr. J. Curran and Mr. G. Swallow provided unvaluable help throughout all this period.

Thanks go also to Dr. R.S. Birch, from the Impact Research Centre, for his friendship and unfailing support. My colleagues Mr. C.C. Yang, Mr. B. Dlodlo and Dr. M. White have contributed in many ways to this work.

Prof. J.L. Yu, from the University of Science and Technology of China, Hefei, China, Mr. Q.M. Li, Ms. C. Jones and Mr. S. James, from the University of Liverpool provided advice on a number of technical matters. Mr. H. Rapp, from Struers GmbH, Germany, was extremely helpful in assisting me with the micro-hardness tests.

I wish to express my gratitude to my mother-in-law and to César José Deschamps for their kind attention. Seu Cilico and Luiz César Caldeira, both recently passed away, will always be heartily remembered.

The privilege of knowing and working with Prof. Norman Jones has been unique. His guidance, attention, respect, simplicity and genuine interest for my work are unforgettable and have played a decisive part in my own attitude towards research. My warm appreciation to him.

I am happily indebted for life to my father, mother and sister for their fundamental support during my stay in Liverpool.

Finally, I owe more than I can say to my beloved Isabel and Taís, without whom this work would not come into existence. To them I dedicate it.

---

# Damage Mechanics Applied to Structural Impact

by **Marcílio Alves**

## Abstract

This work aims at the prediction of failure in impacted structures.

This is achieved by developing a particular formulation of Continuum Damage Mechanics, CDM. Perfectly plastic and linear strain hardening material constitutive laws were used, both taking into account strain rate effects. The model is used to predict the displacement to failure of mild steel impacted beams.

Basic material properties were obtained through dynamic tensile tests on cylindrical specimens. These tests allowed the determination of a dynamic equivalent stress-strain curve. A material constitutive law is proposed for the stresses at any value of strain and strain rate.

Dynamic tensile tests on notched specimens and Finite-Element analyses have shown that the hydrostatic stress has a secondary role on determining the failure site of axisymmetric specimens. Failure takes place at regions where the triaxiality is low but the strains are high, a fact predicted by the CDM model.

Different experimental techniques were used to measure the critical damage parameter. The change of electrical potential, change of hardness, void area and elastic modulus degradation yielded different damage definitions. It was found that the damage parameter is dependent on the experimental technique used to measure it.

By properly defining a hinge length for beams, plastic strains and an average strain rate were determined. They were used, together with the CDM rate-dependent model, to predict the failure of statically loaded and impacted beams. The beams were loaded at different points, by different tup geometries, masses and velocities. The results indicate that the CDM is capable of forecasting well the displacement to failure of the beams as long as the rate-dependent model is used.

**Key words:** failure, impact, beams, rate-dependent damage mechanics, damage, material constitutive law, dynamic tensile test, notched specimens.

---

# Contents

<b>1</b>	<b>Introduction</b>	<b>1</b>
1.1	Fracture mechanisms	2
1.2	Ductile failure	3
1.2.1	Nucleation of voids and microcracks	4
1.2.2	Growth of voids and microcracks	4
1.2.3	Coalescence of voids	5
1.3	Micromechanic models of ductile failure	5
1.4	Rigid-plastic models of ductile failure	7
1.5	Local and global approaches to failure	8
1.6	Continuum Damage Mechanics	9
1.6.1	Applications	11
1.6.2	Limitations	13
1.7	Final remarks	15
<b>2</b>	<b>Material Characterisation</b>	<b>17</b>
2.1	Tensile test	18
2.1.1	Equivalent stress	18
2.1.2	Stress definitions	21
2.1.3	Strain rate	22
2.2	Material	23
2.3	Static tensile tests	25
2.3.1	Validation	26
2.4	Dynamic tensile tests	27
2.4.1	Validation	29
2.5	Results	30
2.6	Constitutive relations	38
2.7	Discussion	42
<b>3</b>	<b>Stress State Influence on Failure</b>	<b>47</b>
3.1	Notch tensile tests	50

3.2	Experimental set-up and results	51
3.3	Finite-Element analysis	58
3.3.1	Results	62
3.3.2	Material influence on triaxiality	66
3.3.3	Validation	68
3.4	Discussion	69
<b>4</b>	<b>Material Damage</b>	<b>75</b>
4.1	Damage definitions	75
4.2	Finite-Element simulation	81
4.3	Damage tests description	86
4.4	Measuring the damage parameters	88
4.4.1	Static damage parameter $D_E$	89
4.4.2	Static damage parameter $D_{HV}^e$	90
4.4.3	Static damage parameter $D_V^e$	92
4.5	Material damage according to the void area	92
4.5.1	Results	95
4.6	Additional experimental parameters	96
4.7	Discussion	98
<b>5</b>	<b>Strain Rate-Dependent Damage Mechanics</b>	<b>105</b>
5.1	Strain rate influence on damage evolution	106
5.2	Particular integration of the damage equation	109
5.3	Damage strength material parameter	113
5.4	Influence of triaxiality on failure strain	113
5.5	Dynamic limit forming diagrams	116
5.6	Discussion	119
<b>6</b>	<b>Strains in a Perfectly Plastic Material</b>	<b>123</b>
6.1	Bending hinge length	124
6.2	Dynamic bending hinge length	128
6.3	Shear hinge length	131
6.4	Membrane hinge length	134
6.5	Equivalent strain	135
6.5.1	Shear strain	135
6.5.2	Axial strain	137
6.6	Equivalent strain rate	139
6.7	Validation of the hinge length definitions	141
6.7.1	Qualitative validation	141

---

6.7.2	Quantitative validation	142
6.8	Final comments	147
<b>7</b>	<b>Static and Dynamic Beam Failure</b>	<b>151</b>
7.1	Experiment in beams	151
7.1.1	Static tests	152
7.1.2	Dynamic tests	153
7.2	Strains measured from grids	156
7.3	Beam failure — Static concentrated load	159
7.3.1	Introduction	159
7.3.2	Static failure prediction	160
7.4	Beam failure — Impact of a mass	162
7.4.1	Introduction	162
7.4.2	Dynamic failure prediction	164
7.5	Discussion	165
7.5.1	Static failure	165
7.5.2	Dynamic failure	168
7.5.3	Triaxiality	171
<b>8</b>	<b>Conclusions</b>	<b>177</b>
8.1	Tensile tests	177
8.2	Notch tensile tests	178
8.3	Material damage	180
8.4	Strain rate influence on the damage parameter	181
8.5	Effective stress	182
8.6	Flow stress	183
8.7	Is CDM a strain criterion?	184
8.8	Closure	185
<b>Appendix</b>		<b>187</b>
<b>A</b>	<b>Fundamentals of Damage Mechanics</b>	<b>187</b>
A.1	Thermomechanics	187
A.2	Damage constitutive equations	191
A.3	Damage evolution	193
<b>Nomenclature</b>		<b>197</b>
<b>List of Figures</b>		<b>203</b>



---

<b>List of Tables</b>	<b>207</b>
<b>Bibliography</b>	<b>209</b>

---

# 1 Introduction

IN A SOCIETY where man-made structures are found everywhere, the importance of predicting structural behaviour is evident. Methods of elastic and plastic analysis, including dynamic behaviour, are now at the disposal of engineers for the design of lighter and safer structures.

The use of computers allows the prediction of the response of a broad class of static and dynamic elasto-plastic structures and components made of homogeneous materials. In spite of that, it is significant that *failure*, in the sense of a structural breakdown, cannot be yet properly predicted in many cases.

This undesirable situation has prompted researches of different fields to strive for the finding of failure mechanisms and criteria to be applied in structural design. However, to date, among the various failure criteria proposed in the literature, none can be considered definitive.

The phenomenon of failure is extremely complex. At a local microscopic level, where all failure starts, the laws of Continuum Mechanics are not fully valid. Fracture Mechanics can be considered a first attempt to approach the problem of failure by using *global* parameters, without paying attention to the micro-mechanisms of failure. Even considering the importance of Fracture Mechanics as a design tool, a *local* approach to failure is necessary in helping the understanding of material behaviour at a grain level. To bridge the gap between local and global interpretations of failure is a difficult task, not yet fully accomplished.

Rupture, fracture and failure are important concepts in this work. Briefly, a material is said to rupture when, pulled in tension, its resistant cross-sectional area reduces to zero,<sup>3</sup> either by necking or shearing-off. Rupture is an extreme case of fracture, which is any material separation taking place before a total area reduction. Fracture occurs due to a multitude of complex mechanisms, summarised in sequence.

Failure has a wider meaning. It can be said that a structure fails when it cannot accomplish any more the functions it has been designed for. In this

sense, a structure exhibiting a slight plastic deformation may be considered to have failed. Nevertheless, in the present work, the concern is with structures subject to such intense loads that formation and eventually growth of a crack is likely. A structure is considered to have failed when all the conditions for crack initiation have been fulfilled. Accordingly, failure and fracture in the present context are, sometimes, mingled concepts. Due to this failure definition, the analyses herein pursued are bounded by elasticity and fracture mechanics.

In the present work, from the main mechanisms of fracture, only ductile rupture at normal temperature will be contemplated. The starting point is the prediction of failure in simple structures, mixing local and global parameters, but from an engineering and not a physical or a metallurgical point of view.

This chapter aims to provide a descriptive background on the main material failure mechanisms and on important theoretical models used to investigate structural failure. It introduces models to predict failure based on the rigid, perfectly plastic assumption and provides a literature review on Continuum Damage Mechanics. The chapter finishes with a discussion, where the present research is outlined.

## 1.1 Fracture mechanisms

It is generally accepted that the interaction among temperature, stress state and its history, strain rate, microstructure of the material, inclusions, second-phase particles and grain boundaries affects the fracture mechanisms. This suggests, as it is, that the phenomena leading to fracture is very involved. Indeed, it is not completely clear nowadays how the different variables leading to failure manifest themselves, interact and grow.

One of the simplest classifications, yet covering a broad range, of fracture mechanisms is due to Ashby *et al.*<sup>3</sup> and is depicted in Figure 1.1.

In one extreme of the diagram, for low temperatures and/or high strain rates, cleavage is likely to occur. Under certain conditions, almost all crystalline solids can fail by cleavage, usually in a transgranular way. It involves nucleation of small cracks due to abrasion, corrosion, slip or growth of defects. The cracks concentrate stresses, following propagation.<sup>59</sup>

The other extreme of Figure 1.1 corresponds to rupture, occurring when

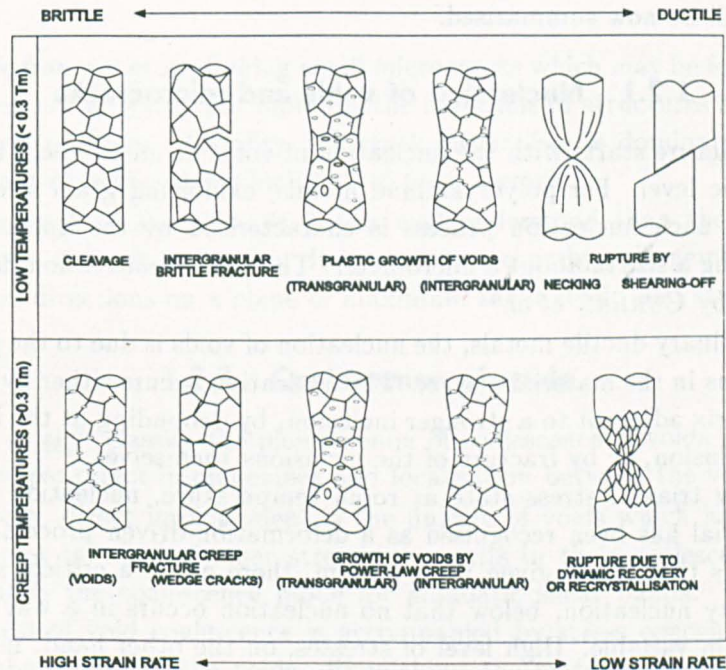


**Figure 1.1:** Classification of fracture mechanisms (after Ashby *et al.*<sup>3</sup>). The strain rate scale has been added.

no other fracture mechanism intervenes. The genuine rupture is usually related to the suppression of nucleation due to the high purity of the material or due to plastic deformation occurring simultaneously with dynamic recrystallisation.<sup>3</sup>

In between these two extremes, ductile fracture is dominant.

Using the classification in Figure 1.1, ASHBY *et al.*<sup>3</sup> have developed various fracture-mechanism maps. Though these maps treat dynamic fracture as a separate fracture mechanism, Curran *et al.*<sup>52</sup> remark that dynamic fracture phenomena are similar to those occurring at quasi-static conditions.

## 1.2 Ductile failure

It is generally accepted that ductile fracture mechanisms are associated with nucleation, growth and coalescence of voids or cracks.<sup>196</sup> Voids nucleate at inclusions, they grow with plasticity and coalesce, leading to fracture. These

aspects will be now summarised.

### 1.2.1 Nucleation of voids and microcracks

Ductile fracture starts with the nucleation of voids or microcracks at a sub-microscopic level. For polycrystalline metals, exhibiting grain sizes of micrometers, such nucleation process is characterised by the appearance of voids having a size of about a micrometer. The sites of nucleation have been described by CURRAN *et al.*<sup>52</sup>

For ordinary ductile metals, the nucleation of voids is due to the presence of inclusions in the material matrix. The nucleation occurs either by fracture of the matrix adjacent to a stronger inclusion, by debonding at the interface matrix-inclusion, or by fracture of the inclusions themselves.<sup>3,51,74</sup>

For low triaxial stress state at room temperature, nucleation of voids in a material has been recognised as a deformation-driven process.<sup>52,74,134</sup> This means that, for a given alloy system, there exists a critical strain to cause cavity nucleation, below that no nucleation occurs in a way to alter a continuum variable. High level of stresses, on the other hand, may drive the nucleation phenomena when the deformation magnitude is low. This suggests that nucleation mechanisms are function of stresses and strains prevailing in the structure and/or material.

The measurement of the strain associated with the nucleation of cavities is a point to be addressed in the present work. At some extent, the accuracy of the failure criterion here explored depends on the correct value of the strain associated with the void nucleation threshold.

### 1.2.2 Growth of voids and microcracks

Once the nucleation process has been set up, the microscopic failures, voids, cracks, shear bands, grow with the loading.

This growth seems to be the result of ductile plastic (viscous) flow, brittle crack extension and shear slipping.<sup>52</sup> They interact with each other according to the material, temperature, stress state and loading rates.

For most polycrystalline metals, the growth of micro-failures is caused by brittle crack propagation and ductile void growth. They can occur at inter or intra grains. At low temperatures and/or high strain rates, the growth is dominated by brittle mechanisms whereas the ductile mode is likely to occur at higher temperatures and lower strain rates. Mixed modes are expected to occur, resulting in a fracture front characterised by brittle cracks and ductile

voids.

Brittle fracture grows linking small microcracks which may be formed due to the presence of voids. For more ductile materials or structures submitted to low level of stress triaxiality, the crack mechanism is dominated by the enlargement of microvoids which link to form a crack.

The growth of shear bands is less well understood than the previous mechanisms of crack formation. It appears to occur by enlargement of the band in all directions on a plane of maximum shear strain and stress.<sup>52</sup>

### 1.2.3 Coalescence of voids

CURRAN et al.<sup>52</sup> classify the phenomenon of coalescence of voids under two major groups: direct impingement and localisation between the voids.

Basically, direct impingement is the linkage of voids which have grown until a point in which further stretching results in their coalescence. Impingement is the coalescence mode for adiabatic shear bands. Of course this process of void coalescence is accompanied by stress concentration in the neighbourhood of the voids, diminishing the material ductility. Such localisation of strains is ultimately what governs the ductility of material. Without localisation, the material would fail by void impingement, exhibiting maximum ductility.

Coalescence due to localisation occurs in sheets between voids. These sheets are formed by smaller voids. COX and LOW<sup>51</sup> sustain that the void sheets are planar, composed of small voids and generally oriented at 45° with the tensile axis.

## 1.3 Micromechanic models of ductile failure

Experimental evidence that ductile fracture is intimately connected with void growth has directed the effort of various researchers into grasping quantitative aspects of this phenomenon.

In this regard, the pioneering work of MCCLINTOCK<sup>146</sup> analyses the expansion of cylindrical holes in a non-hardening material. Disregarding interaction among the various possible holes, the problem was reduced to a hole in an infinite medium. A noteworthy result is the very strong inverse dependence of fracture strain on the tensile stress, transverse to the holes.<sup>146</sup>

RICE and TRACEY<sup>175</sup> treated the case of a spherical void in a remotely

uniform stress and strain field. They found, as McCLINTOCK did, that the void growth rate increases exponentially with the stress triaxiality, meaning that this last parameter greatly affects the strain to failure.

ORTIZ and MOLINARI<sup>168</sup> have treated the same problem of RICE and TRACEY but considering the matrix surrounding the voids as made of a rigid-viscoplastic material. They could assess the influence of hardening and strain rate, concluding that the rate sensitivity of the material has the effect of retarding void expansion, as expected.

The models cited above implicitly assume that the presence of the holes do not affect the plastic potential. GURSON,<sup>75</sup> however, developed a yield surface which has the property to shrink as the voids grow. The yield surface degenerates to the VON MISES one when the void volume is zero. For a void volume fraction equal to unity, the yield surface degenerates to a point. An extension of this model for visco-plastic materials has been developed by PAN *et al.*<sup>170</sup> and by SUN and HUANG.<sup>188</sup>

The GURSON model has been extensively used to grasp the basic features of the mechanisms of nucleation, void growth and coalescence. However, DOOD and BAI<sup>59</sup> point out that, in this model, coalescence always occurs by internal necking of the ligaments between cavities. This contradicts the fact that, at some stage of the fracture, localised shear or planar flaws among the ligaments are likely to occur.<sup>51</sup> Similarly, THOMASON<sup>196</sup> strongly remarks that the validity of the GURSON model is severely limited by the non-appreciation of internal microscopic necking of the intervoid matrix.

These limitations have been partly overcome by various researchers. For instance, TVERGAARD<sup>198,199</sup> has introduced in the GURSON yield function numerical coefficients aiming to bring the theoretical yield surface closer to the actual one. These modifications have been numerically implemented by various authors and are generally accepted as a good fit to the actual yield surface. In particular, ductile fracture in pre-notched beam specimens has been analysed for some static<sup>157,169</sup> and dynamic<sup>92</sup> cases.

PERZYNA<sup>172</sup> has addressed the problem of dynamic failure. He worked with a spherical void embedded in rigid-visco-plastic matrix. His basic failure criterion is that dynamic failure occurs when both void volume fraction and equivalent plastic strain achieve critical values. Later on, the linear hardening rule used by PERZYNA was improved by NEMES *et al.*,<sup>163</sup> who considered a non-linear hardening material.

CLAUSMEYER and ROOS<sup>44</sup> present some results of failure prediction using as a criterion a variable  $q$ , a characteristic quantity of the degree of stress

triaxiality. When  $q$  achieves a critical value, ductile fracture is expected. Other failure criteria applied to metal-forming are commented by CLIFT *et al.*<sup>45</sup>

COCKS and ASHBY<sup>48</sup> have analysed the growth of a spherical void in a rate-dependent plastic material. This void, supposed to be in the grain boundary to simulate creep, was subjected to different stress states. The COCKS and ASHBY model was successfully implemented by BAMMANN *et al.*<sup>5</sup> in a Finite-Element scheme to predict ductile failure of plates subjected to blast loads and disks, cylinders and spheres struck by a rod. They considered a hardening, strain rate material, its properties depending on temperature, which permits consideration of the thermal softening phenomenon.

## 1.4 Rigid-plastic models of ductile failure

Many structural analyses in the plastic regime use a rigid, perfectly plastic material as a constitutive law. The rigid-plastic assumption permits the solution of important practical problems which otherwise would be mathematically intractable.<sup>34,97</sup>

Methods to predict failure in structures based on the rigid-plastic assumption are not fully explored.

JONES<sup>95,96</sup> has applied rigid-plastic methods to analyse beam failure by tensile tearing and shearing. The beam is subjected to a uniformly distributed velocity over its entire span. The values of threshold velocities which cause the so called mode II and III failure have been determined. The results are in reasonable agreement with experimental data available for a non-strain rate sensitive material. For tearing, a hinge length was defined and the uniaxial rupture strain was used in the calculations. A similar procedure was applied to a free-free beam,<sup>101</sup> being determined a critical pressure pulse which causes tearing failure, and for a beam struck transversely by a mass.<sup>137</sup>

SHEN and JONES took another approach. They assumed that rupture in a rigid-plastic structure occurs when the absorption of plastic work per unit volume reaches a critical value. To calculate the actual plastic work in beams, a hinge length was estimated based on experimental data from MENKES and OPATS<sup>147</sup> for impulsively loaded aluminium beams.

This methodology, reviewed by JONES and SHEN,<sup>100</sup> was applied to predict the failure of beams under impulsive loading,<sup>180</sup> the failure of clamped



beams struck by a mass<sup>181</sup> and to circular plates.<sup>182</sup>

The method predicts well the threshold failure impulse that produces tensile tearing and shearing in beams, as well as the permanent transverse deflections of circular plates. Nevertheless, failure in circular plates is not well predicted, the authors suggesting that the non-fulfilment of the clamped boundary condition in the experiments, as assumed in the theory, could be a possible reason for the deviation.

It is important to remark that the rigid, perfectly plastic models for failure are, essentially, global approaches relying on generalised stress fields. Accordingly, details like void coalescence, triaxiality and softening are all more or less disregarded in these models.

## 1.5 Local and global approaches to failure

The interaction among voids is extremely important in determining failure.

Every microvoid is a source of singularity in the distribution of the stress field.<sup>91,172</sup> As the void grows, it interacts with its neighbours, changing completely the matrix configuration. Due to this interaction, the way voids are distributed in the material affect global parameters, as has been confirmed experimentally by MAGNUSEN *et al.*,<sup>145</sup> and experimentally and numerically by BECKER<sup>10</sup> — the failure strain is significantly lower in materials with a non-uniform void distribution.

Voids have different shapes and dimensions, different mechanical properties, are arbitrarily distributed in the material. Clearly, micromechanics plays here the main role in revealing aspects of the interaction among voids and in relating local and global parameters, as illustrated by LEE and MEAR<sup>119</sup> \*. A successful theory to predict failure *based on* micromechanics approach has to be capable of addressing the above cited void characteristics. Clearly, this is a tremendous task in face of the peculiar characteristics of voids and their interrelation with the matrix. Even avoiding complications at microscopic level, sophisticated micromechanic models to predict ductile failure rely on several material constants, as in CURRAN *et al.*<sup>52</sup> Also, the required computational effort is intense.<sup>5,15,114,160</sup>

The extreme alternative to this situation is the use of global failure criteria, disregarding details at a local level. Global approaches to failure have been explored.<sup>114,178</sup> The classical concept of a yield surface has

---

\*Micromechanics is discussed at length by NEMAT-NASSER and HORI<sup>162</sup>

been expanded to *fracture surfaces*, giving rise to techniques to predict failure based mainly on stress and strain parameters, as in THEOCARIS<sup>195</sup> and UKADGAONKER and AWASARE.<sup>203</sup> Failure theories are developed as an extension of the plasticity framework,<sup>189</sup> using generalised stresses<sup>100</sup> and even fractal concepts.<sup>38</sup>

One has then on one side a global approach to fracture where the attention to the details at a local level is overlooked. This makes it more arbitrary but simpler. On the other hand, the micromechanics approach goes to the deepest level of the material microstructure to search there for phenomena that may be helpful in explaining failure.

Bearing in mind these characteristics, it is opportune to enquire whether there exists a theoretical framework which is capable to contemplate both local and global aspects of failure. This is the case of the Continuum Damage Mechanics, CDM.

CDM sees the material as a continuum where the traditional concepts of stress and strain are valid. The presence of voids, small cracks or second phase particles are seen as elements causing stress concentrations, picked up by the so called damage variable. Hence, the possibility of formulating constitutive laws using continuous variables for materials exhibiting voids or small cracks.

The meaning of a damage mechanics model lies in the smearing of local stress concentrations and interaction among voids in order to obtain a continuum model. The voids are assumed to occur in a representative volume element, which is small enough to be considered a material point as well as sufficiently large to contain a representative number of defects.

## 1.6 Continuum Damage Mechanics

The seminal paper published in Russian by L.M.KACHANOV,<sup>42</sup> marks the beginning of Continuum Damage Mechanics \*. He defined a variable, the integrity, whose extreme values are 1 and 0 for fully undamaged and damaged structure, respectively. He then applied this concept to creep analyses. The integrity variable evolved to the damage and was related to void inside a material thanks to ROBOTNOV, as pointed out in reference 112.

Nowadays, there are two major ways of developing damage models: based on micromechanics and/or phenomenological arguments. In the former, the

---

\*According to KRAJCIHOVIC,<sup>112</sup> this term was coined by JANSON and HULT.<sup>90</sup>

damage is introduced in a constitutive law mainly by considering void shape and interaction. In the later, experimental observation aid in formulating damage evolution laws, damage definitions, etc ...

A damage model aims to establish how the presence of voids in a material affects the structural behaviour. In other words, it has to be formally defined the way damage enters in the material constitutive law and how stresses and strains affect the damage evolution.

To assist in this task, thermomechanics plays a special role.<sup>71</sup> It is through the basic principles of thermodynamics that a damage model is developed. This general formalism, as described, for instance, by ZIEGLER<sup>226</sup> has been extensively used to derive constitutive relations in general, as in ZIEGLER and WEHRLI,<sup>227</sup> and including damage in particular, as in COCKS and LECKIE,<sup>46</sup> HANSEN and SCHREYER<sup>78</sup> and LEHMANN.<sup>120,121</sup>

The developing of damage models based on thermodynamics lends to CDM, at first, rigor and the possibility of proposing new models by defining different thermodynamic potentials. If, on one hand, this flexibility is all necessary in face of the various existing materials, on the other hand, it determines a lack of agreement on a more general model, an issue discussed by CAROL *et al.*<sup>32</sup>

The formalism yielded by thermodynamics is frequently used as an argument *pro* CDM, for the later is seen as coming from the former. However, the amount of theoretical CDM models have to be put in contrast with the paucity of good experimental data in the field. This, in turn, puts CDM in a different perspective, where new models are seen rather restrictively until experiments corroborate them.

The relationship between damage and void area is one of the basic concepts of CDM. However, damage can be related to other mechanical properties, as the elastic modulus. Such a relation, proposed by LEMAITRE,<sup>122,127</sup> has been used extensively in theoretical models and confirmed experimentally by many researchers.<sup>4, 23, 49, 55, 110, 130, 152</sup>

CDM becomes then the relation of the damage to a mechanical property and the definition of a thermodynamic potential leading to damage evolution and to a material constitutive law. Eventually, a critical value for the damage parameter at a local material level, beyond which a microcrack is likely to grow in a crack, can be established.

### 1.6.1 Applications

CDM has been applied to a vast area of structural problems. This wide spectrum of applications is mainly due to the possibility of formulating different thermodynamic potentials, specific for each problem, as already indicated.

In maintaining its origin, CDM has been used extensively in creep analysis,<sup>83,153,222</sup> including radioactive effects<sup>154,155</sup> and assessment of weldment integrity.<sup>212</sup>

MURAKAMI *et al.*<sup>153</sup> have simulated a biaxial stress state in a plate where creep is important. Their model included anisotropy and it was able to simulate crack propagation and non-proportional loading. Interestingly, the use of a critical damage equal to unity or equal to one-half does not alter substantially the time and strain to failure. This suggests that, for their model, the critical damage has a second order effect on the failure prediction.

CDM has spread to metal forming problems,<sup>69,109,142,224</sup> fatigue,<sup>37,128</sup> shock loading,<sup>19</sup> buckling,<sup>173</sup> brittle fracture,<sup>25,197</sup> to name a few. The capability CDM has in blending local and global approaches is seen here as a justification for the use of CDM concepts to such different areas. This not only attests its generality but also emphasises the importance of a local approach to phenomena exhibiting a global manifestation. It is here that all the strength of CDM is revealed. Local phenomena are still treated under the frame of continuum mechanics, being subject to analysis.

In studying the failure of fiber-reinforced ceramic-matrix composites, HILD *et al.*<sup>85</sup> used the localisation of deformation, determined via the damage variable, as an indicator of local failure.

Localisation using damage concepts has been developed by BENALLAL *et al.*,<sup>12,13</sup> BILLARDON and DOGHRI,<sup>20</sup> DESOYER and CORMERY,<sup>56</sup> among others. It has been in development because it is attractive to treat the softening regime and to establish a failure condition, as in RIZZI *et al.*<sup>176</sup>

LADEVÈZE *et al.*<sup>116</sup> applied CDM to ceramic composites and established failure criteria for these materials. Criteria for failure or microcrack initiation in composites<sup>23,54,70,107,132,133</sup> and polymers<sup>194</sup> have also been established using CDM framework.

The loss of load carrying capacity of less idealised structures loaded statically has been established using damage concepts.<sup>35,41,58,73,104</sup> In particular, BILBY *et al.*<sup>19</sup> predicted successfully the crack growth of a full scale spinning cylinder test, where temperatures effects were important. KIM and KIM<sup>110</sup> applied CDM to the bending of beams with large strains and rotations

and COMBESURE and JIAJU<sup>47</sup> predict rather reasonably the behaviour of notched pipes in a four point bending test, in a well developed rotation regime.

ROUVRAY and HAUG<sup>54,81</sup> employed material constitutive laws incorporating damage and large strains to analyse a car made of a composite material under different crash situations. Also, FARUQUE and WU<sup>66</sup> used CDM to predict the crash behaviour of an aluminium bumper, obtaining a reasonable agreement with experiments.

It is known that damage may exhibit an anisotropic character.<sup>33,103</sup> Whether this anisotropy is important or not is a topic to be established for each material and load regime. There are quite a few different models capable of taking into account the damage anisotropy.<sup>39,40,49,73,104</sup> These models, though potentially more accurate than isotropic damage formulations, ask for more material parameters to be implemented in a real analysis. This is restrictive in face of the difficulties of accurately measuring them. It is even reasonable to say that the accuracy gained in a anisotropic model is limited by the accuracy of the experimental data. However, damage anisotropy is not a topic of this research and a review of it can be found elsewhere.<sup>33</sup>

GELIN and PREDELEANU<sup>69</sup> offers a review of some damage models and comments on their numerical implementation. It is interesting to note that the applications cited above are the product of a constitutive damage model coded in a Finite-Element programme. This is quite natural in considering that such local phenomena as damage does request a well defined continuum field of strains and stresses. Accordingly, besides the above cited references, different damage models have been implemented with the support of numerical analysis.<sup>63,129,184,187,223,225</sup>

Ductile damage, understood as damage associated with large strains, has been treated by several authors. LEMAITRE,<sup>123-125</sup> in particular, has proposed an elementary model for the damage evolution in a well developed plastic regime.

Inspired by the LEMAITRE ductile damage model, WANG<sup>207-210</sup> has proposed a slightly different potential, obtaining good predictions for the failure of notched specimens, including non-proportional loading. Similar comments are valid for the work of TAI<sup>191</sup> and TAI and YANG.<sup>192,193</sup>

These potentials were proposed on an empirical basis to satisfy some particular experimental finding or to simplify the mathematical model.

On the outset of the present research, no closure effect due to compressive stresses is considered, a topic treated elsewhere.<sup>25,70,126</sup> This is to say that

here a damaged material will behave identically either being compressed or in tension.

### 1.6.2 Limitations

Being a new branch of mechanics, CDM has still to face important problems, some of them commented hereafter.

The constitutive equations for a damaged material is derived in the same way as for the undamaged material but stresses and strains in the damaged material are defined differently. The relation between the damaged and undamaged space has to be somehow defined, measured, hypothesised.

Some hypothesis, to be described later, have been proposed in the literature. Two of them, the strain equivalence hypothesis, due to LEMAITRE<sup>124</sup> and the energy equivalence hypothesis, due to CORDEBOIS and SIDOROFF,<sup>49</sup> are the most relevant and have been explored in theoretical and computational models.<sup>143,186,223-225</sup> However, there is no direct experimental evidence of which one is more appropriate and because they are used in the yield condition, this seems an important unsolved issue.

The very definition of a damaged variable is a topic to be examined further. There are different ways to define and measure the damage, with implications in the CDM formulation,<sup>214</sup> as it will be seen in Chapter 4. Here, it is anticipated that CDM models treat damage as a theoretical parameter, with no distinction among its various definitions and experimental techniques used to measure it.

There is a discussion about the damage variable being local or non-local.<sup>205</sup> In practice, the main reason to consider damage as a non-local variable is to avoid mesh sensitivity and lack of convergence in Finite-Element modelling of failure based on CDM models.<sup>24,31,73,113,164,177</sup> For instance, BAŽANT<sup>9</sup> argues that the local common damage variable cannot be used in the stress-strain relation. Based on a simple model, he shows that the damage is dependent on the microcrack size. Two different circular crack patterns of identical area may lead to different damage, since the crack opening displacement is proportional to the cube of crack diameter in his model.

On the other hand, XIA *et al.*<sup>215</sup> showed that there is little difference between local and non-local models when analysing a plate with a middle crack. Also, good mesh independent results were obtained with local damage models, as in GHRIB and TINAWI.<sup>73</sup>

The relationship between damage and the change of elastic modulus has

been criticised.<sup>102</sup> The reason is that damage, as such, is caused *only* by the release of *elastic* energy. According to JU,<sup>102</sup> this treatment contradicts evidences that plastic variables cooperate with failure mechanisms.

This motivates models where elastic and plastic damages are defined, as advocate by TAHER *et al.*<sup>190</sup> But, it emerges that further experimental and theoretical studies are necessary to investigate the role of plastic strains on damage.

The measurement of the damage variable is difficult. If it is measured by the change of the elastic modulus, it is not yet clear how the damage is affected by the stress state. In other words, it is not well known how the critical damage changes if the stress state changes from uniaxial to axisymmetric or plain. This potential dependence of the damage on the stress state has been approached by LEMAITRE *et al.*,<sup>14,126</sup> but it is still an open issue.

In a review of finite plasticity, NAGHDI<sup>156</sup> emphasises the disagreement among researches about the definition of plastic strain. This is here quoted to emphasise that CDM, though also used to predict failure in ductile materials under large (finite) plastic strains, has its formalism restricted mainly to small strains.

There are a few attempts in the literature to deal simultaneously with large deformation and damage.<sup>47,107,138,225</sup> VOYIADJIS and KATTAN,<sup>108,206</sup> for instance, quantify the degradation of the elastic modulus through elasto-plastic coupling where finite strains are preserved. LUO *et al.*<sup>141</sup> develops a large anisotropic damage theory based on energy equivalence of damaged and undamaged states. Models where large plastic strains are retained are quite recent and the subject is far from being mature and no attempt is here pursued towards their use.

The last topic commented on here is regarded to the growth of the damage zones. CDM aims to predict under which conditions a microcrack *starts* in a structure. Its growth is still the domain of fracture mechanics. Hence, the growth of the damage zone is a subject requiring further study.<sup>126</sup> It is true that it is possible, via Finite-Elements, to set the strength of an element to zero once the critical damage is achieved. By doing so for all the other elements, a crack path can be established. However, the localisation of damage does not assure a convergence of the Finite-Element solution. In fact, it is this point that led researches to develop non-local CDM models, as already commented.

## 1.7 Final remarks

In contradistinction from a broad class of a static and dynamic elasto-plastic analyses, to forecast structural failure and to establish conditions for its initiation is a topic not mastered yet by the current knowledge. This is a major point of attraction for researchers willing to put forward new strategies, concepts and theories to tackle the problem.

Among the options, Continuum Damage Mechanics has become a major theoretical framework for failure prediction. This is partially due to the fact that CDM can be derived on a thermomechanic basis, allowing its application to different fields and to incorporate micromechanical features in continuum constitutive laws. In turn, such characteristics make simpler the implementation of CDM models in Finite-Element codes.

Even considering the limitations commented on above, it seems that CDM can, in quite a few cases, effectively predict a bound for failure in structures. This is meaningfully shown by GHRIB and TINAWI,<sup>73</sup> in analysing failure in a real concrete dam (small strains). Even the crack path could be correctly predicted using a damage model.

Some CDM models consider constitutive damage laws where the strain rate is important enough to affect the material behaviour. The few efforts in this direction, though, as in LUBARDA and KRAJČINOVIC,<sup>139</sup> SIMO and JU,<sup>186,187</sup> and ZHU and CESCOTTO<sup>223,224</sup> are aimed at numerical applications and are not related to structural impact. The strain rate these models have been applied to are quite low. Indeed, CDM models used in the context of structural impact have not been developed yet.

Consider next the remarkable fact that CDM has been used to predict structural failure via numerical procedures only. CDM models are implemented in Finite-Element codes, taking advantage of knowing rather precisely local values of strain and stress.

This intensive use of CDM coupled to numerical codes, establishes a trend where analytical methods of failure prediction based on CDM are relegated. In spite of that, it is worthwhile to investigate whether CDM can be used in conjunction with standard theoretical solutions, as the ones yielded by rigid-plastic methods of analyses.

It is against this background that the present work arises. Its main aim is to use a ductile damage model, applying it to the prediction of failure in impacted structures. As a first step, beams are chosen to test the approach here proposed.



Because the scope of this research is to predict failure in impacted structures, it is most necessary to use a material constitutive law where strain rate effects are taken into account. This is the subject of Chapter 2, which describes how a simple stress–strain–strain rate relation is obtained through a series of dynamic tensile tests.

As already emphasised, the influence of the hydrostatic stress on failure is accepted as very significant. It will be shown that the damage evolution is affected by the hydrostatic stress but it needs to be demonstrated how important is the influence of the hydrostatic stress on failure. This matter is addressed in Chapter 3, where static and dynamic tensile tests on notched specimens will help to clarify the role of the stresses and strains on failure.

The failure criterion yielded by CDM is simple. Local material failure will take place when the damage parameter achieves its critical value. Chapter 4 presents different techniques to measure the damage, its evolution and its critical value. A numerical simulation will be called upon to assist in the task of a more accurate measure of the damage.

Chapter 5 will introduce the basic formulation of CDM and will integrate the damage evolution equation for some special stress–strain relations, strain rate effects being incorporated. Closed form expressions for the damage evolution will then be used to explore the failure sites in notched specimens and the dynamic limit forming diagrams.

It will be shown that the prediction of failure in beams relies on the knowledge of the plastic strains they sustain. By defining an appropriate hinge length and using experimental data, Chapter 6 addresses this problem. It is shown that a reasonable prediction of large plastic strains in beams, including shear, can be obtained by knowing the beam displacement, the load position and one material parameter.

Chapter 7 applies Damage Mechanics, with strain rate effects incorporated, to the prediction of the displacement to failure of beams made of a strain rate sensitive material and impacted by tups of different geometries.

A general discussion about the capability of CDM in predicting failure of beams under impact conditions is left to Chapter 8.

---

## 2 Material Characterisation

A QUANTITATIVE analysis of a structural engineering problem is based on the solution of a set of *equilibrium equations* and a *kinematically admissible* displacement field. They are supplemented by the boundary conditions and initial conditions of a particular problem. Additionally, these statically and kinematically admissible sets are independent of each other and, to link them, the material behaviour, from which the structure is made, should be invoked. This points towards the importance of defining the way the material behaves under different load, temperature, radiation, microstructure changes, etc . . .

The mathematical equation relating some of these variables is called the material constitutive law and it is, in general, gained through a series of experiments. The experimental data are then used to propose functions by curve fitting. Though this procedure might sound less scientific, the other extreme of defining theoretical *equations of state* based, for instance, on micromechanical processes or chemistry is still in its infancy.

Traditionally, the tensile test is the most common procedure to establish a constitutive law. The simplicity of the test, however, is only apparent and its analysis and data interpretation is certainly not mundane. In fact, a full description of what happens when loading a tensile specimen up to rupture is not yet possible.

This chapter aims to present how basic mechanical material properties are determined through a series of static and dynamic tensile tests. A typical tensile test is described, followed by details of the material used in the experiments. The experimental arrangement for the static and dynamic tensile tests is shown with comments about data accuracy and analysis. Next, the results for static and dynamic tests are reported. An equation is then proposed capable of predicting well the experimental data for a broad range of stresses, strains and strain rates. The chapter ends with comments on the

relevant measured data and on the stress–strain–strain rate relation.

## 2.1 Tensile test

A typical tensile test consists in loading a strip or a cylindrical rod up to some desired level of deformation or stress. The load \* increases continuously as the specimen hardens. It then achieves a maximum value and the stress state up to this point is uniform, as demonstrated by MILES.<sup>151</sup> Following the peak load, at some stage, a bifurcation in the uniform stress field occurs and localisation takes place.

The exact stress–strain state associated with localisation is a complex issue. Firstly, it depends on the specimen geometry and material properties.<sup>72</sup> For slender cylindrical specimens, bifurcation occurs nearer to the maximum load than for stubby ones.<sup>88,159</sup> Rectangular specimens tend to bring the localisation point nearer to the maximum load, when compared to cylindrical ones, *ie* rectangular specimens are inherently more unstable.<sup>200</sup>

The test speed, and hence inertia and strain rate, are other factors that influence the strain to necking. The higher the material strain rate sensitivity the greater the delay in localisation. This was treated theoretically by HUTCHINSON and NEALE<sup>89</sup> and numerically by KNOCHE and NEEDLEMAN<sup>111</sup> and PAN *et al.*<sup>170</sup>

Elastic and plastic wave interaction, inertia, strain rate variation, among other variables, promote a complex picture of a dynamic tensile test. As an example of a non-expected feature of a tensile test, at very high strain rates, it is possible that a second point of bifurcation occurs in a specimen. This means that necking starts in two different zones, with one finally overcoming the other and progressing until total fracture. A numerical study of this phenomenon is given by KNOCHE and NEEDLEMAN.<sup>111</sup> Figure 2.1 illustrates the double necking for one of the cylindrical mild steel specimens tested here and for a rectangular cross section aluminium specimen.

### 2.1.1 Equivalent stress

Once a tri-dimensional stress state takes place in the necking zone of a cylindrical specimen, radial and hoop stresses begin to increase to the detriment

---

\*In this work, the precise use of expressions like *measured load* is relaxed. As a matter of fact, in the present context, load, stress, elastic modulus, etc ... are inferred from, among other variables, strain measurements.

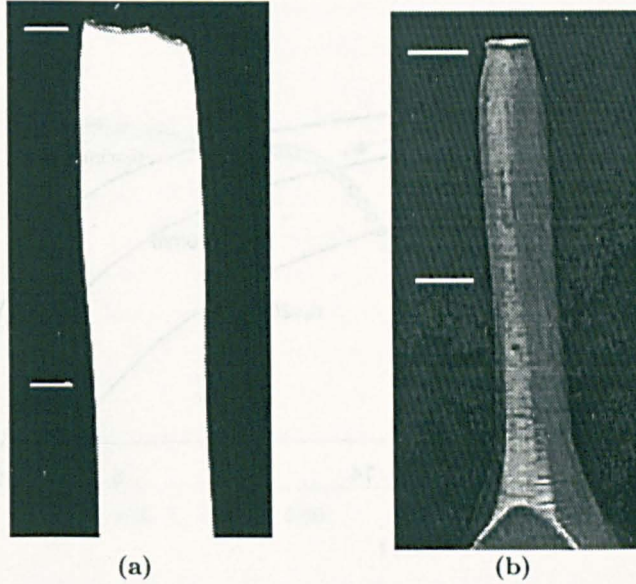


**Figure 2.1:** The phenomenon of double necking indicate by the white lines. (a) Rectangular aluminium specimen. (b) Mild steel cylindrical tensile specimen. Test speed of around 5 m/s.

of the axial stresses. Thereafter, load divided by area is no longer a measure of the tri-dimensional stress state and some sort of equivalent stress should be sought. This is what BRIDGMAN developed:<sup>26,27</sup> a theoretical solution for stresses and strains in a tensile cylindrical specimen made of a VON MISES material.

According to BRIDGMAN, at the minimum cross-section of a cylindrical specimen exhibiting necking, the true equivalent strain, radial, hoop and axial stresses are given, respectively, by

$$\varepsilon_{eq} = 2 \ln(d_0/d), \quad (2.1)$$

$$\sigma_{rr} = \sigma_{\theta\theta} = B_c \ln \left( \frac{a^2 + 2aR - r^2}{2aR} \right), \quad (2.2)$$

$$\sigma_{yy} = B_c \left\{ 1 + \ln \left( \frac{a^2 + 2aR - r^2}{2aR} \right) \right\}, \quad (2.3)$$

where

$$B_c = \frac{\text{load}}{\pi a^2 (1 + 2R/a) \ln(1 + a/2R)}. \quad (2.4)$$

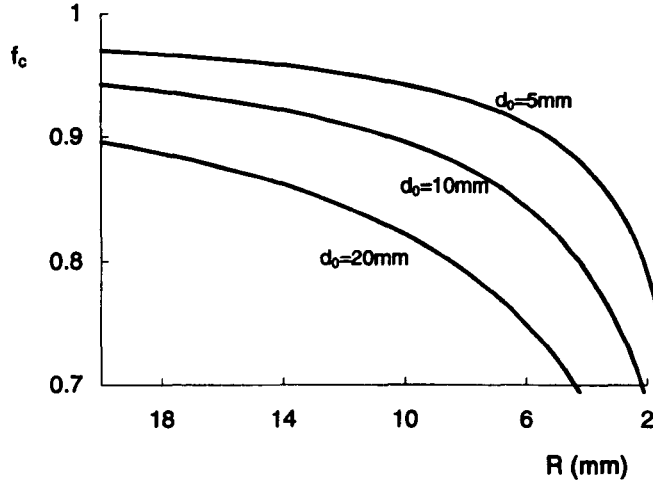


**Figure 2.2:** Correction factor according to equation (2.5), for cylindrical specimens with diameters of 5mm, 10mm and 20mm, as a function of the necking radius.

In these expressions,  $d_0$  and  $d$  are the initial and current diameter,  $a$  is the current cross-section radius,  $R$  the outer radius due to necking and  $r$ ,  $\theta$ ,  $y$  are the cylindrical co-ordinates in the minimum cross-section.

By noting that  $\sigma_{eq} = B_c$  and that  $load/\pi a^2$  is the average axial stress, one can consider

$$f_c = \frac{1}{(1 + 2R/a) \ln(1 + a/2R)} \quad (2.5)$$

as a correction factor by which the average axial stress has to be multiplied to give the material equivalent stress. The smaller the value of  $f_c$  the greater the error in assuming  $\sigma_{eq} = \sigma_{yy}$ .

Figure 2.2 shows this correction factor for specimen diameters of 5mm, 10mm and 20mm as a function of the external radius at necking \*.

It is clear from the above equations that, to infer the material constitutive law from a tensile test, one needs to measure the evolution of the necking

\*BRIDGMAN<sup>27</sup> remarks that the strain hardening curve rises less rapidly with strain in a  $\sigma_{eq}$  versus  $\epsilon_{eq}$  curve than in  $\sigma_{yy}$  versus  $\epsilon_{eq}$  curve. This widens the discrepancy between  $\sigma_{eq}$  and  $\sigma_{yy}$  for high plastic strains.

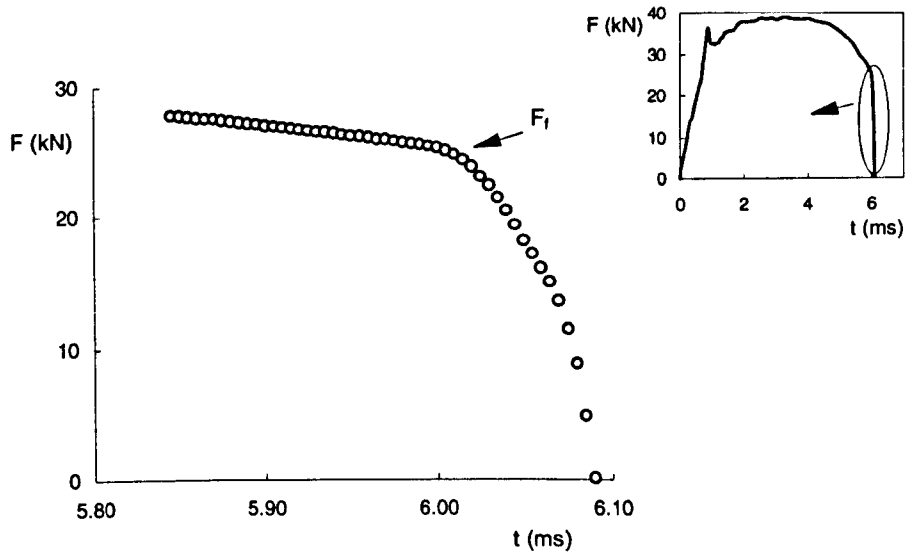


**Figure 2.3:** Load behaviour near fracture in a tensile test conduct at a speed of 1.9m/s.

radius \*. This is not an easy task, especially in dynamic tests, and is reflected in the shortage of material data under dynamic conditions, in the range of high plastic strains.

### 2.1.2 Stress definitions

Next, consider the fracture process. It is a common procedure in engineering practice to define the fracture stress as the fracture load divided by the area of a broken specimen measured after a test. This simple definition introduces some problems. First, the load, when recorded using a high sampling rate, continuously decreases until zero, as illustrated in Figure 2.3. Thus, it might be difficult to define precisely the fracture load. Secondly, the minimum cross section area and the neck radius measured after a test is not necessarily the one prevailing at the time the fracture load was measured.

This calls for a definition of the *failure point*, gained by considering the

---

\*The radius measured on the broken specimen is not the same as at the moment of fracture.

equivalent stress *versus* the equivalent plastic strain curve. The curve will exhibit, at same stage, a sharp drop, as experimentally shown by MACKENZIE *et al.*<sup>144</sup> \* and numerically by TVERGAARD and NEEDLEMAN.<sup>201</sup> This drop in the equivalent stress is a consequence of a macro crack formation in the interior of the specimen and it is, accordingly, defined as the *failure stress*. The equivalent strain at this point is defined as the *failure strain*.

The *equivalent failure stress* should be distinguished from the *axial fracture stress* and from the *equivalent fracture stress*. The axial fracture stress,  $\sigma_{yf}$ , in a macro sense, is nil. Nevertheless, for comparison purposes, the axial fracture stress is defined as the load labelled  $F_f$  in Figure 2.3 divided by the final cross-section area, measured after a test. The equivalent fracture stress,  $\sigma_{fr}$ , is the axial fracture stress corrected for triaxial effects using equation (2.5). Also, the *fracture strain* is defined as a ratio between initial and final (as measured after test) cross-section areas. Clearly, after necking, the equivalent stress is not the true axial stress.

The measurement of the failure strain and stress is difficult, especially in displacement-controlled tensile test machines. The main difficulty here is to accurately record the specimen geometry at the maximum equivalent stress. Even so, this task will be pursued here because it might reveal some differences between failure and fracture stress and/or strain.

### 2.1.3 Strain rate

As previously commented, the actual strain rate in the material is a major issue. As soon as a tensile test commences, the axial strain increases almost linearly, indicating a constant strain rate. Around the upper yield point of the material here tested, there is a noticeable increase of the strain rate, lasting until the lower yield point is reached. The strain rate becomes constant again, but now at a higher level, and it stays more or less so until necking occurs. After necking, it is anticipated that the strain rate changes drastically.

Figure 2.4 illustrates this phenomenon for low strains. For large plastic strains, the strain rate pattern in the necking region is apparently not addressed in the literature, probably because of the difficulty in measuring such parameter at high speeds. Due to the potential importance of this topic, it

---

\*MACKENZIE *et al.*<sup>144</sup> showed that a macrocrack initiation is associated to a peak in the  $\sigma_{yy}$  *versus*  $\epsilon_{eq}$  curve. This implies in a peak in the  $\sigma_{eq}$  *versus*  $\epsilon_{eq}$  curve since  $\sigma_{yy}$  is proportional to  $\sigma_{eq}$ .

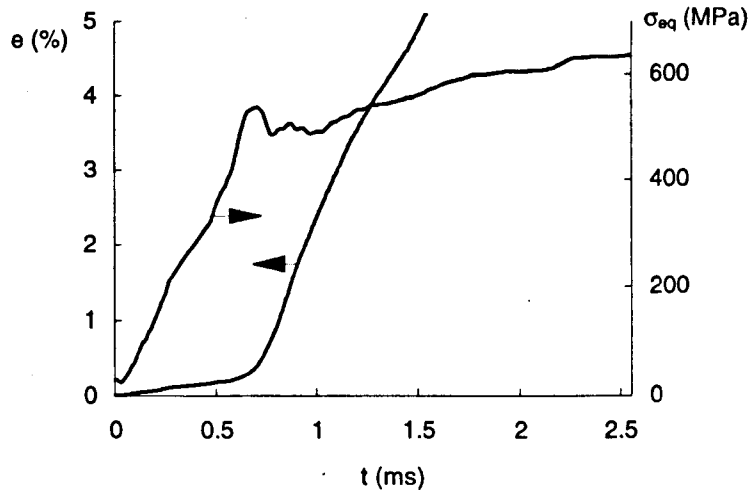


**Figure 2.4:** Evolution of the equivalent stress and engineering strain in a tensile test before necking. The material is a mild steel and the test speed 2.2m/s.

will be shown subsequently how this variable was measured.

Because the strain rate in a displacement controlled tensile test is not constant, it is opportune to introduce a definition of strain rate.

For that matter, consider again Figure 2.4. The marked change of strain rate around the upper yield point makes difficult to consistently use this strain rate in a constitutive equation. On the other hand, the strain rate just after the upper yield point is nearly constant until the ultimate stress. This strain rate, denoted by  $\dot{\epsilon}$ , will be used in the material constitutive law. Because  $\dot{\epsilon}$  is a true strain rate, it is slightly different from the engineering strain rate,  $\dot{\epsilon}$ , defined as the test speed divided by the initial gauge length. The engineering fracture strain rate,  $\dot{\epsilon}_{fr}$ , is defined as the fracture engineering strain divided by the test time.

The issues here commented will now be investigated.

## 2.2 Material

A mild steel is examined in this study with the BRITISH STEEL classification BS EN 10025 FE430A and having the *nominal* properties and composition



**Table 2.1:** Nominal material properties and chemical element concentrations (in weight %) for the BS EN 10025 FE430A steel.  $s_y$  and  $s_u$  are the engineering yield and ultimate stresses in MPa.  $e_{fr}$  is the traditional engineering fracture strain (in %).

$s_y$	$s_u$	$e_{fr}$	C	Si	Mn	P	S	Al
346	511	31	0.18	0.022	0.97	0.015	0.012	0.039

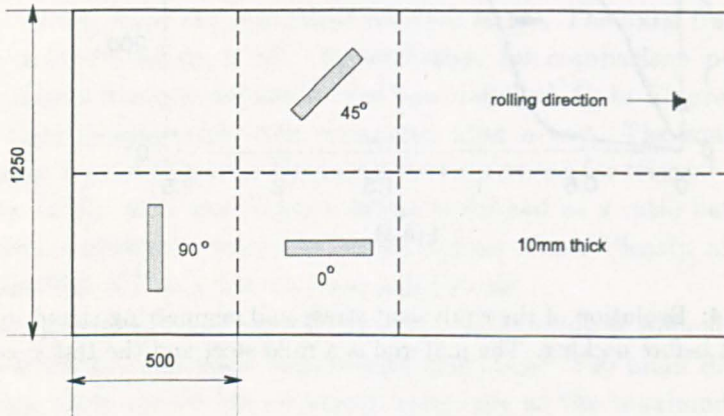


**Figure 2.5:** Plate as delivered indicating the directions used to cut the specimens. Dash lines indicate flame cut.

listed in Table 2.1.

The material was delivered as a long plate and it was flame cut according to the directions shown by the dashed lines in Figure 2.5. It was then cut with a band saw in strips of 12×300mm along the directions shown in the same figure. A few specimens were cut at 45° and 90°. The majority of the specimens are along the rolling direction. The minimum distance from the plate edges was set around 50mm in order to avoid the heat affected zone due to flame cutting. The strips were then turned into cylindrical bars and no heat treatment was performed.

The volume fraction of inclusions can be determined by the expression<sup>67</sup>

$$f_v(\%) = 5.4 \left( S(\%) - \frac{0.001}{Mn(\%)} \right), \quad (2.6)$$

which, using Table 2.1, gives  $f_v = 0.059\%$ . This is to be compared with the value of 0.03% measured for this material through the void counting procedure, as described in Chapter 4. This parameter is quoted here because

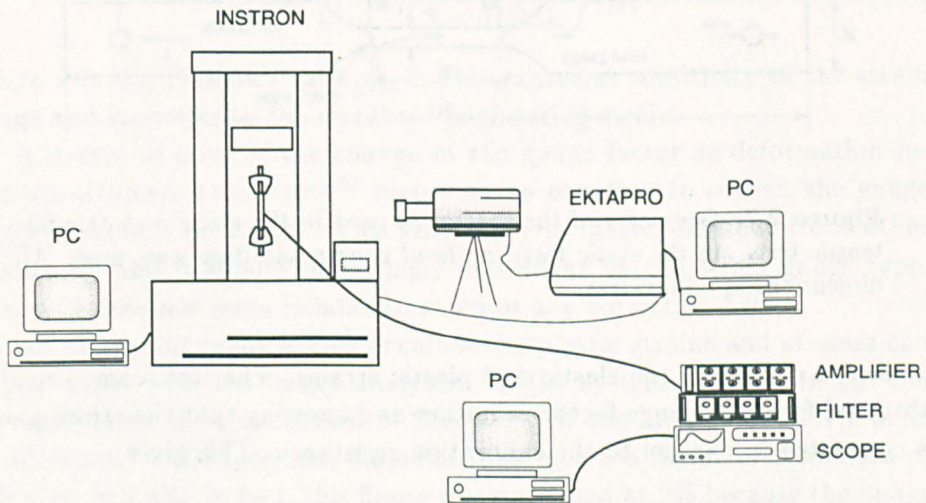


**Figure 2.6:** Schematic representation of the measurement system used in the static tensile tests.

of its importance in the micromechanics theories of failure, as the ones based on GURSON flow potential commented on Chapter 1.

## 2.3 Static tensile tests

The static tensile tests were conducted on an INSTRON 4204 tensile test machine. The head speed was set to 1mm/min, giving an average strain rate of  $\dot{\epsilon} = 4.0 \times 10^{-4} \text{s}^{-1}$ . The load and displacement signals in all the tests were recorded directly from the machine. In some cases, the transverse strain was measured using a mechanical/electrical INSTRON extensometer. Figure 2.6 shows the measurement system and Figure 2.7 shows the specimen geometry.

The strain gauges EP-08-125AD-120 from MICRO MEASUREMENTS, were connected in a quarter-bridge configuration. They are designed to sustain strains as high as 20%. The strain gauge signals were amplified separately in a FYLDE 359TA amplifier, whose linearity in the range of 0 to 5V was confirmed with a high precision signal generator. Two amplifier gains were

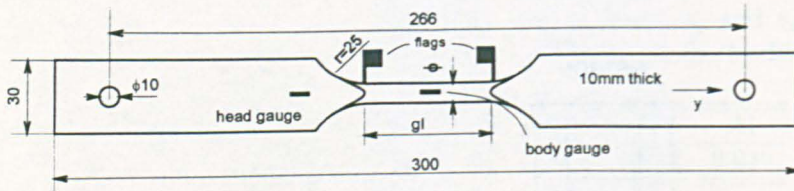


**Figure 2.7:** Geometry of the specimens used in the static and dynamic tensile tests. In the static tests, no head gauges and flags were used. All dimensions in millimetres.

chosen to cope with the elastic and plastic strains. The test scale is readily obtained from the gauge factor definition and knowing that the strain gauge is connected in parallel to the calibration resistance. This gives

$$e = (1/g_f) \times \{R_{sg}/(R_{sg} + R_{cal1})\}, \quad (2.7)$$

where  $e$  is the engineering strain,  $g_f$  is the gauge factor,  $R_{sg}$  is the strain gauge resistance and  $R_{cal1}$  is the internal amplifier resistance. All the resistance were measured with an accurate multimeter, SOLARTRON, model 7150.

The FYLDE output was fed into a TEKTRONIKS AM502 amplifier aiming only to filter eventual noise in the signal. The signals were then recorded in an oscilloscope GOULD 1604. From there, through a GPIB interface, the data were dumped to a PC486DX for eventual analysis.

Lastly, the neck formation was monitored using the EKTAPRO image analysis system, which is basically a video camera with a computer to store the image. Using simple procedures to define the image scale, the diameter and radius in the neck zone were measured. This information was then used to obtain the equivalent stress, as indicated later. A similar arrangement was used in references 28 and 68.

### 2.3.1 Validation

The procedure for static tensile testing is standard apart from the image recording system.

The transverse sensitivity of the strain gauges was corrected through

equation:<sup>150</sup>

$$e = \left( 1 - k_t \nu \frac{g_f}{1 - 0.285k_t} \right) e_m, \quad (2.8)$$

where  $\nu$  is the Poisson's ratio,  $k_t$  is the transverse sensitivity of the strain gauge and  $e_m$  refers to the measured engineering strain.

A source of error is the change in the gauge factor as deformation increases. HUANG AND KHAN<sup>87</sup> report on an equation to correct the gauge factor, function of strain. This correction is rather different from other sources,<sup>150</sup> and it should be strongly dependent on the strain gauge type. Hence, it does not seem reliable to attempt any correction here.

An important point is how accurate the plastic strains and stresses can be measured with the image analyser. In the system used, an image can be represented by a maximum of 238 pixel. If the analyst detects 1 pixel of difference in the specimen diameter, this means a diameter resolution of  $100 \times \frac{1}{238} = 0.4\%$ . In fact, this figure was estimated as 2% because the image does not fill the screen and because a difference of one pixel is not always easy to detect. An error of 2% in the diameter represents an error of 4% in the plastic strain measured by the diameter contraction. These figures, valid also for the axial stress, were confirmed when analysing notched specimens (see Chapter 3).

## 2.4 Dynamic tensile tests

The dynamic tensile tests were conducted in a displacement controlled ESH servo-hydraulic machine. The associated instrumentation is presented in Figure 2.8 and the geometry of the test specimen is depicted in Figure 2.7.

The specimen used in the dynamic tests have a smaller diameter when compared to the static ones. This reduces the dynamic load and allows the ESH machine to operate at higher speeds. Flags were also attached to the ends of the gauge length, as shown in Figure 2.7. They offer a reference mark to the ZIMMER, which records accurately their relative movement\*.

The strains were measured via strain gauges connected to an unbalanced WHEATSTONE bridge circuit. This instrument uses a stable power source and it is intrinsically non-linear, specially for high values of strain. The

\*The displacement transducer attached to the ESH machine gives a poor signal due to the machine compliance.

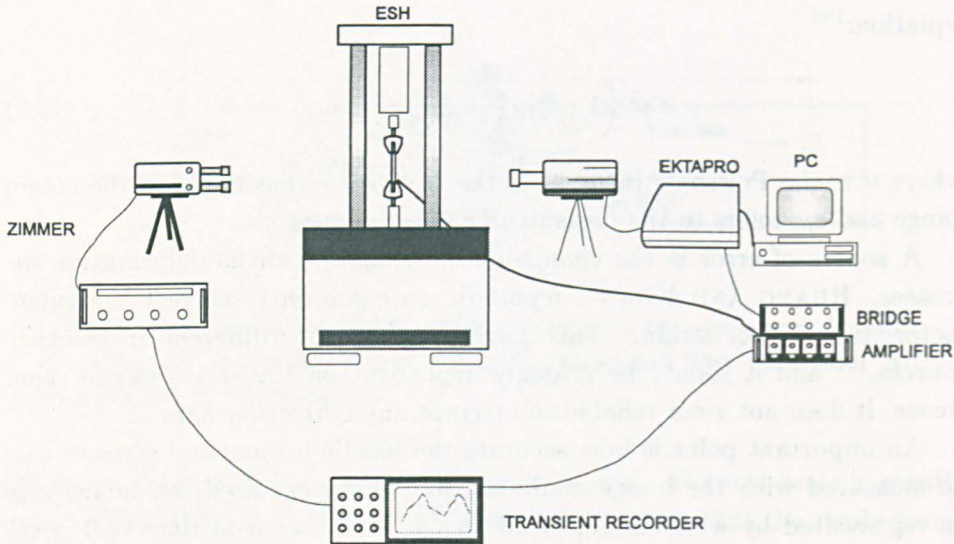


**Figure 2.8:** Schematic representation of the measurement system used in the dynamic tensile tests.

non-linearity was taken into account, when processing the data, through equation<sup>150</sup>

$$e = \left( 1 + \frac{g_f e_m}{2 - g_f e_m} \right). \quad (2.9)$$

The body strain gauges were connected in a half-bridge configuration; the signal was then split in two TEKTRONICS AM502 differential amplifiers with the filter set at 0.1MHz. Different gains were set in the amplifiers so that the elastic and plastic strains exhibited a good resolution. All the strain gauge calibration was direct, *ie* a resistance was connected in parallel to the gauges and the resulted voltage was accurately measured.

The signals were recorded by a 10MHz KONTRON transient recorder, model TRA800, for posterior analyses. In particular, this transient recorder has an amplifier accuracy of  $\pm 0.5\%$  and the time base can be set as small as 20ns\*. This capability was explored in order to fully record the load signal near fracture.

\*A small time base is strongly recommended in dynamic tests. DAVE and BROWN<sup>53</sup> discuss the main sources of error in a tensile test.

The minimum gauge length for the dynamic specimens was 40mm; smaller values would not provide adequate space for fixing the strain gauges and flags.

### 2.4.1 Validation

The image analyser was set in a similar way to the static tests. The main difference here is that the image had to be reduced up to one-eighth, depending on the test speed. At higher speeds, EKTAPRO does not record accurately curved contours. It is estimated that the diameter measured with the image are within a precision of 3%, which means a maximum error of 6% in the readings of strains and stresses. This error is slightly larger than in the static tests.

The signal from the head gauges were also used as an input for the EKTAPRO to synchronise the image system to the transient recorder. In fact, for very high speed tests, there is a delay between the load signal and the image since the former is measured at a different location from the later. This delay may be taken into account by shifting the time associated with the images by an amount which brings the load signal as recorded by EKTAPRO to the same values recorded by KONTRON. This procedure was done for all the tests where such shift occurred.

It is evident that in a tensile test, the load is a fundamental parameter. For static tests, force is relatively easy to measure but in the dynamic case it can be difficult. Figure 2.9 shows the load values in a typical dynamic test as measured by the load cell and by the gauges located on the enlarged end of the specimens. It can be seen that the load cell signal cannot be used in the analysis due to its strong fluctuation.

The scale for the head gauge was determined by keeping the amplifier gain constant throughout all the tests. By comparing head gauge and load cell signals at low speeds, a constant factor *load signal/strain gauge signal* was worked out. By knowing this factor and the strain gauge signal the load can be determined for higher speeds. This method works well, as confirmed by analysing data in regions where the load cell and head gauges signals do not present a significant variation.

Lastly, the accuracy of the displacement values, as recorded by the ZIMMER optical system, was easily checked by measuring the specimen length after the tests. It was confirmed that the figures were correct.

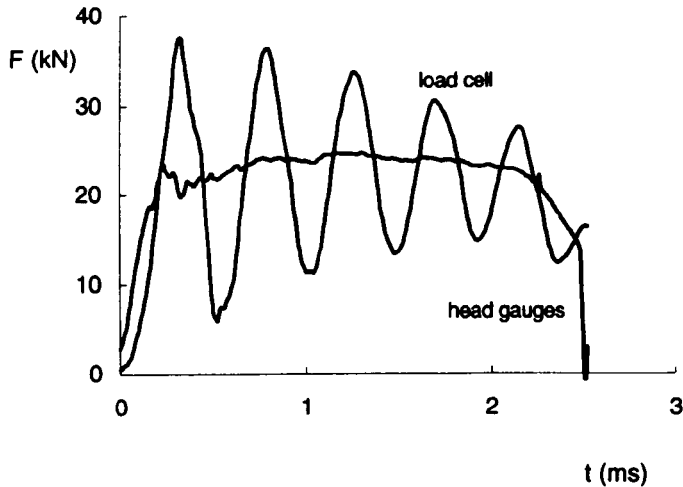


**Figure 2.9:** Load as measured by load cell and by head gauges. Test speed of 5.6m/s.

**Table 2.2:** Summary of some mechanical properties of mild steel at different orientations.

specimen	$E$ (GPa)	$\nu$	$s_{yield}$ (MPa)	$\sigma_{fr}$ (MPa)	$\epsilon_{fr}$
45°	213.5	0.313	332.0	929.1	1.14
90°	213.9	0.279	315.0	803.5	0.92

## 2.5 Results

Table 2.2 reports on the main mechanical properties of the material cut at 45° and 90° from the rolling direction. They are listed here for the sake of completeness though the main focus will be on the material behaviour along the rolling direction, whose data are listed in Table 2.3.

The engineering stress-strain curve is depicted in Figure 2.10. Not all the tests were plotted for the sake of clarity. The data were neither averaged, nor filtered by software nor interpolated. The various strain rates are also quoted.

From these data, it is possible to evaluate the true stress-strain curve using the expressions

$$\sigma_{yy} = s(1 + e) \quad \text{and} \quad \epsilon_{eq} = \ln(1 + e), \quad (2.10)$$

Table 2.3: Main results of the static and dynamic tensile tests.

spec		t028	t029	t036	t041	t080	t053	t087	t085	t082	t054	t086	t083	t084	t081	t089	t091	t090
$d_0$	mm	9.08	8.98	6.00	5.99	9.00	8.98	7.00	7.00	8.95	8.99	6.98	9.00	8.93	8.94	7.00	6.00	6.00
$d_{fr}$	mm	5.03	5.13	3.31	3.28	5.16	5.02	3.84	4.06	5.06	5.04	3.98	5.06	5.04	5.20	3.92	3.19	3.40
$gl$	mm	60	60	40	40	40	55	40	40	55	53	40	40	55	40	40	40	40
$\dot{\epsilon}$	$s^{-1}$		0.0004			1.4	1.8	1.9	2.1	7.8	8.7	16.1	39.2	72.6	105.5	195.1	208.8	239.9
$\dot{\epsilon}_{fr}$	$s^{-1}$				0.3		0.3	3.7	4.6	2.4	7.7	19.3	40.5	48.2	139.9	106.1	138.8	
$\epsilon_{fa}$		1.18	1.12	1.19	1.20	1.06	1.16	1.20	0.99	1.14	1.05	1.00	1.12		1.04		1.14	1.09
$\epsilon_{fr}$		1.18	1.12	1.19	1.20	1.11	1.16	1.20	1.09	1.14	1.14	1.12	1.15	1.14	1.08	1.16	1.26	1.14
$e_{fr}$				0.31	0.34	0.30		0.26	0.31	0.26	0.31	0.29	0.34	0.26	0.29	0.35	0.30	0.27
$e_u$			0.12	0.21	0.21	0.13		0.14	0.16	0.15	0.15	0.15	0.16		0.14	0.09	0.13	0.15
$\epsilon_{F_{max}}$			0.11	0.19	0.19	0.12		0.13	0.15	0.14	0.14	0.14			0.13	0.09	0.12	0.14
$\epsilon_{body}$				0.17	0.17	0.16	0.18	0.15	0.19	0.17	0.17	0.17	0.20	0.13	0.13	0.25	0.19	0.17
$\sigma_{y_{up}}$	MPa	320.0	314.5	333.0	329.3	390.9	386.6	399.6	425.0	426.3	424.6	428.4	515.6	540.4	563.8	579.9	550.1	623.1
$\sigma_{y_{low}}$	MPa	320.0	309.5	331.3	326.2	390.9	369.3	383.3	400.1	410.8	362.7	416.6	433.8	487.4	505.9	543.2	483.2	547.8
$s_u$	MPa	479.3	448.7	498.1	493.4	531.5		524.2	542.4	551.6	551.0	628.5	571.2	581.5	603.1	605.3	599.0	657.8
$\sigma_u$	MPa		502.5	603.7	598.4	601.7		598.6	628.1	635.4	632.5	720.9	661.4		685.7	661.0	676.9	757.8
$\sigma_{fa}$	MPa	908.2	889.6	1034.0	1022.5	911.3	894.8	965.8	1044.3	980.9	928.0	952.8	974.0		1132.9	989.9	952.9	1058.7
$\sigma_{fr}$	MPa			956.4	930.7			903.2	881.0	906.0	880.3	850.7	898.2		1016.9	919.1	915.7	982.5
$\sigma_{yf}$	MPa	1027.5	1049.4	1129.0	1118.3	925.3	974.0	1055.7	1037.4	1066.2	1036.6	1013.6	1092.0		1173.4	1077.2	1076.0	1145.5
$E$	GPa	212.9	206.6															
$R_{fr}$	mm			2.0	1.8	3.2		2.5	2.5	3.2	3.2	2.3	2.5	2.5	3.8	2.5	2.0	2.3
$\nu$		0.286	0.288															



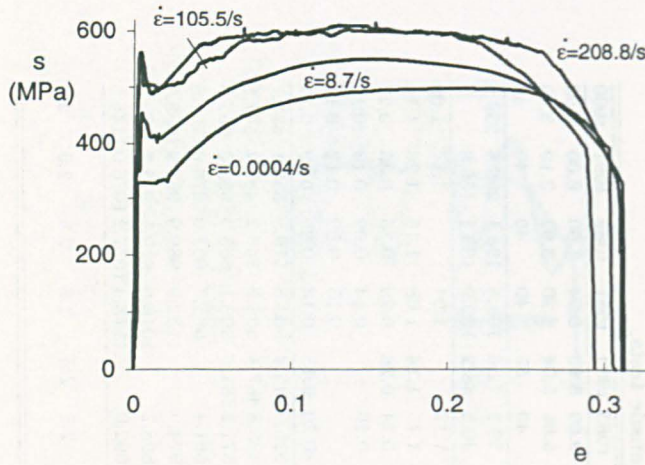


**Figure 2.10:** Engineering stress-strain curves for a mild steel with the strain rate labelled on the curves.

where  $s$  and  $e$  are the engineering stress and strain definitions. These equations are valid up to necking or, roughly, until the engineering stress achieves a maximum value. After this point, localisation occurs and the diameter-time history should be followed if the actual stress-strain points are required. Moreover, if the equivalent stress is being sought, it is necessary to monitor the radius evolution at necking. This can be done with the image system. One then arrive at the true equivalent stress-strain curve for the present material, Figure 2.11 \*. Up to an equivalent strain of around 20%, the curves are fully experimental. After that, only a few discrete points can be measured due to the limited sampling rate of the image system. A straight line was then used to interpolate the image data.

The curves presented in Figure 2.11 are those where an image at the peak equivalent stress was recorded. This was not always the case. To evaluate the failure equivalent stresses quoted in Table 2.3, one needs to know the necking radius and diameter at this point.

The diameter may be interpolated using specific values recorded for each test, as shown in Figure 2.12. The necking radius is used to correct the axial stress through the factor  $f_c$ . This was inferred by plotting the neck radius as a function of the plastic strain for various tests. These data were then

\*Elastic strains were disregarded after necking.

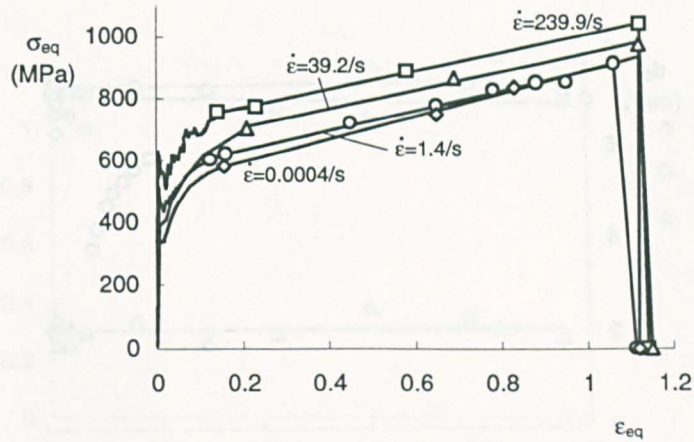


**Figure 2.11:** Equivalent stress–strain curves for a mild steel for various strain rates, as quoted.

interpolated to yield the factor  $f_c$ , plotted in Figure 2.13. It was not possible to infer whether  $f_c$  is affected by the strain rate.

The true equivalent failure and fracture strains and the engineering fracture strain are plotted in Figure 2.14. It can be noted that the failure strain, *ie* the strain associated with a maximum equivalent stress, tends to be slightly smaller than the fracture strain, *ie* the strain obtained measuring the diameter in the broken specimens. Also they are not affected by strain rate. The yield stress of the material is strain rate sensitive but the failure and fracture strains are not, at least within the range of strain rates measured.

Figure 2.15 shows the true equivalent strains at the maximum load,  $\varepsilon_{F_{max}}$ , and as measured by the diameter reduction far from the neck region,  $\varepsilon_{body}$ . If bifurcation had occurred at the maximum load, all the subsequent strain would have concentrated mainly in the neck zone. The fact that  $\varepsilon_{body}$  is higher than  $\varepsilon_{F_{max}}$  shows then that bifurcation takes place after the maximum load point. The strain rate does not affect either variables, again for  $\dot{\varepsilon} \leq 250\text{s}^{-1}$ .

Figure 2.16 shows the behaviour of the upper and lower yield stresses plus the ultimate tensile engineering stress against strain rate. The equivalent failure stress,  $\sigma_{fa}$ , the equivalent fracture stress,  $\sigma_{fr}$ , and the traditional

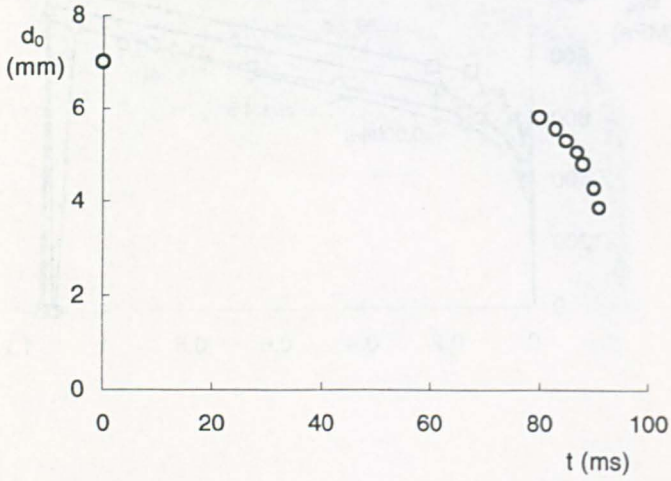


Figure 2.12: Diameter evolution for a tensile test at a speed of 0.1m/s.

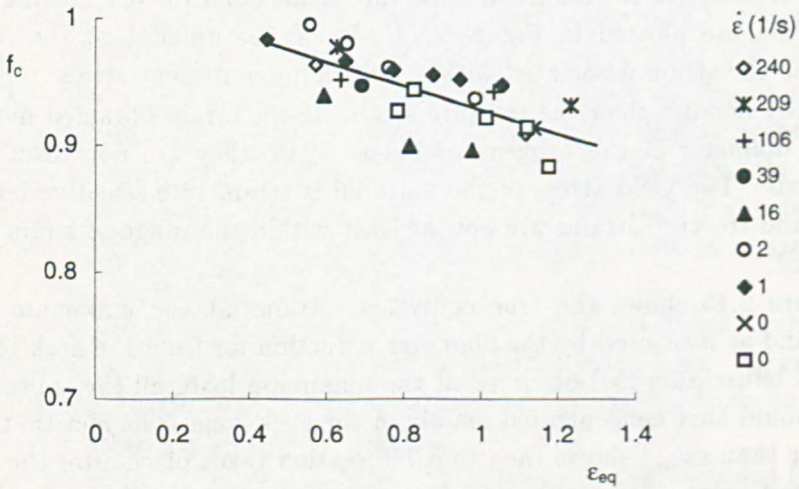
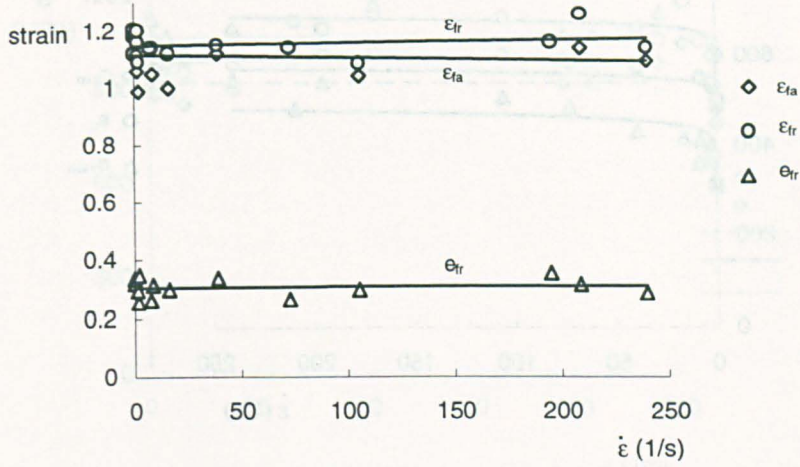
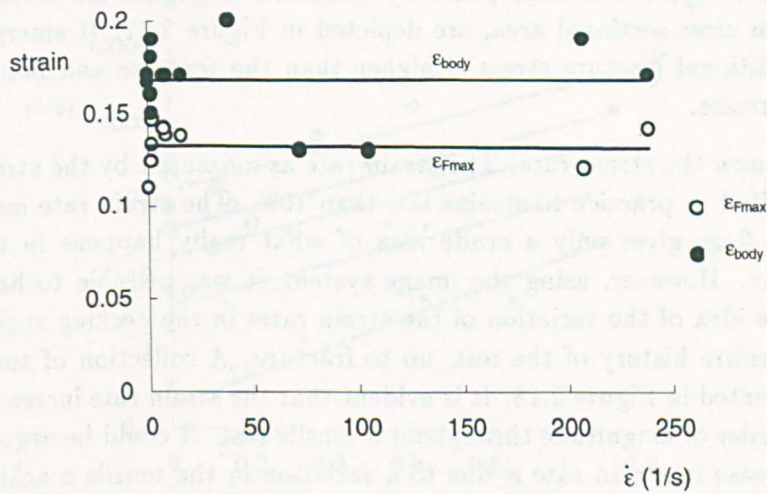


Figure 2.13: Correction factor used to estimate failure stress and strain. The various strain rates are also quoted.



**Figure 2.14:** Equivalent failure and fracture strains and engineering fracture strain *versus* strain rate. The lines are fitted linearly to the data.



**Figure 2.15:** Equivalent strain at maximum load,  $\epsilon_{Fmax}$ , and as measured by the diameter contraction,  $\epsilon_{body}$ , against strain rate. The lines are a linear fit to the data.

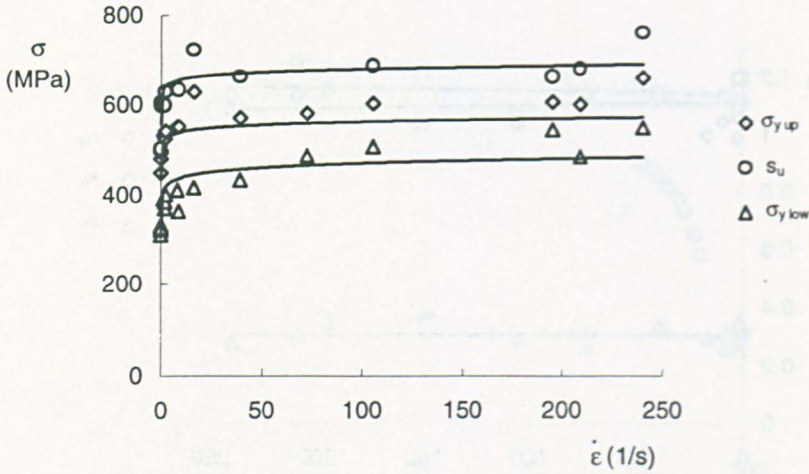


**Figure 2.16:** Evolution of upper and lower yield true stresses plus ultimate tensile engineering stress against strain rate. The lines are a logarithm fit to the data.

fracture stress,  $\sigma_{yf}$ , *ie* the load point  $F_f$  indicated in Figure 2.3 divided by the broken cross-sectional area, are depicted in Figure 2.17. It emerges that the traditional fracture stress is higher than the fracture and failure equivalent stresses.

Consider now the strain rate. The strain rate as measured by the strain gauges is limited in practice to strains less than 10%. The strain rate measured by the flags gives only a crude idea of what really happens in the necking region. However, using the image system, it was possible to have a quantitative idea of the variation of the strain rates in the necking region through the entire history of the test, up to fracture. A collection of some curves is presented in Figure 2.18. It is evident that the strain rate increases at least one order of magnitude throughout a tensile test. It could be argued that this increase in strain rate is due to a variation in the tensile machine speed during the test. To disregard this hypothesis, the displacement behaviour in a low and in a high speed test is depicted in Figure 2.19. It is evident that the speed is nearly constant for both cases, confirming that the change in strain rate is a phenomenon in itself for displacement controlled tensile tests.

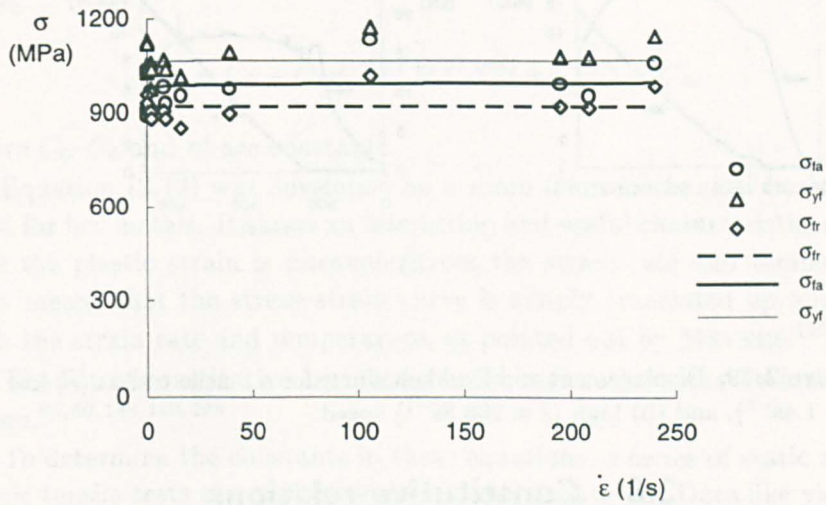


**Figure 2.17:** Equivalent failure stress,  $\sigma_{fa}$ , equivalent fracture stress,  $\sigma_{fr}$ , true axial fracture stress,  $\sigma_{yf}$ , against strain rate. The lines are a logarithm fit to the data.

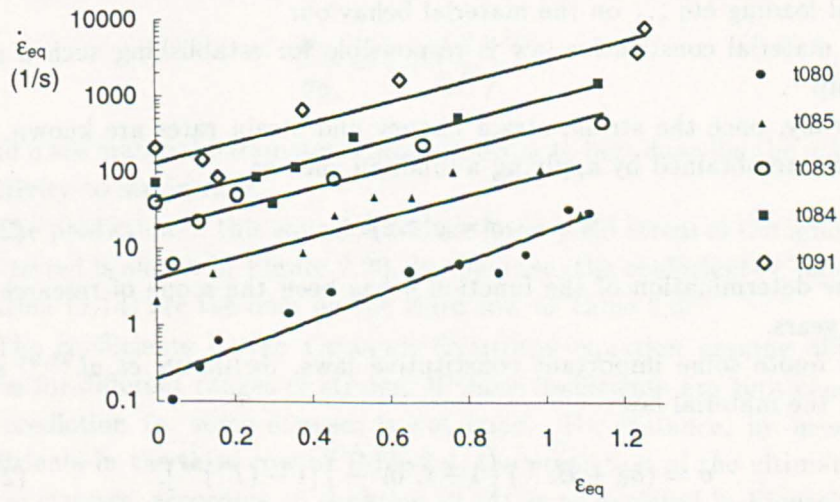


**Figure 2.18:** Equivalent strain rate evolution as a function of the equivalent plastic strain. The straight lines are an exponential fit to the data.

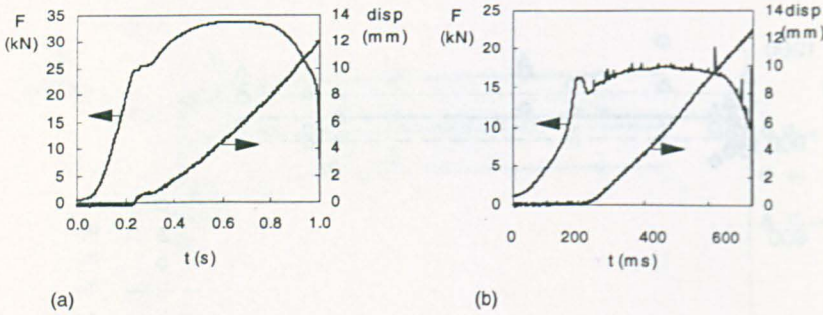


**Figure 2.19:** Displacement and load behaviour for a tensile test at (a) low ( $\dot{\epsilon} = 1.4\text{s}^{-1}$ ), and (b) high ( $\dot{\epsilon} = 208.8\text{s}^{-1}$ ) speed.

## 2.6 Constitutive relations

As anticipated in Figures 2.10 and 2.11, the strain rate plays a fundamental role in the material behaviour and it causes the yield stress to increase by a factor as large as two in the present test programme. Hence, it is important to not only relate stresses to strain but also to strain rate, without mentioning and considering the well known influence of temperature, load history, biaxial loading etc ... on the material behaviour.

A material constitutive law is responsible for establishing such a relationship\*.

Ideally, once the strain, strain history and strain rates are known, the stresses are obtained by applying a function such as

$$\sigma = g(\epsilon, \dot{\epsilon}). \quad (2.11)$$

The determination of the function  $g$  has been the scope of research for many years.

To quote some important constitutive laws, JOHNSON *et al.*<sup>93,94</sup> suggested the material law

$$\sigma = (\sigma_0 + B\epsilon^{n'}) \left( 1 + C \ln \frac{\dot{\epsilon}}{\dot{\epsilon}_0} \right) [1 - (T^*)^{m'}], \quad (2.12)$$

with the experimental parameters  $\sigma_0$ ,  $B$ ,  $C$ ,  $n'$  and  $m'$ .  $T^*$  is a temperature term and  $\dot{\epsilon}_0$  is a reference strain rate. Also, ZERILLI and ARMSTRONG<sup>220,221</sup>

\*HAUPT offers a review on mathematical modelling of material behaviour.<sup>82</sup>

proposed the following relation among stress, strain, strain rate and temperature

$$\sigma = C_0 + C_1 e^{(-C_3 T + C_4 T \ln \dot{\epsilon})} + C_5 \dot{\epsilon}^{n'} + C_6, \quad (2.13)$$

where  $C_0$ – $C_6$  and  $n'$  are constants.

Equation (2.13) was developed on a more micromechanical basis and is valid for bcc metals. It shows an interesting and useful characteristic, namely that the plastic strain is *uncoupled* from the strain rate and temperature. This means that the stress–strain curve is simply translated up and down with the strain rate and temperature, as pointed out by MEYERS.<sup>149</sup>

The list of constitutive laws is extensive and reviews can be found elsewhere.<sup>65, 80, 148, 149, 228</sup>

To determine the constants in these equations, a series of static and dynamic tensile tests are performed for a certain material. Data like yield and ultimate stresses are plotted *versus* strain rate. The coefficients in these equations are then determined in order to bring the prediction of the constitutive equation as close as possible to the data.

Consider now the widely used COWPER–SYMONDS equation\*. It relates the static,  $\sigma_{0_s}$ , and dynamic,  $\sigma_{0_d}$ , flow stresses to the uniaxial strain rate,  $\dot{\epsilon}$ , according to

$$\frac{\sigma_{0_d}}{\sigma_{0_s}} = 1 + \left( \frac{\dot{\epsilon}}{C} \right)^{1/q}. \quad (2.14)$$

$C$  and  $q$  are material parameters chosen in order to best describe the material sensitivity to strain rate.

The prediction of this equation for the lower yield stress of the mild steel here tested is shown in Figure 2.20. In this case, the coefficients  $C$  and  $q$  in equation (2.14) are the ones on the third row of Table 2.4

The coefficients in the COWPER–SYMONDS equation assume different values for different ranges of strains. If these coefficients are kept constant, the prediction for some stresses is not good. For instance, by using the coefficients in the third row of Table 2.4, the prediction of the ultimate and failure stresses, according to equation (2.14), is as depicted in Figure 2.20.

Table 2.4 lists different coefficients for the COWPER–SYMONDS equation according to the stress and strain rate data used.

\*EL-MAGD<sup>65</sup> attributes this expression to P. LUDWIK.



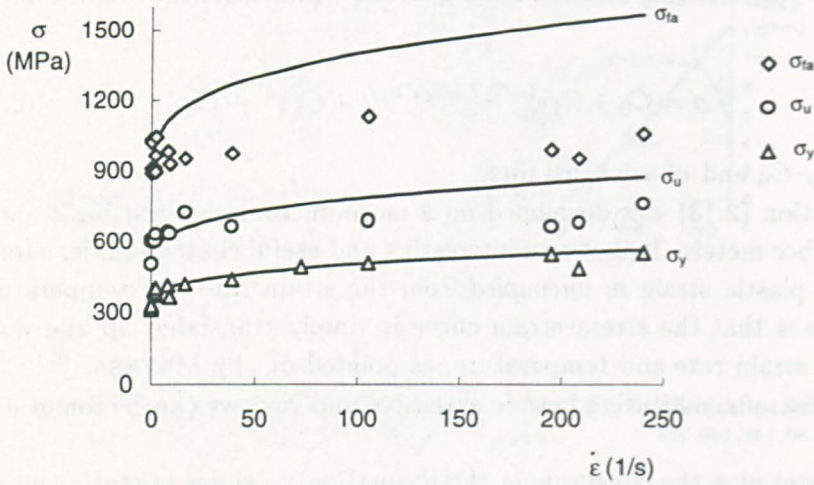


**Figure 2.20:** Prediction of the dynamic yield, ultimate and failure stresses versus the strain rate, according to equation (2.14). The coefficients  $C$  and  $q$  for all the predictions are listed on the third row of Table 2.4. The symbols are experimental data for mild steel.

By making the coefficient  $C$  in equation (2.14) strain dependent, JONES<sup>98</sup> suggested an alternative equation to grasp the material strain rate sensitivity to ultimate stress. The prediction of his equation for the ultimate stress is

$$\frac{\sigma_{u_d}}{\sigma_{u_s}} = 1 + \left( \frac{\dot{\epsilon}}{C_u} \right)^{1/q} \quad (2.15)$$

$C_u$  is obtained in the same way as  $C$  but now using the dynamic and static ultimate stresses,  $\sigma_{u_d}$  and  $\sigma_{u_s}$ .  $q$  is considered a material constant, though there is no restriction of it being strain dependent. Equation (2.15) is valid

**Table 2.4:** Coefficients of the COWPER-SYMONDS equation.

stress	based on strain rate	$C(s^{-1})$	$q$
$\sigma_{y_{up}}$	$\dot{\epsilon}$	360.07	3.428
$\sigma_{y_{low}}$	$\dot{\epsilon}$	598.13	3.052
$\frac{1}{2}(\sigma_{y_{up}} + \sigma_{y_{low}})$	$\dot{\epsilon}$	550.43	3.439
$\sigma_{y_{low}}$	$\dot{\epsilon}_{fr}$	411.62	3.244

up to the ultimate strain and it reduces to the COWPER-SYMONDS equation at yielding if  $C_u$  is replaced by  $C$ .

Clearly, in order to obtain a good prediction for stresses, the coefficients in equation (2.14) have to be strain dependent. An equation with strain dependent coefficients is more complicated to deal with than its counterpart, with constant coefficients. This is especially significant when using analytical methods in structural analysis.

The fact that the COWPER-SYMONDS equation is not suitable for the prediction of a broad range of stresses, unless its coefficients are variables, suggests to search for an alternative equation, with the feature of keeping a balance between simplicity and accuracy. An empirical equation which can fit well over the entire range of stresses, strains and strain rates for the present experimental data is

$$\frac{\sigma_{eqd}}{\sigma_{eqs}} = 1 + \frac{\sigma}{\sigma_{eqs}} \left( \frac{\dot{\epsilon}}{C} \right)^{1/q}, \quad (2.16)$$

or

$$\sigma_{eqd} = \sigma_{eqs} + \bar{m}\dot{\epsilon}^{\bar{n}}, \quad (2.17)$$

where

$$\bar{m} = \frac{\sigma}{C^{1/q}} \quad \text{and} \quad \bar{n} = \frac{1}{q}. \quad (2.18)$$

In equation (2.17),  $\sigma_{eqd}$  and  $\sigma_{eqs}$  are the dynamic and static equivalent stresses, respectively. The coefficients  $C$  and  $q$  in equation (2.16) is determined in the same way as in COWPER-SYMONDS's. The parameters  $\sigma$  and  $\dot{\epsilon}$  can be freely chosen based on the available experimental data or application. Upon this choice, the coefficients  $C$ ,  $q$ ,  $\bar{m}$  and  $\bar{n}$  will assume specific values.

For instance, the coefficients  $C$  and  $q$  could be evaluated using ultimate stresses and overall strain rates in tensile tests, or even stresses and strain rates at a specific strain. Once the coefficients are determined they are kept constant; yet any stress can be predicted.

If the yield stress,  $\sigma_y$ , and the strain rate  $\dot{\epsilon}$  are used for the evaluation of  $\bar{m}$  and  $\bar{n}$ , equation (2.16) is written as

$$\frac{\sigma_{eqd}}{\sigma_{eqs}} = 1 + \frac{\sigma_y}{\sigma_{eqs}} \left( \frac{\dot{\epsilon}}{C} \right)^{1/q}. \quad (2.19)$$

This equation allows the prediction of the dynamic yield, ultimate and failure stresses according to

$$\sigma_{y_d} = \sigma_{y_s} + \sigma_{y_s} \left( \frac{\dot{\epsilon}}{C} \right)^{1/q} \quad (2.20)$$

$$\sigma_{u_d} = \sigma_{u_s} + \sigma_{y_s} \left( \frac{\dot{\epsilon}}{C} \right)^{1/q} \quad (2.21)$$

and

$$\sigma_{f_{a_d}} = \sigma_{f_{a_s}} + \sigma_{y_s} \left( \frac{\dot{\epsilon}}{C} \right)^{1/q}, \quad (2.22)$$

respectively.

These equations make clear that any dynamic stress can be predicted, yet keeping the coefficients  $\bar{m} = \sigma_{y_s}/C^{1/q}$  and  $\bar{n} = 1/q$  constants.

Figure 2.21 plots equations (2.20)–(2.22) together with the experimental data for the mild steel.

## 2.7 Discussion

The various parameters recorded in the experiments help to draw a clear picture of how the material behaves under different strain rates. The material is reasonably homogeneous and its yield point is strain rate sensitive, Figure 2.21, but not the failure strain, Figure 2.14. The results shown in Figure 2.14 indicate a slight difference between the failure and fracture strain. However, this difference is not significant.

The strain at which the onset of inhomogeneous behaviour occurs is higher than the strain at the maximum load, Figure 2.15. Also, it is not strain rate sensitive in the range tested. The bifurcation point is important and it is associated with the beginning of damage growth, as discussed in Chapter 4.

A distinction exists between the traditional true fracture stress,  $\sigma_{yf}$ , ie fracture load divided by the final area, the equivalent fracture stress,  $\sigma_{fr}$ , ie  $\sigma_{yf}$  corrected for triaxial effects, and the equivalent stresses at failure,  $\sigma_{fa}$ , ie at the peak equivalent stress. This difference is attributed mainly to the growth of the hoop and radial stresses in the necking zone, which causes an increase in the hydrostatic stress  $\sigma_h$ .

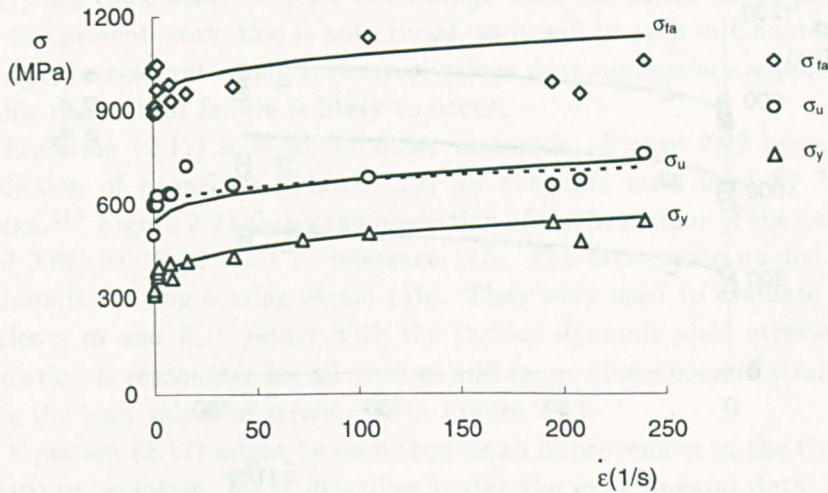


**Figure 2.21:** Experimental results for lower yield, ultimate and equivalent failure true stresses *versus* strain rate. Dotted line is the prediction of equation (2.15),<sup>98</sup> with  $C_u = 14426\text{s}^{-1}$  and  $q = 3.052$ . Thick lines are the prediction of equations (2.20)–(2.22), with  $\bar{m} = 38.4\text{s}$  and  $\bar{n} = 0.328$ . When  $C_u = C$ , equation (2.15) gives the same result as equation (2.20) when predicting the lower yield stress.

Observe that  $\sigma_{fr}$  is smaller than  $\sigma_{fa}$  by 8% because the fractured neck radius is smaller than the radius at the maximum equivalent stress. On the other hand, the common fracture stress,  $\sigma_{yf}$ , is larger than the failure,  $\sigma_{fa}$ , and fracture,  $\sigma_{fr}$ , equivalent stresses, also by a factor of 8%. This is all expected since no triaxial effect due to necking is taken into account. The difference between  $\sigma_{yf}$  and  $\sigma_{fr}$  is about 15%.

YU and JONES<sup>216</sup> have simulated numerically a tensile test and have found a difference of about 12% between the traditional fracture stress,  $\sigma_{yf}$ , and the fracture equivalent stress,  $\sigma_{fr}$ . They have simulated cylindrical tensile specimen made of a mild steel. This difference of 12% is to be compared with the 15% difference here measured\*. The ratio,  $\sigma_h/\sigma_{eq}$ , an important parameter which might govern the failure process, achieves a maximum of about 1/2, according to equation (3.2), at the centre of the specimen, in contrast to the uniaxial case where it is 1/3.

\*GALENKAMP and WIJNGAARDEN<sup>68</sup> reports on a difference between  $\sigma_{yf}$  and  $\sigma_{fa}$  as large as 30% for an aluminium alloy.

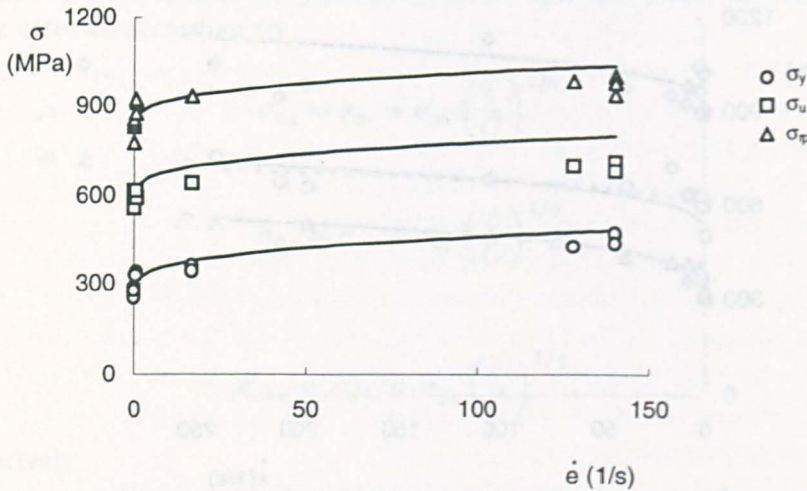


**Figure 2.22:** Experimental results for lower yield, ultimate and fracture true stresses *versus* engineering strain rate for the mild steel used in reference 218. The lines are the prediction of equation (2.17).

As far as the strain rate behaviour in a tensile test is concerned, the literature reports on strain rates at small plastic strains, up to necking. It was shown in Figure 2.18 that there is a rapid increase of the strain rate in the necking region. The high value of strain rates in the necking zone might have some inertial influence on void formation. The exponential character of the strain rate in a displacement controlled test induces also an exponential acceleration. Consequently, the inertia effect tends to be high. This might produce a retarding effect on the void growth. Even so, the complete picture is not clear since other factors are involved in the failure mechanism.

The COWPER-SYMONDS equation is not able to predict the present material behaviour for a broad range of strains, unless its coefficients change. Equation (2.17) offers an alternative, where any stress can be predicted reasonable well for any input plastic strain. It differs from the COWPER-SYMONDS equation just by a coefficient. Also, the dynamic yield stress prediction rendered by equation (2.17) can be reduced to the COWPER-SYMONDS constitutive law, equation (2.14), as shown by equation (2.20).

The advantage of equation (2.17) is that it can predict dynamic stresses of tensile tests at any plastic strain, inclusive of stresses in the softening regime. As already emphasised, once the parameters  $\bar{m}$  and  $\bar{n}$  in equation

(2.17) are calculated, they do not change with the stress to be predicted. For the present work, this is not crucial, as it will be seen in Chapter 5, but it might be relevant where true stress values near rupture are required. It is in this region that failure is likely to occur.

Equation (2.17) is valid for other materials. Figure 2.22 presents the prediction of equations (2.20)–(2.22) for the mild steel used by YU and JONES.<sup>218</sup> Figure 2.23 shows the prediction of the behaviour of the austenitic steel X6CrNi 18 11 used in reference 115. The strain rate quoted by the authors is the engineering strain rate. They were used to evaluate the coefficients  $\bar{m}$  and  $\bar{n}$ , together with the various dynamic yield stresses. The prediction is reasonable for all stresses and range of strains and strain rates. Note the high values of strain rate in Figure 2.23.

Equation (2.17) might be seen then as an improvement in the COWPER-SYMONDS equation, for it describes better the experimental data. Also it contains a more simple mathematical expression when compared to equations (2.12) and (2.13), for instance. This is potentially important for numerical analysis as well as for analytical solutions of structural impact problems.

The prediction of equation (2.17) was demonstrated using basic stress, strain and strain rate data. Needless to say, further studies are necessary to test its validity for other load configurations and for actual structures.

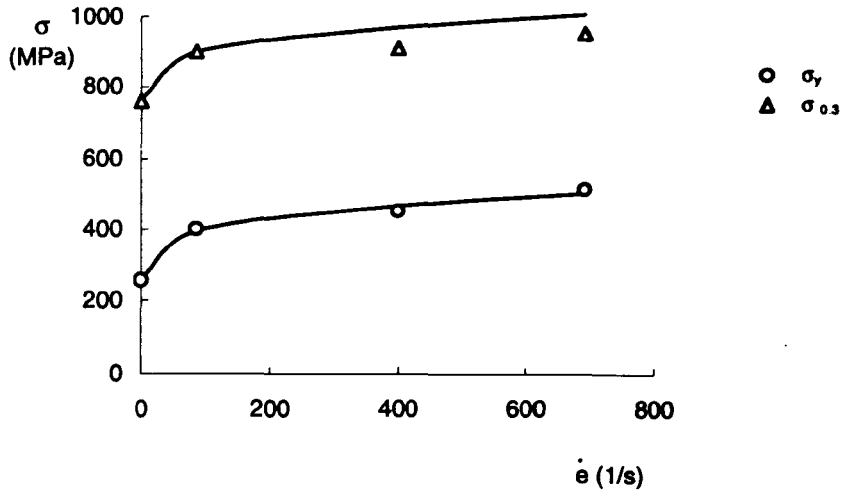


**Figure 2.23:** Experimental results for lower yield and the stress at a true equivalent strain of 0.3 for the austenitic steel used in reference 115. The lines are the prediction of equation (2.17).

---

## 3 Stress State Influence on Failure

IT COULD BE argued that the maximum equivalent stress or strain, which a structure is capable of bearing, coincides with the equivalent failure stress and strain measured in a tensile test. Hence, a failure criterion would be dictated by single and simple parameters as the equivalent strain or, analogously, the equivalent stress. Nonetheless, the problem is far from being simple. In fact, paradoxically or not, a structure can sustain loads that cause strains *higher* than the corresponding material failure values in a tensile test. Conversely, equivalent strains much *lower* than the material rupture values in a tensile test may trigger the rupture process in a structure.

That a structure may sustain strains higher than the corresponding material failure can be seen in Figure 3.1, extracted from reference 5. There, a 6061-T6 aluminium disk was impacted with a hardened steel rod at a velocity of 84m/s. The figure shows the contours of the equivalent plastic strain, whose maximum value is around 0.42. This is nearly three times the material failure strain in a uniaxial tensile test reported in the same reference\*.

On the contrary, a total structure collapse may happen for equivalent strains much lower than the respective material failure strain. This is illustrated in Figure 3.2, where a typical equivalent stress-strain curve is presented together with points associated with structural failure. In this case, failure strains as low as nearly one-half the corresponding material failure strain, measured in a tensile test, were obtained.

There exist several reasons for structure failure with such a broad range of strains. Some of them are not yet known but it is generally acknowl-

---

\*The equivalent fracture strain for the aluminium is inferred from the data in Figure 13 of reference 5.



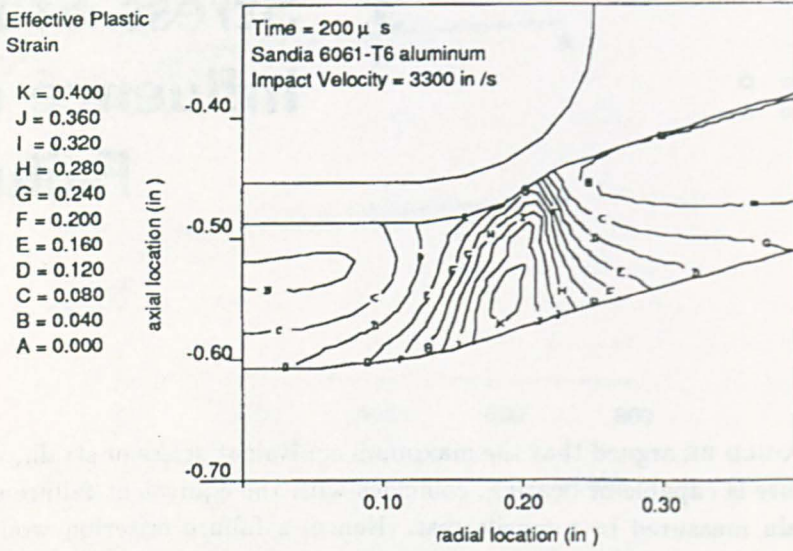


Figure 3.1: Effective plastic strain contour for an aluminium disk impacted by a rod at a velocity of 84m/s. Regions E-K are strained beyond the corresponding material elongation failure in a uniaxial tensile test (after BAMMANN *et al.*<sup>5</sup>).

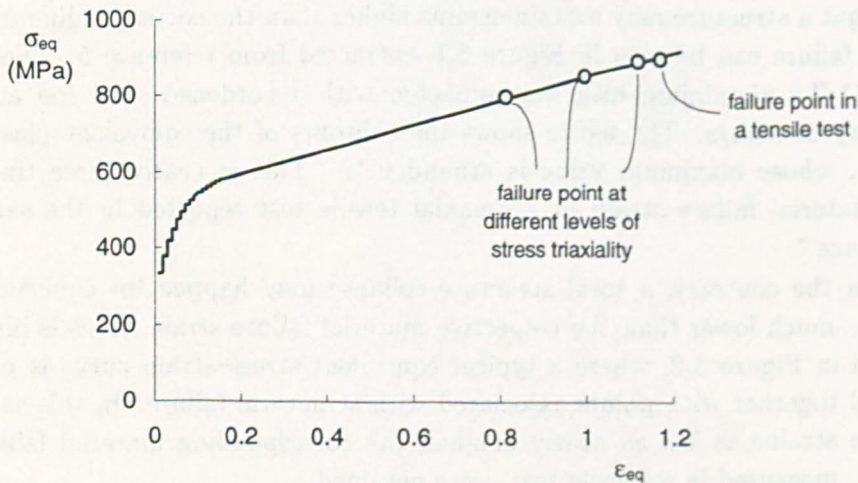


Figure 3.2: Equivalent stress-strain curve and points associated with experimental failure of notched and tensile specimens. The specimens were made from the same mild steel.

---

edged that the hydrostatic stress, or pressure, plays an important role in determining the spectrum of strains to failure.

The hydrostatic stress at a point is defined as the average of the main diagonal of the stress tensor at that point. Some authors prefer to refer to the hydrostatic stress as the negative of the stress tensor trace, but throughout this work, a positive hydrostatic pressure is associated with tension. As such, an external fluid surrounding a structure would apply on it a negative pressure. This pressure would work in a way to avoid material separation, hence retarding failure initiation. Experiments confirm that there is an increase of the ductility of metals with the increase of the fluid pressure surrounding them.<sup>27,28</sup> Even when no fluid is present, it is possible to generate negative pressures in a structure by the sole action of the load. Nevertheless, the most common case is when the load causes a positive pressure, *ie* the stress state is such that tends to act in desegregating the material. Moreover, the commonplace reasoning is that regions in the structure exposed to higher hydrostatic stress are more likely to fail first. In other words, the failure sites are dictated by the pressure intensity.

The above commentaries emphasise the major importance of knowing quantitatively the influence of the hydrostatic stress on material failure. This can be achieved by pulling specimens in tension with an external machined notch. The idea of this test probably comes from the analysis due to BRIDGMAN, who showed that the hydrostatic stress state inside a necked tensile specimen is a function of the necking radius. By changing the machined notch radius, different levels of hydrostatic stress in the specimen are obtained, leading the specimen to fail at different strains.

This chapter describes static and dynamic notch tensile tests performed in specimens made of the same mild steel tested according to Chapter 2. The main results are presented and commented, followed by a static Finite-Element simulation of these tests. The numerical analysis is then compared with the BRIDGMAN prediction. The influence of the material properties on the triaxiality, a parameter defined in sequence, is also explored. The chapter ends with a discussion about the actual influence of the hydrostatic stress on failure, showing that the traditional analysis of notch tests used to generate the so-called envelope failure curves is not suitable for the material here tested.

### 3.1 Notch tensile tests

Basically, the notch tensile tests aim to induce different levels of stresses in the material, obtained by machining specimens with different notch radii  $R$ . This precipitates failure at different strains which are correlated to some measure of the stress state, usually the hydrostatic to equivalent stress ratio, or triaxiality. By using an appropriate analysis, the triaxiality along the minimum cross-section becomes known. This can be partially accomplished by applying the BRIDGMAN formulation described in the previous chapter, originally meant to explore the necking phenomenon in cylindrical rods.

One of the early studies in determining to what extent the hydrostatic stress influences the failure strain is due to MCCLINTOCK.<sup>146</sup> He achieved his theoretical results by analysing a long circular cylindrical cavity embedded in a non-hardening matrix pulled axially while subjected to transverse tensile stress. His analysis was expanded further by RICE and TRACEY,<sup>175</sup> who studied the stress triaxiality influence on the growth of a spherical void and by GURSON,<sup>75</sup> who proposed a flow rule for a porous material. All these studies have confirmed theoretically the pressure influence on the strain to failure.

A pioneering experimental programme using notched specimens is due to MACKENZIE *et al.*<sup>144</sup> By testing different materials and different specimen geometry they were able to produce extensive data about the influence of the pressure on failure strain. Their triaxiality *versus* failure strain plots, also known as failure envelopes, do show a marked decrease of the ductility as the triaxiality increases. Similar static tests were performed by others to explore further the RICE-TRACEY model,<sup>17,18,117</sup> fracture mechanics,<sup>57</sup> failure criteria<sup>36,86,158</sup> and material modelling.<sup>219</sup>

Dynamic notch tensile tests have also been performed.<sup>1,6,61,62</sup> Some results show a decrease of the failure strain with the increase of strain rate and hydrostatic stress.<sup>1,6</sup> Others, on the contrary, show that the strain rate has no influence on failure strain regardless of the triaxiality level, as measured by BARTON *et al.*<sup>6</sup> for copper\*.

Obviously, the influence of the strain rate and pressure on failure is particular to each material. It is natural then to enquire how these parameters affect the failure strain of the mild steel characterised in Chapter 2, a subject to be explored on the next section.

---

\*EL-MAGD<sup>65</sup> reviews these works in a broader context of material properties.

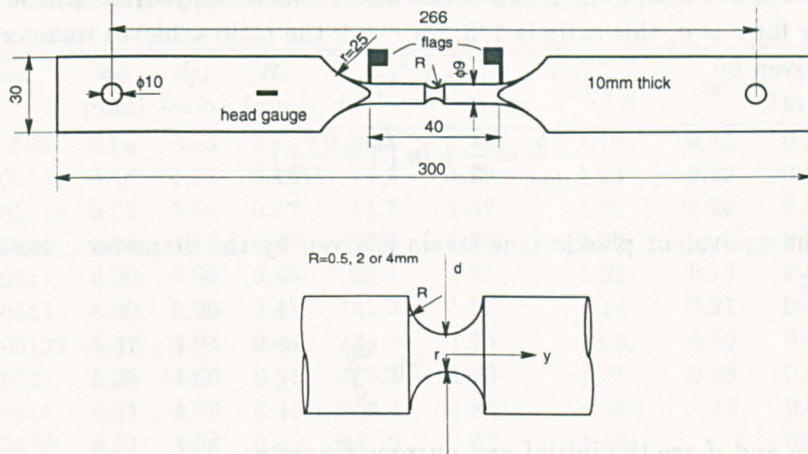


**Figure 3.3:** Geometric representation of a dynamic notched tensile specimen. The static ones are similar except for the non-presence of head gauges and flags. All dimensions are in millimetres.

## 3.2 Experimental set-up and results

A series of static and dynamic notch tensile tests were performed using the same arrangement described in the previous chapter, Figures 2.6 and 2.8, respectively. The specimens, a typical one depicted in Figure 3.3, were cut in the rolling direction from the plate shown in Figure 2.5 of Chapter 2. They were machined with three different notch radii and slightly different diameters. The specimens were designated n05, n2 and n4 for small, medium and large radius (around 0.5mm, 2mm and 4mm), respectively.

As in the tensile tests, a camera was used to monitor the evolution of the diameter and radius in the notch region. Also, the load in the dynamic tests was measured from the head gauges. The calibration procedure and validation are similar to the ones described in the previous chapter. Table 3.1 lists the relevant results from the tests.

The notch tests aim to reveal to what extent the hydrostatic pressure in conjunction with different strain rates influences the strain to failure. From the BRIDGMAN analysis, it is possible to evaluate the ratio  $\sigma_h/\sigma_{eq}$ , where  $h$  stands for hydrostatic and  $eq$  for equivalent. It follows that

$$\frac{\sigma_h}{\sigma_{eq}} = \frac{1}{3} + \ln \left( \frac{a^2 + 2aR - r^2}{2aR} \right), \quad (3.1)$$

where  $r$  measures the radial position at the minimum cross-section,  $a$  is the diameter of the minimum cross-section and  $R$  the notch radius. At the notch base, *ie* for  $r = a$ , this ratio is  $1/3$ ; for  $r = 0$  the ratio achieves its maximum value given by

$$\frac{\sigma_h}{\sigma_{eq}} = \frac{1}{3} + \ln \left( 1 + \frac{a}{2R} \right). \quad (3.2)$$

Also, the equivalent plastic true strain is given by the diameter contraction through

$$\varepsilon_{eq} = 2 \ln \frac{d_0}{d}, \quad (3.3)$$

where  $d_0$  and  $d$  are the initial and current diameter.

Equation (3.1) shows that the smaller the notch radius  $R$ , the bigger the stress ratio at the middle of the specimen, being  $1/3$  at the notch base regardless of the value of  $R$ . Hence the idea of decreasing  $R$  to increase the triaxiality and of measuring the diameter contraction in the broken specimen to infer the fracture strain. By doing that, a plot similar to the one in Figure 3.4 may be obtained.

For the specimens tested here, the nominal peak values of stress triaxiality, according to equation (3.2), are around 1.8, 1.1 and 0.6 for the n05, n2 and n4 specimens, respectively. These figures are based on the initial nominal geometry, a common practice in the literature. Nevertheless, unlike other investigators, the use of a high-speed camera to record the tests allows one to measure the necking geometry, *ie* the current notch radius and diameter, *as the test progresses*. Clearly, the notch radius  $R$  increases and the diameter  $2a$  decreases which, according to BRIDGMAN, would cause a reduction of the stress triaxiality.

After processing the image data, the *geometric* parameters  $\sigma_h/\sigma_{eq}$ , equation (3.2), at the central axes of the specimens, and the equivalent true strain, equation (3.3), were evaluated, Figure 3.5. The various labels in the figure refer to different strain rates averaged between the ultimate and fracture strains. It can be seen that the triaxiality for strains higher than, roughly, the material ultimate strain, tends to values not as large as one would predict from the initial geometry and when using equation (3.2). Also, for the present material, the strain rate does not affect the way the triaxiality evolves.

**Table 3.1:** Basic results of the static and dynamic notch tensile tests.

spec.	$d_0$ (mm)	$d_{fr}$ (mm)	$R_0$ (mm)	$\dot{\epsilon}_{eq}^a$ (s <sup>-1</sup> )	$\left(\frac{\sigma_h}{\sigma_{eq}}\right)_{ini}^b$	$\left(\frac{\sigma_h}{\sigma_{eq}}\right)_{fin}^b$	$\epsilon_u$	$\epsilon = 2 \ln \frac{d_0}{d_{fr}}$
n0509	6.03	5.05	0.44	0.0048	1.83	1.16	0.19	0.36
n0514	6.16	4.73	0.46	4.3	1.79	1.23	0.22	0.53
n05110	5.02	3.84	0.52	11.7	1.57	1.00	0.20	0.53
n0524	6.06	4.53	0.49	12.2	1.75	1.24		0.58
n0511	6.20	4.80	0.46	69.7	1.81	1.23	0.19	0.51
n0544	6.09	5.00	0.45	142.3	1.82	1.14	0.21	0.39
n05122	5.47	4.04	0.44	164.0	1.75	1.08	0.19	0.61
n0521	6.35	4.60	0.51	723.3	1.75	1.31	0.28	0.64
n0515	6.11	4.78	0.44	803.4	1.84	1.16	0.18	0.49
n0523	6.21	4.56	0.42	941.2	1.87	1.46		0.62
n05116	5.14	3.94	0.42	1362.8	1.73	1.16		0.53
n205	6.98	5.31	1.58	0.0042	1.08	0.80		0.55
n225	7.17	5.68	1.68	0.3	1.05	0.78	0.20	0.47
n251	6.79	5.25	1.54	32.1	1.08	0.81	0.17	0.51
n218	7.04	5.39	1.58	77.1	1.08	0.84	0.19	0.54
n2114	5.01	3.58	2.05	159.1	0.81	0.69	0.18	0.67
n250	7.09	5.44	1.51	455.0	1.11	0.74	0.19	0.53
n202	7.02	5.44	1.93	483.3	0.98	0.89	0.21	0.51
n2120	5.23	3.54	2.20	1018.1	0.80	0.88	0.15	0.78
n452	5.15	3.51	4.13	0.0089	0.60	0.52	0.18	0.97
n4111	5.06	3.20	3.59	13.9	0.63	0.51	0.23	0.97
n430	5.14	3.13	4.12	21.6	0.60	0.50	0.18	0.99
n431	5.13	3.32	4.17	74.9	0.60	0.50	0.18	0.87
n420	5.20	3.17	4.17	159.2	0.60	0.61	0.17	0.99
n426	5.21	3.39	3.52	798.5	0.65	0.56		0.86
n4123	5.26	3.34		1206.4			0.16	0.91
n427	5.19	3.28	4.21	1955.3	0.60	0.50	0.33	0.92

<sup>a</sup>Averaged over the interval  $\epsilon_u \leq \epsilon \leq \epsilon_{fr}$ .

<sup>b</sup>From equation (3.2).

The few published dynamic notch tensile tests define the strain rate as the axial displacement rate, as in DUMONT *et al.*<sup>62</sup> With the aid of the camera, it was possible to measure the diametrical contraction during the tests. By knowing the time associated with the images, it is possible to infer a more local value for the strain rate, though averaged over the minimum diameter. A collection of some of these measurements is shown in Figure 3.6. It can be seen that the tests generally start with a low strain rate

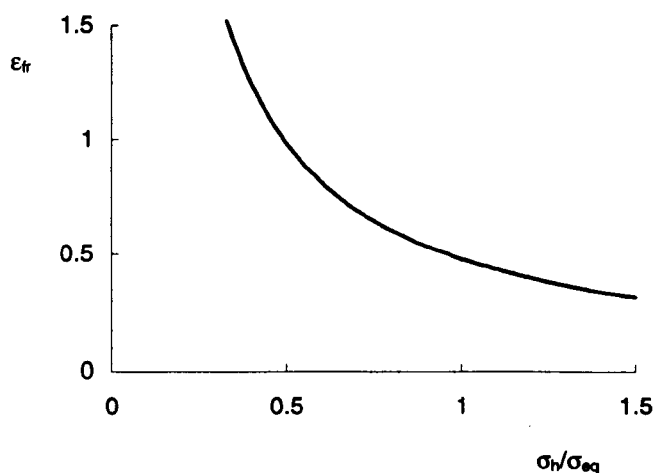


**Figure 3.4:** A hypothetical plot showing the expected influence of the stress triaxiality on the strain to fracture.

which increases vigorously in the region of low plastic strains. As the strains build up, the strain rate tends to assume a steadily exponential character, resembling what occurs in the tensile tests (see Figure 2.18 on page 37).

Figure 3.7 shows the strain measured at maximum load and the fracture strain against strain rate for the batch of n05, n2 and n4 specimens. It can be seen that the strain rate slightly influences the ultimate and fracture strains.

In line with the comments in the previous chapter, a distinction is made between failure and fracture strains. The tensile tests shows quantitatively that this difference is small (see Figure 2.14 on page 35). Because those strains were measured when necking was well developed, the triaxiality was increased from  $1/3$  to  $1/2$ , which is near the value achieved by specimens n4 in Table 3.1. This suggests that no important difference between strain to failure and to fracture should occur for the n4 specimens. This assumption is supplementary endorsed by the numerical simulation by TVERGAARD and NEEDLEMAN<sup>201</sup> who found that once the inner crack starts there is no additional significant change at the necking geometry. For a notch with a more acute angle, a larger difference between fracture and failure strain, as given by equation (3.3), might occur. But such distinction would be meaningless because the strains along the minimum cross-section for these specimens are

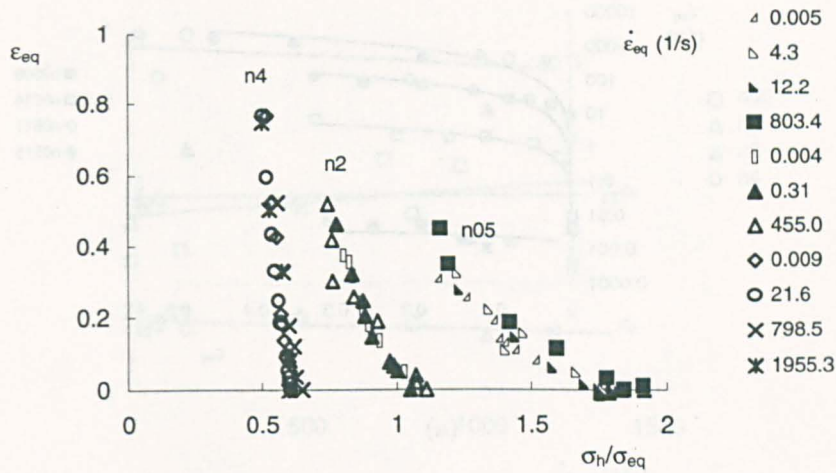


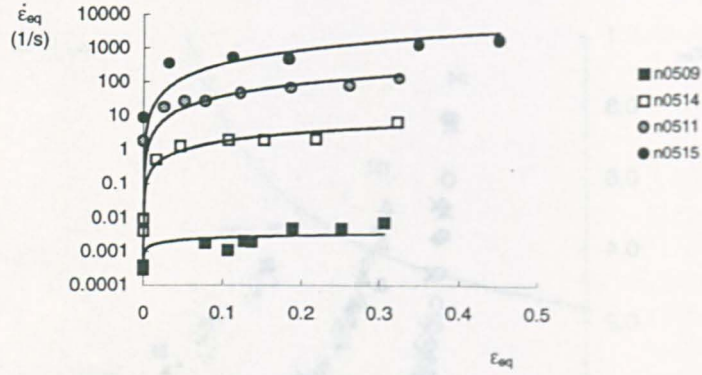
**Figure 3.5:** Evolution of the equivalent plastic strain, equation (3.3), versus maximum stress triaxiality, equation (3.2), for different notched radii specimens. The data are from the beginning of the tests, when the strain is nil, to the total rupture of the specimens. The quoted strain rates are averaged over the interval  $\varepsilon_u \leq \varepsilon \leq \varepsilon_{fr}$ .

strongly non-uniform. Hence, equation (3.3) would yield a poor description of the local values of strain, as it will be seen.

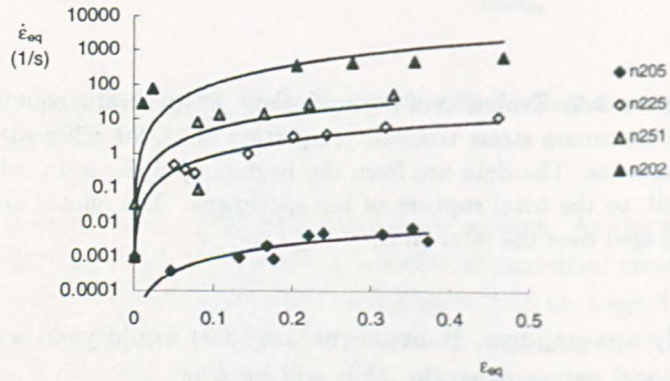
The axial displacement was increased linearly in the static notch tensile tests. This is more difficult to achieve in tests at higher speeds. A typical displacement–time signal measured by the ZIMMER for a n4 dynamic test is shown in Figure 3.8, together with the respective load measured by the head gauges. These data may be compared with the numerical dynamic simulation of geometrically similar notch specimens by TVERGAARD and NEEDLEMAN.<sup>202</sup> They found an oscillatory character in the load, plainly contrasting with the smooth load profile depicted in Figure 3.8. Nevertheless, their analysis use material parameters representative of a high tensile steel and the prescribed end velocity is around four times the maximum here obtained.

Based on the records of load and the notch geometry, it is possible to obtain the true axial,  $\sigma_{yy}$ , and engineering stresses,  $s$ , *ie* load over actual area and load over initial area, respectively. Plots of these stress definitions against the average plastic strain are depicted in Figures 3.9 and 3.10. Ob-

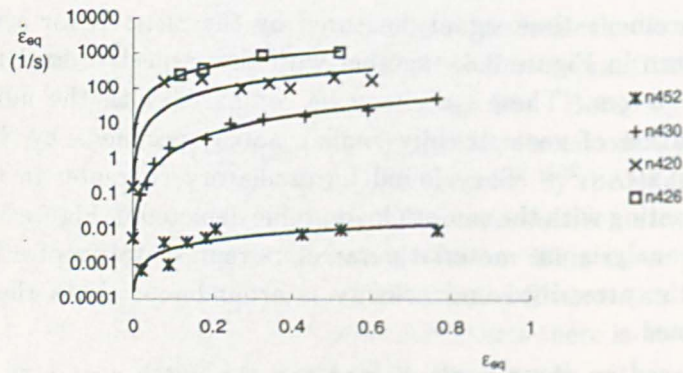




(a)



(b)



(c)

**Figure 3.6:** Evolution of the strain rate for the (a) n05, (b) n2 and (c) n4 notched specimens. The lines are a power fit to the data.

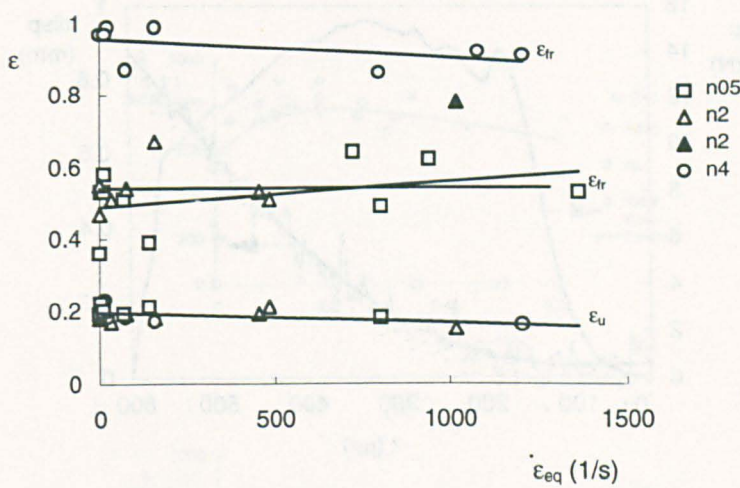


**Figure 3.7:** Evolution of the ultimate and fracture strains *versus* (average) strain rate for the three batches of notched specimens. The lines fit the data linearly (solid triangle not considered in the fit).

serve the fact that higher peak loads are found for the specimens with smaller values of  $R$ . Also, it is evident that the strain rate does have a marked effect on the level of stresses, as expected.

The various images recorded in the tests allows one to plot the previous commented envelope failure curve. This is shown in Figure 3.11 where the traditional trend of decreasing failure strain with increasing stress triaxiality is clearly obtained. This figure was generated with two sets of data; the triaxiality measured from the initial and final \* geometry.

The various points in the graph represent different test speeds and hence different average strain rates. These does not seem to influence the behaviour of the curve, in line with the findings plotted in Figures 3.5 and 3.7. Also, for the same level of triaxiality, there is a difference of around 10% in the failure strain according to the way the ratio  $\sigma_h/\sigma_{eq}$  is evaluated, *ie* from the initial or final geometry. As a matter of fact, this sort of envelope failure curve obtained from notch tests and using the BRIDGMAN formulae have additional limitations, as it will be discussed in the sequence.

This failure *locus* is of the most importance in failure prediction. Indeed,

\*Actually, the geometry comes from the last recorded image in the test before visual failure.

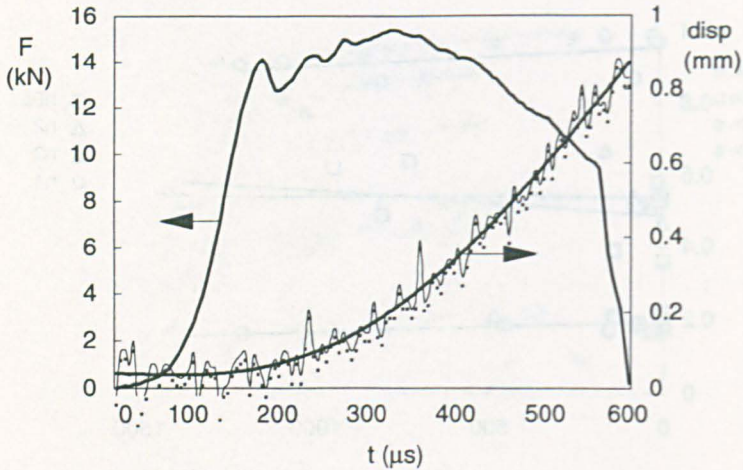


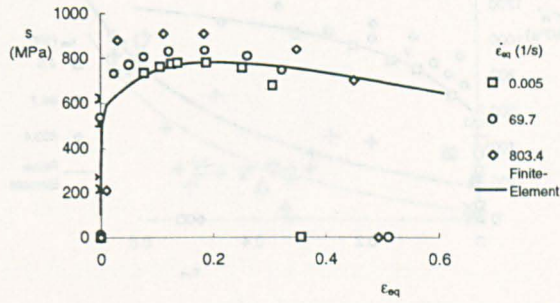
**Figure 3.8:** Prescribed axial displacement and the resulted load *versus* time for the n4123 specimen. The number of measured points shown for the displacement signal was reduced for the sake of clarity. The continuous line for the displacement represents a polynomial fitting of order four.

some failure criteria are developed and applied based on data similar to the ones in Figure 3.11, (see, in particular, the work of BAMMANN *et al.*<sup>5</sup> and HOLMES *et al.*<sup>86</sup>). Hence the important question of how accurate the experimental and analytical procedures are to generate such curves.

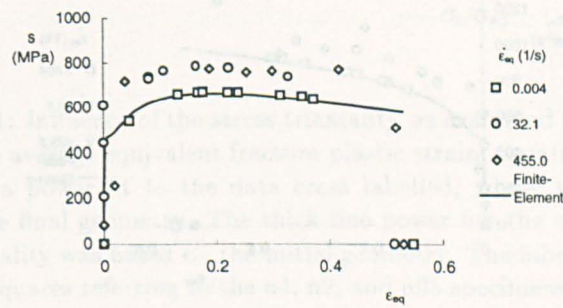
Figure 3.10 suggests that the actual average stress in the specimens increases continuously up to just before fracture. This probably means an increase in the triaxiality, which unambiguously contrasts with the continuous decrease of it pointed out in Figure 3.5. This contrast may be attributed to the BRIDGMAN formulae, formulated originally for cylindrical specimens. To gain a more accurate description of the behaviour of the notched specimens, a numerical analysis seems to be most useful.

### 3.3 Finite-Element analysis

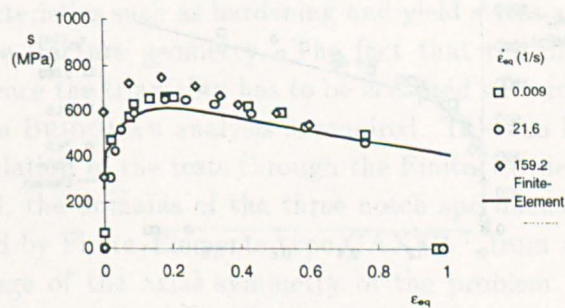
Some failure criteria have been developed by using the envelope failure curves of the kind shown in Figure 3.11. It can be noted that both axes of this graph are essentially obtained from geometrical parameters; it being expected that



(a)

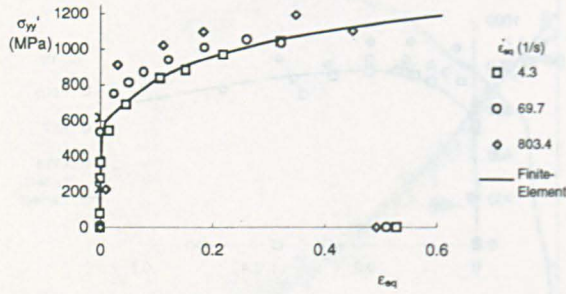


(b)

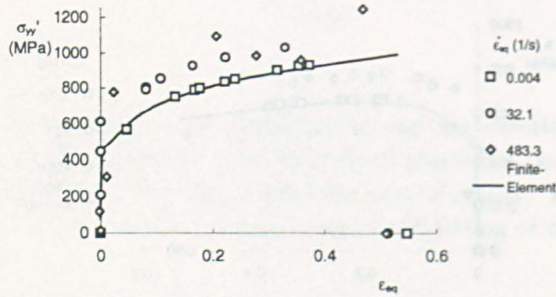


(c)

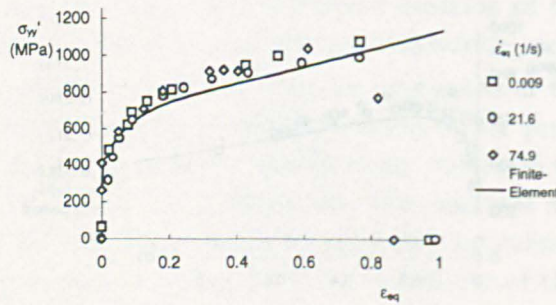
**Figure 3.9:** Experimental engineering axial stress *versus* the average equivalent plastic strain for some (a) n05, (b) n2 and (c) n4 specimens. The labels refer to the strain rate averaged over  $\varepsilon_u \leq \varepsilon_{eq} \leq \varepsilon_{fr}$ . The continuous line is the result of the static Finite-Element analysis.



(a)



(b)



(c)

**Figure 3.10:** Experimental  $\sigma_{yy'}$  stress, load over current cross section area, versus the average equivalent strain for some of the (a) n05, (b) n2 and (c) n4 test specimens. The labels refer to the strain rate averaged over  $\epsilon_u \leq \epsilon_{eq} \leq \epsilon_{fr}$  and the continuous lines represent the static Finite-Element simulation of the tests.

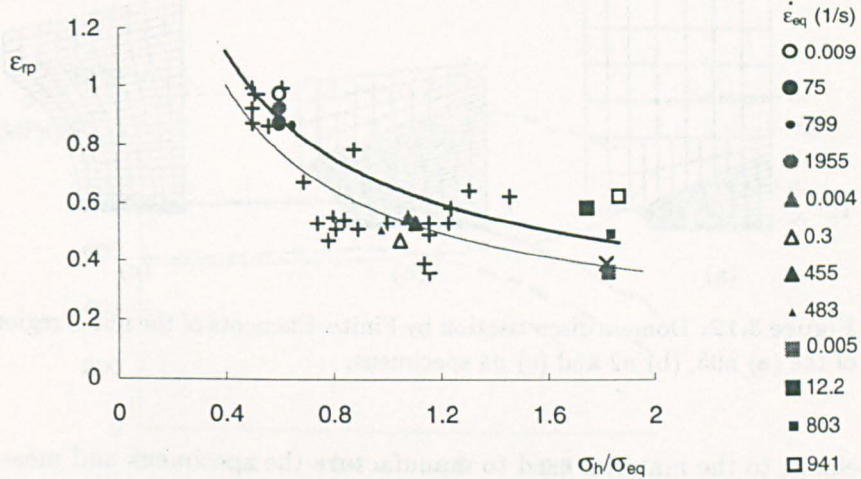


**Figure 3.11:** Influence of the stress triaxiality, as evaluated from equation (3.2), on the average equivalent fracture plastic strain, equation (3.3). The thin line is a power fit to the data cross labelled, whose triaxiality was based on the final geometry. The thick line power fits the other symbols, whose triaxiality was based on the initial geometry. The labels; circles, triangles and squares referring to the n4, n2, and n05 specimens, respectively; indicate the average equivalent strain rate in the tests.

material characteristics such as hardening and yield stress are somehow represented by the fracture geometry. The fact that the material does not explicitly influence the triaxiality has to be accepted with reserve and a confirmation of the BRIDGMAN analysis is required. This can be achieved by a numerical simulation of the tests through the Finite-Element method\*.

To this end, the domains of the three notch specimens n05, n2 and n4 were discretised by Finite-Elements type CAX8R<sup>†</sup>, from ABAQUS package, taking advantage of the axial symmetry of the problem. The meshes in the notch region are indicated in Figure 3.12 and represent the geometry of the specimens tested statically. It was confirmed that the results are not sensitive to two other mesh configurations used.

The input static equivalent stress-strain curve is depicted in Figure 3.2.

\*The accuracy of the BRIDGMAN analysis has been examined in references 16,44,62 and 64, etc ...

<sup>†</sup>This is an axisymmetric, eight-noded, quadratic element. The field variables were evaluated at the integration points.

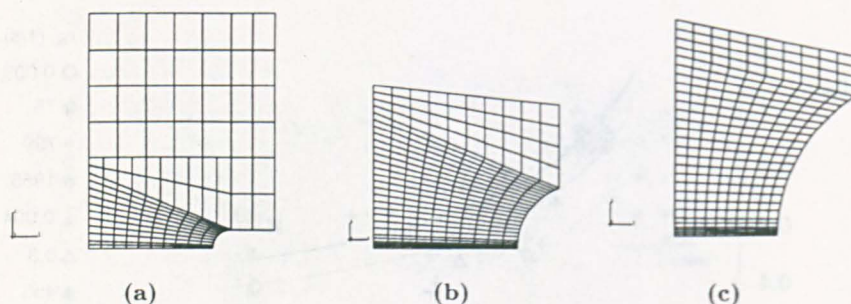


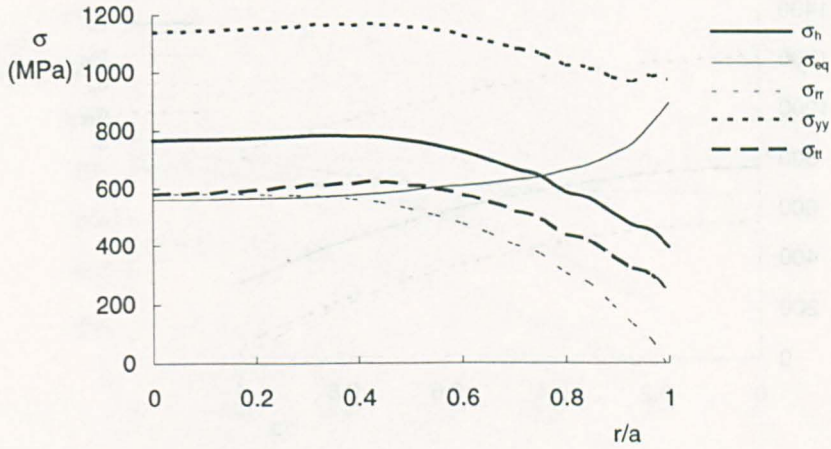
**Figure 3.12:** Domain discretisation by Finite-Elements of the notch region of the (a) n05, (b) n2 and (c) n4 specimens.

It belongs to the material used to manufacture the specimens and measured as described in Chapter 2. The static elastic modulus and Poisson ratio also come from the previous chapter, Table 2.3 on page 31. In the numerical simulation, a linear displacement-time curve was imposed at the end of the specimens and no dynamic effect was considered. No failure criterion was used in the analysis. Hence the equivalent stress increases continuously in the frame of the VON MISES plasticity. Nevertheless, the simulations were interrupted when the notch diameter contraction of the n05, n2 and n4 specimens equal the one measured in the experiments at fracture.

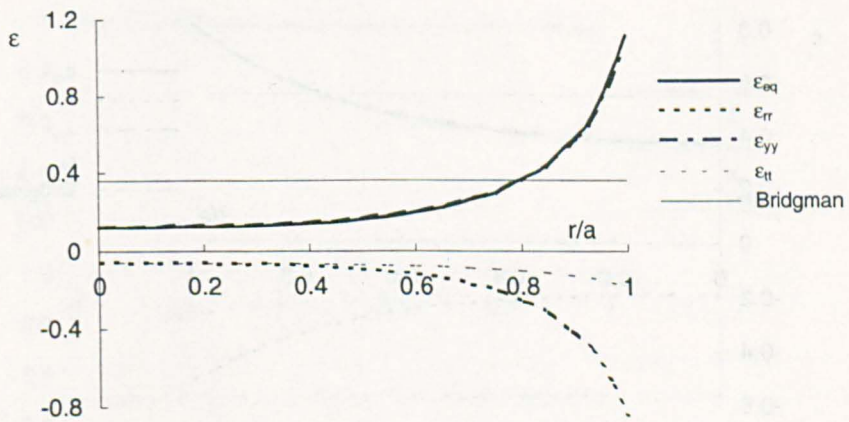
### 3.3.1 Results

Figures 3.13, 3.14 and 3.15 present the stress-strain distribution at the minimum cross-section of the n05, n2 and n4 specimens. These stress-strain profiles occur when the numerical average equivalent strain equals the fracture value obtained in the experiment, both strains measured by the diameter contraction, equation (3.3). Observe that for the n4 specimens the BRIDGMAN theory agrees well in the sense that  $\sigma_{rr} = \sigma_{\theta\theta}$  and that the equivalent plastic strain is nearly constant across the section, though it underestimates the triaxiality. This is not the case for more acute geometry. The smaller the notch radius the less uniform is the equivalent strain and the larger the hoop stress at the notch root, leading to triaxiality values along the cross-section different from the ones predicted by BRIDGMAN equations.

The evolution of the triaxiality at the middle and at the notch base *versus* the average equivalent strain is shown in Figure 3.16, together with the respective BRIDGMAN prediction. Apart from an initial transient period at



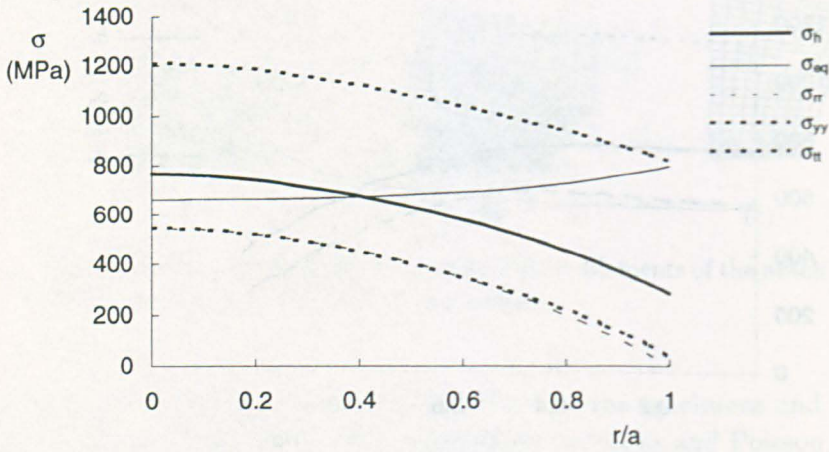
(a)



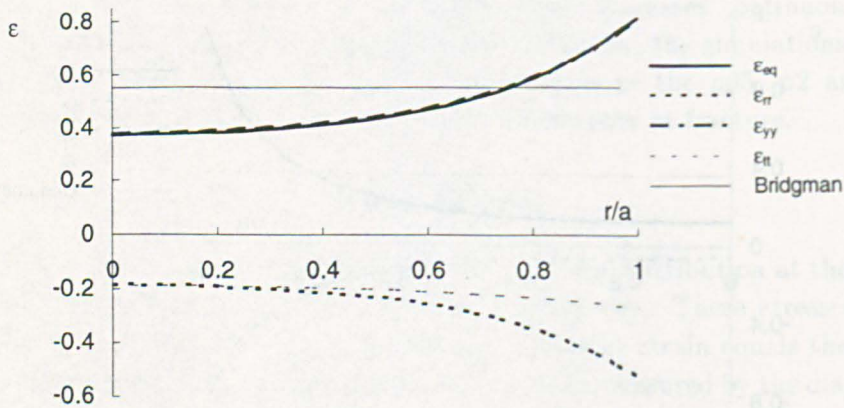
(b)

**Figure 3.13:** (a) Stresses and (b) strains calculated by the Finite-Element method, along the minimum cross-section of the n0509 specimen. The average plastic strain equals the experimental average fracture value of  $\epsilon_{fr} = 0.36$ . The thin line in (b) is the BRIDGMAN prediction, equation (3.3).



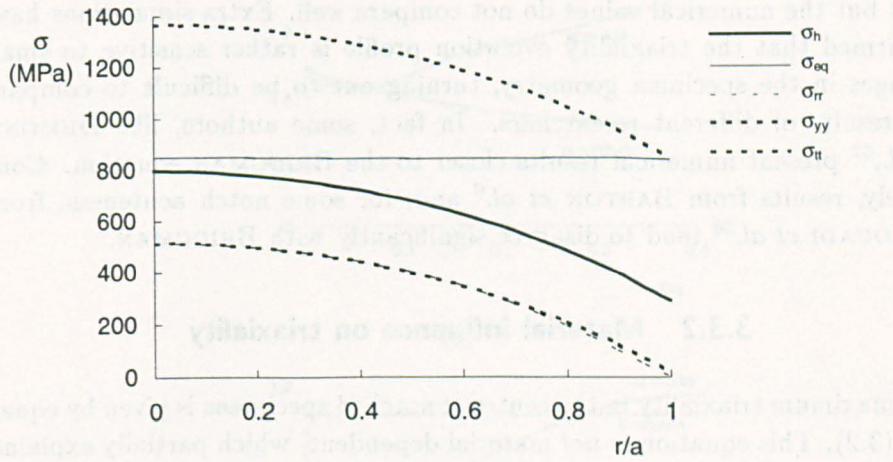


(a)

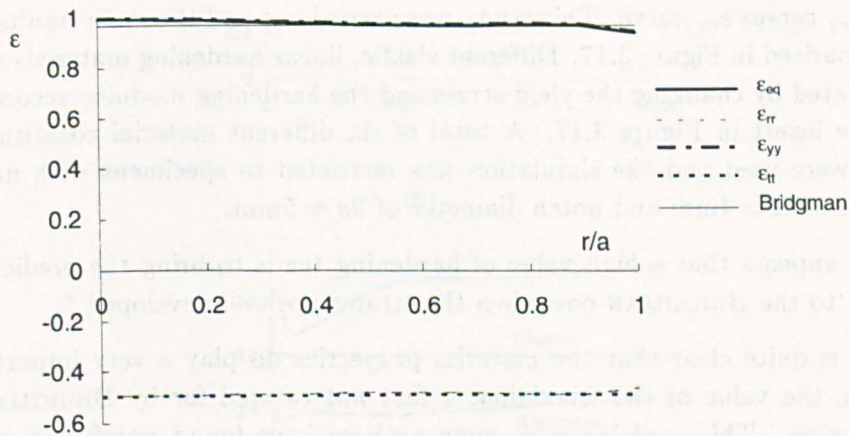


(b)

**Figure 3.14:** (a) Stresses and (b) strains calculated by the Finite-Element method, along the minimum cross-section of the n205 specimen. The average plastic strain equals the experimental average rupture value of  $\epsilon_{fr} = 0.55$ . The thin line in (b) is the BRIDGMAN prediction, equation (3.3).



(a)



(b)

**Figure 3.15:** (a) Stresses and (b) strains calculated by the Finite-Element method, along the minimum cross-section of the n452 specimen. The average plastic strain equals the experimental average fracture value of  $\epsilon_{fr} = 0.97$ . The thin line in (b) is the BRIDGMAN prediction, equation (3.3).

small strains, the triaxiality is always higher at the centre of the specimen, a region where failure would then start. This agrees qualitatively with BRIDGMAN but the numerical values do not compare well. Extra simulations have confirmed that the triaxiality evolution profile is rather sensitive to small changes in the specimen geometry, turning out to be difficult to compare the results of different researchers. In fact, some authors, like DUMONT *et al.*,<sup>62</sup> present numerical results closer to the BRIDGMAN equation. Conversely, results from BARTON *et al.*<sup>6</sup> and, for some notch acuteness, from CHAOUADI *et al.*<sup>36</sup> tend to disagree significantly with BRIDGMAN.

### 3.3.2 Material influence on triaxiality

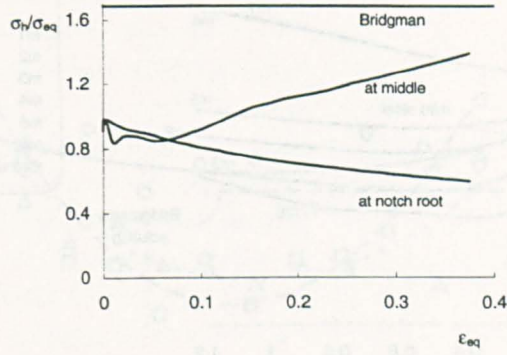
The maximum triaxiality in the centre of notched specimens is given by equation (3.2). This equation is *not* material dependent, which partially explains the reason for the poor prediction of the triaxiality according to BRIDGMAN. As the Finite-Element simulation does take into account the material properties, it is possible to investigate the influence of different materials on the  $\sigma_h/\sigma_{eq}$  versus  $\varepsilon_{eq}$  curve. This study was carried out and the main results are summarised in Figure 3.17. Different elastic, linear hardening materials were simulated by changing the yield stress and the hardening modulus according to the insert in Figure 3.17. A total of six different material constitutive laws were used and the simulation was restricted to specimens with notch radius of  $R = 4\text{mm}$  and notch diameter of  $2a = 5\text{mm}$ .

It appears that a high value of hardening tends to bring the prediction closer to the BRIDGMAN one when the strains are well developed \*.

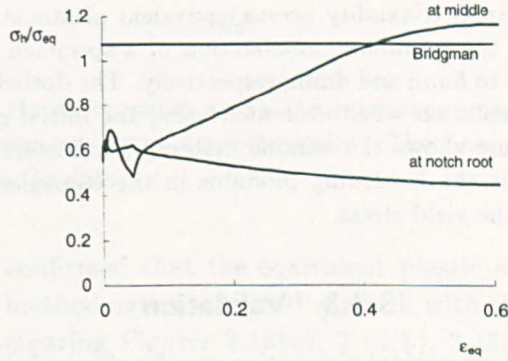
It is quite clear that the material properties do play a very important role in the value of the triaxiality, a fact not catered for by BRIDGMAN's expression. This explains why some authors have found poor<sup>6</sup> and good agreement<sup>219</sup> between their numerical simulations and the theoretical equations, since they used different materials. In this perspective, it is difficult to advocate the use of the BRIDGMAN equation when comparing it with just one material. In short, the BRIDGMAN equations may or not give reasonable results for the triaxiality, according to the material properties.

---

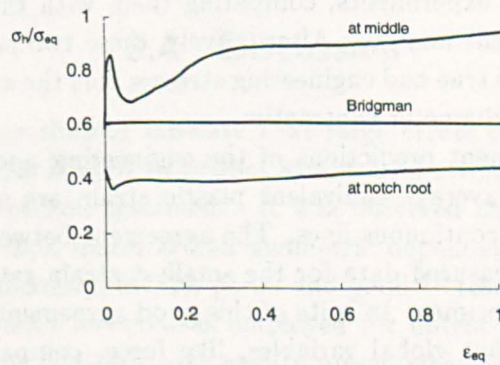
\*The mild steel cannot be fully compared with material m2 because the former does not harden significantly for strains lower than say 20%.



(a)



(b)



(c)

**Figure 3.16:** Triaxiality evolution at the centre and at the notch root of the (a) n0509, (b) n205 and (c) n452 specimens as calculated by the Finite-Element method. The BRIDGMAN prediction, equation (3.2), is valid for the middle of the specimens and is based on the initial geometry.

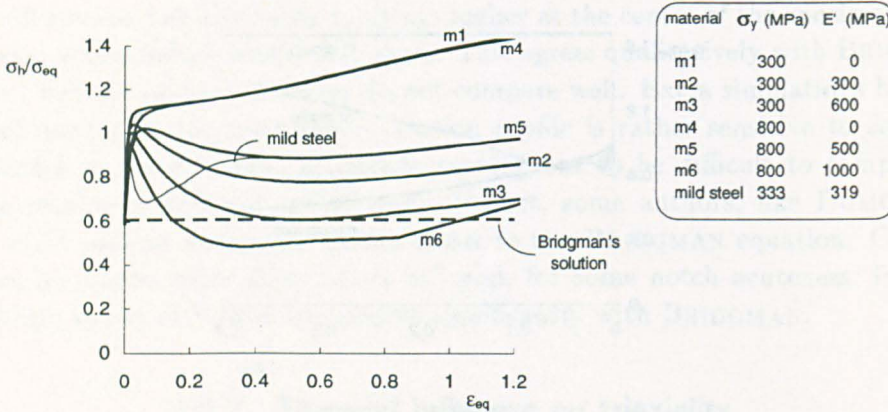


**Figure 3.17:** Stress triaxiality *versus* equivalent plastic strain behaviour at the centre of the minimum cross-section of a specimen with diameter and radius equal to 5mm and 4mm, respectively. The dotted line represent the BRIDGMAN solution when evaluated using the initial geometry. The insert in the figure shows the various material parameters used for each simulation.  $E'$  is the hardening modulus in the equivalent stress-strain space and  $\sigma_y$  is the yield stress.

### 3.3.3 Validation

The accuracy of the numerical simulation can be checked since experimental data are available. One way to do this is to use the load and diameter as measured in the experiments, comparing them with the ones generated by the Finite-Element analysis. Alternatively, these two parameters can be used to calculate the true and engineering stresses plus the average equivalent strain given by the diameter contraction.

The Finite-Element predictions of the engineering and true equivalent stresses *versus* the average equivalent plastic strain are shown in Figures 3.9 and 3.10 by the continuous lines. The agreement between the numerical solution and the measured data for the smallest strain rates is quite good, except for the n4 specimen. In spite of this good agreement, as CLAUSING<sup>43</sup> remarks, the fact that global variables, like force, compare well does not imply good agreement for local variables, like stress-strain components. But local internal variables are difficult to measure.

One indication of the behaviour of a local variables, like strain, is the hardness. Accordingly, the hardness profile was measured for the n05, n2 and n4 specimens tested quasi-statically and the results are plotted in Fig-

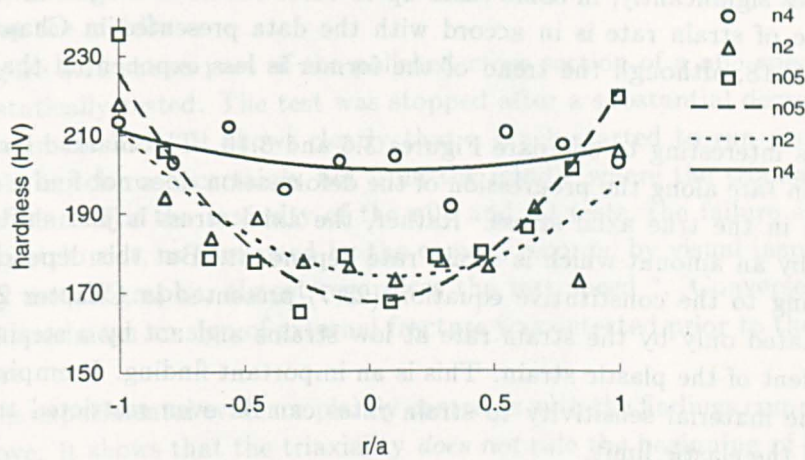


**Figure 3.18:** Hardness values across the minimum cross section of n05, n2 and n4 specimens tested quasi-statically. The lines are a quadratic interpolation to the data.

ure 3.18. It was confirmed that the equivalent plastic strain as calculated by the numerical method agrees qualitatively well with the hardness profile, as inferred by comparing Figures 3.13(b), 3.14(b), 3.15(b) and 3.18. This supports the accuracy of the numerical solution here described.

### 3.4 Discussion

The results of this chapter indicate that large errors can occur when the BRIDGMAN analysis is used to predict strains and stresses at the minimum cross-section of notched specimens. It was observed that the actual value of the triaxiality is a material and geometric dependent parameter. This accounts, simultaneously, for the poor<sup>6</sup> and good<sup>219</sup> results found by others when the BRIDGMAN formulae is employed for notched specimens. It accounts also, for the contradictory results presented in Figures 3.5 and 3.16, the former gained through a direct application of equation (3.2) and the later yielded by the Finite-Element analysis.

A striking experimental result is the behaviour of the strain rate at the minimum cross section of the notched specimens pulled in tension, Figure 3.6. The average strain rate, measured by the change in the necking diameter,

increases significantly, in some cases up to three orders of magnitude. This increase of strain rate is in accord with the data presented in Chapter 2, Figure 2.18, although the trend of the former is less exponential than the later.

It is interesting to compare Figures 3.6 and 3.10. The marked increase of strain rate along the progression of the deformation does not find a counterpart in the true axial stress. Rather, the axial stress is just shifted as whole by an amount which is strain rate dependent. But this dependence, according to the constitutive equation (2.17) presented in Chapter 2, can be dictated only by the strain rate at low strains and not by a strain rate dependent of the plastic strain. This is an important finding. It emphasises that the material sensitivity to strain rates can be even restricted to just around the elastic limit.

The Finite-Element simulation showed that the triaxiality is higher at the middle of the notched specimens \* regardless the notch radius. This is in complete agreement with the findings of other researches.<sup>6,62,144,161</sup>

Consider now the work of NEEDLEMAN and TVERGAARD.<sup>161</sup>

They have simulated numerically plane strain and axisymmetric notched specimens incorporating in their analysis a void volume dependent yield function. Their notch specimens have diameter to notch radius ratios of 12 and 4. This ratio for the n05 and n2 specimens simulated in the previous section are 13.7 and 4.4, respectively. Their material parameters are representative of a steel with a yield stress of around 650MPa.

The major conclusion they arrived at was that the failure site for the plane strain specimens is sometimes in the middle and sometimes in the notch root, according to the notch radius. As for the axisymmetric specimens, the failure site is located *always* in the middle because the triaxiality is higher there, regardless of the value of the plastic strain. In fact, this conclusion was a numerical confirmation of the experiments of MACKENZIE *et al.*<sup>144</sup> and BECKER *et al.*<sup>11</sup> and agrees with the numerical results of HANCOCK and BROWN.<sup>77</sup> Although HANCOCK<sup>76</sup> argues that the influence of the hydrostatic stress on failure has been too much emphasised, it is accepted that ductile failure occurs in regions of high triaxiality.

In the present experiments and analysis, for all the specimens, the triaxiality is higher in the middle than in the notch root, regardless of the notch radius and the plastic strain. If the triaxiality was to govern the failure ini-

---

\*In the elastic regime, the stress concentration is higher at the notch root.

tiation, in line with others, one would expect then the crack site to always occur at the middle.

Figure 3.19 shows part of the polished cross section of a n05 specimen, quasi-statically tested. The test was stopped after a substantial decrease of the maximum load. It shows clearly that a crack started to run probably from the notch root; certainly not from the middle where the triaxiality is a maximum. For the majority of the n05 and n2 tests, the failure started at the notch root, as confirmed by the camera records, by visual inspection and by metallography, almost regardless the test speed \*. Conversely, for the n4 specimens no sign of external fracture was detected prior to the total fracture.

This experimental evidence plainly contrasts with the findings commented on above. It shows that the triaxiality *does not* rule the beginning of failure for the present material and for the notched specimens. Rather, the strains are to be considered the major parameter in defining where the failure starts, as Figures 3.13 and 3.14 suggest. This experimental evidence offers a debatable point. Is the hydrostatic stress really a more important parameter in determining the failure in a structure? Or would a failure criterion giving more importance to the strains be more realistic? The answer to this question will be deferred to Chapter 5, where a convenient way to assess how triaxiality and plastic strains interact to determine the failure site will be pursued.

Some authors report on similar findings.<sup>36,61,219</sup> DUMONT *et al.*<sup>61</sup> states clearly that their results of damage sites in notch specimens, more intense in regions of lower triaxiality, are in complete disagreement with micro-mechanic models like the RICE and TRACEY<sup>175</sup> one. Also, ZAVALIANGOS and ANAND<sup>219</sup> found in their model that fracture in notched specimens occurs at some distance ahead of the notch root but not at the centre.

The prediction of the failure site of notched structures can be seen as a test for a failure criterion. The reason is that the stress-strain field is such that the triaxiality and equivalent plastic strains vary within a broad range. In the present case, for the n05 and n2 specimens, the triaxiality is high where the equivalent plastic strain is low; for the n4 specimens the equivalent strain is constant and the triaxiality higher at the middle. Chapter 5 will address this problem and will show how the failure site can be forecast.

As far as the failure envelope curve is concerned, one might be tempted to

---

\*For very high test speeds it is not possible to actually see the crack site.



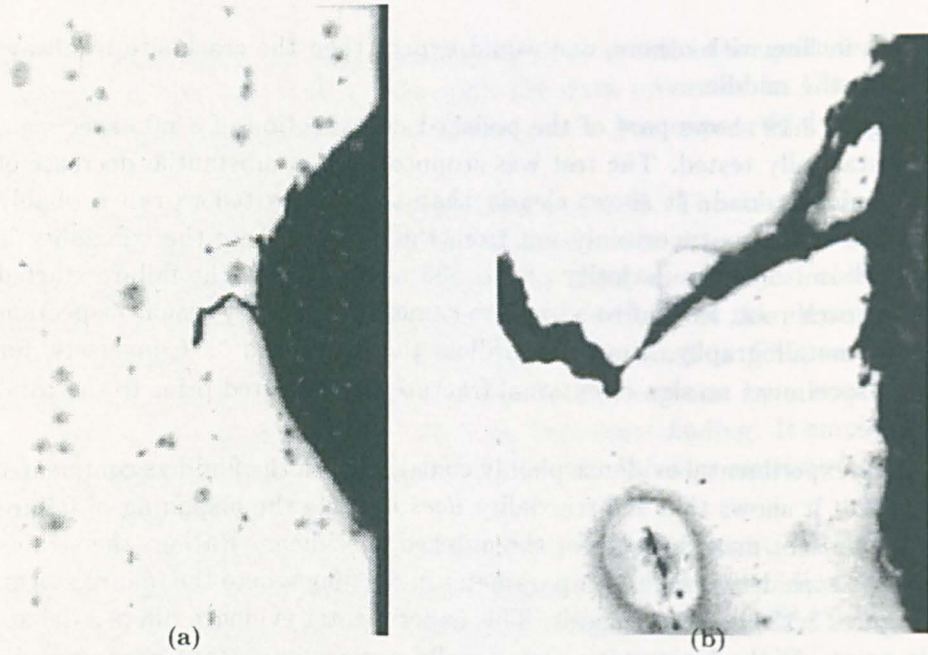


**Figure 3.19:** (a) A photograph of a n05 specimen showing a crack starting far away from the middle. (b) Detail of the notch base.

consider the one depicted in Figure 3.11 as the correct one, but this is difficult to sustain. Firstly, because of the wrong values for the triaxiality. As noted before, the triaxiality via BRIDGMAN is not accurate. More importantly are the fracture strains. Traditionally, they are measured by the diameter contraction but this leads to average values, very different from the local ones obtained in the numerical simulation for the n05 and n2 specimens. Accordingly, for the n05 specimen, Figure 3.13, an average fracture strain of 0.38 means in fact a local strain at the failure point of 1.12.

If the local values of fracture strain and triaxiality for the n05, n2 and n4 static specimens are used to plot the failure locus, a rather considerable change occurs, as shown in Figure 3.20. The solid circles in this figure represent the stress-strain state prevailing at the failure point when evaluated with the Finite-Element results. What this figure shows is that, for the studied material, the range of triaxiality obtained by changing the notch radius is smaller than results based on BRIDGMAN's would suggest. This means that the test of notched specimens may not reveal how the triaxial-

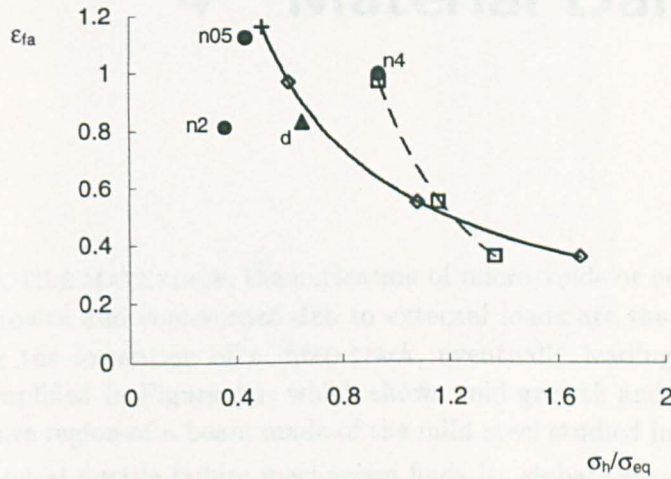


**Figure 3.20:** Failure envelope for a mild steel. The continuous line represents the common approach for inferring the triaxiality, equation (3.2) and the strains, equation (3.3) (includes a tensile test point labelled by a cross). The broken line is rendered using the maximum triaxiality, at the specimen centre, just before fracture and according to the Finite-Element analysis; the strains are given by equation (3.3). The solid circles refer to the stress-strain state prevailing at the failure site in the static notch specimens as calculated by the Finite-Element method. The solid triangle is the stress-strain state at failure for a flat specimen (see Chapter 4).

ity influences the failure strain. Moreover, again for the present material in the range tested, it is not clear how the triaxiality plays its role on failure. In fact, for the n05 and n2 specimens, the failure sites are associated with low triaxiality values for the more acute specimens, a quite unexpected result. For the n4 specimen, the failure site is at centre, where the triaxiality is higher. This chapter focused in exploring the way the triaxiality drives the fracture strains. The aim was clearly to generate an envelope failure *locus* but Finite-Element analysis and experimental evidences have shown that such curves are not valid for the present material. As a matter of fact, because most of the published curves were generated using the BRIDGMAN analysis, they have to be interpreted as an average influence of the triaxiality on an average fracture strain. The present results also suggest that the triaxiality is not fundamental in triggering the failure; the strains seem to be more relevant and a failure criterion should be able to gather this trend.



---

## 4 Material Damage

FOR DUCTILE MATERIALS, the nucleation of micro-voids or micro-cracks, and their growth and coalescence due to external loads are the main steps anticipating the formation of a meso-crack, eventually leading to failure. This is exemplified in Figure 4.1, which shows void growth and coalescence in the fracture region of a beam made of the mild steel studied in Chapter 2.

This classical ductile failure mechanism finds its global expression in the decrease of the capacity of a structure to sustain additional loads. At a local or micro-structure level, the void onset affects various material properties as the elastic modulus, the density and hence the speed of elastic waves, the hardness, the electrical resistance, to name a few.

All these property changes are indicative of material degradation and they can be used to develop suitable experimental techniques to measure damage in a material or structure. This damage at critical conditions might be viewed then as a major parameter in the onset of failure and theoretical approaches relying on it could be employed for failure prediction.

It is the objective of this chapter to describe different experimental and numerical techniques to assess material damage. The chapter starts presenting various material damage definitions. A Finite-Element analysis is described, yielding a reinterpretation of experimental results concerning the damage via the change of the elastic modulus. Then, it follows a detailed description of the damage tests here performed and the main results gained through the different techniques employed. A final discussion debates the meaning of the damage parameter, supported by experimental data from various sources.

### 4.1 Damage definitions

The first obvious way to assess quantitatively the damage presented in a ductile material is to measure the area or number of voids present. The

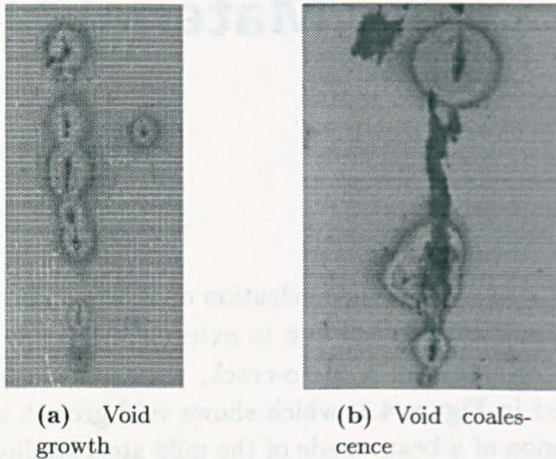


**Figure 4.1:** Micro-pictures of a mild steel beam showing the (a) growth and (b) coalescence of voids in the fracture region. The beam was loaded statically up to total rupture.

damage in this case may be defined as

$$D_S = \frac{S_D}{S}, \quad (4.1)$$

where  $D_S$  is the damage evaluated from voids,  $S$  is the original area of the virgin material and  $S_D$  is the total area of voids, Figure 4.2. This definition has been used in the literature to measure damage in different materials.

Another damage definition can be obtained through the effective stress concept which goes back to KACHANOV.<sup>42,105</sup> The effective stress,  $\tilde{\sigma}$ , is related to the area in the damaged material that effectively resists the load  $F$ , namely  $(S - S_D)$ . It is expressed by

$$\tilde{\sigma} = \frac{F}{S - S_D}. \quad (4.2)$$

The damage definition,  $D_S$ , yields

$$\tilde{\sigma} = \frac{\sigma}{1 - D_S}, \quad (4.3)$$

where  $\sigma$  is a true stress related to the virgin material.

LEMAITRE has hypothesised that *any strain constitutive equation for a damaged material may be derived in the same way as for a virgin material except that the usual stress is replaced by the effective stress.*<sup>126</sup>

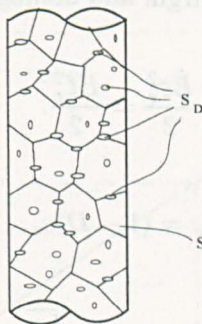


**Figure 4.2:** A damaged element showing schematically the virgin material and the area  $S_D$  of micro-voids.

In an undamaged material, the uniaxial elastic strain is

$$\varepsilon_e = \frac{\sigma}{E}, \quad (4.4)$$

where  $E$  is the elastic modulus. For a damaged material, according to LEMAITRE's assumption, this expression changes to

$$\varepsilon_e = \frac{\tilde{\sigma}}{E} = \frac{\sigma}{E(1 - D_S)}. \quad (4.5)$$

If the elastic modulus in the damaged material is defined by

$$\tilde{E} = \frac{\sigma}{\varepsilon_e}, \quad (4.6)$$

one can write

$$D_S = D_E^\varepsilon = 1 - \frac{\tilde{E}}{E} \quad (4.7)$$

where  $D_E^\varepsilon$  is a damage definition based on the elastic modulus degradation when using the LEMAITRE's strain equivalence hypothesis. Obviously  $D_S \equiv D_E^\varepsilon$  only if this assumption is correct.

In an attempt to analyse anisotropic damage, CORDEBOIS and SIDOROFF<sup>49</sup> used another hypothesis where the *elastic energy* of the damaged material is assumed to be the same as the undamaged one, except that stresses (or strains) are to be replaced by their corresponding effective quantities. A mathematical expression for this statement may be gained by equating the

product stress $\times$ strain in both virgin and damaged materials, the areas 1-2-3 and 1-4-5 in Figure 4.3,

$$\frac{\tilde{E}\tilde{\epsilon}_e^2}{2} = \frac{E\tilde{\epsilon}_e^2}{2}. \quad (4.8)$$

By noting that

$$\tilde{\epsilon}_e = (1 - D)\epsilon_e, \quad (4.9)$$

it follows that

$$D_E^W = 1 - \sqrt{\frac{\tilde{E}}{E}}, \quad (4.10)$$

where  $D_E^W$  is the damage based on the elastic modulus degradation and using the hypothesis of elastic energy equivalence.

It is evident that the hypothesis of strain and energy equivalence allows one to measure the damage from the change in the elastic modulus. Also, the two damage definitions lead to rather different values for the damage variable. The reason for that is further illustrated in Figure 4.3, where the area 1-2-3 is the elastic energy stored in the damaged material. At point 2, the effective stress  $\tilde{\sigma}$  is the point 6, according to the hypothesis of strain equivalence. The area 1-4-5 is imposed to be equal the area 1-2-3 and point 4 is then associated with another effective stress  $\tilde{\sigma}'$ , to be compared with the one in point 6. It is obvious that the effective stress related to the hypothesis of elastic energy equivalence is lower than effective stress related to the strain equivalence approach, which leads to lower damage values. As remarked by HANSEN and SCHREYER,<sup>79</sup> the choice between these principles leads to a marked difference on the behaviour of the model since the effective stress definition is used in the yield function, as it will be shown.

The formation of voids in a ductile material also affects the hardness. Hence the measurement of the hardness yields a method of measuring the damage.<sup>21,130,131</sup> The relation between damage and hardness may be obtained through the hardness definition

$$HV = \frac{F}{S}, \quad (4.11)$$

where  $HV$ ,  $F$  and  $S$  are the hardness, load and area, respectively. Because there is a linear relation between hardness and the flow stress,  $\sigma_{eq}$ , through a constant  $k'$ ,<sup>126</sup> one can write for the damaged material

$$HV = k'\sigma_{eq}(1 - D_{HV}^d), \quad (4.12)$$

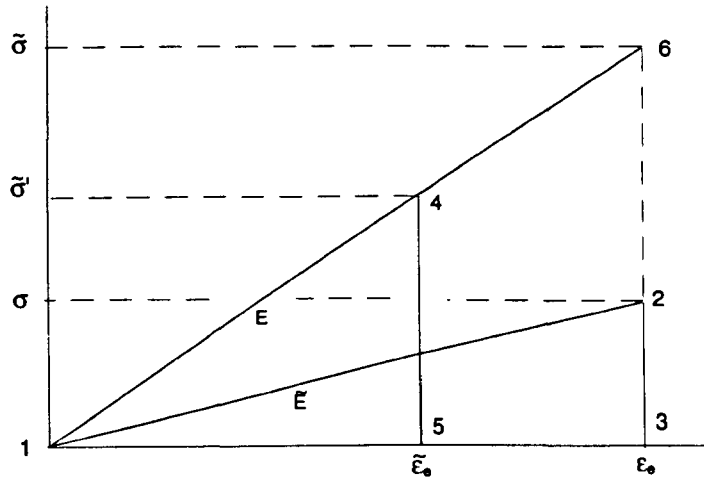


**Figure 4.3:** Illustration of the effect of the strain and energy equivalency hypothesis on the effective stress values. Adapted from HANSEN and SCHREYER.<sup>79</sup>

and for the undamaged one

$$HV' = k' \sigma_{eq}, \quad (4.13)$$

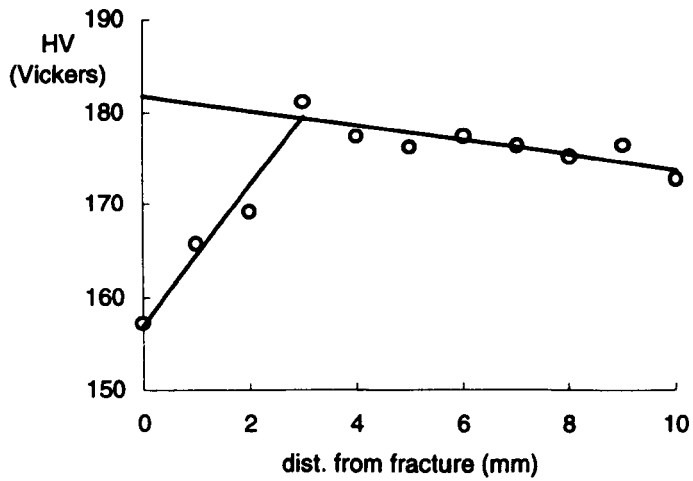
$HV'$  being the hardness in the virgin material at the same level of plastic strain as for  $HV$  in the damaged material. From the above two expressions it follows that

$$D_{HV}^\varepsilon = 1 - \frac{HV}{HV'}, \quad (4.14)$$

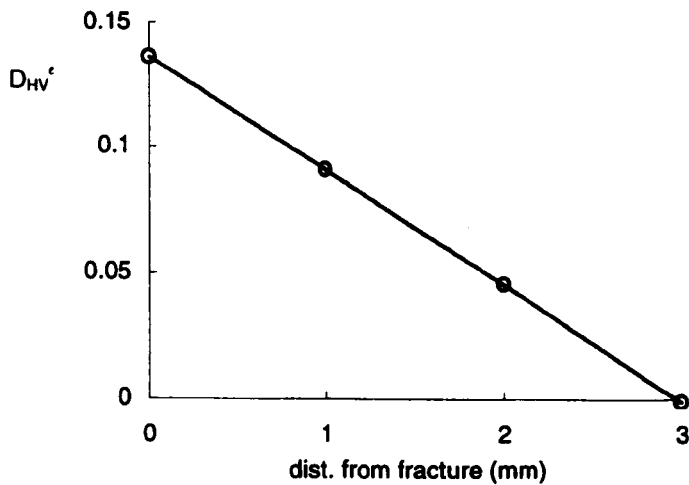
where  $D_{HV}^\varepsilon$  is the damage based on hardness according to the hypothesis of strain equivalence. A drawback of this technique is that, for ductile damage, the hardness  $HV'$  cannot be measured because damage occurs simultaneously with increasing plastic strain. It is proposed then an extrapolation for the curve  $HV' \times \varepsilon_{eq}$ .<sup>21, 130, 131</sup> The extrapolation may be carried out as illustrated in Figure 4.4(a), with the resulting damage parameter,  $D_{HV}^\varepsilon$ , shown in Figure 4.4(b).

The presence of voids also affects the electrical resistance of metals. The monitoring of the change in the electrical potential,  $V$ , may give an indication of the void area or volume and hence damage. The departure point to relate electrical potential change to damage is the effective intensity of electrical





(a)



(b)

**Figure 4.4:** (a) Illustration of the measurement of  $D_{HV}^c$  by extrapolating linearly the hardness curve. (b) Resulting damage near the fracture surface. The tensile specimen is made of an aluminium alloy used in the aero-space industry. The lines are a linear fit to the data and the fracture surface is at 0mm.

current  $\tilde{i}$ . It is defined by<sup>7,8,29,30,130</sup>

$$\tilde{i} = \frac{i}{1 - D_V^\epsilon}, \quad (4.15)$$

where  $i$  is the electrical current intensity and  $D_V^\epsilon$  the damage from the electrical potential according to the principle of strain equivalence. Invoking now Ohm's law for the undamaged element of length  $l$ , area  $S$  and resistivity  $r_s$ , and for the damaged one with resistivity  $\tilde{r}_s$ , it follows that

$$V = r_s \frac{l}{S} i \quad \text{and} \quad \tilde{V} = \tilde{r}_s \frac{l}{S} \tilde{i}, \quad (4.16)$$

where  $\tilde{V}$  is the potential in the damaged element. The relation between the resistivities is \*

$$\frac{\tilde{r}_s}{r_s} = 1 + 2D_V^\epsilon{}^{3/2}, \quad (4.17)$$

which is assumed to be the unity for low values of the damage  $D_V^\epsilon$ .<sup>126</sup> The final relation between damage and electrical potential, according to the hypothesis of strain equivalence, is

$$D_V^\epsilon = 1 - \frac{V}{\tilde{V}}. \quad (4.18)$$

This technique has been applied mainly to measure damage in fatigue, as in references 8, 29, 30 and 130, but it is worthy to explore the method for ductile damage.

## 4.2 Finite-Element simulation of the damage tensile test

By far, the most common technique to measure ductile material damage is by monitoring the elastic modulus variation. This technique, introduced by LEMAITRE and DUFALLY,<sup>60,130</sup> consists in loading in tension a specimen, similar to the one depicted in Figure 4.5, up to some level of plastic deformation. The specimen is then unloaded and the elastic modulus is calculated from the slope of the unloaded stress-strain curve. A new set of

\*This expression is due to P.W. BRIDGMAN. See his work in the Proceedings of the American Academy of Sciences, 60:423, 1925. Also in the volume P.W. Bridgman, *Collected Experimental Papers*, Cambridge University Press, 1964.

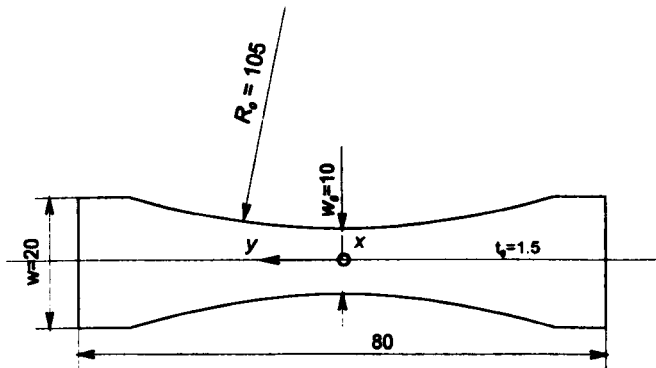
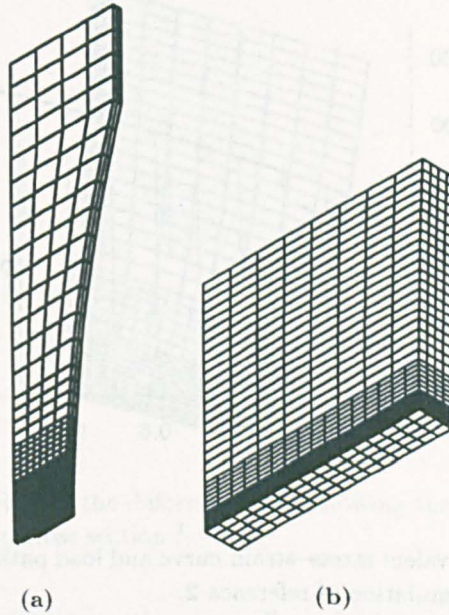


Figure 4.5: A typical damage specimen. All dimensions in millimetres.

strain gauges is installed and the loading starts again, leading the specimen to another level of plastic strain. It is then unloaded and a new slope of the stress–strain curve is recorded. This process is carried on until a visual crack is detected.

The actual specimen adopted by LEMAITRE and DUFAILY exhibits a radius of 80mm aiming to restrict the plastic deformation and, consequently, the damage to a small zone where the elastic modulus can be monitored. It is acknowledged by DUFAILY<sup>60</sup> that this geometry leads to a non-uniform stress field but no further attention is paid in the literature to the influence of the stress field non-uniformity on the measurement of the elastic modulus. Because most of the measurements of  $D$  through the elastic modulus degradation are made in similar specimen geometry, it is important to know whether the measured change in the elastic modulus is due to material damage or to specimen geometry effects.

This problem was examined in reference 2 through a numerical simulation of the test. The specimen geometry in Figure 4.5 was represented by finite elements available in the ABAQUS programme, Figure 4.6. Incremental plasticity theory, the isotropic hardening rule and the VON MISES yield criterion were employed. The input static equivalent stress–strain curve, shown in Figure 4.7 together with the loading–unloading paths, comes from the mild steel specimens tested in Chapter 2. The elastic modulus and Poisson's ratio as measured in cylindrical tensile specimens are 209.8GPa and 0.287, respectively. The simulation is similar to an experiment. The specimen is



**Figure 4.6:** Finite-Element mesh of one-eighth of the damage specimen. (a) Overall mesh and (b) detail of the fine mesh at the minimum cross section.<sup>2</sup>

loaded to some level of plastic strain and unloaded to zero load.

Unlike the experimental test, the simulation does not consider any material degradation. Hence, any deviation of the input elastic modulus, a material property, used in the simulation from the one obtained from numerical data (load, current area and elastic strain), may be safely attributed to geometric effects only.

The usual way to calculate the elastic modulus is to measure the load,  $F$ , the *actual* elastic strain,  $\varepsilon_e$ , at the minimum cross section, the current minimum area  $S$  and to apply the expression

$$E = \frac{F}{S\varepsilon_e}. \quad (4.19)$$

This formula is valid provided the stress field is uniform across the area where the strain gauges are fixed. Obviously this is not exactly the case in the damage specimens since the radius introduces a certain degree of non-uniformity. Moreover, experiments and the numerical simulation in reference 2 show that the specimen thickness distorts significantly at high levels of

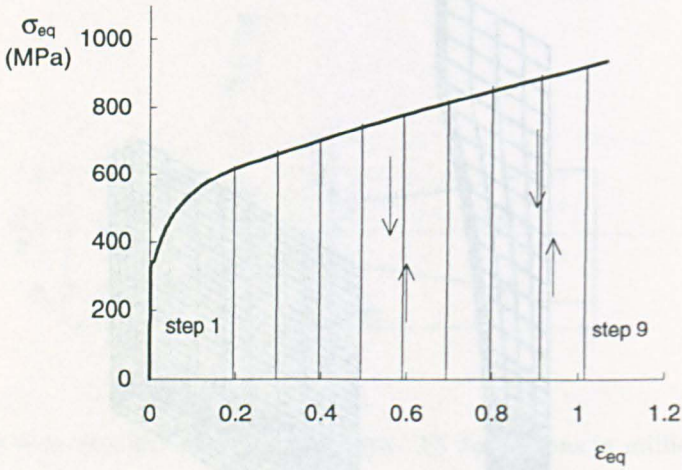


**Figure 4.7:** Equivalent stress–strain curve and load path used in the static Finite-Element simulation of reference 2.

plastic strain, Figure 4.8. This suggests even more important non-uniformity in the stress field and hence additional errors in the elastic modulus if evaluated from expression (4.19). In fact, such elastic modulus is not a material property; it is rather a geometric dependent stress–strain ratio, hence the denomination *apparent elastic modulus*,  $\Xi$ .<sup>2</sup>

This apparent elastic modulus can be defined in different ways. It can be, for instance, a relation between load, area and elastic strains as measured by thickness or width contraction. Some mathematical definitions for the apparent elastic modulus include ratios among:<sup>2</sup>

- load,  $F$ , current cross-section area,  $S$ , and longitudinal elastic strain,  $\varepsilon_s$ , at the minimum thickness and width:

$$\Xi_s = \frac{F}{S\varepsilon_s} \quad (4.20)$$

- load,  $F$ , current cross-section area,  $S$ , and thickness elastic contraction,  $\varepsilon_t$ , at the minimum thickness and width:

$$\Xi_t = \frac{F}{S\varepsilon_t} \quad (4.21)$$

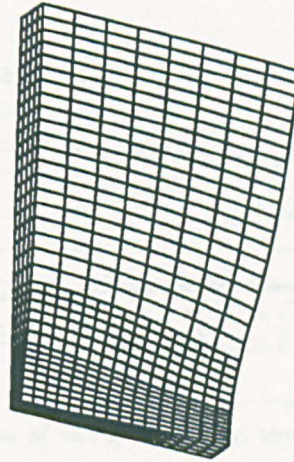


**Figure 4.8:** A detail of the deformed mesh showing the distortion at the specimen minimum cross section.<sup>2</sup>

- load,  $F$ , current cross-section area,  $S$ , and minimum width elastic contraction,  $\varepsilon_w$ :

$$\Xi_w = \frac{F}{S\varepsilon_w} \quad (4.22)$$

- longitudinal plastic strain,  $\varepsilon_s^p$ , load,  $F$ , initial minimum cross-section area,  $S_0$ , and longitudinal elastic strain,  $\varepsilon_s$ :

$$\Xi_S = \frac{F}{S_0 \exp^{-\varepsilon_s^p} \varepsilon_s}. \quad (4.23)$$

This last definition is currently used in the open literature for damage specimens.

The numerical analysis in reference 2 yields the plot of all these apparent elastic moduli against the plastic strain, Figure 4.9, allowing the comparison with the initial input elastic modulus. Any deviation from this value is interpreted as an error introduced by the specimen geometry and by the associated definition.

This error,  $er_E$ , in the value of the elastic modulus affects the damage parameter, as defined by  $D_E^\varepsilon = 1 - \tilde{E}/E$ , by a substantial amount, specially

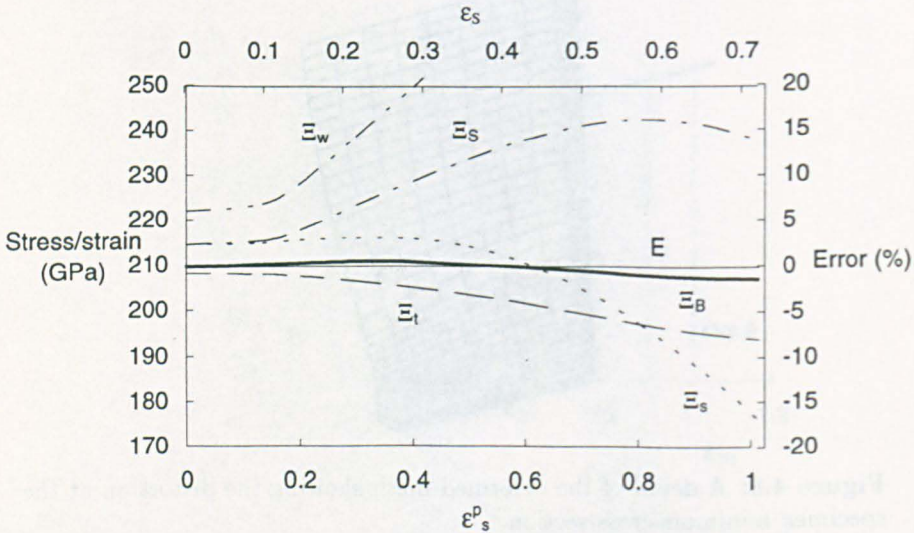


**Figure 4.9:** Change of the apparent elastic modulus and associated error against the actual axial,  $\epsilon_s^p$ , and area reduction,  $\epsilon_s$ , plastic strains.  $\Xi_w$ ,  $\Xi_t$  and  $\Xi_w$  use the strain data from axial, thickness and width elastic change, respectively.  $\Xi_s$  is evaluated using the common literature procedure, equation (4.23), and  $\Xi_B$  is obtained applying the Bridgman correction factor to  $\Xi_t$ .<sup>2</sup>

for low values of  $D_E^\epsilon$ .<sup>2</sup> Hence *all* the data here presented concerning the measurement of  $E$  were corrected according to Figure 4.9. Because in the present work it was possible to measure both  $\Xi_s$  and  $\Xi_s$  definitions, the correction factor was applied accordingly and it was confirmed that both results after correction are equal within 3.7%, at worst.

### 4.3 Damage tests description

To measure the damage parameters according to the various definitions and techniques commented earlier on, the specimen depicted in Figure 4.10 was tested in a tensile test machine.

The specimens were cut from the plate shown in Figure 2.5, on page 24, along the rolling direction and machined in an automatic milling machine. Strain-gauges type EP-08-015DJ-120, from MICRO MEASUREMENTS, were

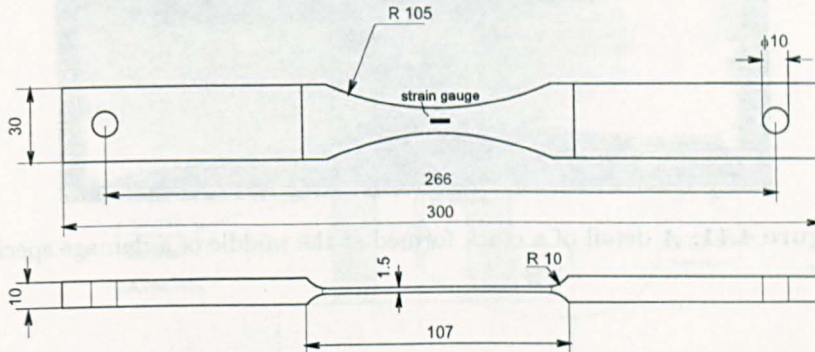


**Figure 4.10:** Illustration of the geometry of the damage specimen. All dimensions in millimetres.

pasted onto them at the middle of the minimum cross-section with the help of a set of amplification lenses. These strain gauges have an effective gauge-length of 0.36mm and are designed to sustain plastic deformations of up to 0.1. The instrumented specimens were then placed in an oven at  $80^\circ$  for 2 to 3 hours to allow the polymerisation of the glue.

Five static tensile specimens were subjected to the load path in Figure 4.7 \*. The head speed of the tensile test machine was set between 0.05 and 2mm/min, to minimise strain rate effects. The data collected during the elastic loading region was used to calculate the various apparent elastic moduli described above †.

The elastic modulus was always measured at the beginning of each load cycle, when then the strain gauges were new. This avoided any change of the strain gauge factor due to the plastic strains.<sup>87</sup> The specimens were unloaded immediately after failure of one of the strain gauges . This was easily checked because the strain gauges were connected in a quarter-bridge configuration. The experimental apparatus was the same as described in Figure 2.6 on page 25, except for the camera, which was not used. The calibration of the system was performed at the end of each load cycle, as described on page 25. The collected data were then recorded in an electronic

\*The actual load path differs slightly from the one in Figure 4.7 since the strain gauges fail at different plastic strain intervals.

†Some authors recommend that elastic stress and strain are recorded on the elastic unloading curves.<sup>60, 126</sup> In the present experiments, it was confirmed that no significant difference exists between the data for the elastic loading and unloading cycles.



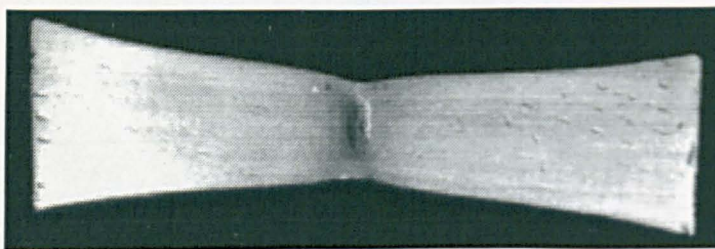


**Figure 4.11:** A detail of a crack formed at the middle of a damage specimen.

file for analysis. This process was carried on until a visible crack occurred in the specimen, Figure 4.11, when then it was considered that the critical damage state had been reached.

Aiming to measure the static Poisson ratio evolution, an electronic extensometer was installed transversely to the specimens at the minimum width. The results obtained are a measure of the material anisotropy. It should be remarked, however, that the elastic strain field at the cross-section is not uniform.<sup>2</sup> Because the extensometers measure only an average value of lateral elastic strains, the measured Poisson ratio has to be seen as an average rather than a local value.

Additionally, the specimens were submitted to a direct current of 5A from a stable power source operating in a constant current mode, Figure 4.12. The specimens were isolated from the tensile machine by an appropriate rig. The change in the potential across two internal points to the power supply connection was monitored continuously by a high precision multimeter SOLARTRON, model 7150. Amplifiers at high gain were also used to monitor the drop in potential due to the damage but the records were too noisy to be used, even after filtering.

#### 4.4 Measuring the damage parameters

By using the techniques and the measurement systems described before, it was possible to calculate the damage according to its different definitions, as now presented.

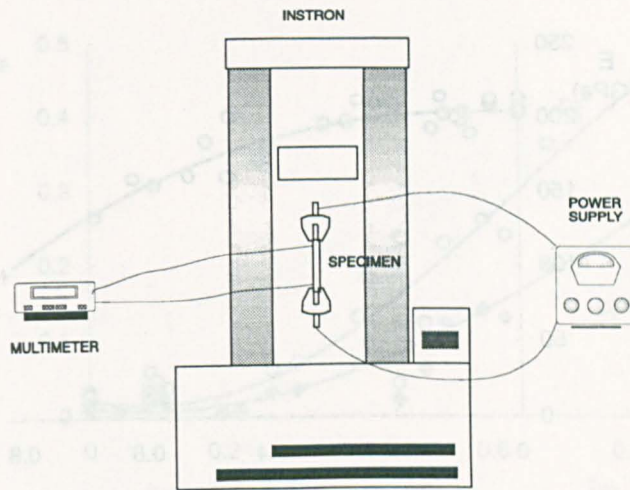


**Figure 4.12:** Schematic representation of the measurement system used to record the electrical potential change due to damage.

#### 4.4.1 Static damage parameter $D_E$

The measurement of the elastic modulus for different levels of plastic strain was carried out along the guidelines above. The elastic modulus decreases with the equivalent plastic strain as indicated in Figure 4.13. The original recorded data were corrected according to the curves labelled  $\Xi_S$  and  $\Xi_s$  in Figure 4.9. As previously commented, no significant difference was found in the final value of the elastic modulus when using either procedure. In passing, reference 2 shows that, by taking into account geometric effects on the evaluation of the elastic modulus, one finds an actual value of damage larger than otherwise predicted.

According to Figure 4.9, the use of the elastic variation of the thickness is potentially a better technique for measurement of the elastic modulus in specimens like the one in Figure 4.10. The elastic change of thickness can be easily measured with a transverse extensometer. However, this finding was not available at the time the tests had been done.

The two most common damage parameters,  $D_E^\epsilon$  and  $D_E^W$ , obtained from the elastic modulus degradation are presented in Figure 4.14. Experimentally, it is difficult to measure the elastic modulus *at* the failure strain because failure is a dynamic phenomenon. Hence, the last elastic modulus measure

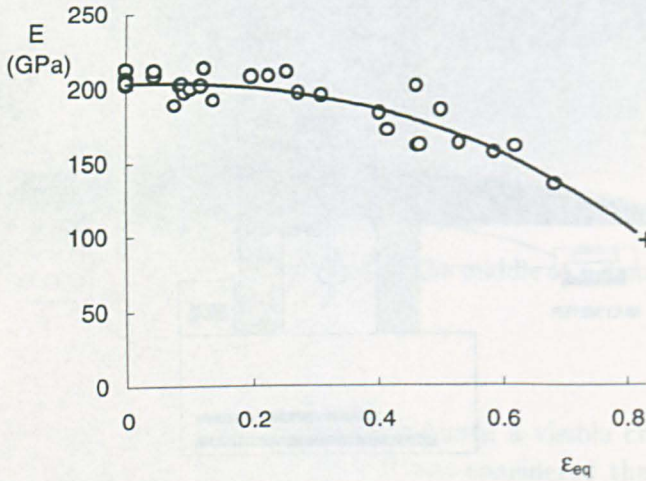


**Figure 4.13:** Change of the elastic modulus against the equivalent plastic strain. The cross is an extrapolation of the third order polynomial fitted to the data.

is associated with an equivalent plastic strain of 0.68 whereas failure took place at 0.83. The cross in Figures 4.13 and 4.14 represents then the extrapolation of the curves. This allows one to infer the critical damage parameters based on the elastic modulus degradation. For the mild steel, one has

$$D_{E_{cr}}^{\epsilon} = 0.45 \quad \text{and} \quad D_{E_{cr}}^W = 0.27. \quad (4.24)$$

#### 4.4.2 Static damage parameter $D_{HV}^{\epsilon}$

The material degradation is reflected on the values of hardness and, as previously shown, this can be related to the damage parameter. The specimens broken in the damage tensile tests were mounted and polished for hardness measurement. An automatic micro-hardness test machine from SHIMADZU, Japan, was programmed to perform hardness measurement at discrete locations along the fracture boundary and along the load axes. The diagonal of the indentation produced by the diamond indenter was measured on a computer screen by the operator and the values were automatically dumped to a data base. In addition to the damage specimens, the notch specimens tested as described in Chapter 3 were also hardness mapped.

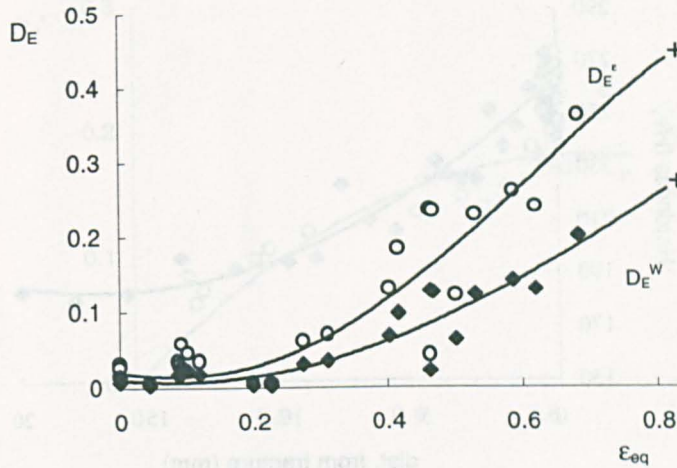


**Figure 4.14:** Damage evolution, according to equations (4.7) and (4.10), versus the equivalent plastic strain. The crosses are obtained by extrapolating the fourth order polynomial used to fit the data.

Unfortunately, despite all the collected data, it appears that, for the mild steel used here, there is no evident decrease of the hardness in the *damaged region* to yield a consistent measure of the damage parameter. Observe that the hardness in the damage region should change at a rate different from the hardness at the non-damaged material to permit the evaluation of the damage parameter  $D_{HV}^{\epsilon}$ , Figure 4.4. Even so, the solid symbols in Figure 4.15, were extrapolated and compared to the average of the open symbols in the same figure to give a measure of  $D_{HV}^{\epsilon}$ . Similar procedures for the notch specimens were also performed and the results are summarised in Table 4.1.

**Table 4.1:** Damage values  $D_{HV}^{\epsilon}$  for damage (d) and notch (n) specimens. The tests are all quasi-static except for the ones where the test speed is quoted.

d057	d061	d060	d068	d064	d062	n0515 <sup>a</sup>	n430	n420 <sup>b</sup>	n404
0.051	0.028	0.020	0.066	0.039	0.043	0.062	0.117	0.161	0.153

<sup>a</sup>Pulled at 3m/s.

<sup>b</sup>Pulled at 0.6m/s.

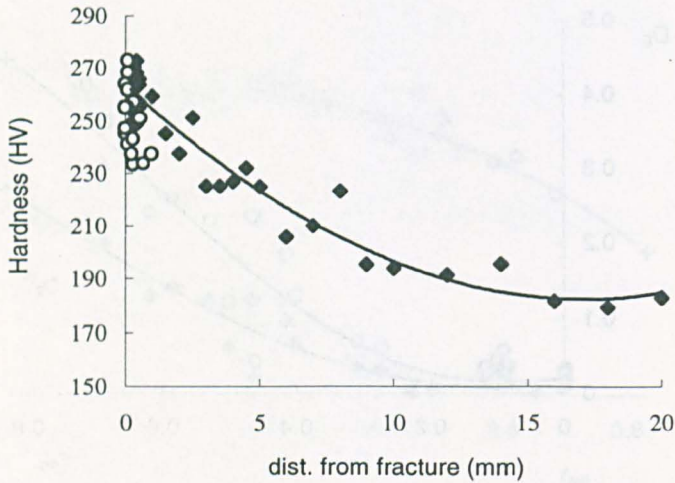


**Figure 4.15:** Hardness values along the length of a damage specimen pulled statically. The continuous line square fits the solid symbols. The open symbols were averaged and assumed to be affected by damage. The fracture occurred at zero millimeters.

#### 4.4.3 Static damage parameter $D_V^\epsilon$

Disregarding any damage effect on the resistivity of the damage specimens, the damage parameter  $D_V^\epsilon$  was measured as a function of the equivalent plastic strains. The averaged results are plotted in Figure 4.16.

### 4.5 Material damage according to the void area

The original definition of damage relies on the measurement of the voids formed inside the specimen tested. This is a destructive method since the specimen has to be sectioned, mounted in a resin and polished.

The polishing is a most delicate task. To illustrate this point, some mild steel samples were polished using two different methods: the standard one recommended for mild steel from the polish machine manufacturer \*, Table 4.2, and other using alumina  $0.3\mu\text{m}$  for three hours, ultrasonic cleaning for 3 minutes followed by alumina  $0.05\mu\text{m}$  for another one hour, as in

\*All the polishing was automatically executed in the PREPAMATIC, from STRUERS.

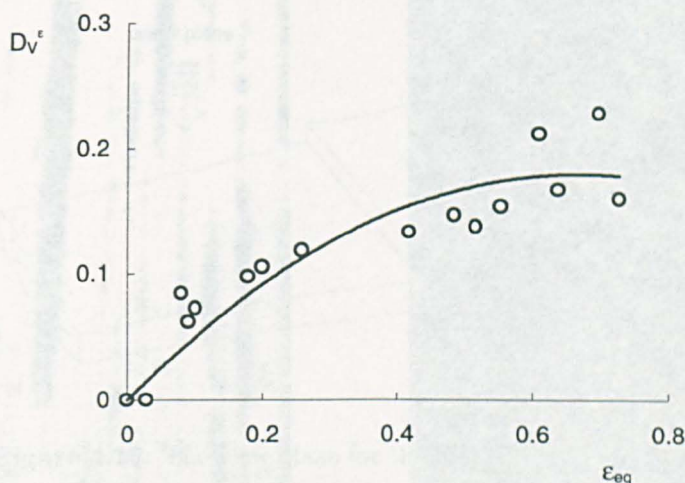


Figure 4.16: Static damage parameter evolution  $D_V^\epsilon$  measured by the electrical potential method against the equivalent plastic strain.

Table 4.2: Polishing route used for the mild steel specimens.

cloth	grain size ( $\mu\text{m}$ )	time (s)	load (N)	rotation (rpm)
stone	150	until remove $500\mu\text{m}$	153	1000
P-M	6	until remove $100\mu\text{m}$	153	150
plus	3	180	126–108	150

reference 219\*.

The result is shown in Figure 4.17. The material in the figure was not plastically deformed and hence no voids were expected; at most some initial impurities. The incorrect polishing, however, introduced voids viewed here as the place occupied by grey and black soft sulphide. Their softness cause them to become elongated during rolling and also allows them to be removed when polishing with alumina for a long time.<sup>174</sup> This point is here stressed to show that an incorrect polishing may lead to wrong values for the damage parameter  $D_S$ .

Using the standard route for polishing mild steel, the damage specimens tested in tension where investigated for voids. Some of the notched tensile specimens tested as described in Chapter 3 were also examined. The mea-

\*Private communication from the first author in reference 219.

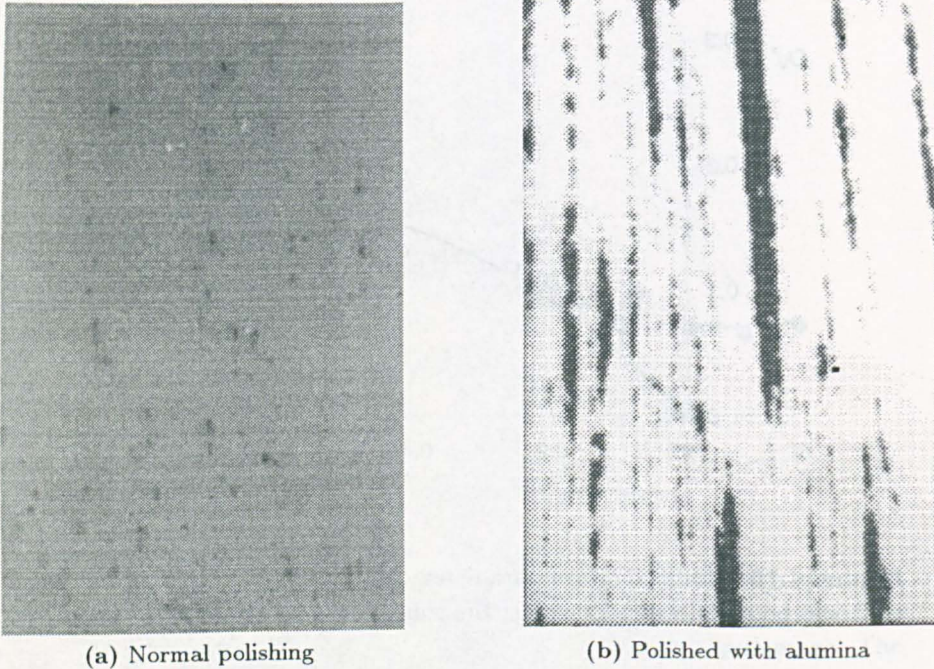


**Figure 4.17:** Micro-photography of an *as received* mild steel specimen. (a) Normal polishing and (b) polished with alumina.

surement of the void area in both the damage and notched specimens was restricted to the near fracture boundary, since voids are more concentrated at this region. The measurement plane is indicated in Figure 4.18 which, according to classical stereology arguments,<sup>204</sup> leads to identical values of void area as if it had been measured in the fracture plane. The experimental procedure consisted in locating the more populated void zones and recording the image in an electronic file by using a camera. The file was then analysed using a software \* with capabilities of measuring voids. Different magnifications were used in the beginning but it was concluded that a magnification of 100 was good since the voids were easily identified and the field of view was small enough to restrict the measurement to a small area.

---

\*Public domain software IMAGE, written by the NATIONAL INSTITUTE OF HEALTH-USA.

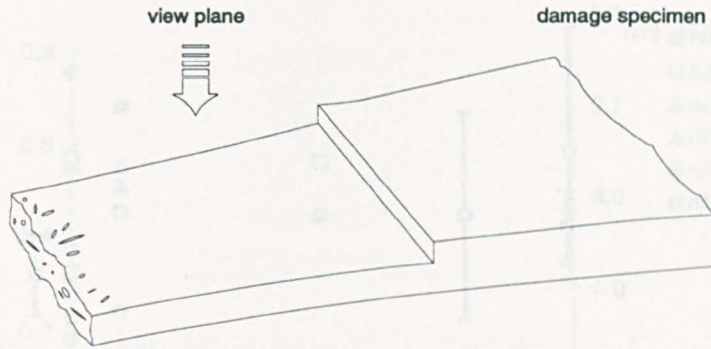


Figure 4.18: The view plane for the measurement of voids.

#### 4.5.1 Results

A typical void for the present material was shown in Figure 4.1. It can be seen that the void is elliptical–shape rather than symmetrical. The void (or micro–crack) orientation suggests an anisotropic effect, which may explain the different stress–strain failure values for different material orientations (see Table 2.2 on page 30).

The results\* obtained for the damage specimens show that the strain rate does not significantly influence the critical values of the damage  $D_S$ , Figure 4.19. A trend is shown in the curve but it was not possible to infer the effect of higher strain rates on void growth.

As far as the notch specimens are concerned, the data in Figure 4.20 also suggests a minor influence of the strain rate on  $D_S$ . More importantly is that the void area is nearly the same at the centre and at the notch base. But for the n05 and n2 specimens, a crack starts to form at the notch base (see Figure 3.19, on page 72), which would lead one to conclude that the void distribution is not an indicator of the failure sites. However, it has to be borne in mind that most of the n specimens were fractured during the tests and hence the voids can propagate along the fracture boundary, making their final values more homogeneous.

This is further corroborated by looking at the damage values of two notch specimens whose tests were interrupted before total fracture. One specimen has a large initial radius of 4mm and, as seen in Chapter 3, fails from the

\*The initial *measured* void fraction of 0.030% was subtracted from all the data.



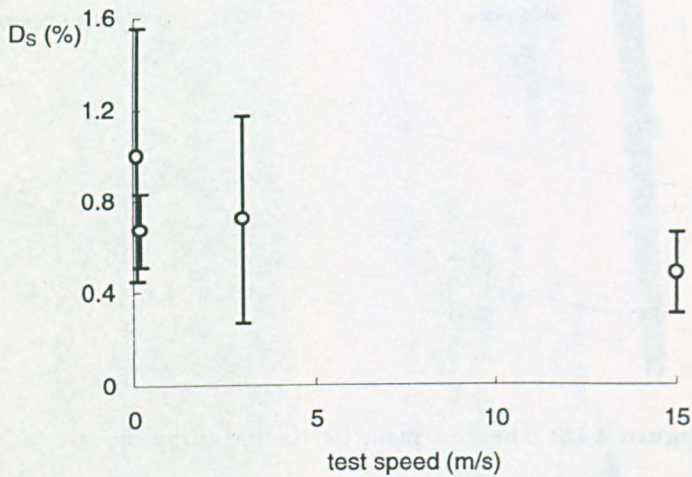


**Figure 4.19:** The damage parameter  $D_S$  versus the nominal test speed.

centre. Indeed, the damage  $D_S$  at the centre is 0.76% to be compared with 0.18% at the notch base. Another specimen of nominal radius of 0.5mm fails at the notch root. The damage value at this point is 0.57%, contrasting with its value at the centre of 0.33%.

It should be remarked that the damage  $D_S$  does not take into account any void interaction, shape, orientation and stress concentration. Hence, it is expected that the actual damage viewed as the weakness of a structure to sustain loads is higher than inferred by measuring the void area. This point was taken by JANSSON and STIGH,<sup>91</sup> when analysing different cavity shapes and orientations embedded in an isotropic, incompressible power law creeping material. They showed that the damage parameter,  $D_S$ , is underestimated by a factor as high as two for spherical cavities.

## 4.6 Additional experimental parameters

The Poisson ratio in the elastic regime evolves with the equivalent plastic strain according to Figure 4.21. The main experimental limitation of these data is that the lateral elastic strain was measured with extensometers. As already remarked, the elastic strains are not constant across the width of a damage specimen, which limits the accuracy of the data.

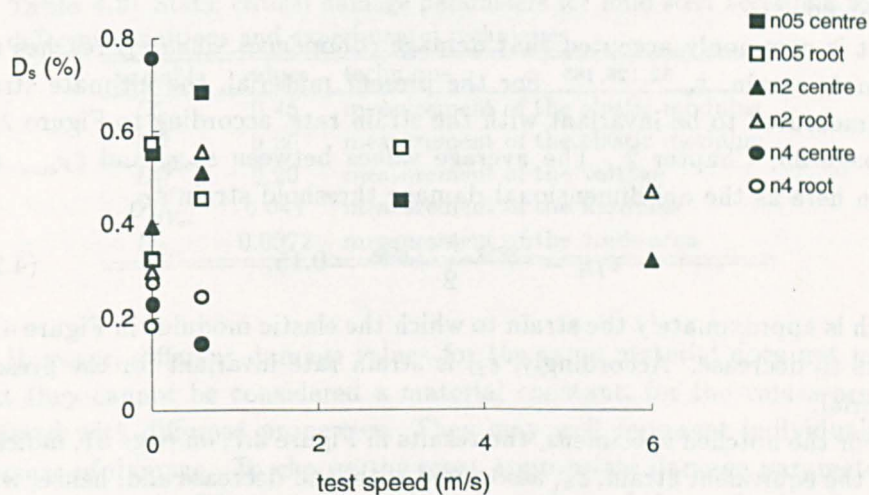


**Figure 4.20:** Damage evolution,  $D_S$ , with the nominal test speed for the notched specimens.

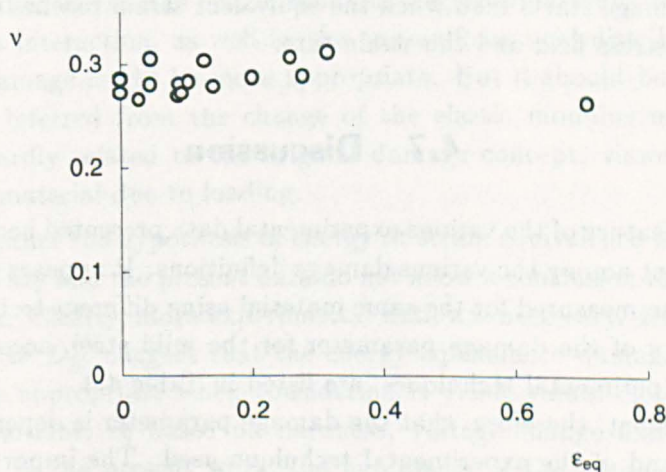


**Figure 4.21:** Elastic Poisson ratio evolution with the equivalent plastic strain measured by axial local strain gauges and width contraction of the damage specimens.

Consider now the uni-dimensional strain associated with the damage threshold,  $\varepsilon_D$ .

It is commonly accepted that damage commences when  $\varepsilon_D$  reaches the ultimate strain,  $\varepsilon_u$ .<sup>52,126,185</sup> For the present material, the ultimate strain was measured to be invariant with the strain rate, according to Figure 2.15 on page 35, Chapter 2. The average values between  $\varepsilon_{body}$  and  $\varepsilon_{F_{max}}$  are taken here as the uni-dimensional damage threshold strain  $\varepsilon_{D_1}$

$$\varepsilon_{D_1} = \frac{\varepsilon_{body} + \varepsilon_{F_{max}}}{2} = 0.15, \quad (4.25)$$

which is approximately the strain to which the elastic modulus in Figure 4.13 starts to decrease. Accordingly,  $\varepsilon_D$  is strain rate invariant for the present material.

For the notched specimens, the results in Figure 3.7, on page 57, indicate that the equivalent strain,  $\varepsilon_u$ , associated with load decrease and, hence, with damage beginning, is not strain rate sensitive. Also, the different stress-strain fields induced by the notch acuity do not have a marked influence on  $\varepsilon_u$ . The average values of  $\varepsilon_u$  for different notch radii is 0.19 which can be averaged with  $\varepsilon_{D_1}$  to finally give

$$\varepsilon_D = 0.17. \quad (4.26)$$

The damage starts then when the equivalent strain reaches 0.17, regardless of the stress field and the strain rate.

## 4.7 Discussion

A striking feature of the various experimental data presented here is the clear disagreement among the various damage definitions. It appears that damage has not been measured for the same material using different techniques. The static values of the damage parameter for the mild steel, according to the different experimental techniques, are listed in Table 4.3.

It is evident, therefore, that the damage parameter is dependent on the definition and of the experimental technique used. The importance of this observation is that failure criteria based upon damage parameters may yield good or poor predictions, according to the critical damage chosen. In this sense, the damage parameter might be seen as an adjustable parameter, a fact pointed out by M. KACHANOV<sup>106</sup> in light of his studies on crack interaction.

**Table 4.3:** Static critical damage parameters for mild steel according to different definitions and experimental techniques.

variable	values	technique
$D_{E_{cr}}^e$	0.45	measurement of the elastic modulus
$D_{E_{cr}}^W$	0.26	measurement of the elastic modulus
$D_{V_{cr}}^e$	0.20	measurement of the voltage
$D_{HV_{cr}}^e$	0.041	measurement of the hardness
$D_{S_{cr}}$	0.0072	measurement of the voids area

However, different damage values for the same material does not mean that they cannot be considered a material constant, for the values are associated with different properties. They may well represent individually a measure of damage. To choose the most appropriate damage parameter is not an easy task. Of course that this is dependent of the goals the parameter has to fulfil. In fact, as pointed out by KRAJČINOVIC,<sup>112</sup> the selection of different damage variable may yield different damage models.

For the present purposes, it is argued here that the damage inferred from voids is too small. It is expected that crack interaction and shape have a decisive influence on the final value of  $D$ . This cannot be measured directly from the void area. As the elastic modulus degradation tends to take into account such interaction, as well as the non-uniform void distribution, the associated damage might be more appropriate. But it should be clear that the damage inferred from the change of the elastic modulus may not be straightforwardly related to the original damage concept, viewed as voids formed in a material due to loading.

Now, whether the hypothesis of energy or strain equivalence holds better is difficult to say and the present data do not allow a conclusion to be formed on this point. Clearly, more experimental data are necessary. However, the lower values of  $D_E^W$  suggest that the energy equivalence damage definition can be more appropriate when considering it yields values closer to other damage definitions, *eg* based on hardness, voltage change and void area. Nonetheless, in the present work, the hypothesis of the strain equivalence will be adopted since its general formulation is better established, as Chapter 5 will show.

Another table similar to Table 4.3 can be obtained from the damage data available in the literature. The damage for different materials is listed on Table 4.4. It can be seen, in line with the data here produced, that the

damage from void measurement tends to be quite low.

It is important to stress that the damage  $D_E$  is usually measured in specimens with a large lateral radius. This induces important errors in the final values of the elastic modulus. Hence, the damage  $D_E$  in the literature, Table 4.4, cannot be directly compared with the ones here obtained since the later were corrected according to the numerical results of reference 2.

In this reference, it is shown that an error,  $er_E$ , in the value of the elastic modulus affects the correct value of the damage,  $D_E$ , through equation

$$D_E = \frac{D_l + er_E}{1 + er_E}, \quad (4.27)$$

where  $D_l$  is the damage measured through the elastic modulus change in specimens with a lateral radius and without any correction. For example, at a strain of around 0.8, the error in the elastic modulus is 16%, Figure 4.9. If the common accepted value of the damage  $D_l$  is 0.20, the correct value will be  $D_E = 0.31$ , a quite large difference.

One open question in the literature is how the critical damage is influenced by tri-dimensional stress fields.<sup>14</sup> As a matter of fact, the so-called uni-dimensional damage parameter, as  $D_E$ , thought considered to be uni-dimensional,<sup>126</sup> takes place under constrains of such order that the prevailing peak triaxiality at the critical moment is as high as 0.65.<sup>2</sup> This is much higher then the accepted value of 0.33. Hence,  $D_E$  cannot be considered uni-dimensional, unless experimentally shown that the stress field has a negligible influence on  $D$ .

As the triaxiality varies drastically with the notch radius, the notch specimens can be used to assess the stress influence on the critical damage. In this case, the damage was measured from the voids. Figure 4.22 shows the averaged measured data, together with bars representing a  $\pm$  one standard deviation. Apart from the values for the damage specimens, which are mainly plane strain deformed, the damage parameter  $D_S$  does not seem to be highly stress state dependent. This suggests that the critical damage can be, in a first approximation, assumed constant for axisymmetric structures when using the void measure technique, regardless of the strain rate and for a triaxiality range between 0.35 and 1.37\*.

On the other hand, BECKER's<sup>10</sup> experimental data indicate a slight decrease of the critical void volume fraction (the damage  $D_S$ ), with the increase

---

\*These are the values for the minimum and maximum triaxiality in the notch specimens. See Figure 3.16 on page 67.

of the triaxiality for the axisymmetric case. For plane strain, he found that  $D_S$  can be considered constant, though initial void volume fraction and hardening dependent. Moreover, results from SHI *et al.*<sup>183</sup> show that the critical void volume fraction increases significantly with the increase of the stress triaxiality. Their material, a structural steel BS4360 grade 50D, is similar to the one used in this study, as far as yielding and elongation are concerned. They concluded that the critical damage at the onset of crack is stress dependent and hence not a material constant.

In line with the results here produced, OTSUKA *et al.*<sup>169</sup> found for their material, a structural steel SM41A, also similar to the one here tested, that the critical void volume fraction attained the same level (2.5%) regardless of the triaxiality\*. These comments lead to the natural conclusion that the stress state influences the critical damage but in a way particular to each material. In the present case, this influence can be assumed negligible.

The experimental technique based on hardness seems to work well for some materials, as shown in Figure 4.4, but not for the mild steel here tested. This is an unfortunate finding because a whole map of hardness in specimens tested at different strain rates may be obtained easily with automatic measurement systems, as the one here used.

It is important to remark that the experimental techniques adopted have been demonstrated to be valid for other materials. This is the case of hardness, where good results for mild steel, comparable to the change in the elastic modulus, were obtained by LEMAITRE and his group.<sup>21,126,130,131</sup> However, in face of the present results, the technique cannot be considered general.

These comments hold also for the damage measured from the potential drop. It does not faithfully indicate the quasi-linear damage evolution obtained from the elastic modulus change. A correction<sup>126</sup> for the change of length,  $l$ , and area,  $S$ , due to the plastic strains was performed but the results did not improve. The technique may be potentially used for dynamic measures of the damage but high precise transient recorders operating with signals as small as  $1\mu V$  with fast response time, are fairly uncommon.

The present data allows one to conclude that, within the range tested, the damage evolves linearly with the plastic strains. The threshold damage strain and the critical damage are neither stress nor strain rate dependent. Theoretically, these features are very appealing. To fully utilise them in

---

\*This does not hold for failure by shear (mode II).<sup>169</sup>

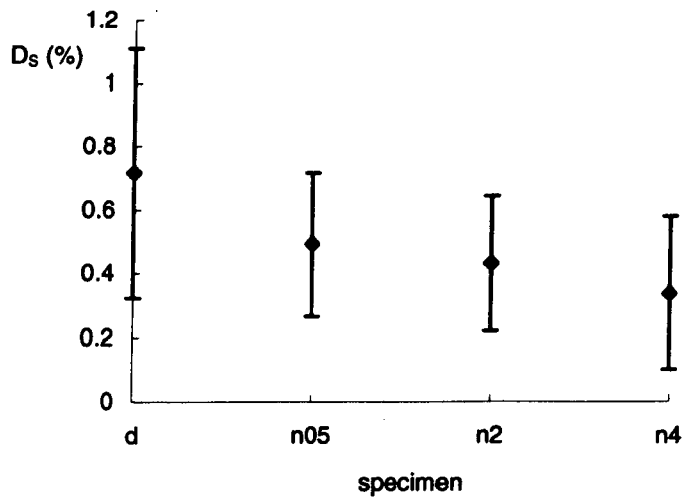


**Figure 4.22:** The damage parameter  $D_S$  averaged per specimen type. The bars are indicative of the data scatter (values of  $\pm$  one standard deviation).

applying a failure criterion, one needs a theoretical framework which, by dealing with quantities as damage, stress and strain, is capable of imposing a limit failure strain or stress in a structure under analysis, beyond which failure is triggered. This is the subject of the next chapter.

**Table 4.4:** Critical damage value for various materials at room temperature evaluated from void area and from the variation of the elastic modulus.

Ref.	Material	$D_{S_{cr}}$	$D_{E_{cr}}^e$	$D_{E_{cr}}^W$
11	sintered iron <sup>a</sup>	0.140		
28	plain carbon steel 1045 coarse carbide	0.035		
55	glass reinforced epox composite	0.180		
118	plain carbon steel 1045 <sup>d</sup>	0.066		
118	plain carbon steel 1090	0.048		
118	plain carbon steel 1015	0.048		
126	steel NiCoMo	0.880		
130	high alloy steel	0.100		
142	mild steel	0.060		
160	347 austenitic steel	0.010		
169	SM41A structural steel <sup>d</sup>	0.025		
183	BS4360 grade 50D structural steel <sup>d</sup>	0.010 <sup>e</sup>		
183	BS4360 grade 50D structural steel <sup>d</sup>	0.003 <sup>f</sup>		
185	A533B pressure vessel steel	0.029		
219	Fe-2%Si <sup>b</sup>	0.105 <sup>c</sup>		
4	carbon-epoxi		0.120	0.062
23	DERAKANE 411-45 resin and E-glass CSM		0.100	0.051
60	copper		0.850	0.613
110	aluminium 2024		0.130	0.067
126	aluminium alloy 2024		0.230	0.123
126	concrete in tension		0.200	0.106
126	steel AISI1010		0.200	0.105
126	stainless steel AISI316		0.150	0.078
132	alumina bounded by carbon fiber-epoxy		0.300	0.163
167	aluminium alloy AU4G1		0.230	0.123
167	steel XC38		0.220	0.117
211	steel 15MnMoVNRe		0.295	0.160

<sup>a</sup>Initial void volume fraction  $f_0 = 0.06$ .

<sup>b</sup>Initial void volume fraction  $f_0 = 0.06$ .

<sup>c</sup>Close to the failure point.

<sup>d</sup>Similar to the material used in this work.

<sup>e</sup>At  $\sigma_h/\sigma_{eq} = 4.1$ .

<sup>f</sup>At  $\sigma_h/\sigma_{eq} = 2.2$ .





---

## 5 Strain Rate-Dependent Damage Mechanics

CONTINUUM DAMAGE MECHANICS, CDM, offers a theoretical framework for the prediction of the damage evolution in a structure. The growth of damage is upper bounded by the beginning of a crack, which occurs when a critical damage in the continuum is achieved.

This threshold between critical damage and crack growth can be seen as a failure criterion. Because the damage is related to the stresses and strains, it is all plausible to admit that damage should affect the structural response even before a critical value is achieved. This has the immediate consequence that the damage should be included in the set of equations governing a particular problem, as demonstrated in Appendix A.

On the other hand, it is evident from the results of Chapter 2 that the strain rate affects the material response. Clearly, if CDM has to be applied in structural impact analysis, it is important to take into account, at least, the influence of the strain rate on the stresses. This, in turn, affects the damage evolution.

These comments set the goals of this chapter. It aims to take into account strain rate effects on the damage evolution. This is achieved by using the stress-strain-strain rate relation proposed in Chapter 2. The so obtained damage model is particularised to linear hardening and perfectly plastic materials. As an application of the damage equation, the triaxiality influence on the failure strain, the failure sites in notched specimens and the dynamic limit forming diagrams are explored. A discussion ends the chapter.

## 5.1 Strain rate influence on damage evolution

Generally speaking, for the few cases where damage is taken into account in a dynamic structural analysis, as in ROUVRAY and HAUG<sup>54,81</sup> and in FARUQUE and WU,<sup>66</sup> CDM models do not bear any special feature which would distinguish them from a static model.

The exceptions are worth of mentioning.

NEMES and SPÉCIEL<sup>164</sup> applied a rate-dependent damage model to composites. They have concentrated on exploring their model as far as stability, convergence and mesh sensitivity of the numerical solution is concerned. Their model is capable of showing, for a fixed plastic strain (smaller than 1%), that the damage parameter decreases with an increase of strain rate. The damage evolution is written in terms of stress and one parameter, known as damage viscosity constant, governs the rate of damage.

SIMO and JU<sup>186</sup> have proposed a viscous-damage linear model in order to retard the growth of microcracks as the strain rate increases. They have implemented the model in a Finite-Element code and have simulated the compression of concrete at two different speeds.<sup>187</sup> The strains and strain rates in the simulation were quite low, with strain rates less than  $0.1\text{s}^{-1}$ .

SIMO and JU's model was also implemented by ZHU and CESCOTTO<sup>224</sup> and used in sheet forming. The strain rate used in the simulation was not quoted but the velocity of the punch was set to 40mm/s.

In another paper, ZHU and CESCOTTO<sup>223</sup> have used a damage model in the numerical simulation of impacted beams. The CDM formulation in this case is standard and it does not add any dynamic feature. The dynamic analysis is restricted to the consideration of inertia terms on ordinary equilibrium equations only and not on the damage evolution.

In fact, damage rate-dependent models geared towards the impact of structures, where the strain rates are high, have not yet been developed, at least within the framework of the CDM presented in Appendix A.

A basic CDM model, taking care of the increase of stresses due to strain rate effects, can be added to the standard damage model presented in Appendix A. There, it was shown that, for a bilinear material, the damage evolves according to

$$\dot{D} = \dot{\lambda} \frac{\partial \mathcal{F}_D}{\partial Y}, \quad (5.1)$$

or

$$\dot{D} = \frac{\bar{\sigma}_{eq}^2 R_\nu}{2E\bar{S}} \dot{p} \bar{H}(p - p_D), \quad (5.2)$$

since

$$\frac{\dot{\lambda}}{1-D} = \frac{\frac{3}{2} \frac{\sigma'_{ij}}{\sigma_{eq}} \frac{\dot{\sigma}'_{ij}}{(1-D)^2}}{E' - \frac{\sigma_{eq}}{(1-D)^2} \frac{\partial \mathcal{F}_D}{\partial Y}} = \dot{p}, \quad (5.3)$$

$$\mathcal{F}_D = \frac{Y^2}{2\bar{S}(1-D)}, \quad (5.4)$$

and

$$Y = \frac{\bar{\sigma}_{eq}^2 R_\nu}{2E}, \quad (5.5)$$

with

$$R_\nu = \frac{2}{3}(1+\nu) + 3(1-2\nu) \left( \frac{\sigma_h}{\sigma_{eq}} \right)^2. \quad (5.6)$$

In equations (5.2)–(5.6),  $D$  is the damage,  $E$  and  $E'$  are the elastic and hardening moduli,  $\nu$  is Poisson's ratio and  $\sigma_{eq}$  and  $\sigma_h$  are the equivalent and hydrostatic stresses, respectively. The function  $\bar{H}$ , defined in Appendix A, indicates that the damage rate is greater than zero only when the accumulated plastic strain,  $p$ , is greater than  $p_D$ , which is a parameter function of the material and stress state. The constant  $\bar{S}$  will be commented on later.

The set of constitutive equations including elasticity, plasticity and damage are given by equations (A.42)–(A.48) in Appendix A.

The potential  $\mathcal{F}_D$  in equation (5.4) is proposed by LEMAITRE<sup>126</sup> and renders the damage evolution one of its simplest form\*.

The plastic multiplier,  $\dot{\lambda}$ , used in equation (5.1) comes from the condition

$$\frac{\partial f}{\partial t} = \frac{\partial f}{\partial \sigma_{ij}} \dot{\sigma}_{ij} + \frac{\partial f}{\partial \bar{R}} \dot{\bar{R}} + \frac{\partial f}{\partial \sigma_y} \dot{\sigma}_y + \frac{\partial f}{\partial D} \dot{D} = 0. \quad (5.7)$$

when the yield function is rendered as

$$f = \bar{\sigma}_{eq} - \bar{R} - \sigma_y. \quad (5.8)$$

\*Other potentials were referred to in Chapter 1.

$\bar{R}$  is the hardening term,  $\sigma_y$  is the (static) yield stress and  $\bar{\sigma}_{eq}$  is the effective stress presented on page 76, Chapter 4.

To incorporate strain rate effects in the damage evolution, equation (5.2), one starts with a dynamic yield function written as

$$f = \bar{\sigma}_{eqd} - \bar{R} - \sigma_y - f_d(\dot{\epsilon}_{eq}), \quad (5.9)$$

where the subscript  $d$  stands for dynamic and  $f_d = f_d(\dot{\epsilon}_{eq})$  is a strain rate-dependent term which contributes to the expansion of the yield surface due to the material strain rate sensitivity.

In this case, the plastic multiplier,  $\dot{\lambda}$ , is obtained via the condition

$$\frac{\partial f}{\partial t} = \frac{\partial f}{\partial \sigma_{ij}} \dot{\sigma}_{ij} + \frac{\partial f}{\partial \bar{R}} \dot{\bar{R}} + \frac{\partial f}{\partial \sigma_y} \dot{\sigma}_y + \frac{\partial f}{\partial f_d} \dot{f}_d + \frac{\partial f}{\partial D} \dot{D} = 0. \quad (5.10)$$

A change of the plastic multiplier,  $\dot{\lambda}$ , due to dynamic effects can be attributed to the term

$$\frac{\partial f}{\partial f_d} \dot{f}_d, \quad (5.11)$$

in equation (5.10).

The stress-strain-strain rate relation presented in Chapter 2

$$\sigma_{eqd} = \sigma_{eqs} + \bar{m} \dot{\epsilon}^{\bar{n}}, \quad (5.12)$$

repeated here for convenience, adds to the static yield surface the dynamic term

$$f_d = \bar{m} \dot{\epsilon}^{\bar{n}}, \quad (5.13)$$

whose time derivative is

$$\frac{df_d}{dt} = \bar{m} \bar{n} \dot{\epsilon}^{\bar{n}-1} \ddot{\epsilon}. \quad (5.14)$$

In rigid-plastic analyses, it is difficult to evaluate the strain rate change, the term  $\ddot{\epsilon}$  in equation (5.14), as a structure is loaded. In the present work, the strain rate will be evaluated in Chapter 6 and it is anticipated that only an average (constant) value can be estimated, making equation (5.14) to be zero.

Under this restriction, the plastic multiplier,  $\dot{\lambda}$ , becomes independent of any consideration of strain rate effects since equation (5.10) reduces to equation (5.7).

It follows that equation (5.1) in the dynamic case changes only due to the potential  $\mathcal{F}_D$  and to the strain energy density release rate,  $Y$ , at most.

The potential  $\mathcal{F}_D$ , as commented in Chapter 1, is a key issue in deriving CDM models. Here, it is considered that it has the same form as in the static case, equation (5.4), except that  $Y$  resumes a dynamic effect. This is to say that the triaxiality,  $\sigma_h/\sigma_{eq}$ , the Poisson's ratio,  $\nu$ , the elastic modulus,  $E$ , the coefficient  $\bar{S}$ , the equivalent stress and the damage ought to be dynamic parameters.

It is considered that the elastic modulus and the Poisson's ratio are material constants, not affected by the strain rate. Also, it is assumed that all the components of the stress tensor are affected in the same way by the strain rate. Hence, the ratio  $\sigma_h/\sigma_{eq}$  is not strain rate dependent.

Under these assumptions, it follows that the coupled dynamic damage evolution,  $D_d$ , equation (5.2), strain rate effects being preserved, is obtained by solving

$$\dot{D}_d = \frac{\bar{\sigma}_{eq}^2 R_\nu}{2E\bar{S}} \dot{p} \bar{H}(p - p_{D_d}), \quad (5.15)$$

or

$$\dot{D}_d = \frac{(\bar{\sigma}_{eq_s} + \bar{m}\bar{\epsilon}^{\bar{n}})^2 R_\nu}{2E\bar{S}} \dot{p} \bar{H}(p - p_{D_d}), \quad (5.16)$$

when using equation (5.12).

The parameters  $\bar{m}$ ,  $\bar{n}$  and  $E$  were determined as shown in Chapter 2. The dynamic threshold accumulated plastic strain,  $p_{D_d}$ , and the parameter  $\bar{S}$  will be commented on later.

## 5.2 Particular integration of the damage equation

For some special cases, it is possible and useful to integrate the dynamic damage kinetic equation. This specialization will be here pursued for two different material models, perfectly plastic and linear hardening material, with strain rate effects taken into account.

In the following integration, the triaxiality ratio,  $\sigma_h/\sigma_{eq}$ , is assumed constant, which makes the factor  $R_\nu$  invariant with stress. In practice, this

load regime is called proportional loading. It occurs when the following requirements are fulfilled<sup>128</sup> \*:

- the load increases proportionally to a unique parameter,
- the initial state is non deformed with no hardening,
- the material obeys the PRANDTL-REUSS law,
- hardening is expressed with a potential,
- the elastic strains are negligible.

Considering first an elastic, perfectly plastic material with a static flow stress  $\bar{\sigma}_{eq} = \sigma_0$ , the kinetic damage law, equation (5.2), may be integrated to give a *static* perfectly plastic version of the damage,

$$\int_0^D dD = \int_{p_D}^p \frac{\sigma_0^2 R_\nu}{2E\bar{S}} dp, \quad (5.17)$$

$$D = \frac{\sigma_0^2 R_\nu}{2E\bar{S}} (p - p_D) \quad \text{for} \quad p \geq p_D. \quad (5.18)$$

In the case of proportional loading, the accumulated plastic strain equals the equivalent strain, *ie*

$$p = \varepsilon_{eq} \quad \text{and} \quad p_D = \varepsilon_D, \quad (5.19)$$

rendering equation (5.18) as

$$D = \frac{\sigma_0^2 R_\nu}{2E\bar{S}} (\varepsilon_{eq} - \varepsilon_D) \quad \text{for} \quad \varepsilon_{eq} \geq \varepsilon_D. \quad (5.20)$$

It may be appreciated that equation (5.20) is quite simple. Indeed, by knowing the triaxiality value, the equivalent plastic strain plus some material parameters,  $E$ ,  $\bar{S}$ ,  $\nu$ ,  $\sigma_0$ ,  $\varepsilon_D$ , one can evaluate the damage field and predict failure, as it will be seen.

---

\*These requirements are necessary but not sufficient. The numerical simulation of notched specimens in Chapter 3 fulfils these conditions. Yet, the triaxiality is not constant (see Figure 3.16 on page 67).

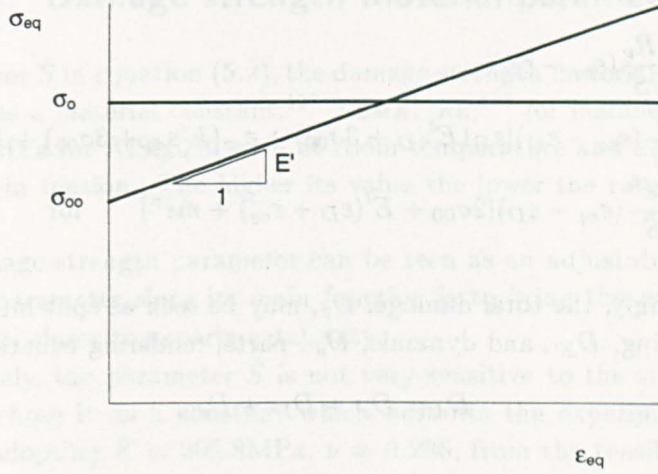


Figure 5.1: Definition of the flow stress.

The material model can be improved by considering a linear hardening law such that

$$\tilde{\sigma}_{eq} = \sigma_{00} + E' \epsilon_{eq}. \quad (5.21)$$

Here,  $E'$  is the hardening modulus and  $\sigma_{00}$  is a initial flow stress, usually different from  $\sigma_0$ , Figure 5.1.

By inserting equation (5.21) in equation (5.2), using equation (5.19), and performing the integration for proportional loading, the static damage evolves with the plastic strain according to

$$D = \frac{\sigma_{00}^2 R_\nu}{2ES} (\epsilon_{eq} - \epsilon_D) + \frac{R_\nu E'}{6ES} (\epsilon_{eq} - \epsilon_D) [\epsilon_D (E' \epsilon_D + 3\sigma_{00}) + \epsilon_{eq} (E' \epsilon_{eq} + 3\sigma_{00}) + E' \epsilon_D \epsilon_{eq}] \quad \text{for } \epsilon_{eq} \geq \epsilon_D. \quad (5.22)$$

Consider now the integration of equation (5.2) where not only linear hardening but also strain rate sensitivity is taken into account.

Now, inserting the equation

$$\tilde{\sigma}_{eqd} = \sigma_{00} + E' \epsilon_{eq} + \bar{m} \dot{\epsilon}^{\bar{n}}, \quad (5.23)$$

into equation

$$D_d = \frac{R_\nu}{2ES} \int_{\epsilon_D}^{\epsilon_{eq}} (\sigma_{00} + E' \epsilon_{eq} + \bar{m} \dot{\epsilon}^{\bar{n}})^2 d\epsilon_{eq}, \quad (5.24)$$



one has, after the integration,

$$\begin{aligned}
 D_d = & \frac{\sigma_{00}^2 R_\nu}{2E\bar{S}} (\varepsilon_{eq} - \varepsilon_D) \\
 & + \frac{R_\nu E'}{6E\bar{S}} (\varepsilon_{eq} - \varepsilon_D) [\varepsilon_D (E' \varepsilon_D + 3\sigma_{00}) + \varepsilon_{eq} (E' \varepsilon_{eq} + 3\sigma_{00}) + E' \varepsilon_D \varepsilon_{eq}] \\
 & + \frac{R_\nu \bar{m} \dot{\varepsilon}^{\bar{n}}}{2E\bar{S}} (\varepsilon_{eq} - \varepsilon_D) [2\sigma_{00} + E' (\varepsilon_D + \varepsilon_{eq}) + \bar{m} \dot{\varepsilon}^{\bar{n}}] \quad \text{for } \varepsilon_{eq} \geq \varepsilon_D.
 \end{aligned} \tag{5.25}$$

Accordingly, the total damage,  $D_d$ , may be seen as split into the static,  $D_{s'}$ , hardening,  $D_{E'}$ , and dynamic,  $D_{d'}$ , parts, rendering equation (5.25) as

$$D_d = D_{s'} + D_{E'} + D_{d'}, \tag{5.26}$$

where

$$D_{s'} = \frac{\sigma_{00}^2 R_\nu}{2E\bar{S}} (\varepsilon_{eq} - \varepsilon_D), \tag{5.27}$$

$$D_{E'} = \frac{R_\nu E'}{6E\bar{S}} (\varepsilon_{eq} - \varepsilon_D) [\varepsilon_D (E' \varepsilon_D + 3\sigma_{00}) + \varepsilon_{eq} (E' \varepsilon_{eq} + 3\sigma_{00}) + E' \varepsilon_D \varepsilon_{eq}], \tag{5.28}$$

and

$$D_{d'} = \frac{R_\nu \bar{m} \dot{\varepsilon}^{\bar{n}}}{2E\bar{S}} (\varepsilon_{eq} - \varepsilon_D) [2\sigma_{00} + E' (\varepsilon_D + \varepsilon_{eq}) + \bar{m} \dot{\varepsilon}^{\bar{n}}]. \tag{5.29}$$

If the strain rate,  $\dot{\varepsilon}$ , and the hardening coefficient,  $E'$ , are set to zero, the flow stress,  $\sigma_{00}$ , becomes  $\sigma_0$  and the static damage equation reported in the literature,<sup>126</sup> equation (5.20), is recovered, as expected.

A useful particular case of equation (5.26) occurs when the term  $D_{E'}$  is set to zero. One has then the damage evolution for a perfectly plastic material where strain rate effects are preserved,

$$D_{d_0} = \frac{(\sigma_0 + \bar{m} \dot{\varepsilon}^{\bar{n}})^2 R_\nu}{2E\bar{S}} (\varepsilon_{eq} - \varepsilon_D). \tag{5.30}$$

Observe that, for the threshold dynamic plastic strain,  $\varepsilon_{D_d}$ , its static counterpart,  $\varepsilon_D$ , was used. This is suggested by the experimental data shown in Figures 2.15 and 3.7, on pages 35 and 57, respectively. These data support a constant threshold plastic strain, independent of the strain rate, as already commented on Chapter 4.

### 5.3 Damage strength material parameter

The parameter  $\bar{S}$  in equation (5.2), the damage strength material parameter, is regarded as a material constant.<sup>127</sup> LEMAITRE,<sup>126</sup> for instance, quotes a value of 2.4MPa for AISI1010 steel at room temperature and  $2.5 \cdot 10^{-7}$ MPa for concrete in tension. The higher its value the lower the rate of damage growth.

The damage strength parameter can be seen as an adjustable, material dependent, parameter since its main function is to bring the prediction of equation (5.2) closer to experimental data.

Fortunately, the parameter  $\bar{S}$  is not very sensitive to the strains. It is possible to chose it as a constant which best fits the experimental data. Indeed, by adopting  $E = 209.8$ MPa,  $\nu = 0.286$ , from the tensile test data on page 31,  $\varepsilon_D = 0.17$  from page 98, a triaxiality of  $\sigma_h/\sigma_{eq} = 0.5$ , which was calculated in reference 2 for the specimen in Figure 4.5, page 82, and stress-strain data from the tensile tests on damage specimens, Chapter 4, equation (5.20) behaves as indicated in Figure 5.2 when  $\bar{S}=2.2$ MPa.

Clearly, a constant value for the damage strength material parameter, yields a reasonable fit to the experimental data. The benefits in having  $\bar{S}$  as a material constant justify any slight deviation in the comparison with the experimental data.

### 5.4 Influence of triaxiality on failure strain

It is accepted that the hydrostatic stress is a major variable in dictating ductile failure, as already commented in Chapter 3. The higher the triaxiality the lower the failure strain. It is important to incorporate this trend in a failure criterion. Equally important for a failure criterion is to predict the failure site. This section explores how CDM can be applied to assess the interplay between triaxiality and failure strain. Also, it is shown how strain rate effects are taken into account via the formulation developed in section 5.2.

From equation (5.30), it is straightforward to express the equivalent failure strain as a function of the critical damage, the triaxiality, the strain rate and a few material parameters:

$$\varepsilon_{fa} = \frac{2E\bar{S}D_{cr}}{R_\nu(\sigma_0 + \bar{m}\dot{\varepsilon}^{\bar{n}})^2} + \varepsilon_D. \quad (5.31)$$

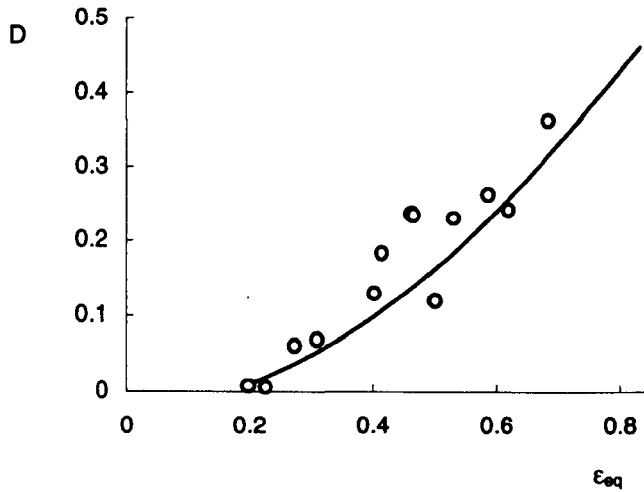


**Figure 5.2:** Static damage *versus* equivalent strain evolution as predicted by equation (5.20) with  $\bar{S} = 2.2\text{MPa}$ ,  $\sigma_h/\sigma_{eq}=0.5$  and stress-strain experimental data. The open symbols represent experimental data from Chapter 4.

This equation is plotted in Figure 5.3. The parameters used are for mild steel, tested as presented in the previous chapters. In particular, the flow stress  $\sigma_0$  is a critical variable and does alter the so-called *master curves of ductile fracture*. Its value was set to 600MPa. By choosing different flow stresses, one can obtain lower and upper boundaries for these master curves.

It is possible to use a linear hardening constitutive law to obtain the failure strain. The resulting equation, though, equation (5.25), is cubic for the failure strain, making it difficult to use.

It is now opportune to discuss the above iso-failure curves in the light of the experimental results obtained in Chapter 3.

Figure 5.3 shows clearly that an increase of the hydrostatic stress makes, in a way, the material more brittle, for the failure strain decreases. Nevertheless, it was shown in Chapter 3 that the actual failure site in small radius notch specimens occurred at the base of the notch. In this region, the triaxiality is quite low, compared to the high values achieved at the middle.

Therefore, the triaxiality does not exclusively control the failure, as a first glance in Figure 5.3 would suggest. Here, the equivalent plastic strain must be fully considered in order to determine the failure site and under

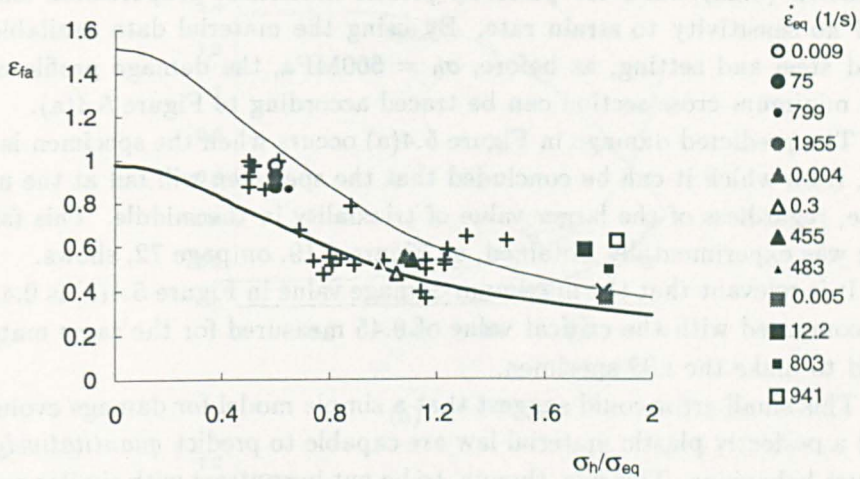


**Figure 5.3:** Influence of the triaxiality and strain rate on failure strain. Thin and thick lines represent equation (5.31) for strain rates of 0 and  $100\text{s}^{-1}$ , respectively. The parameters are representative of a mild steel. The various symbols are *experimental* data, labeled with the average strain rate in the test. Circles, triangles and squares are for the n4, n2 and n05 specimens, respectively. The plus signs are *experimental* data based on the final geometry of the test specimens with different average strain rates.

which conditions failure takes place. This raises an important issue. Can CDM predict not only that an increase of triaxiality decreases the failure strain but, also and at the same time, that failure can take place in regions of low level of triaxiality?

To judge whether CDM is capable of predicting correctly the failure site in structures, the notch specimens are quite useful. One can evaluate the damage along their minimum cross-sections and infer whether the maximum damage coincides with the failure site. Observe that, for the n05 and n2 notched specimens, the triaxiality is higher at the middle whereas the equivalent plastic strain is higher at the notch base.

Figure 5.4(a) depicts the triaxiality ratio and the equivalent strain along the minimum diameter for the n05 cylindrical notch specimen loaded statically, according to the Finite-Element simulations in Chapter 3. These data were calculated for a diameter contraction matching the one occurring at the actual instant of failure of the n05 specimen. They can be substituted into

equation (5.20), valid for perfectly plastic materials, proportional loading and no sensitivity to strain rate. By using the material data available for mild steel and setting, as before,  $\sigma_0 = 600\text{MPa}$ , the damage profile along the minimum cross section can be traced according to Figure 5.4(a).

The predicted damage in Figure 5.4(a) occurs when the specimen is failing, from which it can be concluded that the specimen will fail at the notch base, regardless of the larger value of triaxiality in the middle. This failure site was experimentally obtained, as Figure 3.19, on page 72, shows.

It is relevant that the maximum damage value in Figure 5.4(a) is 0.41, to be compared with the critical value of 0.45 measured for the same material used to make the n05 specimen.

This small error could suggest that a simple model for damage evolution and a perfectly plastic material law are capable to predict *quantitatively* the failure behaviour. This has, though, to be put in contrast with similar results but now for the statically tested n2 and n4 specimens, Figure 5.4(b) and (c).

The experimental failure site for specimen n2 is at the notch root, as theoretically predicted in Figure 5.4(b), but the damage is too low. Also, as commented in Chapter 3, the failure site for the n4 specimens is at the centre, again as predicted in Figure 5.4(c). But now the damage value seems to be too high; the specimen would be expected to fail at an earlier stage.

## 5.5 Dynamic limit forming diagrams

It is illustrative to apply the so far developed formulation to a more practical case.

Consider the deep drawing of a thin sheet under a plane stress state \* with the assumptions of negligible elastic strains, proportional loading and no strain rate effect on the triaxiality. Equation (5.31) can be used to predict the strain to failure of this problem.

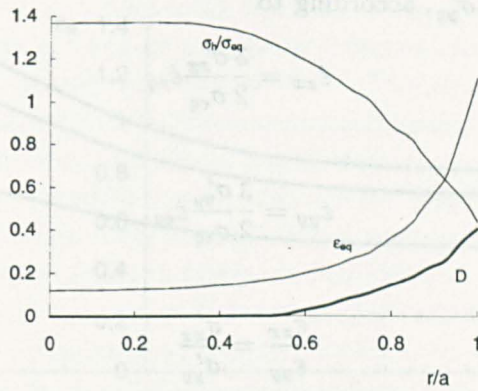
In the plane stress case, the stress tensor reads

$$[\sigma_{ij}] = \begin{bmatrix} \sigma_{xx} & 0 & 0 \\ 0 & \sigma_{yy} & 0 \\ 0 & 0 & 0 \end{bmatrix}. \quad (5.32)$$

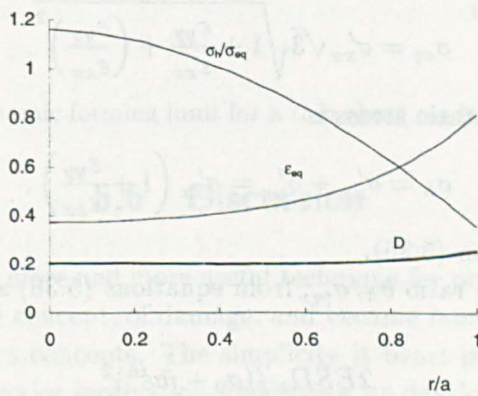
By noting that the principal strains,  $\epsilon_{xx}$  and  $\epsilon_{yy}$ , are related to the stress

---

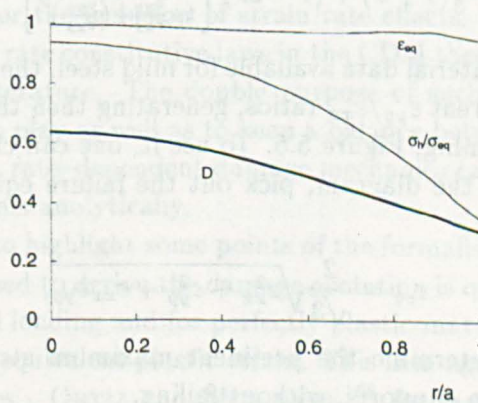
\*This example is presented in references 126 and 211 in a different form and for the static case.



(a)



(b)



(c)

**Figure 5.4:** Stress triaxiality, equivalent plastic strain and damage along the minimum cross-section of mild steel cylindrical specimens with a notch radius of (a) 0.44mm, (b) 1.58mm and (c) 4.13mm.

deviators,  $\sigma'_{xx}$  and  $\sigma'_{yy}$ , according to

$$\dot{\epsilon}_{xx} = \frac{3}{2} \frac{\sigma'_{xx}}{\sigma_{eq}} \dot{\epsilon}_{eq} \quad (5.33)$$

and

$$\dot{\epsilon}_{yy} = \frac{3}{2} \frac{\sigma'_{yy}}{\sigma_{eq}} \dot{\epsilon}_{eq}, \quad (5.34)$$

it follows that

$$\frac{\epsilon_{xx}}{\epsilon_{yy}} = \frac{\sigma'_{xx}}{\sigma'_{yy}}. \quad (5.35)$$

The equivalent stress reads then

$$\sigma_{eq} = \sigma'_{xx} \sqrt{3} \sqrt{1 + \frac{\epsilon_{yy}}{\epsilon_{xx}} + \left(\frac{\epsilon_{yy}}{\epsilon_{xx}}\right)^2}, \quad (5.36)$$

whereas the hydrostatic stress is

$$\sigma_h = \sigma'_{xx} + \sigma'_{yy} = \sigma'_{xx} \left(1 + \frac{\epsilon_{yy}}{\epsilon_{xx}}\right), \quad (5.37)$$

when using equation (5.35).

Introducing the ratio  $\sigma_h/\sigma_{eq}$ , from equations (5.36) and (5.37), in equation (5.31) yields

$$\epsilon_{fa} = \frac{2E\bar{S}D_{cr}/(\sigma_0 + \bar{m}\bar{\epsilon}^{\bar{n}})^2}{\frac{2}{3}(1+\nu) + (1-2\nu) \left[ \frac{(1 + \frac{\epsilon_{yy}}{\epsilon_{xx}})^2}{1 + \frac{\epsilon_{yy}}{\epsilon_{xx}} + (\frac{\epsilon_{yy}}{\epsilon_{xx}})^2} \right]^2} + \epsilon_D. \quad (5.38)$$

By using the material data available for mild steel, the above equation can be plotted for different  $\epsilon_{yy}/\epsilon_{xx}$  ratios, generating then the dynamic fracture limits in metal forming, Figure 5.5. To use it, one can choose a strain ratio  $\epsilon_{yy}/\epsilon_{xx}$  and, from the diagram, pick out the failure equivalent strain. By noting that

$$\epsilon_{eq} = \frac{2}{\sqrt{3}} \sqrt{\epsilon_{xx}^2 + \epsilon_{yy}^2 + \epsilon_{xx}\epsilon_{yy}}, \quad (5.39)$$

it is possible to determine the pertinent maximum strain state the sheet under consideration supports, without failing.

Clearly, the strain rate plays an important role. The damage model predicts that an increase of the strain rate decreases the failure strain substantially.

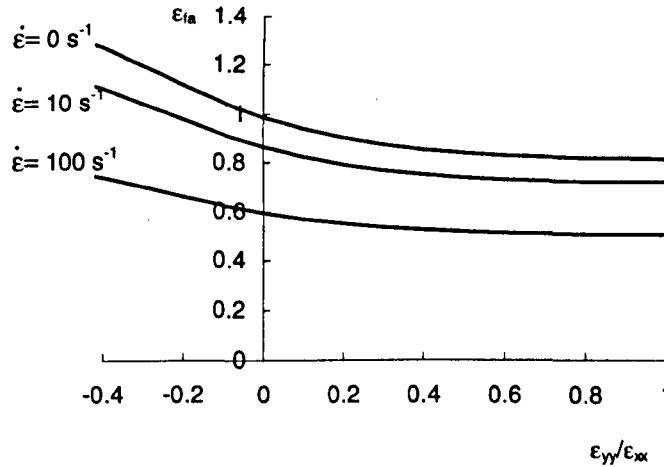


Figure 5.5: Dynamic forming limit for a thin sheet made of a mild steel.

## 5.6 Discussion

CDM is becoming a more and more useful technique for predicting failure. It grew out of a simple concept, of damage, and became more formal by applying thermomechanics concepts. The simplicity it bears is rather appealing, being perhaps the major motivation underlying its development.

The previous sections followed more or less established routes in the CDM formalism, except for the inclusion of strain rate effects. The use of simple stress–strain–strain rate constitutive laws in the CDM theoretical framework is missing in the literature. The double purpose of such effort is to bring dynamic effects into play as well as to keep a balance between accuracy and simplicity. Hence, a rate–dependent damage mechanics can be used to solve some simple problems analytically.

It is important to highlight some points of the formalism here developed.

The potential used to derive the damage evolution is quite simple. In the case of proportional loading and for perfectly plastic materials, the model is proportional to the equivalent plastic strain. This is in agreement with some theoretical evidences. ORTIZ and MOLINARI,<sup>168</sup> for instance, in studying the dynamic expansion of a spherical void in an unbounded solid, concluded that the expansion of the void is linear with time or, for proportional loading, linear with strain. A linear growth of damage with the plastic strain is also



a good approximation for the data in Chapter 4.

It is not difficult, though, to add a non-linear term to the equations. Indeed, various authors,<sup>191,207-209</sup> by choosing potentials slightly different from the one in equation (5.4), have modeled damage in other materials.

The potential in equation (5.4), introduced by LEMAITRE, and part of the formalism developed by him, have been criticised.

First because the model is isotropic.<sup>103</sup> This implies that the damage is the same regardless the orientation, which conflicts with some experimental data, as in CORDEBOIS and SIDOROFF.<sup>49</sup>

It is not clear how important the effect of anisotropy is in terms of anticipating or retarding the failure in an actual structure. Also, although it can be expected that the damage parameter exhibits anisotropic effects, experimental results have to be interpreted with care. It is difficult to measure the damage anisotropy in a material. If the damage is investigated using the elastic modulus change, as in CORDEBOIS and SIDOROFF<sup>49</sup> and in CHOW and WANG,<sup>39,40</sup> it is fundamental to consider the non-uniformity of the stress and strain fields, as shown in reference 2. Moreover, the damage has to be monitored locally, a procedure not followed in references 39,40,194 and not stated in reference 49. These comments assume special relevance when considering that damage in different directions do not differ from each other by a great amount.

LEMAITRE's model considers that ductile damage is due to the release of the *elastic* strain energy only. JU<sup>102</sup> criticises the fact that plastic strains do not contribute to the microcrack growth process, whereas TAHER<sup>190</sup> suggest an alternative model, in the spirit of LEMAITRE's, capable to couple damage, stress, and elastic and plastic strains.

In working with the potential given by equation (5.4), the resulting dynamic damage evolution equation was integrated for perfectly plastic and bilinear materials. Formally, it is possible to adopt other stress-strain laws but the integration may be difficult and the resulting expression not suitable for the purposes of this work. This was anticipated by equation 5.22, where the simplest hardening model, *ie* linear, yielded an equation of difficult use.

The triaxiality influence on failure strain is well captured by CDM, as illustrated in Figure 5.3. Nonetheless, it should be kept in mind that the comparison with the experimental data in the figure is misleading since the data are in fact a manipulation, according to BRIDGMAN's theory, of some measurable parameters. The correct way to interpret Figure 5.3 is that CDM grasps the well known decrease of failure strain with the increase of

triaxiality. But the failure site may not be at the maximum triaxiality region. Indeed, it was shown in Chapter 3 that, for acute specimens, failure starts at the base of the notch root.

This experimental evidence is qualitatively predicted by CDM, according to Figures 5.4(a), (b) and (c). Observe that in these figures, the stress-strain information comes from a full elastic-plastic analysis and are introduced in a perfectly plastic damage evolution equation.

The value of the damage in the n05 specimen,  $D = 0.41$  in Figure 5.4(a), is similar to the critical damage of 0.45, as it should be for a failed specimen.

However, for the n2 specimen, Figure 5.4(b), the damage is quite low and even so the specimen has failed. Because the triaxiality at the failure site for the n05 and n2 specimens are more or less the same, the equivalent plastic strain for the n2 specimen would have to increase substantially in order to yield a critical damage of 0.45.

For the n4 specimen, Figure 5.4(c) shows that the damage is larger than the critical value, suggesting that the specimen should have failed at an earlier stage.

The reasonable results for the n05 specimen are difficult to sustain in face of the poor results for the n2 and n4 specimens. One explanation for such discrepancy could be an influence of the axisymmetric stress field on the critical damage, a supposition not supported by some experimental data, Figure 4.20 on page 97.

Turning now to Figure 3.10, on page 60, a good agreement of the numerical simulation with the experiments in notched specimens is shown, but up to a certain point. The expected softening regime near fracture is not grasped by the solution, clearly because the numerical model does not consider damage. At this point, the damage should play a decisive influence in dictating the strain and stress field, fields used to obtain the results in Figure 5.4. How important is this influence it is not known, unless a fully elastic-plastic-damage model is implemented in a Finite-Element code.

Noteworthy in Figure 5.4 is that the triaxiality does not seem, in principle, to dictate the failure site, as it is usually accepted.<sup>86,144,146,175</sup> CDM is capable of predicting that, in this case, failure takes place at regions of low triaxiality and high plastic strains.

According to these results, it is possible to conclude that CDM can effectively predict the failure site in notched specimens. It also suggests, with theoretical arguments, that the importance attributed to the triaxiality influence on failure is overestimated.

As far as strain rate effects are concerned, most of the discussion has to be postponed to Chapter 7, where failure will be predicted using the model here developed. However, it is interesting to observe that the use of perfectly plastic and linear hardening materials, together with the implicit assumption that the strain rate does not affect the hardening modulus, implies that the strain rate affects the flow stress only. This influence of strain rate on flow stress can be catered for by both the COWPER-SYMONDS law, equation (2.14), and by equation (5.12). In both cases, the coefficients  $C$ ,  $q$ ,  $\bar{m}$  and  $\bar{n}$  in these equations are constants. This means that equation (5.12) has no particular advantage over the COWPER-SYMONDS constitutive law.

The present rate-dependent model will be used to predict failure in impacted beams. Observe that the model requires the knowledge of plastic strains. This is not possible in the framework of rigid-plastic analysis, unless it is considered that the strains are distributed within a certain region of a structure.

The determination of strains in a perfectly plastic material is the subject of the next chapter.

---

## 6 Strains in a Perfectly Plastic Material

THE RIGID-PLASTIC methods of analysis are quite important as a design tool for engineering structures. By assuming that the stress-strain material behaviour is well represented by a single parameter, the flow stress, the governing equations of a problem are solved, sometimes in closed form. This helps a great deal in providing a physical understanding of the phenomena underlying the analysis.

However, the plastic methods of structural analysis have a major disadvantage, namely, the impossibility of calculating the strains. This is due to the lack of uniqueness between stress and strain since, in a perfectly plastic material, the same flow stress is associated with an infinite number of different strains. On the other hand, it has been shown in Chapter 5 that the strains are a fundamental parameter for the evaluation of the damage. Hence, knowing them is imperative.

One way to approximately evaluate the strains is by defining a *hinge length*, ie a region in a structure where the otherwise infinite curvature is somehow distributed along it. Examples of such definitions may be found in the literature.

NONAKA<sup>165, 166</sup> proposed a deflection dependent hinge length for beams. He assumed that, for a clamped beam, the plastic region is formed by two isosceles right triangles, one in compression and the other in tension. As the beam displaces, one triangle expands and, concomitantly, the other contracts. LIU and JONES<sup>137</sup> have assumed, again for beams, a variable hinge length proportional to the beam thickness and to the distance from the neutral axis to the central axis of the beam cross-section. SHEN AND JONES<sup>180</sup> chose another approach. By analysing experimental data from MENKES and OPAT,<sup>147</sup> they proposed a hinge length related to the beam thickness and

to the plastic work dissipated in a hinge. Their empirical relation has not been directly compared to other beam materials and configurations, so it is not known whether it leads to reasonable values of strains. Also, WEN *et al.*<sup>213</sup> have used a constant hinge length, equal to the thickness of a beam, for evaluating the strains due to bending.

It is the aim of this chapter to explore the concept of hinge length and the strains plus strain rates derived from it. To this end, bending, shear and membrane hinge length will be defined. The various hinge length definitions are then tested against experimental and numerical data available in the literature. This comparison is extended to simple expressions for the equivalent strain developed in the chapter. Also, strain rate expressions are derived from the equivalent strain by assuming an appropriate impact time, based on experimental data.

## 6.1 Bending hinge length

Consider a beam loaded by a concentrated load at any position on its span, Figure 6.1, which produces infinitesimal displacements. At the core of it and at the point of maximum displacement, the material is fully plastic. This is also the region where the moment achieves its peak value. As one moves away from this point, the plastic zone dies out, initially at the inner core and later at the outer surface. This decrease of the plastic zone is directly related to the decrease of the moment. Accordingly, for small displacements of the beam, the region where the plastic strain takes place is bounded by the yield moment,  $M_y$ . Hence, a definition of *bending hinge length* may be stated as

Bending hinge length,  $l_M$ , is the distance along a structure between two points  $A$  and  $B$  where  $M_A = M_0$  and  $M_B = M_y$ .  $M_y$  is the initial yield moment in a structure.  $M_0$  is the fully plastic collapse moment.

This definition, if leading to reasonable results, is interesting since rigid-plastic methods of analysis are, usually, capable of readily describing the moment behaviour along a structure. Hence, once the moment function is known, it is possible to calculate the hinge length. Moreover, the bending moment distribution in static cases is described by relatively simple equations, which allows closed form expressions for the hinge length.

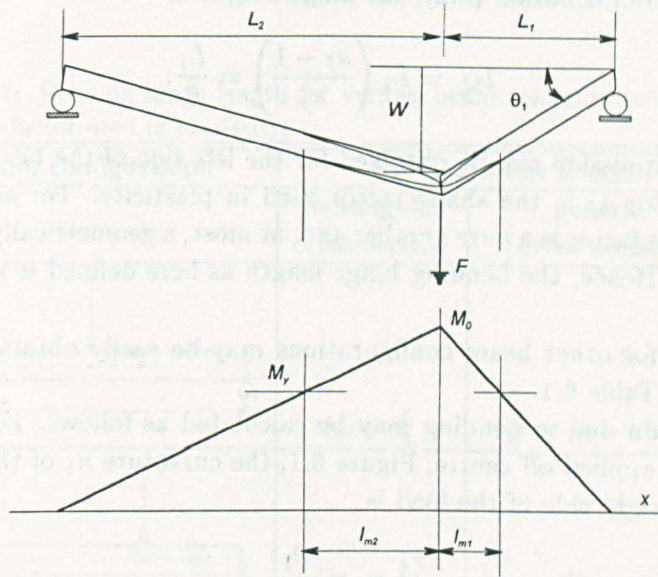


**Figure 6.1:** a) A beam loaded off centre showing the bending hinge length definition. b) Associated bending moment distribution. The beam displacement is exaggerated.

As an example of application of the hinge length concept, consider a portion on the right hand side of the load point in the simply supported rectangular beam of Figure 6.1. From the relation \*

$$\frac{M_0}{L_1} = \frac{M_0 - M_y}{l_{M_1}}, \quad (6.1)$$

the bending hinge length is written as

$$l_{M_1} = L_1 \left( 1 - \frac{M_y}{M_0} \right). \quad (6.2)$$

For a rectangular beam with thickness  $H$ , the collapse moment  $M_0$  and the yield moment  $M_y$  are related as

$$s_f = \frac{M_0}{M_y} = \frac{3}{2}, \quad (6.3)$$

\*Throughout all the Chapter, it is assumed that  $L_1 \leq L_2$ .

rendering, from equation (6.2), the hinge length as

$$l_{M_1} = L_1 \left( \frac{s_f - 1}{s_f} \right) = \frac{L_1}{3}. \quad (6.4)$$

A similar expression can be obtained for the left side of the beam.

The factor  $s_f$  is the shape factor used in plasticity. For simple cross-sections, this factor is a pure number and, at most, a geometrically dependent parameter. Hence, the bending hinge length as here defined is not material dependent.

Results for other beam configurations may be easily obtained, as summarised on Table 6.1.

The strain due to bending may be calculated as follows. For a concentrated load applied off centre, Figure 6.1, the curvature  $\kappa_1$  of the *centroidal axis* at the right side of the load is

$$\kappa_1 = \frac{\theta_1}{l_{M_1}}. \quad (6.5)$$

The curvature is related to the axial strain through

$$\varepsilon_1 = \kappa_1 z, \quad (6.6)$$

where  $z$  defines the through-thickness co-ordinate. For moderate displacements, the angle  $\theta_1$  may be approximated by

$$\theta_1 = \frac{W}{L_1}, \quad (6.7)$$

inducing a strain due to bending at the outmost external fibre,  $z = H/2$ , of

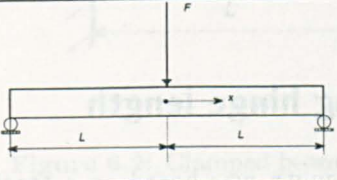
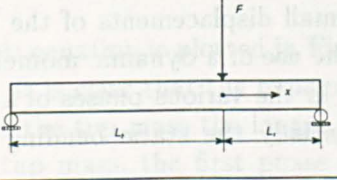
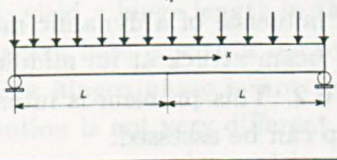
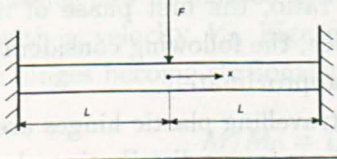
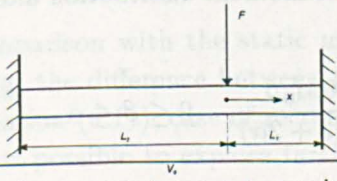
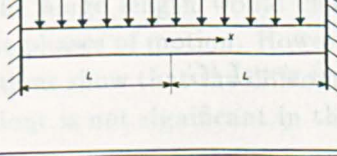
$$\varepsilon_{M_1} = \frac{3H}{2L_1^2} W. \quad (6.8)$$

This curvature and strain attain their maximum values around the point loaded region, as experimental and numerical evidence, to be presented later, confirms. It is assumed that the curvature decreases linearly from its maximum value, at  $x = 0$ , to nil, at  $x = l_M$ . This linear behaviour of the curvature implies a cubic function for a beam profile in the hinge region\*.

---

\*A cubic profile in this region does not lead to an exact solution in the sense of the upper and lower bound theorems of plasticity. Accordingly, it cannot be used to calculate the exact collapse load of the beam in Figure 6.1.

**Table 6.1:** Bending hinge length for various beam configurations.  $s_f$  is the shape factor used in plasticity.

beam configuration	bending hinge length	
	rectangular cross-section	general cross-section
	$l_M = \frac{L}{3}$	$l_M = (1 - s_f^{-1})L$
	$l_{M_1} = \frac{L_1}{3}$ $l_{M_2} = \frac{L_2}{3}$	$l_{M_1} = (1 - s_f^{-1})L_1$ $l_{M_2} = (1 - s_f^{-1})L_2$
	$l_M = \frac{L}{\sqrt{3}}$	$l_M = \frac{L}{\sqrt{1 - s_f^{-1}}}$
	$l_M = \frac{L}{6}$	$l_M = \frac{s_f^{-1}}{2s_f} L$
	$l_{M_1} = \frac{L_1}{6}$ $l_{M_2} = \frac{L_2}{6}$	$l_{M_1} = \frac{s_f^{-1}}{2s_f} L_1$ $l_{M_2} = \frac{s_f^{-1}}{2s_f} L_2$
	$l_M = \frac{L}{\sqrt{6}}$	$l_M = \frac{L}{\sqrt{2(1 - s_f^{-1})}}$



A similar procedure can be developed for the left-hand side of the beam.

It is evident that, for off-centre loads, there is a discontinuity of curvature and strain due to bending. The closer the load is applied to the support, the stronger the discontinuity of the curvature at the loading point. In fact, a very sharp change of the curvature occurs in this region and data to be presented later will confirm the assertion.

Likewise, the curvature and bending strain can be calculated for different loads and boundary conditions.

## 6.2 Dynamic bending hinge length

The previous definition of bending hinge length was based on a static moment distribution, strictly valid only for small displacements of the beam. It would be interesting to assess whether the use of a dynamic moment distribution, *ie* the moment profile occurring in the various phases of a beam loaded dynamically, would change substantially the static bending hinge length definition.

A simple analysis may reveal the basic influence of a dynamic moment distribution. Consider, at first, a clamped beam struck at its middle by a mass  $G$  travelling at a velocity  $V_0$ , Figure 6.2. This problem is interesting because the influence of the mass of the tup can be assessed.

For very small tup to the beam mass ratio, the first phase of motion dominates the response of the beam.<sup>97</sup> Hence, the following consideration is valid for those ratios larger than one-half, approximately.

After the first phase of motion, \* when travelling plastic hinges are moving from the centre towards the supports, the moment distribution along the beam reads<sup>97</sup>

$$M = M_0 - \frac{2M_0(3\bar{\alpha} - \beta)\beta^2}{\bar{\alpha}^2(3 + 2\bar{\alpha})} - \frac{6M_0\beta}{\bar{\alpha}(3 + 2\bar{\alpha})}, \quad 0 \leq \beta \leq \bar{\alpha}, \quad (6.9)$$

where

$$\beta = mx/G \quad \text{and} \quad \bar{\alpha} = mL/G, \quad (6.10)$$

and  $m$  is the mass per unit beam length.

---

\*Only the second phase of motion will be studied because failure will occur at this phase when shear effects are not considered.

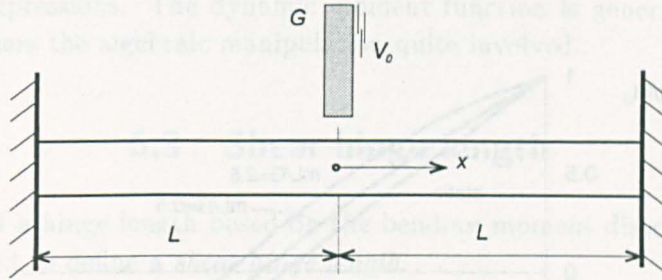


Figure 6.2: Clamped beam struck at its middle by a falling mass.

This equation is plotted in Figure 6.3 for two different beam to tup mass ratios. It is clear that the moment function changes with the tup mass; the smaller the tup mass the longer the hinge length. As remarked, for a very small tup mass, the first phase of motion is more relevant and might be used to yield a hinge length in the spirit of the present definition. However, the concern here is with a relatively large tup mass, which means that the travelling hinges phase is not very important and that the static moment distribution is not very different from the dynamic one.<sup>99</sup>

Consider now a clamped beam impulsively loaded throughout its entire span with a velocity  $V_0$ , Figure 6.4. The moment distribution after the plastic hinges become stationary is given by

$$M/M_0 = 1 + (x/L)^3 - 3(x/L)^2. \quad (6.11)$$

In comparison with the static moment distribution for a uniform pressure loading, the difference between the values of  $x/L$  for which  $M_y/M_0 = 2/3$  in equation (6.11), case of rectangular cross-section, is only 5.3%.

It is possible to explore further, for different beam supports and loads, how the hinge length would change as the moment profile alters with the various phases of motion. However, further calculations for other beam configurations show that the difference between the static and dynamic moment behaviour is not significant in the phase of motion when the hinges are stationary.

A dynamic moment distribution is potentially more accurate to evaluate the bending hinge length according to the present definition. This possible

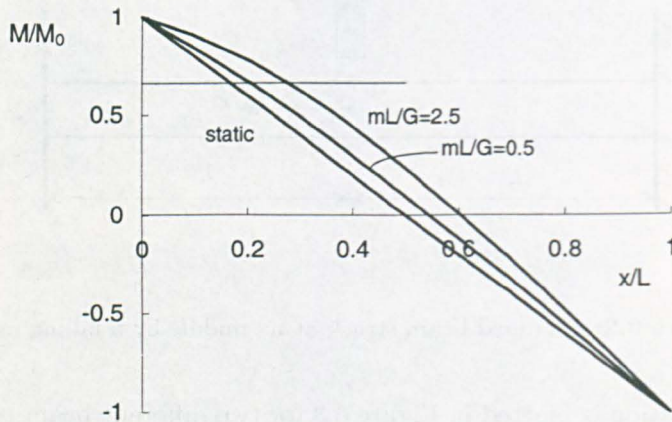


**Figure 6.3:** Static and dynamic moment distribution, in the second phase of the motion, along the clamped beam shown in Figure 6.2 and struck by different masses.  $m$  is the beam mass per unit length,  $L$  is half of the beam length and  $G$  the tup mass. The horizontal thin line defines  $M_y/M_0 = 2/3$ .

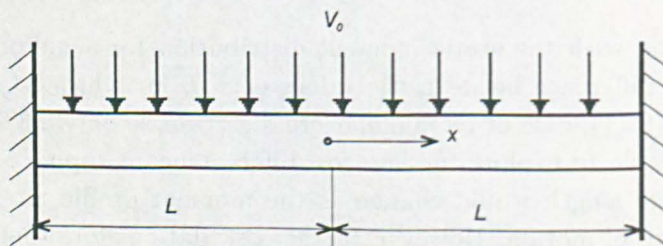


**Figure 6.4:** A clamped beam loaded impulsively with a velocity  $V_0$ .

increase in accuracy, though, is overshadowed by the simplicity of the static moment expressions. The dynamic moment function is generally a cubic, which renders the algebraic manipulation quite involved.

### 6.3 Shear hinge length

The idea of a hinge length based on the bending moment distribution may be expanded to define a *shear hinge length*.

Shear hinge length,  $l_Q$ , is the distance along the length of a structure between two points  $A$  and  $B$  where  $Q_A = Q_0$  and  $Q_B = Q_y$ .  $Q_y$  is the initial yield shear force and  $Q_0$  is the plastic collapse force, *ie* the forces which cause initial yielding of the cross-section and produce a fully plastic cross-section of a structure, respectively\*.

The evaluation of the shear hinge length is more involved than the bending one. Restricting the discussion to beams, it is known that shear effects are potentially more significant for dynamic loads. This suggests that it is necessary to infer  $l_Q$  from a full analysis of a dynamically loaded beam.

Consider first the simply supported beam depicted in Figure 6.5 and subjected to a uniformly distributed impulsive velocity of magnitude  $V_0$ . During the first phase of motion, it is possible to show<sup>97</sup> that the shear force is distributed along the beam span according to

$$Q = -Q_0 \left( \frac{x - \xi_0}{L - \xi_0} \right), \quad (6.12)$$

when  $L \geq 3H/2$ . Here,  $Q_0 \approx \sigma_0 BH/2$  is the transverse shear force necessary to fully deform, plastically and independently, the rectangular beam of length  $2L$  and cross-section dimensions  $B$  and  $H$  made from a material with flow stress  $\sigma_0$ .  $\xi_0 = L - 3H/2$  defines the position of the stationary bending hinge.

If now the previous definition of shear length is applied, *ie*

$$\frac{Q}{Q_0} = \frac{Q_y}{Q_0} = \frac{2}{3}, \quad (6.13)$$

---

\*To satisfy the equilibrium at the outer surfaces of a structure, the shear stress must be zero. However, for a perfectly plastic material, it is accepted that flow can occur at any point of the transverse section. Though not exactly true, this approximation is useful to infer the stress and strain state at the plastic region.

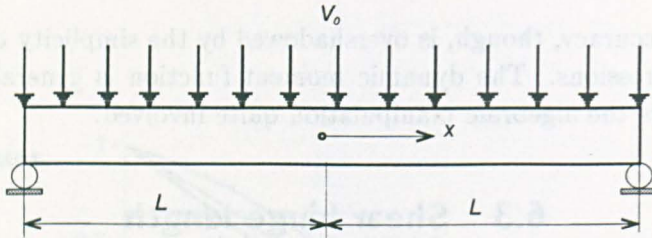


Figure 6.5: A simply supported beam loaded impulsively with a velocity  $V_0$ .

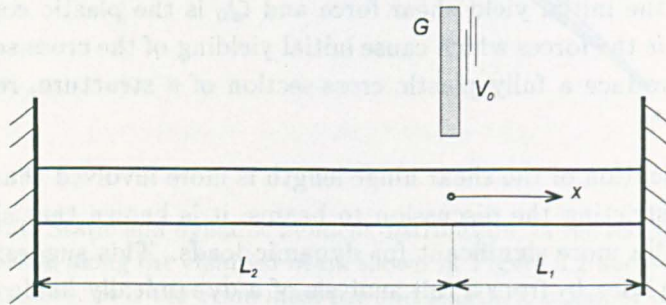


Figure 6.6: Clamped beam struck transversely by a mass  $G$ .

one has

$$l_Q = \frac{3 - \sqrt{6}}{2} H = 0.275H. \tag{6.14}$$

A similar procedure applied to the previous beam but now clamped at both sides yields

$$l_Q = (3 - \sqrt{6})H = 0.551H. \tag{6.15}$$

In the case of a mass  $G$  impacting at any position on a rectangular clamped beam with a velocity  $V_0$ , Figure 6.6, the analysis was established by LIU and JONES.<sup>136</sup> Accordingly, three cases may be drawn: CASE I,  $3 < \nu_1 \leq \nu_2$ ; CASE II,  $1 < \nu_1 \leq 3$  and  $3 < \nu_2$ ; CASE III,  $0 < \nu_1 \leq 1$  and  $3 < \nu_2$ , where  $\nu_1 = L_1/H$  and  $\nu_2 = L_2/H$ .

For CASE I, the shear force is symmetrical about the struck point and the followings relations, extracted from reference 136, hold

$$G\ddot{W}_0 = -2Q_0, \quad (6.16)$$

$$Q = m\ddot{W}_1[x - x^2/(2\xi_0)] - Q_0, \quad (6.17)$$

$$z_1\ddot{W}_1 = 8u\nu_1/g = -\ddot{W}_0/g, \quad (6.18)$$

$$Q = 2Q_0[x/\xi_0 - x^2/(2\xi_0^2)] - Q_0, \quad (6.19)$$

where  $W_0$  and  $W_1$  are the transverse displacement at the impact point and at the right-hand side of the beam adjacent to the impact point, respectively,  $\bar{W}_0 = W_0/L_1$ ,  $\bar{W}_1 = W_1/L_1$ ,  $g = mL_1/G$ ,  $z_1 = \xi_0/L_1$  and  $u = GV_0^2/(2M_0)$ .

By adopting  $Q = 2Q_0/3$  and  $\xi_0 = 3H$ <sup>136</sup> in equation (6.19) and solving it for  $x$ , one has

$$l_Q = (3 - \sqrt{6})H = 0.551H, \quad (6.20)$$

which is identical to the case of a fully clamped beam loaded impulsively throughout its span.

For CASE II and provided  $1.5 \leq \nu_1 < 3$ , there are two different hinge lengths, for the shear force distribution at the left of the tup is different from that at the right. In the first phase of motion, the shear force is distributed in such a way that the shear hinge lengths are

$$l_{Q_1} = \frac{1}{3} \frac{L_1}{H - L_1} \left[ 3(H - L_1) + \sqrt{7L_1^2 - 16HL_1 + 9H^2} \right] \quad (6.21)$$

and

$$l_{Q_2} = -(3 - \sqrt{6})H, \quad (6.22)$$

at the right and left of the tup, respectively.

For CASE III, the load is applied at a distance from the support less than the beam thickness and the shear hinge lengths read

$$l_{Q_1} = L_1 \quad (6.23)$$

and

$$l_{Q_2} = -(3 - \sqrt{6})H, \quad (6.24)$$

at the right and left of the tup, respectively.

Observe that the shear hinge length depends on the load position, type of support and beam thickness, not on the material. Also, it is rather small, a fraction of the beam thickness.

In all the above equations, only the first phase of motion is being considered. This is because in the dynamic case, shear is more relevant in this phase. The expressions for these beam configurations are simple, in line with the bending hinge length definition.

## 6.4 Membrane hinge length

Generally speaking, large values of displacement in a structure induce severe membrane forces. These membrane forces will spread the otherwise restricted plastic strain region. For a centrally loaded beam, when axial inertia is disregarded, the membrane force is constant along the beam length. This suggests that the membrane strain spreads evenly along the beam length. Hence, the membrane hinge is the whole beam length, regardless of the load type or support configuration.

The axial strain,  $\varepsilon_N$ , at the right side of the beam in Figure 6.1, due to the normal force  $N$ , reads

$$\varepsilon_{N_1} = \frac{\Delta L_1}{L_1} = \sqrt{1 + (W/L_1)^2} - 1. \quad (6.25)$$

This expression may be expanded in series and, for values of the ratio  $(W/L_1)^2$  which are not too large, only the first term may be retained, yielding

$$\varepsilon_{N_1} = \frac{1}{2} \left( \frac{W}{L_1} \right)^2. \quad (6.26)$$

For one side of the beam, this strain is assumed to be evenly distributed along the beam length,  $L_1$ , and through the cross-section. Since the rigid-plastic analysis usually gives the displacement, the membrane strains can be calculated. Observe that, for the present model, this strain is not dependent on the type of support or material.

It is not the aim here to expand further the present bending, shear and membrane hinge length definitions to structures other than beams. However, the main features of these hinge definitions seem to be applicable to more complex structures, *eg* plates and shells.

## 6.5 Equivalent strain

Because the primary interest here is to predict failure in clamped beams, the following equations will be deduced for a clamped beam subjected to a concentrated load acting at any position on its span.

The equivalent strain is defined in rectangular co-ordinates as

$$\varepsilon_{eq} = \frac{\sqrt{2}}{3} \sqrt{(\varepsilon_{xx} - \varepsilon_{yy})^2 + (\varepsilon_{yy} - \varepsilon_{zz})^2 + (\varepsilon_{zz} - \varepsilon_{xx})^2 + 6(\varepsilon_{xy}^2 + \varepsilon_{xz}^2 + \varepsilon_{yz}^2)}, \quad (6.27)$$

and it is an important parameter for failure prediction. It is the aim now to express it as a function of the kinematic and geometry of a beam in the  $x$ - $z$  plane. In this case, it is assumed that

$$\varepsilon_{xy} = \varepsilon_{yz} = 0 \quad (6.28)$$

and

$$\varepsilon_{yy} = \varepsilon_{zz} = -\frac{\varepsilon_{xx}}{2}, \quad (6.29)$$

rendering the equivalent plastic strain as

$$\varepsilon_{eq} = \sqrt{\varepsilon_{xx}^2 + \frac{\gamma_{xz}^2}{3}}, \quad (6.30)$$

where  $\gamma_{xz} = 2\varepsilon_{xz}$  is an average shear strain, calculated as follows.

### 6.5.1 Shear strain

The shear strain, taken to be constant along the shear hinge length, is evaluated approximately as<sup>213</sup>

$$\gamma_{xz} = \frac{W_s}{l_{Q_1}/2}, \quad (6.31)$$

where  $W_s$  is the indentation.



The results in section 6.3 point towards a common approximate value for the shear hinge length of

$$l_{Q_1} = l_{Q_2} = H/2, \quad (6.32)$$

in the case of a clamped beam, simplifying equation (6.31) to

$$\gamma_{xz} = 4 \frac{W_s}{H}. \quad (6.33)$$

A shear hinge length of about half of the beam thickness was also found experimentally by measuring the angles of initially square grids pasted on impacted beams (see Chapter 7).

As far as the shear displacement,  $W_s$ , is concerned, experimental data in Chapter 7 suggest that the following relation holds well

$$W_{s_f} = k \frac{W_f}{L_1}, \quad (6.34)$$

where  $W_{s_f}$  is the final indentation (shear displacement),  $W_f$  is the final beam displacement (including  $W_{s_f}$ ) and  $k$  a constant. Also, numerical investigations by YU and JONES,<sup>217</sup> suggest that it is reasonable to assume

$$W_s = \frac{W_{s_f}}{W_f} W, \quad (6.35)$$

or

$$W_s = k \frac{W}{L_1}, \quad (6.36)$$

where  $W$  is the beam displacement.

In words, the shear displacement increases proportionally to the beam displacement.

From equations (6.33) and (6.36), it follows that the shear strain at the impact point of a clamped beam is

$$\gamma_{xz} = \frac{4kw}{L_1}, \quad (6.37)$$

where

$$w = \frac{W}{H}. \quad (6.38)$$

### 6.5.2 Axial strain

The axial strain in a clamped beam is the result of the strain due to bending,  $\varepsilon_M$ , and the strain due to the membrane force,  $\varepsilon_N$ .

The strain due to bending, at the point of maximum displacement of the beam, is

$$\varepsilon_M = \frac{1}{2} \left( \frac{W}{L_1 l_{M_1}} z + \frac{W}{L_2 l_{M_2}} z \right), \quad (6.39)$$

where the strains at the left- and right-hand side of the point load were averaged.

For a clamped beam, the bending hinge lengths,  $l_{M_1}$  and  $l_{M_2}$ , are

$$l_{M_1} = \frac{L_1}{m} \quad (6.40)$$

and

$$l_{M_2} = \frac{L_2}{6}. \quad (6.41)$$

Observe the introduction here of the parameter  $m$ . Suppose that a clamped beam is loaded very close to the support, say at  $L_1 = H$ . The bending hinge length for this case would be too small,  $l_{M_1} = H/6$ , yielding very large values for the strain  $\varepsilon_M$ . This can be compensated by letting  $m$  to assume values different from 6, as discussed in sequence.

Comparisons of the axial strains with experimental and numerical results, as later presented, indicates that, for some cases, a fairer agreement may be obtained when the origin of the coordinate  $z$  in equation (6.39) is allowed to vary between the centroidal and the neutral axis.

It can be shown that the distance between the neutral axis and the outmost fibre for a clamped beam is<sup>97</sup>

$$z = \frac{1 + N/N_0}{2} H = \frac{1 + nW/H}{2} H. \quad (6.42)$$

By setting  $n = 0$ , the maximum value  $z$  achieves is the (usual) half-thickness of the beam. For a clamped beam, the parameter  $0 \leq n \leq 1$  can be adjusted in order to improve the prediction, as it will be seen.

According to these simplifications, the strain due to bending, equation (6.39), reduces to

$$\varepsilon_M = \left( \frac{m}{4} + \frac{3\xi^2}{2} \right) (1 + nw) h^2 w, \quad (6.43)$$

when defining

$$\xi = \frac{L_1}{L_2}, \quad (6.44)$$

$$w = \frac{W}{H} \quad (6.45)$$

and

$$h = \frac{H}{L_1}, \quad (6.46)$$

and using equations (6.40) and (6.41).

The strains due to the membrane force, equation (6.26), are different on each side of the beam span. At the point load, they are averaged such that

$$\varepsilon_N = \frac{1}{2} \left[ \frac{1}{2} \left( \frac{W}{L_1} \right)^2 + \frac{1}{2} \left( \frac{W}{L_2} \right)^2 \right] \quad (6.47)$$

or

$$\varepsilon_N = \frac{1 + \xi^2}{4} (hw)^2, \quad (6.48)$$

when adopting equations (6.44)–(6.46).

Equations (6.37), (6.43) and (6.48) can now be manipulated to give the equivalent plastic strain in a clamped beam. The axial strain,  $\varepsilon_{xx}$ , in equation (6.30), has to be calculated from  $\varepsilon_M$  and  $\varepsilon_N$ . This is done by adding them, *ie*

$$\varepsilon_{xx} = \varepsilon_M + \varepsilon_N, \quad (6.49)$$

or

$$\varepsilon_{xx} = [1 + mn + (1 + 6n)\xi^2] \left( \frac{hw}{2} \right)^2 + [m + 6\xi^2] \frac{h^2 w}{4}, \quad (6.50)$$

from equations (6.43) and (6.48).

This additive property of the strains is accepted here without further proof and has been used elsewhere.<sup>213</sup> However, it is not known whether this geometrical relation leads to a consistent set of equilibrium equations. In other words, the principle of virtual velocities has to be satisfied if this additive property strictly holds.

Now, by introducing equations (6.37) and (6.50) into equation (6.30), one has a final expression for the maximum equivalent strain in a beam,

$$\varepsilon_{eq} = \sqrt{\left\{ [1 + mn + (1 + 6n)\xi^2] \left(\frac{hw}{2}\right)^2 + [m + 6\xi^2] \frac{h^2w}{4} \right\}^2 + \left\{ \frac{4kw}{\sqrt{3}L_1} \right\}^2}. \quad (6.51)$$

## 6.6 Equivalent strain rate

The variation of the strain rate taking place in an impacted structure has very complicated features.

A rough estimative of the average strain rate,  $\dot{\varepsilon}_m$ , occurring in a clamped beam, is given by PERRONE and BHADRA<sup>171</sup> as

$$\dot{\varepsilon}_m = \frac{W_f V_0}{3\sqrt{2}L_1^2}, \quad (6.52)$$

where  $W_f$  is the final displacement and  $V_0$  is the initial velocity.

The authors arrived at this equation by studying the simple model of a mass supported by two strain rate sensitive wires of equal length, where only membrane strains are presented. Equation (6.52) has been used by others in an attempt to estimate the strain rate in beams loaded at any position on the span. However, it is evident that the strain rate as such increases quadratically with the decrease of  $L_1$ .

To show that the PERRONE and BHADRA<sup>171</sup> equation does not describe faithfully the strain rate in off centre loaded beams, take the strain rate variation at the bottom underneath of an aluminium beam impacted at one-quarter of its span. Results of a numerical simulation of this problem, by YU and JONES,<sup>217</sup> indicate that the strain rate behaves as shown in Figure 6.7. In the same figure, the prediction according to PERRONE and BHADRA,<sup>171</sup> equation (6.52), is plotted. The predicted strain rate is not good. It underestimates the peak strain rate a great deal, in part because the moment is disregarded in the model leading to equation (6.52).

This poor result motivates the search for a better accurate description of the strain rate in a clamped beam. Since the hinge length definitions yielded the equivalent strains, the average strain rate is a matter of defining the impact time.

Numerical data of reference 217 and experimental data from Chapter 7, indicate that a reasonable approximation to the total motion time of a

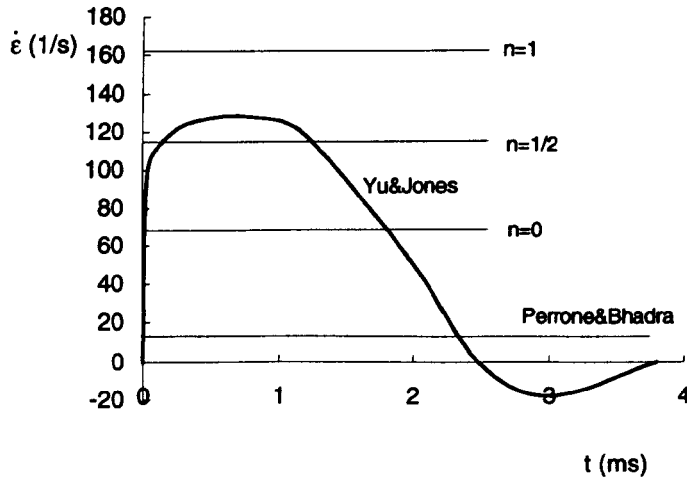


**Figure 6.7:** Strain rate *versus* time at the bottom underneath an aluminium beam impacted at one-quarter of its span. The thick line is the tensile strain rate, according to the numerical simulation in reference 217. The horizontal lines are the predictions according to Perrone and Bhadra,<sup>171</sup> equation (6.52), and according to equation (6.55) for various values of  $n$ .

clamped beam is

$$t = \frac{W_f}{V_0/2}, \quad (6.53)$$

where  $W_f$  is the final displacement achieved by a clamped beam subjected to an initial velocity  $V_0$ .

By differentiating equation (6.51), using  $t$  as above and disregarding shear strains, it is possible to obtain the equivalent strain rate as

$$\dot{\epsilon}_{eq} = \frac{V_0}{8L_1} \{ (m + 6\xi^2)h + 2[(1 + nm) + (1 + 6n)\xi^2]\bar{w}_f \} \quad (6.54)$$

where  $\bar{w}_f = W_f/L_1$ .

Observe that the above equation was derived disregarding the shear strain. This makes equation (6.54) simpler to use, yet leading to reasonable results.

Equation (6.54) can now be used to calculate the average strain rate at the bottom, underneath the clamped beam struck at one-quarter of its span

analysed in reference 217. Adopting  $m = 6$ , since the load point is not close to the support, and  $\xi = 1/3$ , one has

$$\dot{\epsilon}_{eq} = \frac{5V_0}{6L_1} \left\{ h + \frac{1+6n}{3} \bar{w}_f \right\}. \quad (6.55)$$

The result is presented in Figure 6.7, where it can be seen the role of  $n$  as an adjustable parameter.

This simple model does not capture the variation of the strain rate throughout the motion. However, it is useful as an approximation for an average strain rate. Unfortunately, due to a lack of numerical and experimental data, it was not possible to further compare the strain rate equations for beams loaded at other positions.

## 6.7 Validation of the hinge length definitions

It is important to assess whether the hinge lengths defined here agree with what takes place in a structure. Most importantly, the strains yielded by the expressions of the previous sections should be investigated inasmuch as accuracy is concerned. To draw the comparison, experimental and numerical data will be used, as hereafter shown.

### 6.7.1 Qualitative validation

Considering first some experimental evidences, the work of MENKES and OPAT<sup>147</sup> presents aluminium beams loaded impulsively along their entire span. For moderate impulses, where shear effects are not dominant, one can plot the beam deformed profile and mark on it the boundaries of the bending hinge length definition which, for a clamped beam and distributed load, is  $L/\sqrt{6}$ . The result is presented in Figure 6.8. It can be seen that the hinge length as here defined predicts that nearly all the beam has a non-zero curvature, as a glance in Figure 6.8 suggests.

Figure 6.9 shows the permanent deformed profile of mild steel beams struck at different positions by different masses and velocities. The bending and shear hinge lengths are marked in the figure. The bending hinge length for these clamped beams is  $L/6$ . The shear length varies according to the load point but, as discussed, it is assumed to be one-half of the beam thickness, regardless of the side and position of the tup.

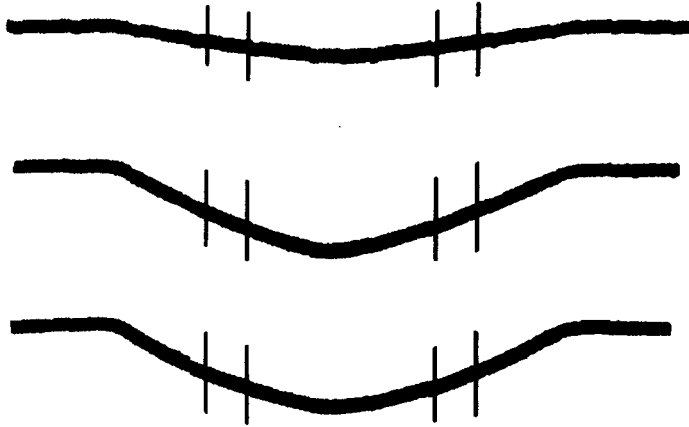


**Figure 6.8:** Displacement profile of fully clamped aluminium beams loaded impulsively throughout all their span.<sup>147</sup> The smaller distance between the vertical lines define the boundaries where the curvature is zero, according to the bending hinge length based on a static moment distribution.

It can be seen that the boundaries of the bending hinge length more or less coincide with the regions where the curvature drops to zero. The grids marked on the beam in the figure (b) show regions where shear is present \*, more or less coinciding with the shear hinge here defined.

### 6.7.2 Quantitative validation

YU and JONES<sup>217</sup> conducted a Finite-Element simulation of some experiments on beams by LIU and JONES.<sup>135</sup> Their results are specially interesting in the present context because they provide a detailed description of some field variables.

Consider the simulation of a clamped aluminium beam with a length of 101.2mm struck by a mass of 5kg at one-quarter of its span and at a velocity of 5.34m/s. YU and JONES<sup>217</sup> obtained a curvature profile at the instant of maximum deflexion of the beam as depicted in Figure 6.10. In the same figure is also plotted the theoretical curvature calculated by

$$\kappa_1 = \frac{W}{L_1 I_{M_1}} = \frac{6W}{L_1^2} \quad \text{and} \quad \kappa_2 = \frac{W}{L_2 I_{M_2}} = \frac{6W}{L_2^2}, \quad (6.56)$$

\*Shear occurs wherever the angles of the grid corners differ from 90°.

where subscripts 1 and 2 refer to right and left side of the tup, respectively. As assumed, these values are the maximum achieved along the beam length. They decrease linearly from these maximum values to zero, at the boundary of the hinge length.

It was remarked before that, for off-centre loads, there are two bending hinge lengths, implying a curvature discontinuity at the impact point. However, no load is concentrated in a point and, in this case, the maximum curvature at the left (right) of the point load is assumed to occur at the left (right) of the tup, whose thickness is 5.08mm. Also, the maximum curvature was set constant from the left side of the tup until its middle.

The good correlation for the curvature does not necessarily imply accurate values for the strains. Fortunately, the same reference 217 presents the evolution of the maximum axial strain (no shear) at the bottom of the impact region. This maximum strain, which is the sum of membrane and bending strains, is an experimental curve inferred from LIU and JONES.<sup>135</sup> Figure 6.11 presents the experimental value plus the theoretical prediction, derived from equation (6.51) when  $\xi = 1/3$ ,  $m = 6$ , and shear is neglected, *ie*

$$\varepsilon_{eq} = \left( \frac{5h^2w}{18} \right) [6 + (6n + 1)w]. \quad (6.57)$$

Consider now the shear strains. For an aluminium beam struck at its quarter span, YU and JONES<sup>217</sup> calculated the shear strains along the cross-section immediately to the right and left side of the tup, when the beam reaches its maximum deflection. An average value is about  $\varepsilon_{xz} = 0.05$ , or  $\gamma_{xz} = 0.10$ . From equation (6.33), the average shear strain reads

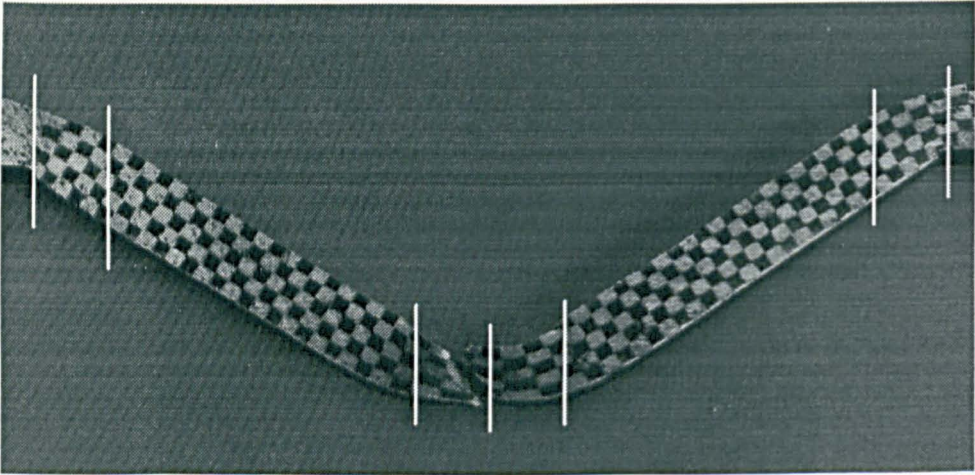
$$\varepsilon_{xz} = \frac{W_s}{l_Q} = \frac{0.225}{H/2} = 0.06, \quad (6.58)$$

with  $H = 7.62\text{mm}$  and  $W_s = 0.225\text{mm}$  given by reference 217.

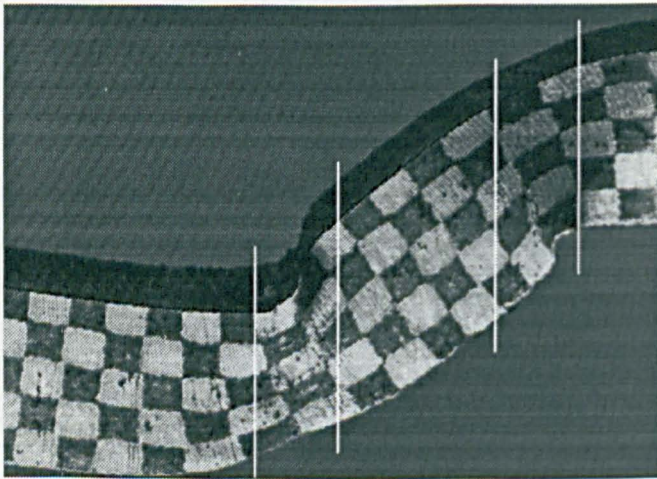
The above results suggest that the theory can predict the strains in a clamped beam with a tolerable error. But the fact that the strains are not very large precludes one to conclude that larger strains are equally well predicted.

To illustrate this point, it is interesting to consider a ductile clamped beam loaded at its middle. This is the subject of a recent numerical simulation by YU and JONES.<sup>216</sup> The authors have compared their Finite-Element





(a) Beam impacted at the middle span.



(b) Beam impacted at around one-fifth of its span.

**Figure 6.9:** (a) Beam struck by a round tup at its mid-span by a mass of 6.5kg and  $V_0 = 14.9\text{m/s}$ . (b) Beam struck by a sharp tup at one-fifth of its span by a mass of 19.5kg and  $V_0 = 6.14\text{m/s}$ . The white lines mark the boundaries of the (a) bending and (b) shear hinge length, respectively.

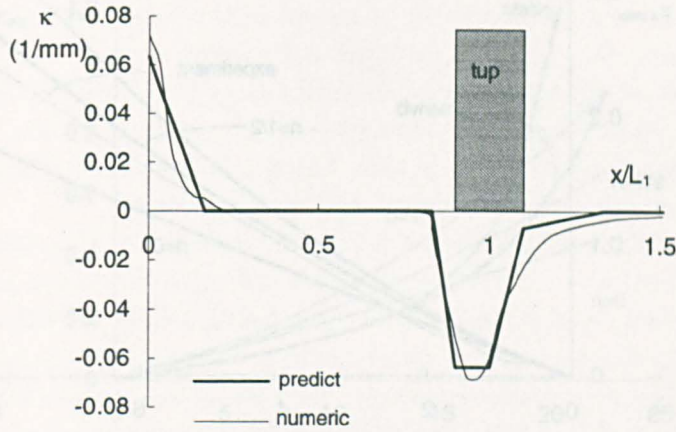


**Figure 6.10:** Curvature profile of a fully clamped aluminium beam struck by a falling mass at one-quarter of its span ( $x/L_1 = 0$  is at the clamp and  $x/L_1 = 1$  is at the impact point). Thin and thick lines represent the Finite-Element results from reference 217 and equation (6.56), respectively.

results with experimental data from tests on mild steel beams, obtaining very good agreement.

According to YU and JONES,<sup>216</sup> the equivalent strain at the lower surface of the beam, underneath the striker, evolves with the maximum displacement as shown in Figure 6.12. In the same figure, it is also shown the strains as predicted by equation (6.51) when  $\xi = 1$  and  $m = 6$ , *ie*

$$\epsilon_{eq} = \sqrt{\left(\frac{h^2 w}{2}\right)^2 [6 + (6n + 1)w]^2 + \left[\frac{4kw}{\sqrt{3}L_1}\right]^2}. \quad (6.59)$$

The figure shows the interesting feature that the equivalent strain increases significantly when the displacement to failure is about to be reached. This is important because the strains at failure need to be known as accurate as possible. Hence, the change of  $n = 1/2$  to  $n = 1$  improves the prediction of the strain to rupture. The character of  $n$  as an adjustable parameter becomes once more evident.

It is important to remark that, in face of the good agreement between experiments and the Finite-Element simulation in reference 216, the numerical

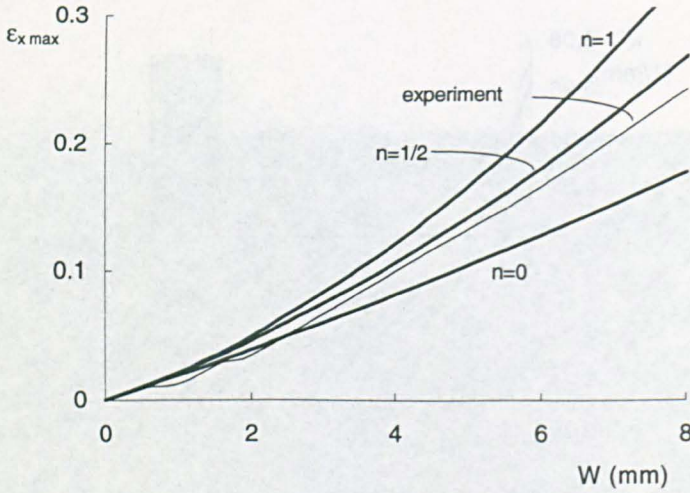


**Figure 6.11:** Maximum axial strain (no shear) at the bottom of the load point underneath a fully clamped aluminium beam *versus* its displacement. The beam was struck by a falling mass at one-quarter of its span. Thin and thick lines represent experimental results from reference 135 and the prediction of equation (6.57), respectively.

equivalent strain describes what actually takes place at the bottom of the beam. At the same time, the theoretical equation for the equivalent strain, being able to yield a reasonable prediction, is considered attractive due to its simplicity and closed form.

Equation (6.59) is dependent on the geometry of the beam, on  $n$ , on  $m$  and on the factor  $k$ . As said before,  $m = 6$  because the beam is not loaded close to the support. The factor  $k$  can be considered a material parameter. Experimental results for mild steel beams to be presented in the next chapter give  $k = 2.29\text{mm}$ . It is not known whether  $k$  would change significantly for other metals.

YU and JONES<sup>216</sup> have also evaluated the shear strains for the mild steel beam struck at its middle. The maximum value quoted throughout all the response is  $\varepsilon_{xz} = 0.33$ , which yields  $\gamma_{xz} = 0.66$ . For comparison, the present shear hinge definition yields a maximum shear strain of

$$\gamma_{xz} = \frac{W_s}{l_Q/2} = \frac{W_s}{(H/2)/2} = 2k \frac{W_f/L}{H/2} = 0.65, \quad (6.60)$$

which is in good agreement with the numerical one.

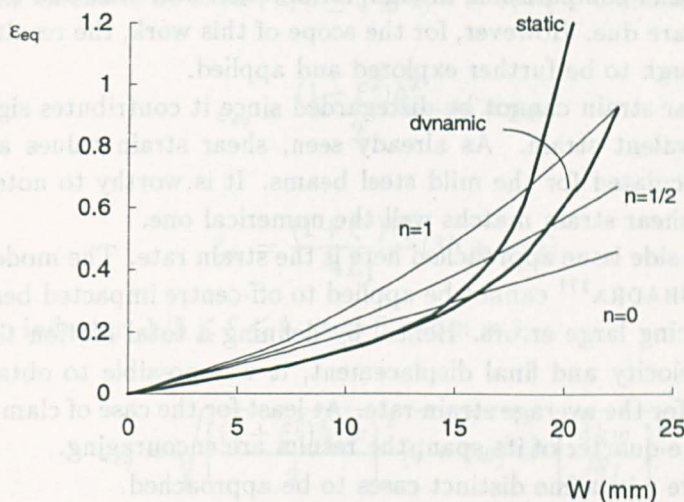


**Figure 6.12:** Equivalent strain at the lower surface underneath the striker for mild steel beams *versus* its displacement. The impact velocity is  $V_0 = 10.5\text{m/s}$ . Thin and thick lines represent equation (6.59) and numerical results from reference 216, respectively.

## 6.8 Final comments

The unlimited flow stress of a perfectly plastic material imposes severe restrictions on the knowledge of strains. The strains can be calculated if one assumes a finite length around the regions where the flow stress takes place. Though there exists some definitions of hinge length in the literature, they are not always directly compared with experimental or Finite-Element results. This is specially true for the values of strains yielded by the use of hinge lengths.

In this chapter, a new definition of bending and shear hinge length was developed and explored in order to assess the strains in a perfectly plastic material. Emphasis has been placed in how these hinge lengths lead to the curvature and extensional, shear and equivalent strains. Strains and curvatures obtained from the hinge lengths are in reasonable agreement with experimental and numerical data for aluminium and mild steel beams impacted at different positions along their span.

The comparison presented here used data from beams made of two very distinctive materials, especially as far as the strain rate sensitivity is con-

cerned. Further comparisons, though, for different materials and for different load points are due. However, for the scope of this work, the results are reasonable enough to be further explored and applied.

The shear strain cannot be disregarded since it contributes significantly to the equivalent strain. As already seen, shear strain values as high as 0.3 were calculated for the mild steel beams. It is worthy to note that the theoretical shear strain matches well the numerical one.

Another side issue approached here is the strain rate. The model of PERONE and BHADRA<sup>171</sup> cannot be applied to off-centre impacted beams without introducing large errors. Hence, by defining a total motion time based on initial velocity and final displacement, it was possible to obtain simple expressions for the average strain rate. At least for the case of clamped beam struck at one-quarter of its span, the results are encouraging.

There are now some distinct cases to be approached.

As already commented, for a clamped beam loaded quite close to the support, the moment hinge length would be too small ( $L_1/6$ ) to yield realistic values of axial strain. Also, in this case, the beam displacement will not be large and it is possible to set  $n$  equal zero. Accordingly, for  $0 < \xi \leq 1/5$ , it is adopted  $m = 1$  and  $n = 0$ . The strain rate for these beams,  $\xi < 1/5$ , is deduced from equations (6.51) and (6.53), disregarding any contribution of the axial strains.

The shape of the indenter will play a decisive role on the strains. Unfortunately, for a round tup, there is no numerical data which allows to compare the prediction of strains. Surely, the membrane strains are dominant, for the shear strains are quite small due to the tup geometry. This is supported by observing the shape of grids pasted on these beams (see Chapter 7). Now, the experimental data in Figure 6.11 suggests that the membrane strain are better predicted when using a value for  $n$  equal one-half. Accordingly, for a round tup loading the beam at or near to the middle beam span, the shear strains are negligible, allowing to set  $k = 0$ ,  $n = 1/2$  and  $m = 6$ .

These values for the parameters  $m$  and  $n$ , when introduced into equations (6.51) and (6.54) reduce them to the following: \*

---

\*It is possible to express these equations in series of  $w$ . This might be useful if the square roots are to be eliminated from them.

- round indenter, no shear,  $2/3 \leq \xi \leq 1$ ,  $k = 0$ ,  $m = 6$  and  $n = 1/2$

$$\varepsilon_{eq} = \frac{(1 + \xi^2)h^2}{2} w(3 + 2w) \quad (6.61)$$

$$\dot{\varepsilon}_{eq} = \frac{(1 + \xi^2)V_0}{4L_1} (3h + 4\bar{w}_f) \quad (6.62)$$

- sharp indenter,  $1/5 \leq \xi \leq 1$ ,  $m = 6$  and  $n = 1$

$$\varepsilon_{eq} = \sqrt{\left[ \frac{(1 + \xi^2)h^2 w}{4} \right]^2 [6 + 7w]^2 + \left[ \frac{4kw}{\sqrt{3}L_1} \right]^2} \quad (6.63)$$

$$\dot{\varepsilon}_{eq} = \frac{(1 + \xi^2)V_0}{4L_1} (3h + 7\bar{w}_f) \quad (6.64)$$

- sharp indenter,  $0 < \xi < 1/5$ ,  $m = 1$  and  $n = 0$

$$\varepsilon_{eq} = \sqrt{\left[ \frac{h^2 w}{4} \right]^2 [1 + 6\xi^2 + (1 + \xi^2)w]^2 + \left[ \frac{4kw}{\sqrt{3}L_1} \right]^2} \quad (6.65)$$

$$\dot{\varepsilon}_{eq} = \frac{kV_0}{\sqrt{3}hL_1^2}. \quad (6.66)$$

where  $\bar{w}_f = W_f/L_1$  is an adimensional displacement.

These expressions for the equivalent strain and its rate are relatively simple to use. In fact, the simplicity and rationality of the hinge length definitions here employed is in harmony with a perfectly plastic material constitutive law.

The theoretical equivalent strain changes continuously along the beam length and across the transverse section and can now be mapped throughout a whole beam made of a perfectly plastic material. This is exactly what is called for by some failure criteria. In this sense and within the scope of this work, failure prediction will be a matter of application of the Continuum Damage Mechanics, whose necessary parameters are now all available.



---

# 7 Static and Dynamic Beam Failure

A STRUCTURE is said to have failed when any further attempt to increase the load results in a complete local material discontinuity.

In a real structure, it is difficult to define precisely this limit, sometimes tenuous, of the beginning of local material failure, crack formation, crack propagation and total collapse. Likewise, it is difficult to test dynamically a structure in order to just trigger a local material failure. Hence, failure energy, displacement to failure, strain to failure, etc ... are quite imprecise concepts.

Bearing in mind these comments, this chapter aims to predict the threshold energy beyond which local or global material separation takes place. This means to assume that the energy absorbed by the propagation of a crack is neglected.

The chapter starts by describing static and dynamic experiments aimed to induce failure on beams. CDM is then used to predict the displacement to failure of the beams loaded statically. The displacement to failure of the impacted beams is predicted by using the static and rate-dependent version of CDM presented in Chapter 5. The results obtained are compared with the experiments. A discussion then follows on the main features of static and dynamic failure prediction.

## 7.1 Experiment in beams

The same mild steel described in the previous chapters was used to make rectangular beams with approximate dimensions of  $B = 8\text{mm}$ ,  $H = 9\text{mm}$  and  $L = 102\text{mm}$ . The length of the beams coincides with the rolling direction



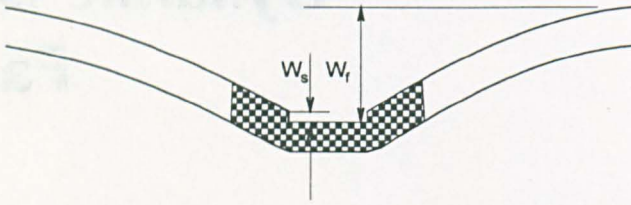


**Figure 7.1:** Definition of the final global displacement of beams. The grids were used to measure plastic strains.

of the plate (see Figure 2.5 on page 24). These beams were tested statically and dynamically.

The maximum displacement of the beams was measured after the tests.

It was shown in Chapter 6 that the equivalent strain in beams impacted by a sharp tup takes into account shear. The shear strain in the model is due to the indentation left by the tup. Hence, it seemed more appropriated to add the local indentation caused by the tup to the global displacement of the beam, as depicted in Figure 7.1.

This definition of beam displacement has been previously used by LIU and JONES.<sup>135</sup> However, different ways of measuring the displacement can be adopted, as in YU and JONES.<sup>218</sup>

### 7.1.1 Static tests

The static tests were conducted in a DARTEC tensile machine. The head speed was set to 0.05mm/s and the beams were fully clamped by the same rig used in reference 135. Two indenter shapes were used to apply the load at different positions of the beam span; one round, with diameter 20mm, and another rectangular, having a width of 5.08mm. For both indenters, the breadth is much larger than the beam breadth. Figure 7.2 shows the load position, the indenter used and the measured load displacement–curve. Other details of the tests are listed on Table 7.1.

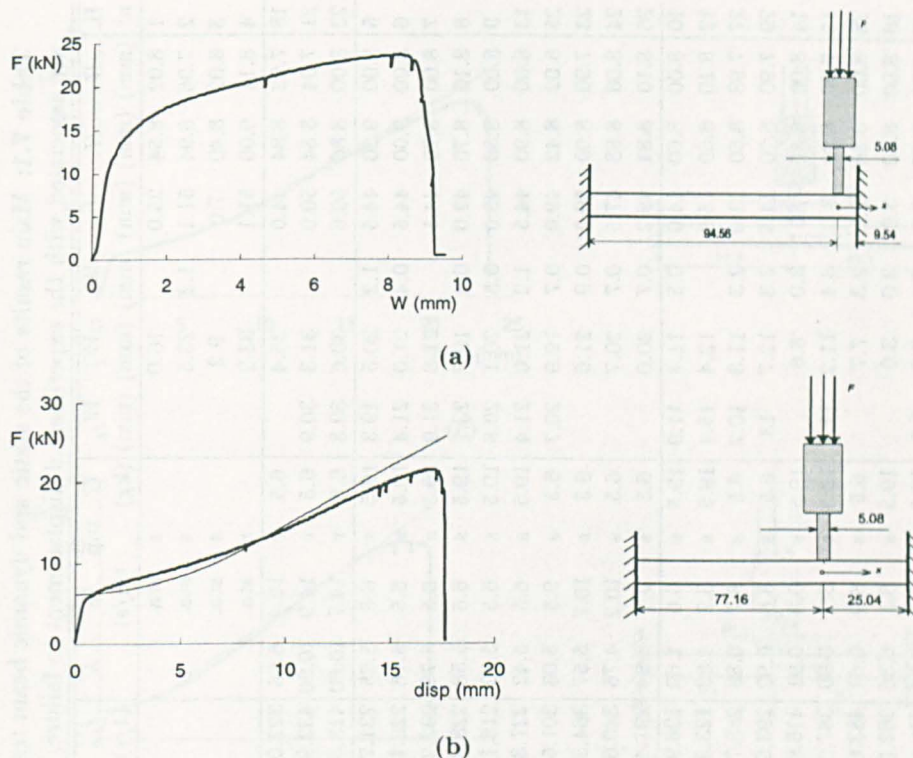


**Figure 7.2:** Load–displacement experimental (thick line) and theoretical (thin line), equation (8.2), curve for clamped beams loaded statically at (a) 9.5mm; (b) 25.0mm and (c) middle, with a sharp indenter. (d) Same as in (c) but with a round indenter.

### 7.1.2 Dynamic tests

A number of dynamic tests were performed in a drop tower. Two different masses,  $G = 6.5\text{kg}$  and  $G = 19.5\text{kg}$ , were attached to the same round,  $r$ , and sharp,  $s$ , indenters used in the static tests. The most relevant parameters of the tests are summarised on Table 7.1.

During the tests, the velocity–time history of the tup was recorded by a laser instrument according to the technique described in reference 22. A typical velocity–time recorded trace, after filtering with a cut-off frequency of 1kHz, is depicted in Figure 7.3(a). This trace can be integrated and differentiated to obtain the displacement,  $W_{fL}$ , and load history, as shown in Figures 7.3(b) and (c). Figure 7.3(d) presents the load *versus* displacement

**Table 7.1:** Main results of the static and dynamic beam tests. The damage parameters are for  $\sigma_h/\sigma_{eq} = 1/2$  and are associated with the experimental displacement to failure.

B. n°	B (mm)	H (mm)	L <sub>1</sub> (mm)	W <sub>s</sub> (mm)	W <sub>f</sub> (mm)	W <sub>fL</sub> (mm)	G (kg)	tup	V <sub>0</sub> (m/s)	λ	ε <sub>eq</sub> (1/s)	ε <sub>eq</sub>	D <sub>s</sub>	D <sub>d0</sub>	D <sub>d</sub>	comments
1	8.02	8.54	25.0		16.0			s	sta.			1.18	0.46	0.46	0.48	broken at angle
2	7.96	8.94	51.1	1.4	23.5			s	sta.			1.02	0.39	0.39	0.36	broken at angle
3	8.02	8.40	7.0		9.2			s	sta.			1.18	0.46	0.46	0.48	broken (shear)
4	8.14	9.00	51.1		33.2			r	sta.			1.19	0.47	0.47	0.49	broken (necking)
18	7.92	8.84	44.0		25.4		6.5	r	12.4	6.68	322.0	0.80	0.22	0.59	0.49	not broken, no crack
21	7.94	8.84	50.0		31.3	30.9	6.5	r	14.9	10.96	432.9	1.07	0.39	0.89	0.86	just broken (necking)
22	8.00	8.86	50.6		30.6	30.8	6.5	r	14.7	10.60	418.5	1.03	0.37	0.84	0.80	just broken (necking)
5	8.00	9.00	44.5	1.2	20.5	19.3	19.5	s	6.8	5.65	231.7	0.86	0.32	0.60	0.52	broken (at angle)
6	8.00	9.00	44.5	0.4	21.0	21.4	19.5	s	6.5	5.16	226.1	0.89	0.33	0.63	0.55	broken (at angle)
7	8.00	8.70	44.5		21.8	21.9	19.5	s	6.5	5.72	232.2	0.95	0.36	0.68	0.62	not broken, no crack
8	8.10	8.70	42.0	0.4	19.7	23.1	19.5	s	6.6	5.58	228.2	0.84	0.31	0.59	0.50	broken (at angle)
9	8.00	8.80	45.0	0.5	20.1	20.8	19.5	s	6.5	5.72	218.1	0.82	0.30	0.57	0.48	just broken (at angle)
13	8.00	8.90	44.5	1.2	21.0	21.4	19.5	s	6.5	5.42	227.3	0.89	0.33	0.63	0.55	not broken but cracked
25	8.02	8.42	49.0	0.7	19.9	20.7	6.5	s	9.5	5.03	301.5	0.77	0.28	0.55	0.46	broken (at angle)
23	7.90	8.90	50.2	0.9	21.6		6.5	s	10.7	5.57	364.3	0.88	0.33	0.68	0.60	broken (at angle)
24	8.06	8.88	47.5	0.7	20.7		6.5	s	10.2	4.76	340.6	0.84	0.31	0.63	0.54	broken (at angle)
26	8.10	8.84	49.2	0.7	20.0		6.5	s	9.1	3.94	291.4	0.78	0.28	0.56	0.46	not broken, no crack
10	8.00	8.60	14.0	0.5	11.4	11.9	19.5	s	6.0	1.60	126.9	0.59	0.19	0.33	0.24	not broken, no crack
12	8.10	8.60	15.0		12.4	15.4	19.5	s	6.2	1.83	123.3	0.60	0.20	0.34	0.25	not broken, no crack
27	7.98	8.60	11.0	2.3	11.3	10.7	6.5	s	8.7	0.88	288.7	0.80	0.29	0.57	0.48	slightly cracked
29	7.90	8.70	11.5	2.3	12.7	13	6.5	s	8.8	0.92	293.0	0.86	0.32	0.63	0.55	not broken, no crack
14	8.00	8.50	7.0	3.0	8.6		19.5	s	6.3	0.91	416.9	1.08	0.42	0.90	0.87	broken (shear)
15	7.90	8.90	8.0	3.4	11.2	11.7	19.5	s	6.2	0.90	387.0	1.23	0.48	1.02	1.06	broken support (shear)
28	8.00	8.68	7.5	2.3	7.7		6.5	s	8.9	0.61	483.6	0.85	0.31	0.69	0.59	broken (shear)
16	8.00	8.60	3.0	3.0	3.0		19.5	s	6.1	0.36	262.5	1.15	0.45	0.91	0.91	broken (shear)
17	8.00	8.80	3.0	3.4	2.6	6.6	19.5	s	6.1	0.34	256.6	0.98	0.37	0.75	0.69	broken (shear)

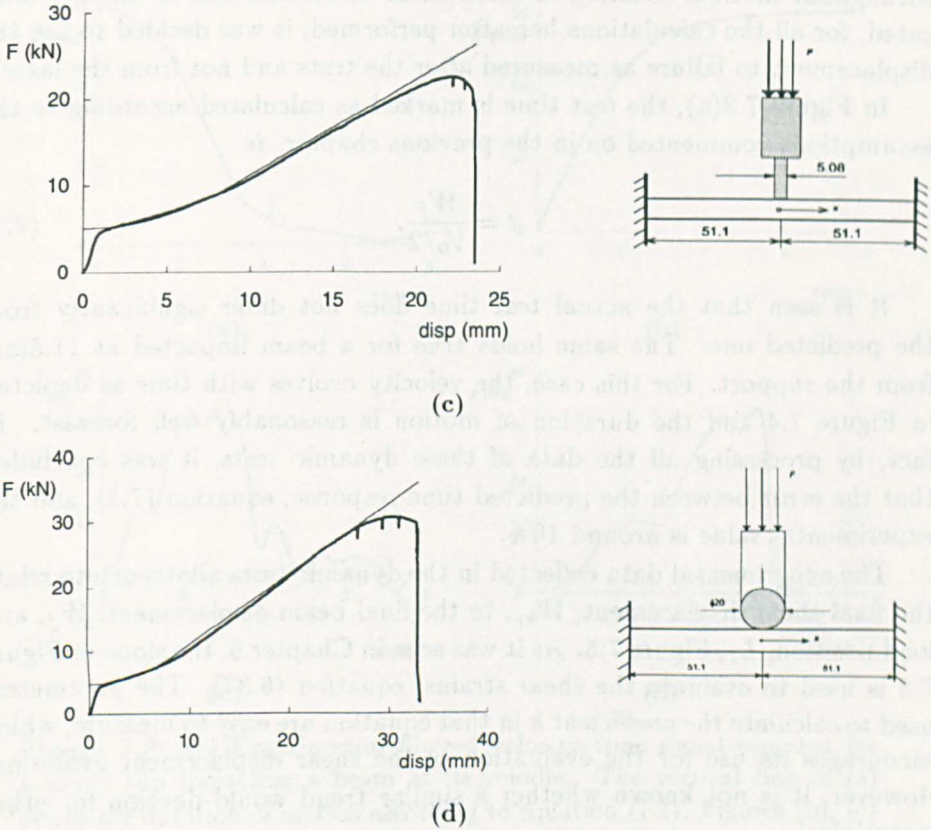


Figure 7.2: —contd.

curve.

The laser data are potentially important. They were used for measuring the final beam displacement at failure. As Table 7.1 shows, there is a reasonable agreement between the displacement to failure as recorded by the laser,  $W_{fL}$ , and as measured after the tests,  $W_f$ .

Generally speaking, the failure takes place when there is a marked discontinuity in the velocity-time signal. But, because the time when the beam was just impacted is difficult to measure consistently and accurately, it is also difficult to precisely define the displacement to failure from the laser signal. A small variation of the start test time affects significantly the area, *ie* the displacement, under the velocity-time trace since, at the beginning, the velocity is high. Moreover, for beams loaded closer to the support, it is not always evident when the beam breaks, for the velocity decreases steeply

throughout motion. Bearing in mind these comments and as already indicated, for all the calculations hereafter performed, it was decided to use the displacement to failure as measured after the tests and not from the laser.

In Figure 7.3(a), the test time is marked as calculated according to the assumptions commented on in the previous chapter, *ie*

$$t = \frac{W_f}{V_0/2}. \quad (7.1)$$

It is seen that the actual test time does not differ significantly from the predicted one. The same holds true for a beam impacted at 11.5mm from the support. For this case, the velocity evolves with time as depicted in Figure 7.4 and the duration of motion is reasonably well forecast. In fact, by processing all the data of these dynamic tests, it was concluded that the error between the predicted time response, equation (7.1), and the experimental value is around 10%.

The experimental data collected in the dynamic tests allows one to relate the final shear displacement,  $W_{sf}$ , to the final beam displacement,  $W_f$ , and load position,  $L_1$ , Figure 7.5. As it was seen in Chapter 6, the slope in Figure 7.5 is used to evaluate the shear strains, equation (6.37). The parameters used to calculate the coefficient  $k$  in that equation are easy to measure, which encourages its use for the evaluation of the shear displacement evolution. However, it is not known whether a similar trend would develop for other materials.

## 7.2 Strains measured from grids

A grid was deposited by electrolysis on the face side of some beams, Figure 7.1. The grids are squares of side dimensions around one fifth of the beam thickness. After the test, the squares became rhomboidal and it is possible to measure the new angles and side lengths and calculate the strains.

Table 7.2 lists the values of plastic true shear strain and plastic true equivalent strain measured for some beams. The predicted values for shear strain for beams 16, 17 and 27, are given by equation (6.37). For beams 21 and 22, the equivalent strain is predicted according to equation (6.61). The necessary geometric data in these equations comes from Table 7.1.

It is noteworthy that the beams chosen for measuring the strains have all failed under very different conditions. Beams 21 and 22 were struck by

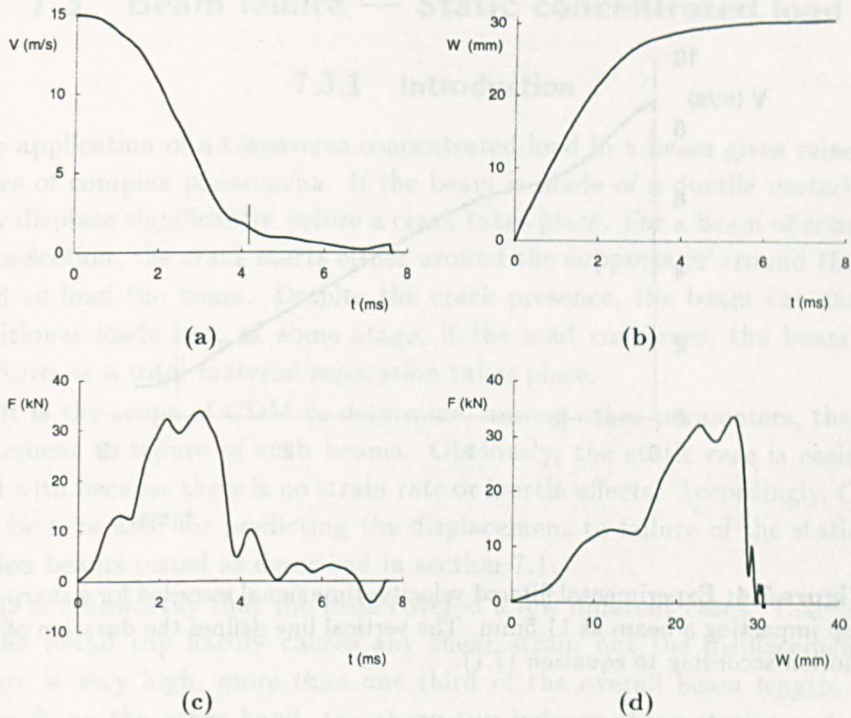


**Figure 7.3:** (a) Experimental filtered velocity-time signal recorded for a round tup impacting a beam at its middle. The vertical line in (a) marks the duration of motion according to equation (7.1). Figures (b), (c) and (d) show the corresponding displacement-time, load-time and load-displacement curves, respectively.

a round tup at the middle span and failed by necking. Beams 16, 17 and 27 have failed by shear and were struck very close to the support. In this case, the measurement of the strain was concentrated on the angles of the grids. The extension of the grids in this case is minimum. Having said that, it is important to realise that the measurement of the grid geometry is prone to errors because the boundaries between dark and bright squares sometimes are not very clear (see Figure 6.9 on page 144).

It is evident that more experimental data are necessary to fully validate the approach taken in the last chapter for the calculation of strains in a perfectly plastic material. Nevertheless, in line with the reasonable prediction for some cases, it will hereafter be taken for granted that the formulation yields good results for the strains.

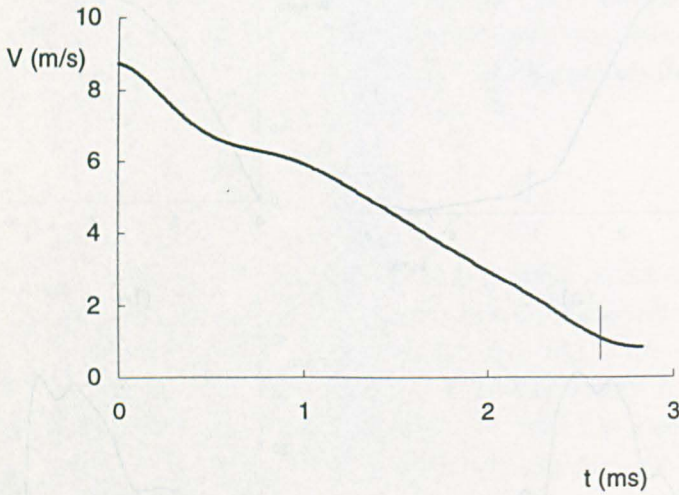


**Figure 7.4:** Experimental filtered velocity-time signal recorded for a sharp tup impacting a beam at 11.5mm. The vertical line defines the duration of motion according to equation (7.1).

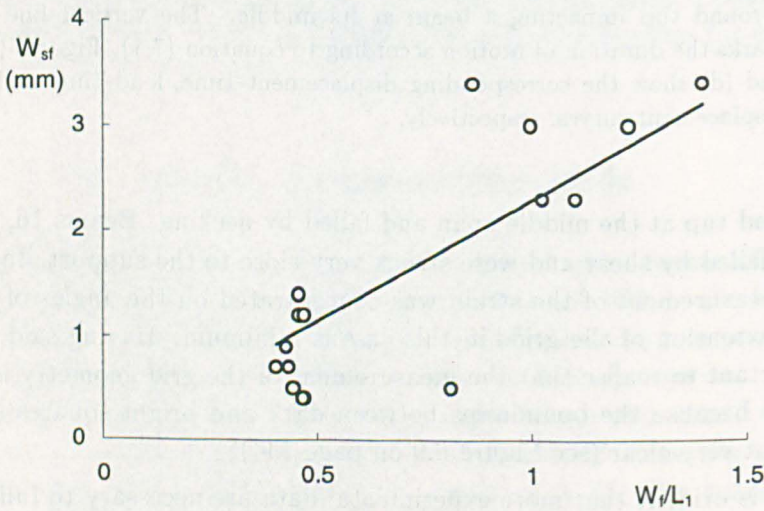


**Figure 7.5:** Final shear displacement,  $W_{sf}$ , versus final displacement to impact position ratio,  $W_f/L_1$ , for mild steel beams.

## 7.3 Beam failure — Static concentrated load

### 7.3.1 Introduction

The application of a transverse concentrated load in a beam gives rise to a series of complex phenomena. If the beam is made of a ductile material, it may displace significantly before a crack takes place. For a beam of constant cross-section, the crack starts either around the supports or around the tup used to load the beam. Despite the crack presence, the beam can sustain additional loads but, at some stage, if the load continues, the beam will fracture, *ie* a total material separation takes place.

It is the scope of CDM to determine, among other parameters, the displacement to failure of such beams. Obviously, the static case is easier to deal with because there is no strain rate or inertia effects. Accordingly, CDM will be here used for predicting the displacement to failure of the statically loaded beams tested as described in section 7.1.

It is noteworthy that the tests covered a few different cases. Take beam 4; the round tup hardly causes any shear strain but the displacement to failure is very high, more than one third of the overall beam length. For beam 2, on the other hand, the sharp tup induces shear strains and does precipitate failure at a displacement lower than the displacement achieved by the beam loaded with the round tup. As the load point is moved closer to a support, shear strains should prevail and the displacement to failure is quite low, around the beam thickness for beam 3. Hence, although the static case is easier to study, it challenges the correct prediction of the displacement to failure.

The beams were intentionally tested in a such way that they can fail by

**Table 7.2:** Comparison between measured and calculated shear and axial strains on the face side of the impact point of some beams.

Beam	$\gamma_{xz}$				$\epsilon_{eq}$			
	exp.	eq.(6.37)	error (%)	st.dev.	exp.	eq.(6.61)	error (%)	st.dev.
16	0.79	1.07	35	0.02				
17	0.91	0.99	8	0.14				
27	1.03	1.09	6	1 datum				
21					0.87	0.85	3	0.12
22					0.91	0.84	9	0.06



shear, case of beam 3, by a more predominant action of membrane strains, case of beam 4, by strains due to the moment, beam 2, and, finally, by an interplay of shear and axial strains, as in beam 1.

### 7.3.2 Static failure prediction

The simplest way to apply the CDM to predict failure in beams, is to employ the elastic, perfectly-plastic version of it, equation (5.2), repeated here for convenience,

$$D = \frac{\sigma_0^2 R_\nu}{2E\bar{S}} (\varepsilon_{eq} - \varepsilon_D). \quad (7.2)$$

Beam 4 was loaded centrally by a round tup. It is assumed that the transverse shear displacement is negligible. In this case, the equivalent strain comes from equation (6.61), which is substituted into equation (7.2) to render the damage evolution as

$$D = \frac{\sigma_0^2 R_\nu}{2E\bar{S}} [h^2 w(3 + 2w) - \varepsilon_D]. \quad (7.3)$$

This equation states that the damage evolves with the square of the beam displacement. Theoretically, the displacement increases up to  $D = D_{cr}$ , when failure then occurs.

The parameters  $E = 209.8\text{GPa}$  and  $\nu = 0.287$  in equation (7.3) are listed on Table 2.3,  $\varepsilon_D = 0.17$  was determined in section 4.6 and  $\bar{S} = 2.2\text{MPa}$  in section 5.3.

The triaxiality, necessary in the calculation of  $R_\nu$ , is, in theory, equal to one-third since the beam is a unidimensional structure. But for high values of strain, a localised non-uniform region breaks down the beam uniformity, increasing the hydrostatic stress. This is a difficult parameter to evaluate and, hereafter, it will be assumed that the triaxiality is  $\sigma_h/\sigma_{eq} = 1/2$ . This value was found in tensile specimens, which exhibits a smooth transition between the straight and necked region, qualitatively similar to what takes place on the beams. As one basic assumption underlying equation (7.2) is that the load is proportional, the triaxiality assumes a constant value, independent of the strain state.

The flow stresses  $\sigma_{00}$  and  $\sigma_0$  were set equal the yield and ultimate stresses of the mild steel, ie  $330\text{MPa}$  and  $600\text{MPa}$ , respectively, according to Table 2.3 on page 31. This initial flow stress is of use in the hardening damage model.

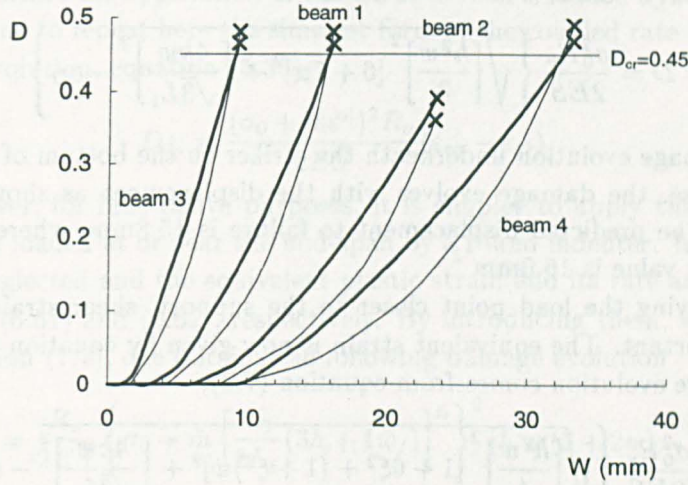


**Figure 7.6:** Damage evolution at the most critical part of beams loaded statically. Thin and thick lines represent the linear hardening and perfectly plastic model, respectively. The crosses mark the actual beam failure and the continuous horizontal line define the static critical damage.

Using now equation (7.3), the damage underneath the striker at the bottom of the beam 4 evolves with the displacement as depicted in Figure 7.6. It can be seen that the critical damage is achieved for a displacement of 32.7mm, to be compared with the measured displacement to failure of 33.2mm.

For beam 2, loaded at the middle ( $\xi = 1$ ), the indenter with sharp edges induces shear strains, which have to be taken into account. The equivalent strain for this case comes from equation (6.63), to be introduced into equation (7.2) to yield the damage evolution as

$$D = \frac{\sigma_0^2 R_v}{2ES} \left\{ \sqrt{\left[ \frac{h^2 w}{2} \right]^2 [6 + 7w]^2 + \left[ \frac{4kw}{\sqrt{3}L_1} \right]^2} - \varepsilon_D \right\}. \quad (7.4)$$

Accordingly, the predicted damage evolution underneath the striker at the bottom of beam2, when using the same material parameters as before, is shown in Figure 7.6. The calculated displacement to failure is 25.1mm, to be compared with the experimental value of 23.5mm.

Beam 1 was loaded at  $L_1 = 25.5$  by the sharp indenter. The equivalent strain is again equation (6.63), the same as for beam 2, except that now

$\xi = 1/3$ . Applying equation (6.63) in equation (7.2), one has

$$D = \frac{\sigma_0^2 R_\nu}{2ES} \left\{ \sqrt{\left[ \frac{h^2 w}{3} \right]^2 [6 + 7w]^2 + \left[ \frac{4kw}{\sqrt{3}L_1} \right]^2} - \varepsilon_D \right\}, \quad (7.5)$$

as the damage evolution underneath the striker on the bottom of the beam. In this case, the damage evolves with the displacement as shown in Figure 7.6. The predicted displacement to failure is 15.8mm, whereas the experimental value is 16.0mm\*.

By moving the load point closer to the support, shear strains become more important. The equivalent strain is now given by equation (6.65) and the damage evolution comes from equation (7.2),

$$D = \frac{\sigma_0^2 R_\nu}{2ES} \left\{ \sqrt{\left[ \frac{h^2 w}{4} \right]^2 [1 + 6\xi^2 + (1 + \xi^2)w]^2 + \left[ \frac{4kw}{\sqrt{3}L_1} \right]^2} - \varepsilon_D \right\}. \quad (7.6)$$

The predicted displacement to failure is 9.0mm and the experimental value is 9.2mm.

The evolution of the damage parameter, according to the perfectly plastic model, at the bottom underneath the load point for all the four beams tested statically, is depicted in Figure 7.6. The same figure shows also the linear hardening model. In this case, equation (5.22) has to be used for the damage prediction but the plastic strains are the same, *ie* the ones used in equations (7.3) to (7.6).

## 7.4 Beam failure — Impact of a mass

### 7.4.1 Introduction

The drop of a heavy mass on a beam may cause severe deformations. By increasing the height of the drop mass, the impact position and velocity, or by changing the geometry of the tup, the beam may fail, in the sense that a crack is formed locally or throughout the whole cross-section. This section shows how the rate-dependent CDM can be used to predict at which conditions, *ie* tup geometry, impact point, impact energy, the beams fail.

\*This value, measured after the test, is smaller than  $W_f = 17.6mm$  measured from the load-displacement curve. This is attributed to spring-back effects and the fact that the load does not drop immediately to zero after the beam cracks or breaks. Further loading is necessary to effectively separate the two broken parts of the beam.

To facilitate the application of the CDM to beams loaded dynamically, it is opportune to repeat here the simplest form of the coupled rate-dependent damage evolution, equation (5.30),

$$D_{d_0} = \frac{(\sigma_0 + \bar{m}\bar{\epsilon}^{\bar{n}})^2 R_\nu}{2E\bar{S}} (\epsilon_{eq} - \epsilon_D). \quad (7.7)$$

Moreover, for illustrative purposes, it is simpler to apply this equation for a beam loaded at or near the mid-span by a round indenter. In this case, shear is neglected and the equivalent plastic strain and its rate are given by equations (6.61) and (6.62), respectively. By introducing them, with  $\xi = 1$ , into equation (7.7), one obtains the following damage evolution

$$D_{d_0} = \frac{R_\nu}{2E\bar{S}} \left\{ \sigma_0 + \bar{m} \left[ \frac{V_0}{2L_1} (3h + 4\bar{w}_f) \right]^{\bar{n}} \right\}^2 [h^2 w (3 + 2w) - \epsilon_D]. \quad (7.8)$$

In order to predict the damage throughout the beam response via equation (7.8), one needs to know the final beam displacement, obtained from the initial conditions of the problem. This knowledge of the final displacement is necessary for the evaluation of the equivalent strain rate and of the shear strain, when it is taken into account. This is all expected because the strain rate used is an average value. Hence, the final displacement of the beam needs to be known.

It is at this point that rigid-plastic analysis comes into play. Several solutions exist for the prediction of the final displacement of a beam, based on initial and boundary conditions.

For instance, for a clamped beam struck at its middle by a heavy mass, LIU and JONES<sup>136</sup> obtained the non-dimensional final displacement of the beam from

$$\bar{w}_f = \frac{h}{2} (\sqrt{1 + 4\lambda} - 1), \quad (7.9)$$

where

$$\lambda = \frac{GV_0^2 L_1}{2BH^3 \sigma_0}. \quad (7.10)$$

In passing, the non-dimensional energy,  $\lambda$ , can be used for other beam configurations provided the strike position is changed accordingly through  $L_1$ .

Alternatively, SHEN and JONES<sup>179</sup> and JONES<sup>99</sup> describe how the final displacement of low velocity impacted beams can be predicted using simple quasi-static methods.

**Table 7.3:** Material parameters used for the dynamic failure prediction.

$\sigma_0$	$\sigma_{00}$	$E'$	$E$	$\dot{S}$	$\nu$	$\varepsilon_D$	$\bar{m}$	$\bar{n}$	$D_{cr}$
(MPa)	(MPa)	(MPa)	(GPa)	(MPa)			(s)		
600	330	400	209.8	2.2	0.287	0.17	38.4	0.328	0.45

Nonetheless, it was decided that the final displacement used in equation (7.8) is the experimental value and not any predicted one. This holds for all the beams analysed. If theoretical values were used, it would not have been possible to actually assess the accuracy of CDM in predicting failure. Errors other than from the model here proposed would be incorporated.

The evolution of the damage underneath an impacted beam, below the point struck by a round tup, is forecast by equation (7.8). This equation is valid for a perfectly plastic material. Alternatively, it is possible to adopt a linear hardening material. In this case, the damage equation was deduced in Chapter 5, equation (5.25), and the strain and strain rate are the same equations (6.61) and (6.62), respectively.

For the other beams, struck at different positions by a sharp indenter, the damage equations are essentially the same, *ie* equations (5.25) and (5.30), for the linear hardening and perfectly plastic material, respectively. The difference between these beams struck by a sharp tup and the ones struck by a round tup is that, for the former, the shear strain contributes to the equivalent strain. The expressions for the equivalent strain when shear is taken into account, plus their range of validity, are listed on page 149.

The material parameters necessary to apply equations (5.25) and (5.30) were presented in the previous chapters for the mild steel used to make the beams and are summarised on Table 7.3.

### 7.4.2 Dynamic failure prediction

The experimental non-dimensional displacement to failure of the beams struck at the mid-span by a round tup is presented in Figure 7.7(a) and identified by crosses.

The solid circles represent the predicted non-dimensional displacement to failure when equation (7.3) is used together with the parameters listed on Table 7.3. In this case, no strain rate effects were considered.

The open circles were obtained from equation (7.8), which adds strain rate effects to the damage evolution.

**Table 7.4:** Comparison between measured and calculated displacement to failure and damage parameter of static beams.

Beam	Displacement (mm)			Max. error (%)	Critical Damage			Max. error(%)
	exp.	perf.pl.	lin.hard.		exp.	perf.pl.	lin.hard.	
1	16.0	15.8	15.7	1.9	0.45	0.46	0.48	6.7
2	23.5	25.1	25.0	6.8	0.45	0.39	0.36	20.0
3	9.2	9.0	9.0	2.2	0.45	0.46	0.48	6.7
4	33.2	32.7	32.4	2.4	0.45	0.47	0.49	8.9

The triangles are also a dynamic version of the damage equation but now with linear hardening included, according to equation (5.25). The strain and strain rate are given by equations (6.61) and (6.62), respectively.

Likewise, Figure 7.7(b) presents the experimental non-dimensional displacement to failure but for beams struck by a sharp indenter, with the restriction that the impact point is such that  $\xi \geq 1/5$ . The predicted static non-dimensional displacement to failure according to equation (7.4) is also shown in the figure, as well as the dynamic version, equation (5.25), with and without hardening included. The equivalent strain and its rate are given by expressions (6.63) and (6.64).

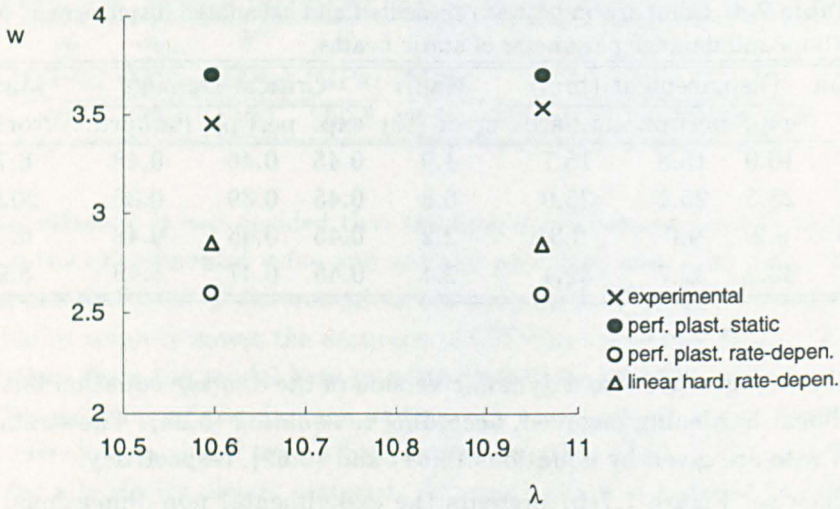
Figure 7.7(c) is as above but for the beams struck very close to the support. The equivalent strain is given by equation (6.65) and its rate by equation (6.66).

## 7.5 Discussion

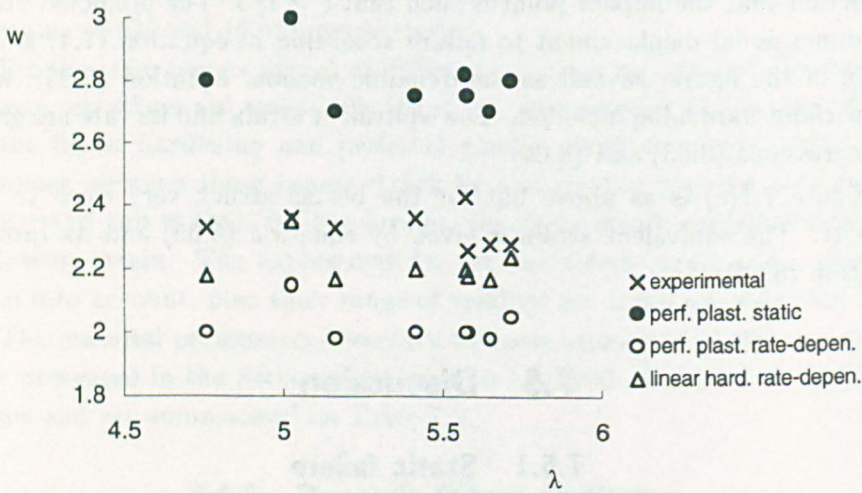
### 7.5.1 Static failure

The use of a simple failure criterion as the one derived from Continuum Damage Mechanics has shown a good capability of predicting failure in statically loaded beams. The main results shown in Figure 7.6 can be collected in Table 7.4.

In columns 7 and 8 on Table 7.4, the critical damages are those associated with the experimental displacement to failure. Hence, for beam 2, the predicted damage at failure, according to the linear hardening damage model, when  $W = 23.5\text{mm}$ , is 0.36, indicating that the beam was, in theory, able to displace further.

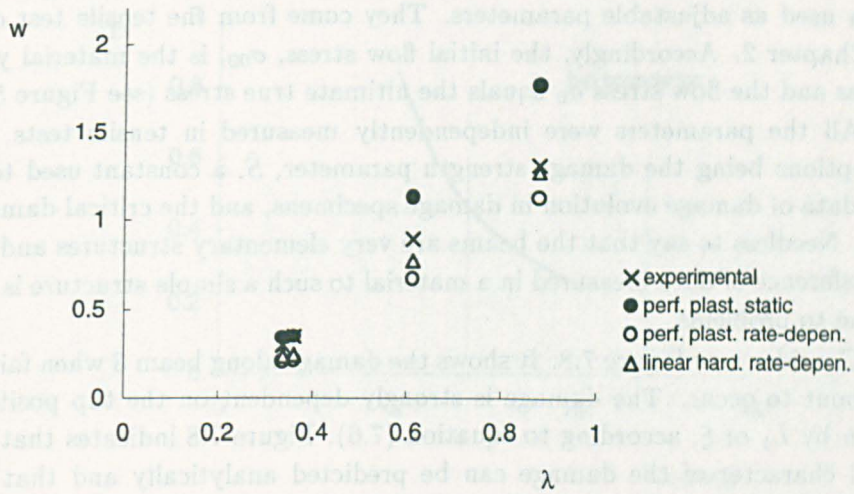


(a)



(b)

**Figure 7.7:** (a) Non-dimensional displacement *versus* non-dimensional impact energy for mild steel beams impacted at or near to the mid-span by a round tup. Solid circles, open circles and triangles are non-dimensional displacements associated with the perfectly plastic static damage model, the perfectly plastic rate-dependent damage model and the linear hardening rate-dependent damage model, respectively. Crosses are experimental data. (b) Same as in (a) but for a sharp indenter. (c) Same as in (b) but for  $\xi < 1/5$ . Only data from broken beams are shown.



(c)

Figure 7.7: —contd.

The critical damage of 0.36 for beam 2 yields the large error of 20% in the damage parameter, associated with an error of 6.8% of the displacement to failure. As Table 7.4 indicates, the error in the displacement to failure is smaller than the error in the critical damage for all the beams. This suggests that the displacement to failure of beams is not very sensitive to the actual critical damage.

Large errors in the critical damage parameter induces smaller errors on the displacement to failure of beams. This may explain why failure can be reasonable well predicted, as in references 47, 191, 209 and 110, yet not correcting the damage parameter for stress and strain non-uniformities, as described in Chapter 5 and in reference 2.

It is evident from Table 7.4 that the displacement to failure for the statically loaded beams is predicted with a good accuracy for all the beams. Both perfectly plastic and linear hardening models yield good results, lending support to these simple models.

The linear hardening model, though, predicts a different damage evolution, Figure 7.6. This is expected because this model adds non-linear displacement terms, as indicated in equation (5.22). It is difficult to infer from these two models how more accurate values of stress, strain and damage, as obtained numerically, would alter the damage evolution.



It is relevant to observe that the flow stresses in both models have not been used as adjustable parameters. They come from the tensile test data in Chapter 2. Accordingly, the initial flow stress,  $\sigma_{00}$ , is the material yield stress and the flow stress  $\sigma_0$  equals the ultimate true stress (see Figure 5.1).

All the parameters were independently measured in tensile tests, the exceptions being the damage strength parameter,  $\bar{S}$ , a constant used to fit the data of damage evolution in damage specimens, and the critical damage,  $D_{cr}$ . Needless to say that the beams are very elementary structures and the transference of data measured in a material to such a simple structure is less prone to problems.

Consider now Figure 7.8. It shows the damage along beam 3 when failure is about to occur. The damage is strongly dependent on the tup position, given by  $L_1$  or  $\xi$ , according to equation (7.6). Figure 7.8 indicates that the local character of the damage can be predicted analytically and that the measurement of the load position has to be done consistently. This strong influence of the load point position on the damage field is not so important for beams loaded towards their centre.

The same ideas are valid for the dynamically loaded beams. For off-centre loads, numerical results from YU and JONES<sup>216,217</sup> suggest that the edge of the tup nearer to the support tends to induce more severe strains. Hence, for all the calculations, with  $\xi \leq 1/5$ ,  $L_1$  measures the distance from the support to the nearest tup edge. This parameter is difficult to predict before an impact test since, due to the clearance in an impact rig, it is not easy to ensure that the tup strikes the beam exactly at a pre-defined position. Accordingly, the load point was measured after the tests with reference to the reference frame of the initial configuration.

### 7.5.2 Dynamic failure

The main results for the prediction of the failure in the impacted beams were shown in Figure 7.7.

It is possible, in principle, to disregard any strain rate effect on the material behaviour. To this end, one has to employ equations (7.3) to (7.6) for the prediction of the damage evolution, when hardening is not considered\*. By doing so, one forecasts that the non-dimensional displacement to failure for all the beams is higher than the actual ones. This is shown by compar-

---

\*The consideration of hardening alters the predicted displacement to failure by a factor smaller than 1% when compared to the perfectly plastic model, static case.

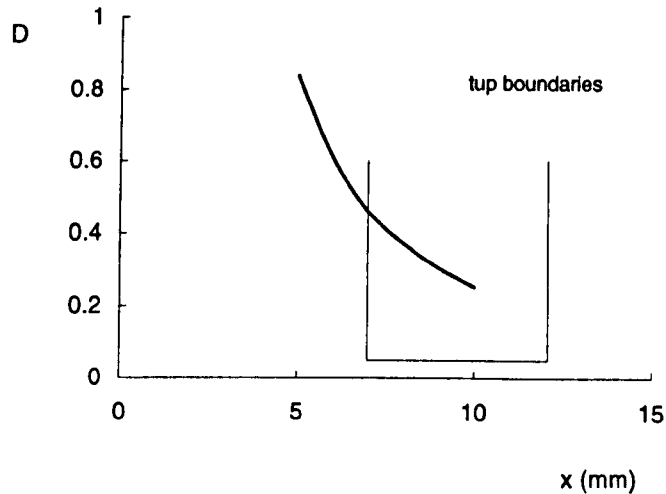


**Figure 7.8:** Damage profile at the load region along beam 3 when it is about to fail.  $x = 0$  locates the clamped support.

ing the solid circles, associated with the perfectly plastic model in Figures 7.7(a), (b) and (c) with the experimental data represented by crosses.

If the predicted displacement is higher than the actual one, it means that the predicted damage at the actual failure point is lower than the critical one, allowing the beam to displace further, as the solid circles in Figure 7.9 show. There, the predicted damage at the instant of the actual failure, for all the broken beams, is plotted against the non-dimensional input energy. It is evident that the damage yielded by the perfectly plastic static model does not reach its critical value, except for beams 15 and 16 (see Table 7.1).

The importance of the *static* tests on the beams is now clear. The displacement to failure was reasonably well predicted in the static case, according to Table 7.4. The poorer prediction in the dynamic case, according to the non-rate-dependent CDM model, suggests to take into account strain rate effects on the damage evolution.

Indeed, the rate-dependent formulation developed in Chapter 5 and applied according to section 7.4, yields, in general, a better prediction of the displacement to failure of the dynamically loaded beams, as shown in Figure 7.7(a)–(c). This is particularly true for the rate-dependent hardening model applied to the beams impacted by the sharp tup. The reason is that,

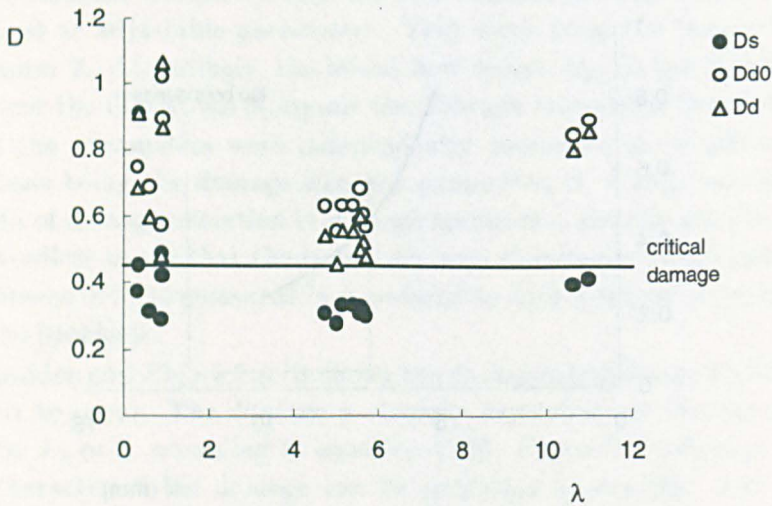


**Figure 7.9:** Predicted damage *versus* non-dimensional impact energy for mild steel beams at the instant of failure. Solid circles, open circles and triangles are the damage associated with the perfectly plastic, the rate-dependent perfectly plastic and the rate-dependent linear hardening damage models, respectively. Only data from broken beams are shown.

in this model, the material behaviour is better described.

The prediction of the perfectly plastic models could be improved by altering the flow stress. However, such a procedure would preclude one to correctly judge CDM capabilities of failure prediction.

The theoretical damage according to the rate-dependent model, represented by the open symbols in Figure 7.9, always exhibit a value for the damage higher than the critical one. According to this, the beams are allowed to displace further than they actually did. For beams impacted by the sharp tup, this extra displacement is marginal, Figure 7.7(b)–(c). For the round tup case, though, the predicted displacement according to the static model is closer to the actual one, indicating a poor performance of the dynamic model.

The linear hardening, rate-dependent model shows that strain rate effects cooperate substantially with the damage evolution. This is shown in Figure 7.10, where the total damage was split in its static, hardening and dynamic part, according to equation (5.26) on page 112, Chapter 5. The contribution of the strain rate is more important than the hardening.

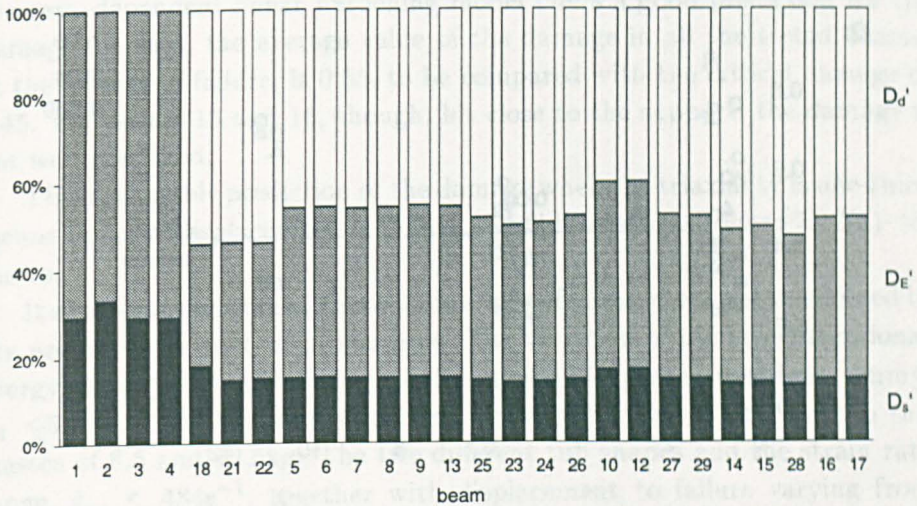


**Figure 7.10:** Partition of the damage parameter for mild steel beams at the instant of failure. The damage is split in its static,  $D_s'$ , hardening,  $D_E'$ , and dynamic,  $D_d'$ , parts, according to equation (5.26). Beams 1, 2, 3 and 4 were tested statically ( $D_d' = 0$ ).

The relative large error on the forecast critical damages, Figure 7.9, affects the prediction of the displacement to failure. However, this error is not imparted to the displacement to failure straightforwardly, as already indicated in Table 7.4. An extreme example is for the beams impacted closer to the support. In this case, the non-dimensional energy,  $\lambda$ , is less than one and the damage is poorly predicted by the rate-dependent model, Figure 7.9. Even so, the non-dimensional displacement to failure was predicted within a reasonable error, Figure 7.7(c).

Table 7.1 also lists the non-broken beams and the associated calculated damage. They are beams 18, 7, 26, 10, 12, 29. According to the rate-dependent linear hardening model, beams 7, 18, 26 and 29 were expected to fail because the damage is larger than the critical one. This is a wrong prediction since these beams did not fail at all.

### 7.5.3 Triaxiality

The damage rate equation was integrated in Chapter 5 under the assumption that the load is proportional. In this load regime, the triaxiality is constant throughout the structural response, facilitating the integration of equation (5.17).

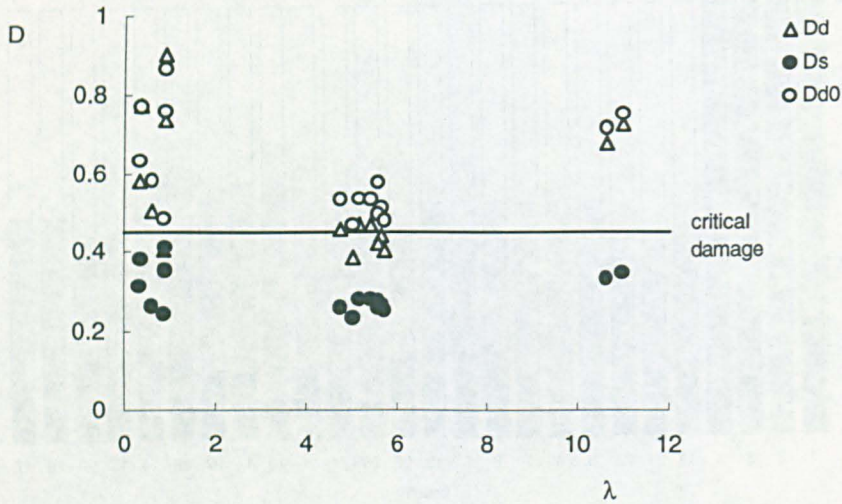


**Figure 7.11:** Predicted damage *versus* non-dimensional impact energy for mild steel beams at the instant of failure. Solid circles, open circles and triangles are the damage associated with the perfectly plastic, the rate-dependent perfectly plastic and the rate-dependent linear hardening damage models, respectively. Only data from broken beams are shown. The triaxiality value is  $1/3$ .

In experimenting with the beams, it was observed that the failure region for beams loaded towards the centre and whose failure mode was by necking, exhibited a curved profile similar to the one found in tensile specimens. Because the maximum triaxiality in the tensile tests was about one-half, it was assumed that this value holds good for the beams. Nevertheless, this assumption is not supported by any further data, except for the good failure prediction in the static case, when  $\sigma_h/\sigma_{eq} = 1/2$  was also used.

By noting that quite a few beams broke at an angle and not by necking, it is instructive to consider a value for triaxiality as found in uni-dimensional structures before entering in the softening regime, *ie* one-third. This value reduces the parameter  $R_\nu$  in equation (7.2) from 1.18 to 1.00. Now, equations (5.20) to (5.30), starting on page 110, are all linearly proportional to  $R_\nu$ , meaning that Figure 7.9 can be immediately replotted, as shown in Figure 7.11.

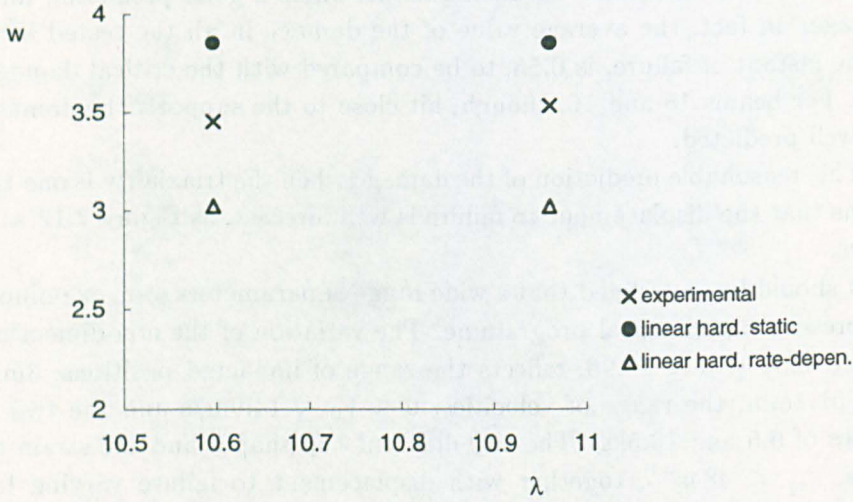
The static model in Figure 7.11 predicts that no failure at all occurs for all the beams, contradicting experimental evidences. On the other hand,

the rate-dependent linear hardening model offers a good prediction for the damage. In fact, the average value of the damage in all the tested beams, at the instant of failure, is 0.55, to be compared with the critical damage of 0.45. For beams 15 and 16, though, hit close to the support, the damage is not well predicted.

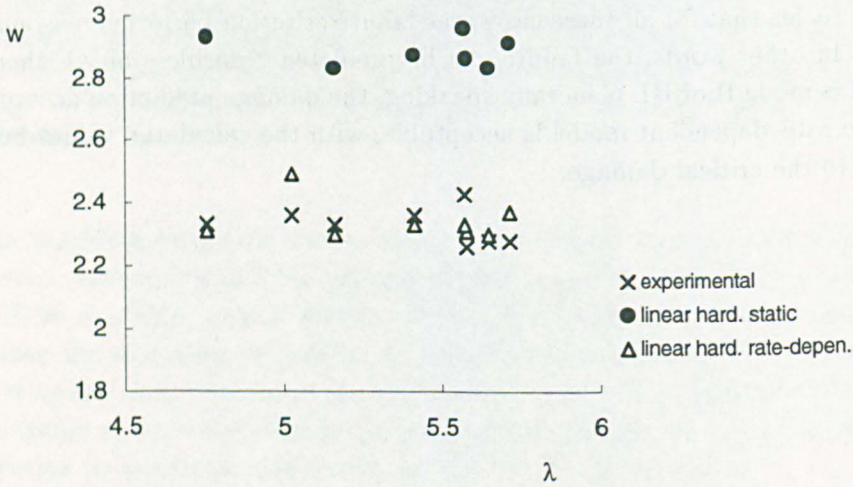
This reasonable prediction of the damage when the triaxiality is one-third means that the displacement to failure is well forecast, as Figure 7.12(a)-(c) shows.

It should be underlined that a wide range of parameters were examined in the present experimental programme. The variation of the non-dimensional energy,  $0.34 \leq \lambda \leq 10.96$ , reflects the range of impacted positions,  $3\text{mm} \leq L_1 \leq 51.1\text{mm}$ , the range of velocities,  $0 \leq V_0 \leq 14.9\text{m/s}$  and the two tup masses of 6.5 and 19.5kg. The two different tup shapes and the strain rate range,  $\dot{\epsilon}_{eq} \leq 484\text{s}^{-1}$ , together with displacement to failure varying from 2.6mm to 33.2mm promote a good start for assessing the capability of the CDM and of the rate-dependent model in predicting failure.

It seems that for all these cases, the failure criterion performs reasonably well. In other words, the failure can be predicted regardless of whether or not it is mode II or III. Generally speaking, the damage prediction according to the rate-dependent model is acceptable, with the calculated values being close to the critical damage.

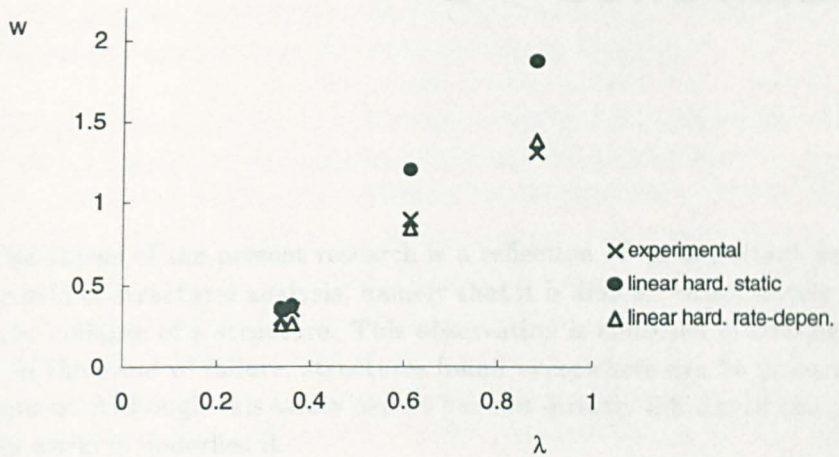


(a)



(b)

**Figure 7.12:** (a) Non-dimensional displacement *versus* non-dimensional impact energy for mild steel beams impacted around the mid-span by a round tup. Solid circles, open circles and triangles are non-dimensional displacements associated with the linear hardening static damage model, the perfectly plastic rate-dependent damage model and the linear hardening rate-dependent damage model, respectively. Crosses are experimental data. The triaxiality is one third. (b) Same as in (a) but for a sharp indenter. (c) Same as in (b) but for  $\xi < 1/5$ . Only data from broken beams are shown.



(c)

Figure 7.12: —contd.





---

## 8 Conclusions

The status of the present research is a reflection of an important aspect of the field of structural analysis, namely that it is difficult to accurately predict the collapse of a structure. This observation is endorsed in considering that, in the event of failure, structures found everywhere can be potentially dangerous. Although this safety aspect has not directly influenced the goals of this work, it underlies it.

Among the various attempts used to predict structural failure, the Continuum Damage Mechanics, CDM, was chosen because it was felt that it could be used in conjunction with the rigid-plastic methods of analysis. The simplicity of this union is reflected in the present work.

This last chapter intends to give a global view of the present work, the main results and contribution achieved and to suggest guidelines for future research in the field of CDM.

### 8.1 Tensile tests

At the outset of this research, it was believed that an equivalent stress-strain curve was required in dealing with failure, since failure occurs usually at high levels of plastic strain. Such an equivalent stress-strain curve demanded that the radius in the necking region be measured under dynamic conditions, a feature that was not found elsewhere.

One conclusion of these experiments is the expected result that the dynamic equivalent stresses between ultimate and failure strain follow a linear profile. The maximum equivalent stress in the various dynamic tensile tests was measured. This stress was defined as the failure stress, in contrast with the true fracture stress, *ie* fracture load divided by the final area, and the equivalent fracture stress, *ie* the fracture stress corrected for triaxial effects. It was found that the failure stress is 8% smaller than the true fracture stress and 8% higher than the equivalent fracture stress, Figure 2.17 on page 37.

This result indicates that the procedure of measuring the necking radius

after a tensile test, which aims to take into account triaxial effects, leads to the some sort of error as if no correction was attempted. The only difference is that, with and without corrections, the stresses will lie below and above the actual equivalent failure stress, respectively.

The failure strain is slightly smaller than the fracture strain, Figure 2.14 on page 35. Both strains are not strain rate dependent, which is an interesting feature of this material. It can be useful in considering that the critical damage parameter under dynamic conditions is likely to be also strain rate insensitive, a point to be discussed in sequence.

The measurement of the strain rate in the necking region reveals a fast increase of the strain rate in the softening regime. This increase of more than one order of magnitude poses an interesting test for a constitutive law. At least for the COWPER-SYMONDS equation, this strain rate behaviour makes the coefficients  $C$  and  $q$  to be strongly strain dependent. When such a constitutive law is used in a structure under a proportional loading regime and until failure, the non consideration of this dependence, as it is usually the case due to the lack of stress-strain-strain rate data beyond the ultimate strain, implies a large error in the stress prediction, as Figure 2.20 on page 40 indicates.

If, on one hand, this error in the stress prediction is very large, on the other hand, it does not necessarily mean a poor prediction of the structural response. For instance, YU and JONES<sup>216</sup> have simulated impacted beams using true stress-strain data and keeping the COWPER-SYMONDS coefficients constant. They obtained a very good agreement between the simulation and experiments for the global beam response.

An accurate stress-strain-strain rate relation was also not necessary in a TAYLOR test simulation by ZERILLI and ARMSTRONG.<sup>220,221</sup> The strain rates were as large as  $100000\text{s}^{-1}$ , but the constitutive equation used was based on data obtained at strain rates below  $1000\text{s}^{-1}$ . Certainly, the material behaviour in the simulation is different from the one inferred by mere extrapolation of the constitutive equation.<sup>80</sup> Even so, the macroscopic response of the test specimen was well predicted in terms of the global behaviour.

## 8.2 Notch tensile tests

The results found in Chapter 3 seemed all contradictory with the common belief that the triaxiality governs failure. As a matter of fact, the initial idea

of testing notched specimens was that they could be used to quantitatively assess the influence of the triaxiality on the failure strain. From these tests, a failure envelope curve could be used as a failure criterion.

However, it was found that the failure site for some specimens was not at the maximum triaxiality, it was located, rather, at the minimum. This finding offers a tough test for a failure criterion, namely to forecast failure sites at low levels of triaxiality.

An increase of the average strain rate in the necking of notched specimens was measured. A numerical simulation of these dynamic tests would be very instructive. It would be possible, for instance, to assess the accuracy of constitutive laws since these notch tests, differently from the beam tests, exhibited a continuous increase of the strain rate, all the way to failure. Therefore, a constitutive law has to be able to predict stresses in the softening regime, at high levels of plastic strain and strain rates. It is possible then to investigate how the prediction would be affected by keeping the parameters  $C$  and  $q$  of the COWPER-SYMONDS equation constants.

Another reason for experimenting with notched specimens was to know whether the plastic strain associated with the maximum load would be dependent on the stress state and on the strain rate. As Figure 3.7 on page 57 shows, it was found that this threshold strain is neither stress nor strain rate dependent, a welcome result when considering its use in the CDM analytical model.

The range of triaxiality one obtains by using initial notch radius ranging from 0.42mm to 4.21mm is not as large as the BRIDGMAN analysis suggests. Accordingly, BRIDGMAN analysis forecast a range of triaxialities from 0.60 to 1.87, Table 3.1, whereas this range is restricted to 0.6 to 1.0, according to the Finite-Element results in Figure 3.16 on page 67.

Moreover, it was shown that the traditional failure envelope curves, exhibiting a marked decrease of the failure strain with the increase of the triaxiality, cannot be obtained from the notched tests of the present material. The ultimately reason is that failure occurred at low levels of triaxiality.

These comments emphasise that notch tests are not suitable for inferring failure curves of the mild steel used here. They turned out to be useful, though, as much as they offer an important test for a failure criterion, namely to predict the failure site in regions of low triaxiality.

### 8.3 Material damage

Chapter 4 presented various techniques to measure the damage parameter. The striking result is that the value of the damage is dependent of the experimental technique. This finding is relevant in considering that theoretical CDM models do not distinguish among the various damage definitions presented in Chapter 4.

Taking, for instance, the common damage model presented in the Appendix A, one can see that damage is defined and used in a broad sense. Suppose now that the displacement to failure in Chapter 7 was to be predicted using as the critical damage the one based on the void area. Certainly the results would be far off from the experimental ones. On the other hand, a damage definition yielded by a different relation between the effective and equivalent stress spaces, as in CORDEBOIS and SIDOROFF's,<sup>49</sup> does lead to another damage model. Hence, it is difficult to compare critical damage values. This only underlies the fact that the variable damage used in CDM is not a specific material constant; it is rather a parameter which depends upon its definition.

The experimental procedures used in Chapter 4 were drawn from the literature. Some of them are not suitable for the present material. The measure of damage using hardness, in particular, was found to be suitable for an aluminium alloy, Figure 4.4, but not for the mild steel used in the present experimental programme. This is to put in contrast with the work of BILLARDON *et al.*,<sup>21</sup> who obtained good results using this technique in a mild steel, even comparable with the change in the elastic modulus.

A deficiency of the measure of the damage via the void area is worthy of comment.

Suppose that the magnification of the microscope is set to some value and used to measure the area of voids. The damage will be the ratio between voids area and area in the field of vision, according to equation (4.1). Suppose now that the magnification is increased by two. The damage is still defined by the same area ratio. However, the area of voids has increased and the field of vision decreased, with the net result of an increase in the damage. The conclusion is that the damage as measured by voids area is dependent of the magnification, which can bring its value as close as the one signalled by the change of elastic modulus.

It seems that this undesirable situation deserves further studies. In the present tests, the magnification was chosen to be 100 because this allowed

a field of vision where a set of voids could be seen, being thought that this would give a better average value of the damage parameter. A technique yielding a good description of the damage, understood as voids, needs to be developed, perhaps relying on statistics.

As already commented, the experimental data in Chapters 2, 3 and 4 indicate that the threshold strain beyond which damage starts,  $\varepsilon_D$ , is not strain rate and/or stress dependent. This is important because it allows the integration of the damage equation in a closed form. However, this finding of a constant threshold strain is in contrast with theoretical arguments of LEMAITRE,<sup>126</sup> who introduces a more general accumulate plastic strain threshold.

The results of this work do not suggest an important influence of the stress field on the damage parameter, Figure 4.22 on page 102. The failure criterion becomes elementary, *ie* failure starts when  $D = D_{cr}$ , irrespective of the stress field. Of course, this cannot be considered a general finding, bearing in mind that only one material was tested. LEMAITRE,<sup>126</sup> on the other hand, proposes a decrease of the critical damage with an increase of the triaxiality.

The measure of the damage from the change in elastic modulus is not as straightforward as it seems. Whatever specimen geometry used, localisation always takes place for ductile materials, changing significantly the stress and strain field in the region where damage is being monitored. This calls for a correction factor, in the spirit of reference 2. If such a correction factor is not used, the critical damage parameter may be in considerable error, affecting the failure prediction.

Further studies are necessary in order to understand how the critical damage value affects the failure prediction. Note that different failure parameters can be chosen according to the structure. It can be internal pressure in a pressure vessel, the displacement in a beam, the impact velocity in a plate, and so on.

## 8.4 Strain rate influence on the damage parameter

CDM was applied in Chapter 7 to predict failure in statically and impacted loaded beams. The only difference of the CDM in these two cases was the consideration of strain rate effects on the stresses. However, it would be interesting to know whether strain rate affects the damage parameter.

Generally speaking, the damage parameter should be influenced by the strain rate. This is most evident in considering that, for quite a few materials, the strain rate affects the failure strain. Fortunately, this is not the case for the mild steel used in the present experimental programme, Figure 2.14, which lends support for the use of a strain rate independent critical damage parameter.

It is difficult to measure the influence of the strain rate effect on the damage. If the damage is obtained by the change of the elastic modulus, it is necessary to measure this last parameter under dynamic conditions. HOPKINSON bar tests are not suitable because it is intrinsic to this technique that data in the elastic region of the material behaviour are not accurate.

The ordinary dynamic tensile test can be used to measure an initial dynamic elastic modulus. However, such a procedure needs special care because of the difficulties involved in the measurement of the load. The use of head gauges might be seen as an alternative to load cells but it is difficult to determine an accurate calibration factor valid for the very beginning of the tests. Moreover, the measurement of the dynamic elastic modulus at different levels of plastic strain requires the tests to be interrupted under dynamic conditions, which is also difficult. Above all, the geometry of the damage specimen will lead to a complicated interaction of elastic waves and it is possible that an elastic modulus measured under dynamic conditions is, in fact, another stress-strain ratio to add to the ones listed on page 84.

The measurement of a dynamic damage parameter is a challenge and a point worthy of further research.

## 8.5 Effective stress

The effective stress,  $\tilde{\sigma}$ , was defined in Chapter 4 as the stress acting over the net material area, *ie* when the voids area,  $S_D$ , is subtracted from the nominal area,  $S$ . This stress definition is related to the true stress,  $\sigma$ , by

$$\tilde{\sigma} = \frac{\sigma}{1 - D_S}, \quad (8.1)$$

Because the critical damage,  $D_{S_{cr}} = 0.7\%$ , is quite small for the mild steel used here, the effective stress space is nearly coincident with the true stress space. This does not hold true, though, if the voids induce severe stress concentrations in the material.

In Chapter 5, the effective stress space was taken to be the equivalent stress space via equation (5.23). This could be thought a valid procedure in face of the low value of void area. Underlying this interchange of stress definitions is LEMAITRE's hypothesis of strain equivalence, stated on page 76. This hypothesis allows to replace the stresses in a damaged material by the effective stress, so deriving the material behaviour law according to Appendix A.

Nonetheless, it is noteworthy that LEMAITRE's hypothesis implies a common value for the damage measured by either void area or by the change of the elastic modulus, equation (4.7). Clearly, this is not a valid result for quite a few materials, as Table 4.4 on page 103 shows.

This paradox does not seem easy to be understood and overcome. Other hypothesis relating stress spaces may be of use, as CORDEBOIS and SIDOROFF's,<sup>49</sup> but they should be corroborated by direct experiments. Such a difficult task and its relevance points towards further studies.

## 8.6 Flow stress

The flow stress plays an important role in the damage evolution, as expected. In rigid-plastic models, it can be seen as an adjustable parameter to construct upper and lower bounds for certain solutions. But the aim here was not to use the flow stress as such. Rather, it was kept constant in the static case and allowed to increase only due to strain rate effects in the dynamic case, according to the material constitutive law developed in Chapter 2, equation (2.17).

The adopted initial static flow stress,  $\sigma_{00} = 330\text{MPa}$ , and the hardening modulus of  $E' = 400\text{MPa}$  for the failure prediction in Chapter 7 are material parameters measured in tensile tests. They are requested by the rate-dependent hardening damage model and have not been adjusted in order to improve the prediction. For the perfectly plastic model, a flow stress of  $\sigma_0 = 600\text{MPa}$  was used. This flow stress coincides with the ultimate stress for the mild steel but can be considered a parameter adjusted at will to improve the prediction. Again, for the linear hardening model, the input material parameters were not adjusted whatsoever; they were all measured independently.

If one now returns to Figure 7.2, on page 153, it will see a theoretical load-displacement curve matching fairly well the experimental one, for



beams loaded towards the centre. The prediction is due to HAYTHORNTHWAITE,<sup>84</sup> rendered as

$$F = \frac{4M_0}{L} \left\{ 1 + \left( \frac{W}{H} \right)^2 \right\}, \quad 0 \leq W/H \leq 1, \quad (8.2)$$

$$F = \frac{8M_0}{L} \frac{W}{H}, \quad W/H \geq 1,$$

where  $F$  is the load,  $W$  is the displacement at the point load,  $H$  and  $L$  are the thickness and the length of the beam, respectively, and  $M_0$  is the collapse moment given by

$$M_0 = \frac{s_0 B H^2}{4}. \quad (8.3)$$

The *engineering flow stress*,  $s_0$ , used in the collapse moment, equation (8.3), was set equal to 400MPa in order to match the experimental data presented in Figure 7.2. This flow stress is different from the flow stress used in the damage equations, *ie*  $\sigma_0 = 600\text{MPa}$ , which emphasises the difference in the stress spaces used by CDM and by the above solution. In the case of the HAYTHORNTHWAITE's solution,<sup>84</sup> the stress space is the engineering one, whereas CDM works basically on a true stress-strain space.

## 8.7 Is CDM a strain criterion?

Chapter 3 has shown that the triaxiality does not rule the failure site. The region where failure will occur in notched specimens can be well predicted by the CDM, as shown in Chapter 5, Figure 5.4 on page 117. The failure site is associated with high values of equivalent strain, which poses the question of what is the failure criterion. Is failure predicted when the damage variable achieves its critical value or when the equivalent strain reaches some limit? Is the failure criterion yielded by Damage Mechanics a strain criterion?

The simplest damage model used to predict static failure in the beams is described by

$$D = \frac{\sigma_0^2 R_\nu}{2ES} (\varepsilon_{eq} - \varepsilon_D) \quad \text{for} \quad \varepsilon_{eq} \geq \varepsilon_D. \quad (8.4)$$

If the triaxiality is constant so is the parameter  $R_\nu$ , allowing to rewrite equation (8.4) as

$$D = a_1 \varepsilon_{eq} - a_2, \quad (8.5)$$

where

$$a_1 = \frac{\sigma_0^2 R_\nu}{2ES} \quad (8.6)$$

and

$$a_2 = \frac{\sigma_0^2 R_\nu}{2ES} \varepsilon_D \quad (8.7)$$

are constants.

Equation (8.5) states that the damage is linearly proportional to the equivalent plastic strain. The failure criterion can be set according to

$$\varepsilon_{eq_{cr}} = \frac{D_{cr} + a_2}{a_1}, \quad (8.8)$$

implying that CDM can be seen as a plastic strain criterion. This was already anticipated in Figure 5.3, on page 115, where a fixed value of the triaxiality yields a fixed value of the failure strain, when strain rate effects are not considered.

A close look on Table 7.1, page 154, shows that the calculated equivalent strain at failure is almost constant, as should be the case for the perfectly-plastic CDM model. This not only emphasises the importance of a good prediction of the strains but also supports the concept of the hinge length used in Chapter 6, in face of the good agreement between the predicted and experimental displacement to failure of the beams.

It is possible to treat CDM as a strain failure criterion only when simple stress-strain relations, as the perfect-plastic and bilinear ones, are used. However, the set of equations in Appendix A is more general. In the case of a more accurate description of the material behaviour, CDM fully resumes its character of being a stress-strain dependent failure criterion. If now, the rate-dependent model developed in Chapter 5 is added, then CDM becomes also a strain rate-dependent failure criterion.

The fact that the rate-dependent CDM yields a stress-strain-strain rate dependent failure criterion is important. It can be seen as an energetic failure criterion, thought to be a more universal failure criterion<sup>45</sup> and enjoying theoretical and numerical support.<sup>100, 216</sup>

## 8.8 Closure

It was demonstrated in this research that CDM can be used to predict failure in statically and dynamically loaded beams. Also, the use of CDM in a more

analytical basis has proved successful and deserves further work.

It is believed that CDM models, as the one here developed, can be applied to more complex loading regimes and to structures other than beams. A class of structural problems can be adapted to render CDM applicable. In these cases, the failure prediction becomes a more tenable issue and can be brought down to a reasonable level of applicability.

An accurate failure criterion for dynamically loaded structures needs to know in detail the stresses, strains and strain rates. Such a knowledge and the consideration of the damage on the global response of a structure are feasible tasks nowadays. Accordingly, the implementation of a rate-dependent damage model, like the one described in Chapter 5 and Appendix A, in a Finite-Element code is important. By so proceeding, one can infer how the damage and the strain rate simultaneously influence the global response of a structure.

To generalise the findings of this research to other materials might be risky. In this study, a wide range of strain rates and load conditions was investigated. Also, the large ductility of the mild steel and its strain rate sensitivity promoted a complex picture, successfully dealt with by CDM. One is then tempted to suggest that, for materials less strain rate sensitive and less ductile than the mild steel, CDM can be considered as a good candidate to predict failure in beams.

The rate-dependent damage model may be used to structures other than beams. The good correlation obtained for beams encourages further developments of the methodology to circular plates and cylindrical shells.

As stressed in Chapter 1, the literature extensively demonstrates the feasibility in using CDM together with numerical solution schemes. The fact that CDM suits an analytical approach, for both statically loaded and impacted structures, as here shown, is seen as a major contribution of the present research.

In closing, the Continuum Damage Mechanics is a feasible approach to analytically predict failure in beams subjected to impact loads. An improvement of the predictions is achieved by considering a dynamic version of it.

---

# Appendix

## A Fundamentals of Damage Mechanics

### A.1 Thermomechanics

The CDM has a relatively strong formalism thanks to the specialisation of thermodynamics laws to the mechanics of the continuum and to the use of concepts from plasticity.<sup>32,78,79</sup> Hence, the necessity of a brief background in thermomechanics.

The second law of thermodynamics may be written as<sup>128,226</sup>

$$\sigma_{ij}\dot{\varepsilon}_{ij} - \rho(\dot{\Psi} + \bar{s}\dot{T}) - q_i \frac{T_{,i}}{T} \geq 0, \quad (\text{A.1})$$

where  $\sigma_{ij}$  and  $\varepsilon_{ij}$  are the components of the stress and strain tensor,  $\rho$  is the density,  $T$  the temperature,  $q$  the heat flow and  $\bar{s}$  the entropy density.

$$\Psi = \bar{e} - T\bar{s}, \quad (\text{A.2})$$

is the specific free energy and  $\bar{e}$  is the specific internal energy. Equation (A.1) is known as the CLAUSIUS–DUHEM inequality. It can be transformed

to<sup>128</sup>

$$\left( \sigma_{ij} - \rho \frac{\partial \Psi}{\partial \varepsilon_{ij}^e} \right) \dot{\varepsilon}_{ij}^e + \sigma_{ij} \dot{\varepsilon}_{ij}^p - \rho \left( \bar{s} + \frac{\partial \Psi}{\partial T} \right) \dot{T} - \rho \frac{\partial \Psi}{\partial V_k} \dot{V}_k - q_i \frac{T_{,i}}{T} \geq 0, \quad (\text{A.3})$$

by noting that

$$\dot{\Psi} = \frac{\partial \Psi}{\partial \varepsilon_{ij}^e} \dot{\varepsilon}_{ij}^e + \frac{\partial \Psi}{\partial T} \dot{T} + \frac{\partial \Psi}{\partial V_k} \dot{V}_k, \quad (\text{A.4})$$

since

$$\Psi = \Psi(\varepsilon_{ij}^e, T, V_k). \quad (\text{A.5})$$

The superscripts <sup>e</sup> and <sup>p</sup> stand for elastic and plastic, respectively and  $V_k$  is any internal variable. The plastic strains can be related with the total and elastic strains through

$$\varepsilon_{ij} = \varepsilon_{ij}^e + \varepsilon_{ij}^p, \quad (\text{A.6})$$

implying that such additive property restricts the formalism to small deformations.<sup>140</sup> Even so, ductile damage, where large deformation may occur, is commonly treated within the small deformation frame and this rule will be here accepted, as already commented in Chapter 1.

From the CLAUSIUS–DUHEM inequality, equation (A.3), it is possible to imagine a phenomenon where the temperature is constant and uniform, and the plastic strain rates and internal variables do not change, yielding<sup>128</sup>

$$\sigma_{ij} = \rho \frac{\partial \Psi}{\partial \varepsilon_{ij}^e}, \quad (\text{A.7})$$

or

$$\sigma_{ij} = \rho \frac{\partial \Psi}{\partial \varepsilon_{ij}} = -\rho \frac{\partial \Psi}{\partial \varepsilon_{ij}^p}, \quad (\text{A.8})$$

in view of equation (A.6).

Similarly, the following relation holds

$$\bar{s} = -\frac{\partial \Psi}{\partial T}, \quad (\text{A.9})$$

and, by analogy, one can write

$$A_k = \rho \frac{\partial \Psi}{\partial V_k}, \quad (\text{A.10})$$

where  $A_k$  is a thermodynamic force.

Disregarding henceforth temperature effects, from above, the CLAUSIUS-DUHEM inequality reads

$$\Phi = \sigma_{ij} \dot{\varepsilon}_{ij}^p - A_k \dot{V}_k \geq 0. \quad (\text{A.11})$$

Introducing a potential of dissipation

$$\phi(\varepsilon_{ij}^p, \dot{V}_k), \quad (\text{A.12})$$

and writing the (normality) relations

$$\sigma_{ij} = \frac{\partial \phi}{\partial \varepsilon_{ij}^p} \quad (\text{A.13})$$

and

$$A_k = -\frac{\partial \phi}{\partial \dot{V}_k}, \quad (\text{A.14})$$

it can be shown that the following inverse relations hold:<sup>140</sup>

$$\varepsilon_{ij}^p = \frac{\partial \bar{\phi}}{\partial \sigma_{ij}}, \quad (\text{A.15})$$

$$-\dot{V}_k = \frac{\partial \bar{\phi}}{\partial A_k}, \quad (\text{A.16})$$

with  $\bar{\phi}$  being the corresponding dual potential of  $\phi$ .

Observe that the above equations are powerful in the sense that they satisfy the basic principles of thermodynamics equilibrium and that they can be used to infer the basic laws of plasticity. To this end, take the potential

$$\mathcal{F} = \mathcal{F}(\sigma_{ij}, \bar{R}, \varepsilon_{ij}^p, \bar{r}) + \mathcal{F}_D, \quad (\text{A.17})$$

where  $\bar{R}$  is the *thermodynamic force* associated with the parameter  $\bar{r}$  and representing the isotropic hardening, kinematic hardening not being considered.  $\mathcal{F}_D$  is a dissipative potential associated with damage. Now, in order to force the dissipation between two stable states to be a maximum,<sup>79</sup> the following relations must hold:

$$\dot{\varepsilon}_{ij}^p = \dot{\lambda} \frac{\partial \mathcal{F}}{\partial \sigma_{ij}}, \quad (\text{A.18})$$

$$\dot{r} = -\dot{\lambda} \frac{\partial \mathcal{F}}{\partial \bar{R}} \quad (\text{A.19})$$

and

$$\dot{D} = \dot{\lambda} \frac{\partial \mathcal{F}_D}{\partial Y}, \quad (\text{A.20})$$

where  $D$  is the damage and  $\bar{Y}$  its associate variable. The term  $\dot{\lambda}$  is a LAGRANGE multiplier.

The so called associated plasticity may be derived from the potential  $\mathcal{F}$  by setting  $\mathcal{F}_D$  to zero in equation (A.17). Accordingly, let

$$\mathcal{F} = f = \sigma_{eq} - \bar{R} - \sigma_y \quad (\text{A.21})$$

be the loading function where  $\sigma_y$  is the yielding stress. The equivalent VON MISES stress is

$$\sigma_{eq} = \sqrt{\frac{3}{2} \sigma'_{ij} \sigma'_{ij}}, \quad (\text{A.22})$$

with

$$\sigma'_{ij} = \sigma_{ij} - \frac{1}{3} \sigma_{kk} \delta_{ij} \quad (\text{A.23})$$

being the stress deviator ( $\delta_{ij} = 1$  if  $i = j$  and  $\delta_{ij} = 0$  if  $i \neq j$ ).

Plastic strains occurs only if  $f = 0$ . Moreover, the plastic strains grow if  $\dot{f} = 0$ , i.e.

$$\dot{\epsilon}^p_{ij} \neq 0 \quad \text{if} \quad \begin{cases} f = 0 \\ \text{and} \\ \dot{f} = 0 \end{cases}. \quad (\text{A.24})$$

It is this consistency condition that allows one to determine the multiplier  $\dot{\lambda}$  which, in the case of the non-damaged associated plasticity, is the equivalent plastic strain rate

$$\dot{\lambda} = \dot{\epsilon}_{eq} = \sqrt{\frac{3}{2} \dot{\epsilon}^p_{ij} \dot{\epsilon}^p_{ij}}. \quad (\text{A.25})$$

From equation (A.18), the plastic strain rate reads

$$\dot{\epsilon}_{ij} = \frac{3}{2} \frac{\sigma'_{ij}}{\sigma_{eq}} \dot{\epsilon}_{eq}, \quad (\text{A.26})$$

which is a well known standard form.

## A.2 Damage constitutive equations

The present formulation of the CDM is drawn mainly from LEMAITRE.<sup>126</sup>

Isotropic damage will be assumed throughout the following derivation, meaning identical behaviour in tension and compression, with no closure crack effect. Only isotropic linear hardening is taken into account though it is equally possible to consider other hardening laws as well as kinematic hardening. It is assumed that there is coupling between damage and the load function, which is not a strong restriction but simplifies the integration of the kinetic damage equation. Also, it is more realistic since damage does occur simultaneously with the change in the loading function. No temperature effect is considered<sup>50</sup> and lastly, the hypothesis of strain equivalence (see Chapter 4) is implicit in all the derivations.

Define the general potential of dissipation coupled with damage as

$$\mathcal{F} = \bar{\sigma}_{eq} - \bar{R} - \sigma_y + \mathcal{F}_D, \quad (\text{A.27})$$

or

$$\mathcal{F} = f + \mathcal{F}_D, \quad (\text{A.28})$$

with

$$f = \bar{\sigma}_{eq} - \bar{R} - \sigma_y \quad (\text{A.29})$$

and

$$\bar{\sigma}_{eq} = \frac{\sigma_{eq}}{1 - D} \quad (\text{A.30})$$

being the equivalent effective stress.

The plasticity condition,  $\dot{f} = 0$ , reads

$$\frac{\partial f}{\partial t} = \frac{\partial f}{\partial \sigma_{ij}} \dot{\sigma}_{ij} + \frac{\partial f}{\partial \bar{R}} \dot{\bar{R}} + \frac{\partial f}{\partial \sigma_y} \dot{\sigma}_y + \frac{\partial f}{\partial D} \dot{D} = 0. \quad (\text{A.31})$$

The various coefficients in this equation can be resolved as:

$$\frac{\partial f}{\partial \sigma_{ij}} = \frac{\partial \bar{\sigma}_{eq}}{\partial \sigma_{ij}} = \frac{3 \sigma'_{ij}}{2 \sigma_{eq}} \frac{1}{1 - D}, \quad (\text{A.32})$$

$$\frac{\partial f}{\partial D} = \frac{\partial \left( \frac{\sigma_{eq}}{1 - D} \right)}{\partial D} = \frac{3 \sigma'_{ij}}{2 \sigma_{eq}} \frac{\sigma'_{ij}}{(1 - D)^2} = \frac{\sigma_{eq}}{(1 - D)^2}, \quad (\text{A.33})$$



$$\frac{\partial f}{\partial \bar{R}} = -1 \quad \text{and} \quad \frac{\partial f}{\partial \sigma_y} = -1. \quad (\text{A.34})$$

Moreover, there exists a class of materials which harden isotropically and linearly with the plastic strains, as the data in Chapter 2 suggest.

By assuming a linear hardening law

$$\bar{R} = E' \bar{r}, \quad (\text{A.35})$$

where  $E'$  is the plastic modulus and  $\bar{r}$  is the associated variable to  $\bar{R}$ , it follows from equations (A.19) and (A.34) that

$$\dot{\bar{R}} = E' \dot{\lambda}. \quad (\text{A.36})$$

By introducing equations (A.20), (A.32) to (A.36) in equation (A.31), it is shown that the plastic multiplier reads<sup>126</sup>

$$\frac{\dot{\lambda}}{1-D} = \frac{\frac{3}{2} \frac{\sigma'_{ij}}{\sigma_{eq}} \frac{\dot{\sigma}'_{ij}}{(1-D)^2}}{E' - \frac{\sigma_{eq}}{(1-D)^2} \frac{\partial \mathcal{F}_p}{\partial Y}}, \quad (\text{A.37})$$

Now define the accumulated plastic strain  $p$  such that \*

$$\dot{p} = \sqrt{\frac{3}{2} \dot{\epsilon}_{ij}^p \dot{\epsilon}_{ij}^p}. \quad (\text{A.38})$$

The plastic strain rate, equation (A.18), is

$$\dot{\epsilon}_{ij}^p = \dot{\lambda} \frac{\partial \mathcal{F}}{\partial \sigma_{ij}} = \frac{3}{2} \frac{\sigma'_{ij}}{\sigma_{eq}} \frac{\dot{\lambda}}{1-D}, \quad (\text{A.39})$$

rendering equation (A.38) as

$$\dot{p} = \frac{\dot{\lambda}}{1-D}. \quad (\text{A.40})$$

Equations (A.39) and (A.40) give the plastic strain increment rate as

$$\dot{\epsilon}_{ij} = \frac{3}{2} \frac{\sigma'_{ij}}{\sigma_{eq}} \dot{p}. \quad (\text{A.41})$$

The set of damage elasto-visco-plastic equations is, finally, ( $\nu$  is the Poisson's ratio and  $E$  is the elastic modulus)

\*For proportional loading,  $\dot{p} = \dot{\epsilon}_{eq}$ .

- the strain relation

$$\varepsilon_{ij} = \varepsilon_{ij}^e + \varepsilon_{ij}^p, \quad (\text{A.42})$$

- the damage elastic stress-strain relation

$$\varepsilon_{ij}^e = \frac{1+\nu}{E} \tilde{\sigma}_{ij} - \frac{\nu}{E} \tilde{\sigma}_{kk} \delta_{ij}, \quad (\text{A.43})$$

- the plastic strain rate

$$\dot{\varepsilon}_{ij}^p = \frac{3}{2} \frac{\sigma'_{ij}}{\sigma_{eq}} \dot{p}, \quad (\text{A.44})$$

- the hardening rule

$$\bar{R} = E' \bar{r}, \quad (\text{A.45})$$

- the yield function

$$f = \tilde{\sigma}_{eq} - R - \sigma_y, \quad (\text{A.46})$$

- the damage growth

$$\dot{D} = \dot{\lambda} \frac{\partial \mathcal{F}_D}{\partial Y}, \quad (\text{A.47})$$

- the plastic multiplier

$$\frac{\dot{\lambda}}{1-D} = \dot{p} = \frac{\frac{3}{2} \frac{\sigma'_{ij}}{\sigma_{eq}} \frac{\dot{\sigma}'_{ij}}{(1-D)^2}}{E' - \frac{\sigma_{eq}}{(1-D)^2} \frac{\partial \mathcal{F}_D}{\partial Y}}, \quad (\text{A.48})$$

### A.3 Damage evolution

It was shown in section A.1 that the damage evolution is ruled by equation

$$\dot{D} = \dot{\lambda} \frac{\partial \mathcal{F}_D}{\partial Y}, \quad (\text{A.49})$$

where  $\bar{Y}$  is the associated variable. The physical meaning of  $\bar{Y}$  can be gained by noting that

$$\bar{Y} = \rho \frac{\partial \Psi}{\partial D} \quad (\text{A.50})$$

and

$$\sigma_{ij} = \rho \frac{\partial \Psi}{\partial \varepsilon_{ij}^e}. \quad (\text{A.51})$$

Adopting the specific free energy as

$$\Psi = \frac{1}{\rho} \left( \frac{1}{2} a_{ijkl} \varepsilon_{ij}^e \varepsilon_{kl}^e (1 - D) + \frac{1}{2} E' \bar{r}^2 \right), \quad (\text{A.52})$$

equations (A.50) and (A.51) give

$$\dot{Y} = -Y = -\frac{1}{2} a_{ijkl} \varepsilon_{ij}^e \varepsilon_{kl}^e \quad (\text{A.53})$$

and

$$\sigma_{ij} = (1 - D) a_{ijkl} \varepsilon_{kl}^e. \quad (\text{A.54})$$

By definition, the elastic strain energy density,  $w_e$ , is

$$w_e = \int \sigma_{ij} d\varepsilon_{ij}^e, \quad (\text{A.55})$$

rendering  $Y$  as

$$Y = \frac{w_e}{1 - D} \quad (\text{A.56})$$

when using equations (A.53) and (A.54).

It is possible to show that the following relation holds<sup>126</sup>

$$Y = \frac{1}{2} \frac{dw_e}{dD} \Bigg|_{\sigma=\text{const}}, \quad (\text{A.57})$$

giving the meaning to  $Y$  of a *elastic strain energy density release rate*.

Bearing in mind that the elastic stress and strain tensors can be split into deviatoric components,  $\sigma'_{ij}$ ,  $\varepsilon'_{ij}$ , and hydrostatic parts,  $\sigma_h$ ,  $\varepsilon_h$ , the isotropic elasticity law coupled with damage reads

$$\varepsilon_{ij}^{e'} = \frac{1 + \nu}{E} \frac{\sigma'_{ij}}{1 - D} \quad \text{and} \quad \varepsilon_h^e = \frac{1 - 2\nu}{E} \frac{\sigma_h}{1 - D}, \quad (\text{A.58})$$

from which the elastic strain energy density is

$$w_e = \int \sigma_{ij} d\varepsilon_{ij}^e = \int \sigma'_{ij} d\varepsilon_{ij}^{e'} + \delta_{ij} \delta_{ij} \int \sigma_h d\varepsilon_h, \quad (\text{A.59})$$

or

$$w_e = \frac{\sigma_{eq}^2}{2E(1-D)^2} \left\{ \frac{2}{3}(1+\nu) + 3(1-2\nu) \left( \frac{\sigma_h}{\sigma_{eq}} \right)^2 \right\}, \quad (\text{A.60})$$

when using the VON MISES equivalent stress definition, equation (A.22).

Finally, the strain energy density release rate may be written as<sup>126</sup>

$$Y = \frac{\tilde{\sigma}_{eq}^2 R_\nu}{2E}, \quad (\text{A.61})$$

with

$$R_\nu = \frac{2}{3}(1+\nu) + 3(1-2\nu) \left( \frac{\sigma_h}{\sigma_{eq}} \right)^2. \quad (\text{A.62})$$

To obtain the damage evolution it remains to define the potential  $\mathcal{F}_D$ . This potential is established according to micromechanics and phenomenological arguments. Also, the potential may be derived on more empirical base, aiming to simplify the damage kinetic equation, to add a non-linear behaviour to it or to model a more particular laboratory observation. A well known and used potential for ductile failure was proposed by LEMAITRE<sup>122-124</sup> in the form

$$\mathcal{F}_D = \frac{Y^2}{2\bar{S}(1-D)}, \quad (\text{A.63})$$

rendering the damage kinetic equation as

$$\dot{D} = \frac{Y}{\bar{S}} \dot{p} \bar{H}(p - p_D), \quad (\text{A.64})$$

or

$$\dot{D} = \frac{\tilde{\sigma}_{eq}^2 R_\nu}{2E\bar{S}} \dot{p} \bar{H}(p - p_D), \quad (\text{A.65})$$

where  $\bar{S}$  is a material constant and  $\bar{H}$  is the HEAVISIDE step function defined by

$$\bar{H}(p - p_D) = \begin{cases} 1 & \text{if } p \geq p_D \\ 0 & \text{if } p < p_D. \end{cases} \quad (\text{A.66})$$

The function  $\bar{H}$  just states that the damage rate is different from zero when the accumulated plastic strain becomes higher than a certain threshold strain,  $p_D$ . This strain in the uniaxial case is denoted by  $\varepsilon_D$ . The relation between  $p_D$  and  $\varepsilon_D$  is presented in Chapter 4.



---

# Nomenclature

- $a$  radius of the minimum cross-section  
in a notched specimen
- $A_k$  thermodynamic force
- $B_c$  load times correction factor,  $f_c$
- $C, q$  coefficients in the COWPER-SYMONDS equation
- $d$  diameter
- $disp$  displacement
- $D_d$  dynamic damage
- $D_{d'}$  dynamic contribution to the total damage
- $D_{d_0}$  dynamic damage based on the flow stress
- $D_l$  damage parameter measured by the change of elastic  
modulus without correction
- $D_s$  static damage based on the flow stress
- $D_{s'}$  static damage based on the initial flow stress
- $D_{E'}$  damage due to hardening
- $D_E^e$  damage according to the change in the elastic modulus  
based on the hypothesis of strain equivalence
- $D_E^W$  damage according to the change in the elastic modulus  
based on the hypothesis of energy equivalence
- $D_{HV}^e$  damage according to the hardness  
based on the hypothesis of strain equivalence
- $D_S$  damage according to the void area
- $D_V^e$  damage according to the change in the electrical potential  
based on the hypothesis of strain equivalence
- $e$  engineering strain
- $\bar{e}$  specific internal energy
- $e_m$  measured engineering strain
- $er_E$  error in the elastic modulus value
- $E$  elastic modulus
- $\bar{E}$  elastic modulus in the damaged material

$E'$	hardening modulus
$f$	yield function
$f_c$	correction factor
$f_d$	dynamic term in the yield function
$f_v$	volume fraction of inclusions
$F$	load
$F_f$	load near fracture
$\mathcal{F}$	general potential
$\mathcal{F}_D$	damage potential
$g_f$	gauge factor
$gl$	gauge length
$G$	impact mass
$h$	beam thickness divided by the length $L_1$
$H$	beam thickness
$H$	step function
$HV$	hardness
$HV'$	hardness in a virgin material
$i$	electrical current
$k$ and $k'$	constants
$k_t$	transverse sensitivity of the strain gauge
$l$	length
$L_1, L_2$	minimum and maximum distance between the load position and the beam supports, respectively
$l_{M_1}, l_{M_2}$	bending hinge lengths
$l_Q$	shear hinge length
$\bar{m}, \bar{n}$	coefficients in the material constitutive law
$m$	mass per unit length
$m$ and $n$	parameters used in the equivalent strain equation
$M$	moment
$p$	accumulated plastic strain
$p_D$	accumulated threshold plastic strain
$q$	heat flow
$Q$	shear force
$r$	coordinate
$\bar{r}$	associated variable to $\bar{R}$
$r_s$	resistivity
$R$	radius
$\bar{R}$	hardening term

---

$R_{cal}$	calibration resistance
$R_{sg}$	strain gauge resistance
$R_v$	defined by equation (5.6)
$s$	engineering stress
$s_f$	shape factor
$S$	area
$\bar{S}$	damage strength parameter
$S_D$	area of voids
$t$	time
$T$	temperature
$V$	voltage
$V_0$	impact velocity
$V_k$	internal variable
$w$	beam displacement divided by beam thickness
$w_e$	elastic strain energy density
$\bar{w}_f$	final displacement of the beam divided by the length $L_1$
$W$	beam displacement at the loading point
$W_f$	final beam displacement at the loading point
$W_{fL}$	final beam displacement at the loading point as measured by the laser
$W_s$	indentation
$W_{sf}$	final indentation
$x, y$ and $z$	rectangular coordinates
$Y$	elastic strain energy density release rate

### Greek symbols

$\gamma$	shear strain
$\varepsilon$	true strain
$\varepsilon_{body}$	strain measured by the diameter contraction outside the neck region
$\varepsilon_s$	longitudinal elastic strain
$\varepsilon_t$	thickness elastic contraction
$\varepsilon_w$	width elastic contraction
$\varepsilon_D$	threshold strain
$\varepsilon_{F_{max}}$	strain at the maximum load
$\varepsilon_M$	strain due to the moment



$\varepsilon_N$	membrane strain
$\theta$	angle
$\kappa$	curvature
$\lambda$	non-dimensional energy
$\dot{\lambda}$	plastic multiplier
$\nu$	Poisson ratio
$\nu_1, \nu_2$	$L_1/H, L_2/H$
$\xi$	$L_1/L_2$
$\Xi$	apparent elastic modulus
$\Xi_s$	apparent elastic modulus calculated using axial strains
$\Xi_w$	apparent elastic modulus calculated using width contraction
$\Xi_t$	apparent elastic modulus calculated using thickness contraction
$\Xi_B$	apparent elastic modulus calculated using thickness contraction and Bridgman correction factor
$\Xi_S$	apparent elastic modulus as evaluated in the current literature
$\rho$	density
$\sigma$	true stress
$\sigma_0$	flow stress
$\sigma_{00}$	initial flow stress
$\sigma_{eq}$	equivalent stress
$\sigma_{fa}$	failure stress
$\sigma_{fr}$	fracture stress
$\sigma_h$	hydrostatic stress
$\sigma'_{ij}$	stress deviator
$\sigma_y$	yield stress
$\sigma_{yf}$	axial fracture stress
$\sigma_{yy'}$	load divided by current area in a notch tensile test
$\sigma_{yy}$	stress in the $y$ direction
$\bar{\sigma}$	effective stress
$\phi$	potential of dissipation
$\dot{\phi}$	dual potential of the potential of dissipation
$\Psi$	specific free energy

---

### Subscripts

$0$	initial
$cr$	critical
$d$	dynamic
$e$	elastic
$eq$	equivalent
$f$	final
$fa$	failure
$fr$	fracture
$r$	coordinate
$s$	static
$u$	ultimate
$x, y$	coordinates
$y_{low}$	low yield
$y_{up}$	upper yield
$\theta$	coordinate

### Superscript

$\cdot$	time derivative
$\ddot{\phantom{x}}$	second time derivative
$\sim$	effective variable



---

## List of Figures

1.1	Classification of fracture mechanisms.	3
2.1	The phenomenon of double necking.	19
2.2	Correction factor, $f_c$ .	20
2.3	Load behaviour near fracture.	21
2.4	Evolution of the equivalent stress and engineering strain.	23
2.5	Plate as delivered.	24
2.6	Measurement system used in the static tensile tests.	25
2.7	Specimens used in the static and dynamic tensile tests.	26
2.8	Measurement system used in the dynamic tensile tests.	28
2.9	Load as measured by load cell and by head gauges.	30
2.10	Engineering stress-strain curves.	32
2.11	Equivalent stress-strain curves.	33
2.12	Diameter evolution for a tensile test.	34
2.13	Correction factor.	34
2.14	Strains <i>versus</i> strain rate.	35
2.15	Ultimate strain.	35
2.16	Yield stress <i>versus</i> strain rate.	36
2.17	Failure stress <i>versus</i> strain rate.	37
2.18	Equivalent strain rate evolution.	37
2.19	Displacement and load behaviour for a tensile test.	38
2.20	COWPER-SYMONDS's prediction.	40
2.21	Prediction of various stresses.	43
2.22	Prediction of stresses for a mild steel.	44
2.23	Prediction of stresses for austenitic steel.	46
3.1	Effective plastic strain contour for an aluminium disk.	48
3.2	Equivalent stress-strain curve and points associated with experimental failure.	48
3.3	Notched tensile specimen.	51
3.4	Expected influence of the stress triaxiality on the strain to fracture.	54

3.5	Equivalent plastic strain <i>versus</i> stress triaxiality.	55
3.6	Evolution of the strain rate for notched specimens.	56
3.7	Evolution of the ultimate and fracture strains <i>versus</i> strain rate.	57
3.8	Load <i>versus</i> axial displacement.	58
3.9	Engineering axial stress <i>versus</i> the average equivalent plastic strain.	59
3.10	Load over current cross section area <i>versus</i> the average equivalent strain.	60
3.11	Influence of the stress triaxiality on the average equivalent fracture plastic strain.	61
3.12	Domain discretisation by Finite-Elements of the notched specimens.	62
3.13	Stresses and strains calculated by the Finite-Element method for the n05 specimen.	63
3.14	Stresses and strains calculated by the Finite-Element method for the n2 specimen.	64
3.15	Stresses and strains calculated by the Finite-Element method for the n4 specimen.	65
3.16	Triaxiality evolution at the centre and at the notch root for the n05, n2 and n4 specimens.	67
3.17	Stress triaxiality <i>versus</i> equivalent plastic strain in a n4 notched specimen made of different materials.	68
3.18	Hardness across the minimum cross section of notched specimens.	69
3.19	A photograph of a n05 specimen cracked at the notch root.	72
3.20	Failure envelope for a mild steel.	73
4.1	Growth and coalescence of voids.	76
4.2	A damaged element.	77
4.3	Effect of the strain and energy equivalency hypothesis on the effective stress.	79
4.4	Illustration of the measurement of $D_{HV}^e$ .	80
4.5	A typical damage specimen.	82
4.6	Finite-Element mesh of one-eighth of the damage specimen.	83
4.7	Equivalent stress-strain curve and load path used in the static Finite-Element simulation of a damage specimen.	84
4.8	A detail of the deformed mesh on a damage specimen.	85
4.9	Change of the apparent elastic modulus <i>versus</i> plastic strain.	86

4.10	Illustration of the geometry of the damage specimen.	87
4.11	A detail of a crack formed at the middle of a damage specimen.	88
4.12	Measurement system used to record the electrical potential change due to damage.	89
4.13	Elastic modulus against the equivalent plastic strain.	90
4.14	Damage evolution <i>versus</i> the equivalent plastic strain.	91
4.15	Hardness values along the length of a damage specimen.	92
4.16	Static damage parameter evolution $D_V^s$ .	93
4.17	Micro-photography of an <i>as received</i> mild steel specimen.	94
4.18	The view plane for the measurement of voids.	95
4.19	The damage parameter $D_S$ <i>versus</i> the nominal test speed.	96
4.20	Damage evolution, $D_S$ , with the nominal test speed for the notched specimens.	97
4.21	Elastic Poisson ratio evolution with the equivalent plastic strain.	97
4.22	The damage parameter $D_S$ averaged per specimen type.	102
5.1	Definition of the flow stress.	111
5.2	Static damage <i>versus</i> equivalent strain.	114
5.3	Influence of the triaxiality and strain rate on failure strain.	115
5.4	Stress triaxiality, equivalent plastic strain and damage along the minimum cross-section of a notched specimen.	117
5.5	Dynamic forming limit for a thin sheet made of a mild steel.	119
6.1	A beam showing the bending hinge length definition.	125
6.2	Clamped beam struck at its middle by a falling mass.	129
6.3	Moment distribution along a clamped beam struck by different masses.	130
6.4	A clamped beam loaded impulsively with a velocity $V_0$ .	130
6.5	A simply supported beam loaded impulsively with a velocity $V_0$ .	132
6.6	Clamped beam struck transversely by a mass $G$ .	132
6.7	Strain rate <i>versus</i> time at the bottom underneath an aluminium beam.	140
6.8	Displacement profile of fully clamped aluminium beams.	142
6.9	Pictures of beams impacted by a mass.	144
6.10	Curvature profile of a fully clamped aluminium beam.	145
6.11	Axial strain at the bottom of the load point underneath an aluminium beam <i>versus</i> its displacement.	146
6.12	Strain at the lower surface underneath the striker for mild steel beams <i>versus</i> its displacement.	147

---

7.1	Definition of the final global displacement of beams.	152
7.2	Load–displacement curves for clamped beams.	153
7.3	Experimental filtered velocity–time signal for a round tup impacting a beam at its middle.	157
7.4	Experimental filtered velocity–time signal recorded for a sharp tup impacting a beam.	158
7.5	Final shear displacement <i>versus</i> final displacement to impact position ratio.	158
7.6	Damage evolution at the most critical part of beams loaded statically.	161
7.7	Non-dimensional displacement <i>versus</i> non-dimensional impact energy for mild steel beams.	166
7.8	Damage profile at the load region along beam 3 when it is about to fail.	169
7.9	Predicted damage <i>versus</i> non-dimensional impact energy for mild steel beams at the instant of failure.	170
7.10	Partition of the damage parameter for mild steel beams at the instant of failure.	171
7.11	Predicted damage <i>versus</i> non-dimensional impact energy for mild steel beams at the instant of failure. The triaxiality value is 1/3.	172
7.12	Non-dimensional displacement <i>versus</i> non-dimensional impact energy for mild steel beams.	174

---

## List of Tables

2.1	Nominal material properties and chemical element concentrations.	24
2.2	Mechanical properties of mild steel.	30
2.3	Main results of the static and dynamic tensile tests.	31
2.4	Coefficients of the COWPER-SYMONDS equation.	40
3.1	Results of the static and dynamic notch tensile tests.	53
4.1	Damage values $D_{HV}^*$ for damage (d) and notch (n) specimens.	91
4.2	Polishing route used for the mild steel specimens.	93
4.3	Static critical damage parameters for mild steel.	99
4.4	Critical damage value for various materials.	103
6.1	Bending hinge length for various beam configurations.	127
7.1	Main results of the static and dynamic beam tests. The damage parameters are for $\sigma_h/\sigma_{eq} = 1/2$ and are associated with the experimental displacement to failure.	154
7.2	Measured and calculated shear and axial strains.	159
7.3	Material parameters used for the dynamic failure prediction.	164
7.4	Comparison between measured and calculated displacement to failure and damage parameter of static beams.	165





---

## Bibliography

- [1] M.M. Al-Mousawi, W.F. Deans, and S.R. Reid. A new method for high rate tension test. In C.Y. Chiem, H.-D. Kunze, and L.W. Meyer, editors, *Impact Loading and Dynamic Behaviour of Materials*, pages 469–474. DGM Informationsgesellschaft mbH, 1988.
- [2] M. Alves, J.L. Yu, and N. Jones. Elastic modulus degradation in continuum damage mechanics. *In preparation*.
- [3] M.F. Ashby, C. Gandhi, and D.M.R. Taplin. Fracture-mechanism maps and their construction for f.c.c. metals and alloys. *Acta Metallurgica*, 27(5):699–729, 1979.
- [4] A. Asundi, Y.J. Liu, S.Y. Du, and C.L. Chow. Damage characterization on stiffness loss of multi-directional composite laminates with matrix cracks. In A. Miravete, editor, *Composites Behaviour*, pages 63–70. University of Zaragoza and Woodhead Publishing Ltd., 1993.
- [5] D.J. Bammann, M.L. Chiesa, M.F. Horstemeyer, and L.I. Weingarten. Failure in ductile materials using finite element methods. In N. Jones and T. Wierzbicki, editors, *Structural Crashworthiness and Failure*, pages 1–54. Elsevier Science Publishers, Barking, Essex, 1993.
- [6] D.C. Barton, J.L. Sturges, M.S. Mirza, and P. Church. Deformation and fracture; modelling techniques to take account of strain-rate behaviour and stress state. *Journal de Physique IV, suppl au Journal de Physique III*, 1(C3):931–936, October 1991.
- [7] G. Baudin and H. Policella. Nouvelle méthode de mesure électrique de longueur de fissure. *La recherche aérospatiale*, (4):195–203, Jul-Aug 1978.
- [8] G. Baudin and H. Policella. D'étermination de fronts de fissure dans les pièces métalliques tridimensionnelles par mesure électrique. *La Recherche Aérospatiale*, (1):73–85, Jan-Feb 1979.

- [9] Z.P. Bažant. Why Continuum Damage is nonlocal: Micromechanics arguments. *Journal of Engineering Mechanics*, 117(5):1070–1087, May 1991.
- [10] R. Becker. The effect of porosity distribution on ductile fracture. *Journal of the Mechanics and Physics of Solids*, 35(5):577–599, 1987.
- [11] R. Becker, A. Needleman, O. Richmond, and V. Tvergaard. Void growth and failure in notched bars. *Journal of the Mechanics and Physics of Solids*, 36(3):317–351, 1988.
- [12] A. Benallal, R. Billardon, and G. Geymonat. Conditions de bifurcation à l'intérieur et aux frontières pour une classe de matériaux non-standards. *C.R. Acad. Sci. Paris*, 308(Série II):893–898, 1989.
- [13] A. Benallal, R. Billardon, and G. Geymonat. Phénomènes de localisation à la frontière d'un solide. *C.R. Acad. Sci. Paris*, 310(Série II):679–684, 1990.
- [14] A. Benallal, C. Comi, and J. Lemaitre. Critical damage states at crack initiation. In J.W. Ju and K.C. Valanis, editors, *Damage Mechanics and Localization*, volume AMD-142, pages 13–23. ASME, 1992.
- [15] D.J. Benson. An analysis of void distribution effects on the dynamic growth and coalescence of voids in ductile metals. *Journal of the Mechanics and Physics of Solids*, 41(8):1285–1308, 1993.
- [16] F.M. Beremin. Calculs élastoplastiques par la méthode des éléments finis d'éprouvettes axisymétriques entaillées circulairement. *Journal de mécanique appliquée*, 4(3):307–325, 1980.
- [17] F.M. Beremin. Influence de la triaxialité des contraintes sur la rupture par déchirement ductile et la rupture fragile par clivage d'un acier doux. *Journal de Mécanique Appliquée*, 4(3):327–342, 1980.
- [18] F.M. Beremin. Experimental and numerical study of the different stages in ductile rupture: application to crack initiation and stable crack growth. In S. Nemat-Nasser, editor, *Three-dimensional Constitutive Relations and Ductile Fracture*, pages 185–205. North-Holland Publishing Company, 1981.

- [19] B.A. Bilby, I.C. Howard, A.M. Othman, Z.H. Li, D.P.G. Lidbury, and A.H. Sherry. Prediction of spinning cylinder tests 2 and 3 using Continuum Damage Mechanics. In *Fracture Mechanics Applications*, volume PVP-287/MD-47, pages 239–294. ASME, 1994.
- [20] R. Billardon and I. Doghri. Pr evision de l'amorage d'une macro-fissure par localisation de l'endommagement. *C.R. Acad. Sci. Paris*, 308(S erie II):347–352, 1989.
- [21] R. Billardon, J. Dufailly, and J. Lemaitre. A procedure based on Vickers' micro-hardness tests to measure damage fields. In F.H. Wittmann, editor, *Structural Mechanics in Reactor Technology*, pages 367–373. A.A. Balkema, Rotterdam, 1987.
- [22] R.S. Birch and N. Jones. Measurement of impact loads using a laser Doppler velocimeter. *Proceedings Institution of Mechanical Engineers*, 204:1–8, Part C 1989.
- [23] P.-E. Bourban, W.J. Cantwell, H.H. Kausch, and S.J. Youd. Damage initiation and development in chopped strand mat composites. In A. Miravete, editor, *Composites Behaviour*, pages 79–86. University of Zaragoza and Woodhead Publishing Ltd., 1993.
- [24] W.A.M. Brekelmans and J.H.P. de Vree. Reduction of mesh sensitivity in Continuum Damage Mechanics. *Acta Mechanica*, 110(1-4):49–56, 1995.
- [25] W.A.M. Brekelmans, P.J.G. Schreurs, and J.H.P. de Vree. Continuum Damage Mechanics for softening of brittle materials. *Acta Mechanica*, 93:133–143, 1992.
- [26] P.W. Bridgman. The stress distribution at the neck of a tension specimen. *Trans. A.S.M.*, 32:553–574, 1944.
- [27] P.W. Bridgman. *Studies in Large Plastic Flow and Fracture*. McGraw-Hill Book Company, Inc., New York, 1952.
- [28] A. Brownrigg, W.A. Spitzig, O. Richmond, and D. Teirlinck. The influence of hydrostatic pressure on the flow stress and ductility on a spherodized 1045 steel. *Acta Metallurgica*, 31(8):1141–1150, 1983.

- [29] G. Cailletaud, H. Policella, and G. Baudin. Mesure de déformation et d'endommagement par méthode électrique. *La Recherche Aéronautique*, (1):69-75, Jan-Feb 1980.
- [30] G. Cailletaud, H. Policella, and G. Baudin. Influence de l'endommagement sur la résistance électrique des métaux. *C. R. Acad. Sc. Paris*, 292(II):1103-1106, May 1981.
- [31] J. Carmeliet and H. Hens. Probabilistic nonlocal damage model for continua with random field properties. *Journal of Engineering Mechanics*, 120(10):2013-2027, October 1994.
- [32] I. Carol, E. Rizzi, and K. Willam. A unified theory of elastic degradation and damage based on a loading surface. *International Journal of Solids and Structures*, 31(20):2835-2865, 1994.
- [33] J.-L. Chaboche. On the description of damage induced anisotropy and active/passive damage effect. In J.W. Ju, D. Krajcinovic, and H.L. Schreyer, editors, *Damage Mechanics in Engineering Materials*, volume AMD-109, MD-24, pages 153-166. ASME - Applied Mechanics Division, 1990.
- [34] J. Chakrabarty. *Theory of Plasticity*. McGraw-Hill, New York, 1987.
- [35] S. Chandrakanth and P.C. Pandey. A FEM study of ductile failure using continuum damage model coupled with plasticity. In N.K. Gupta, editor, *Plasticity and Impact Mechanics*, pages 173-184. Wiley Eastern Ltd., New Dehli, 1993.
- [36] R. Chaouadi, P. de Meester, and W. Vandermeulen. Damage work as ductile fracture criterion. *International Journal of Fracture*, 66:155-164, 1994.
- [37] G. Cheng, Z. Lou, and Z. Kuang. A new damage variable for low cycle fatigue of metallic materials. *Engineering Fracture Mechanics*, 48(2):281-287, 1994.
- [38] G.P. Cherepanov, A.S. Balankin, and V.S. Ivanova. Fractal fracture mechanics - a review. *Engineering Fracture Mechanics*, 51(6):997-1033, 1995.

- [39] C.L. Chow and J. Wang. An anisotropic theory of continuum damage mechanics for ductile fracture. *Engineering Fracture Mechanics*, 27(5):547–558, 1987.
- [40] C.L. Chow and J. Wang. An anisotropic theory of elasticity for continuum damage mechanics. *International Journal of Fracture*, 33:3–16, 1987.
- [41] A. Cipollina, A. López-Inojosa, and J. Flórez-López. A simplified Damage Mechanics approach to nonlinear analysis of frames. *Computer & Structures*, 54(6):1113–1126, 1995.
- [42] L.M. Kachanov (cited in D. Krajcinovic). Time of the rupture process under creep conditions. *Izv. Akad. Nauk SSR. Otd. Tech. Nauk.*, 8:26–31, 1958.
- [43] D.P. Clausing. Stress and strain distribution in a tension specimen with a circumferential notch. *Journal of Materials*, 4(3):566–582, Sept 1969.
- [44] H. Clausmeyer, K. Kussmaul, and E. Roos. Influence of stress state on the failure behaviour of cracked components made of steel. *Applied Mechanics Review*, 44(2):77–92, 1991.
- [45] S.E. Clift, P. Hartley, C.E.N. Sturgess, and G.W. Rowe. Further prediction in plastic deformation process. *International Journal of Mechanical Sciences*, 32(1):1–17, 1990.
- [46] A.C.F. Cocks and F.A. Leckie. Creep constitutive equations for damage materials. In J.W. Hutchinson and T.Y. Wu, editors, *Advances in Applied Mechanics*, volume 25, pages 239–294. Academic Press, Inc., 1987.
- [47] A. Combescure and Y. Jiaju. Finite element method for large displacement and large strain elasto-plastic analysis of shell structures and some application of Damage Mechanics. *Engineering Fracture Mechanics*, 36(2):219–231, 1990.
- [48] C.F. Cocks and M.F. Ashby. Intergranular fracture during power-law creep under multiaxial stresses. *Metal Science*, 14:395–402, 1980.

- [49] J.P. Cordebois and F. Sidoroff. Damage induced elastic anisotropy. In J.P. Boehler, editor, *Mechanical Behaviour of Anisotropic Solids*, pages 761–774. Martinus Nijhoff Publishers, London and Editions du CNRS, Paris, 1979.
- [50] R. Cortes. The growth of microvoids under intense dynamic loading. *International Journal of Solids and Structures*, 29(11):1339–1350, 1992.
- [51] T.B. Cox and J.R. Low Jr. An investigation of the plastic fracture of AISI 4340 and 18 nickel-200 grade maraging steels. *Mettallurgical Transactions*, 5(6):1457–1470, 1974.
- [52] D.R. Curran, L. Seaman, and D.A. Shockey. Dynamic failure of solids. *Physics Reports (Review Section of Physics Letters)*, 147(5&6):253–388, 1987.
- [53] V.R. Dave and S.B. Brown. Critical experiments used to determine flow relations for rate-dependent metal deformation. *International Journal of Plasticity*, 10(3):237–262, 1994.
- [54] A. de Rouvray and E. Haug. Damage and fracture material models for the numerical simulation of structural failure. In P. Ladevèze and O.C. Zienkiewicz, editors, *New Advances in Computational Structural Mechanics*, pages 379–396. Elsevier Science Publishers, 1992.
- [55] M. Delaet, J.L. Lataillade, and C. Wolff. Intralaminar shear loading effects on the damage process of multiply composites at impact rates. In *International Conference on Mechanical and Physical Behaviour of Materials under Dynamic Loading - Journal de Physique IV*, pages 213–218. Les Éditions de Physique and DYMAT, 1994.
- [56] T. Desoyer and F. Cormery. On uniqueness and localization in elastic-damage materials. *International Journal of Solids and Structures*, 31(5):733–744, 1994.
- [57] J.C. Devaux, G. Rousselier, F. Mudry, and A. Pineau. An experimental program for the validation of local ductile fracture using axisymmetrically cracked bars and compact tension specimens. *Engineering Fracture Mechanics*, 21(2):273–283, 1985.

- [58] J.C. Devaux, P. Saillard, and A. Pellissier-Tanon. Elastic-plastic assessment of a cladded pressurized-water-reactor vessel strength since occurrence of a postulated underclad crack during manufacturing. In J.D. Landes, A. Saxena, and J.G. Merkle, editors, *Nonlinear Fracture Mechanics. Vol. II- Elastic-Plastic Fracture*, pages 454-469. ASTM, 1989.
- [59] B. Dood and Y. Bai. *Ductile Fracture and Ductility with Applications to Metalworking*. Academic Press, 1987.
- [60] J. Dufailly. *Modelisation mecanique et identification de l'endommagement plastique des metaux*. PhD thesis, Laboratoire de Mecanique et Technologie, Universite P.M. Curie - Cachan - France, 1980.
- [61] C. Dumont and C. Levaillant. Ductile fracture of Cu-1% Pb at high strain rates. In M.A. Meyers, L.E. Murr, and K.P. Staudhammer, editors, *Shock-wave and High-Strain-Rate Phenomena in Materials*, pages 181-190. Marcel Dekker, Inc., 1992.
- [62] C. Dumont, C. Levaillant, M. Arminjon, J.P. Ansart, and R. Dorneval. Ductile fracture of metals investigated by dynamic tensile tests on smooth and notched bars. In J. Harding, editor, *Mechanical Properties of Materials at High Rates of Strain*, pages 65-72. Institute of Physics, 1989.
- [63] N.L. Dung. Prediction of fracture initiation using a finite element method and various damage models. In J.-P. Boehler and A.S. Khan, editors, *Anisotropy and Localization of Plastic Deformation*, pages 607-610. Elsevier Applied Science, 1991.
- [64] J.C. Earl and D.K. Brown. Distributions of stress and plastic strain in circumferentially notched tension specimens. *Engineering Fracture Mechanics*, 8:599-611, 1976.
- [65] E. El-Magd. Mechanical properties at high strain rates. *Journal de Physique IV - Colloque C8, supplément au Journal de Physique III*, 4:149-170, September 1994.
- [66] M.O. Faruque and H. Wu. Damage mechanics based constitutive model: application in crash analysis of aluminium components. In



- J.W. Ju and K.C. Valanis, editors, *Damage Mechanics and Localization*, volume AMD-142, pages 41–52. ASME, 1992.
- [67] A.G. Franklin. Comparison between a quantitative microscope and chemical methods for assessment of non-metallic inclusions. *Journal of the Iron and Steel Institute*, pages 181–186, 1969.
- [68] H. Galenkamp and H. van Wijngaarden. Determining the von Mises stress from the neck of a tensile test specimen. *Philips Technical Review*, 42(1):11–19, April 1985.
- [69] J.C. Gelin and M. Predeleanu. Recent advances in Damage Mechanics: modelling and computational aspects. In Chenot, Wood, and O.C. Zienkiewicz, editors, *Numerical Methods in Industrial Forming Processes*, pages 89–98. Balkema, Rotterdam, 1992.
- [70] A. Gerard and S. Baste. A constitutive relation for microcracked materials including the effects of microcrack opening–closing. *International Journal of Engineering Science*, 32(4):557–567, 1994.
- [71] P. Germain, Q.S. Nguyen, and P. Suquet. Continuum thermodynamics. *Journal of Applied Mechanics*, 50:1010–1020, 1983.
- [72] A.K. Ghosh. Tensile instability and necking in materials with strain hardening and strain-rate hardening. *Acta Metallurgica*, 25:1413–1424, 1977.
- [73] F. Ghrib and R. Tinawi. Nonlinear behaviour of concrete dams using Damage Mechanics. *Journal of Engineering Mechanics*, 121(4):513–527, April 1995.
- [74] S.H. Goods and L.M. Brown. The nucleation of cavities by plastic deformation. *Acta Metallurgica*, 27(1):1–15, 1979.
- [75] A.L. Gurson. Continuum theory of ductile rupture by void nucleation and growth: Part I - Yield criteria and flow rules for porous ductile media. *Journal of Engineering Materials and Technology*, 99:2–15, Jan 1977.
- [76] J.W. Hancock. Constraint and stress state effects in ductile fracture. In A.S. Argon, editor, *Topics in Fracture and Fatigue*, pages 99–144. Springer-Verlag, New York, 1992.

- [77] J.W. Hancock and D.K. Brown. On the role of strain and stress state in ductile failure. *Journal of the Mechanics and Physics of Solids*, 31(1):1-24, 1983.
- [78] N.R. Hansen and H.L. Schreyer. Thermodynamically consistent theories for elastoplasticity coupled with damage. In J.W. Ju and K.C. Valanis, editors, *Damage Mechanics and Localization*, volume AMD-142, pages 13-22. ASME, 1992.
- [79] N.R. Hansen and H.L. Schreyer. A thermodynamically consistent framework for theories of elastoplasticity coupled with damage. *International Journal of Solids and Structures*, 31(3):359-389, 1994.
- [80] J. Harding. The development of constitutive relationships for material behaviour at high rates of strain. In *International Conference on Mechanical Properties of Materials at High Rates of Strain*, pages 189-203. IOP Publishing Ltd., 1989.
- [81] E. Haug and A. de Rouvray. Crash response of composite structures. In N. Jones and T. Wierzbicki, editors, *Structural Crashworthiness and Failure*, pages 237-294. Elsevier Science Publisher, Ltd., Barking, Essex, 1993.
- [82] P. Haupt. On the mathematical modelling of material behaviour in continuum mechanics. *Acta Mechanica*, 100:129-154, 1993.
- [83] D.R. Hayhurst. The use of continuum damage mechanics in creep analysis for design. *Journal of Strain Analysis*, 29(3):233-241, 1994.
- [84] R. M. Haythornthwaite. Beams with full end fixity. *Engineering*, 183:103-105, Jan 1957.
- [85] F. Hild, P. Larsson, and F.A. Leckie. Localization due to damage in fiber-reinforced composites. *International Journal of Solids and Structures*, 29(24):3221-3238, 1992.
- [86] B.S. Holmes, S.W. Kirkpatrick, J.W. Simons, J.H. Giovanola, and L. Seaman. Modelling the process of failure in structures. In N. Jones and T. Wierzbicki, editors, *Structural Crashworthiness and Failure*, pages 55-93. Elsevier Science Publishers, Ltd., Barking, Essex, 1993.

- [87] S. Huang and A.S. Khan. On the use of electrical resistance metallic foil strain gages for measuring large dynamic plastic deformation. *Experimental Mechanics*, pages 122–125, June 1991.
- [88] J.W. Hutchinson and J.P. Miles. Bifurcation analysis of the onset of necking in an elastic–plastic cylinder under uniaxial tension. *Journal of the Mechanics and Physics of Solids*, 22:61–71, 1974.
- [89] J.W. Hutchinson and K.W. Neale. Influence of strain–rate sensitivity on necking under uniaxial tension. *Acta Metallurgica*, 25:839–846, 1977.
- [90] J. Janson and J. Hult (cited in D. Krajcinovic). Fracture Mechanics and Damage Mechanics — a combined approach. *J. Mech. Appl.*, 1:69, 1977.
- [91] S. Jansson and U. Stigh. Influence of cavity shape on damage parameter. *Journal of Applied Mechanics*, 52:609–614, September 1985.
- [92] M. Jha and R. Narasimhan. A finite element analysis of dynamic fracture initiation by ductile failure mechanisms in a 4340 steel. *International Journal of Fracture*, 56(3):209–231, 1992.
- [93] G.R. Johnson and W.H. Cook. Fracture characteristics of three metals subjected to various strains, strain rates, temperatures and pressures. *Engineering Fracture Mechanics*, 21(1):31–48, 1985.
- [94] G.R. Johnson, J.M. Hoegfeldt, U.S. Lindholm, and A. Nagy. Response of various metals to large torsional strains over a large range of strain rates. Part I—Ductile metals. *Journal of Engineering Materials and Technology*, 105:42–47, 1983.
- [95] N. Jones. Plastic failure of ductile beams loaded dynamically. *Journal of Engineering for Industry*, 98(1):131–136, 1976.
- [96] N. Jones. On the dynamic inelastic failure of beams. In T. Wierzbicki and N. Jones, editors, *Structural Failure*, pages 133–159. John Wiley and Son Inc., 1989.
- [97] N. Jones. *Structural Impact*. Cambridge University Press, Cambridge, 1989.

- [98] N. Jones. Material properties for structural impact problems. In P. Rama Rao, editor, *Advances in Material and their Applications*, pages 151–163. Wiley Eastern Ltd., 1993.
- [99] N. Jones. Quasi-static analysis of structural impact damage. *J. Construct. Steel Research*, 33:151–177, 1995.
- [100] N. Jones and W.Q. Shen. Criteria for the inelastic rupture of ductile metal beams subjected to large dynamic loads. In N. Jones and T. Wierzbicki, editors, *Structural Crashworthiness and Failure*, pages 95–130. Elsevier Science Publisher, Ltd., Barking, Essex, 1993.
- [101] N. Jones and T. Wierzbicki. Dynamic plastic failure of a free-free beam. *International Journal of Impact Engineering*, 6(3):225–240, 1987.
- [102] J.W. Ju. On energy-based coupled elastoplastic damage theories: constitutive modelling and computational aspects. *International Journal of Solids and Structures*, 25(7):803–833, 1989.
- [103] J.W. Ju. Isotropic and anisotropic damage variables in continuum damage mechanics. *Journal of Engineering Mechanics*, 116(12):2764–2770, December 1990.
- [104] J.S. Jubran and W.F. Cofer. Ultimate strength analysis of structural components using the continuum damage mechanics approach. *Computers & Structure*, 39(6):741–752, 1991.
- [105] L.M. Kachanov. *Introduction to Continuum Damage Mechanics*. Martinus Nijhoff Publishers, Dordrecht, 1<sup>st</sup> edition, 1986.
- [106] M. Kachanov. Elastic solids with many cracks and related problems. In J.W. Hutchinson and T.Y. Wu, editors, *Advances in Applied Mechanics*, pages 259–445. Academic Press, Inc., 1994.
- [107] P.I. Kattan and G.Z. Voyiadjis. Micromechanical modelling of damage in uniaxially loaded unidirectional fiber-reinforced composite laminae. *International Journal of Solids and Structures*, 30(1):19–36, 1993.
- [108] P.I. Kattan and G.Z. Voyiadjis. A plasticity-damage theory for large deformation of solids – II. Applications to finite simple shear. *International Journal of Engineering Science*, 31(1):183–199, 1993.

- [109] J.H. Kim, S.J. Kim, and W.D. Kim. Finite element analysis of damage propagation during metal forming process. *Engineering Fracture Mechanics*, 51(6):915–931, 1995.
- [110] S.J. Kim and W.D. Kim. A progressive damage modelling based on the continuum damage mechanics and its finite element analysis. *Journal of Applied Mechanics*, 61:45–53, March 1994.
- [111] P. Knoché and A. Needleman. The effect of size on the ductility of dynamically loaded tensile bars. *European Journal of Mechanics, A/Solids*, 12(4):585–601, 1993.
- [112] D. Krajcinovic. Damage Mechanics. *Mechanics of Materials*, 8(2–3):117–197, December 1989.
- [113] S. Kruch. A nonlocal damage theory. In J.W. Ju and K.C. Valanis, editors, *Damage Mechanics and Localization*, volume AMD-142, pages 13–22. ASME, 1992.
- [114] K. Kussmaul, U. Eisele, and M. Seidenfuss. On the applicability of local approaches for the determination of the failure behaviour of ductile steels. *Journal of Pressure Vessel Technology*, 115:214–220, 1993.
- [115] K. Kussmaul and M. Schuele. Dynamic tensile tests on ferritic and austenitic steels with improved testing and measuring technique. *Journal de Physique IV - Colloque C8, supplément au Journal de Physique III - International Conference on Mechanical and Physical Behaviour of Materials under Dynamic Loading*, 4:141–146, Septembre 1994.
- [116] P. Ladevèze, A. Gasser, and O. Allix. Damage mechanisms modelling for ceramic composites. *Journal of Engineering Materials and Technology*, 116:331–336, July 1994.
- [117] J.C. Lautridou and A. Pineau. Crack initiation resistance in A508 steels in relation to inclusion distributions. *Engineering Fracture Mechanics*, 15(1-2):55–71, 1981.
- [118] G. le Roy, J.D. Embury, G. Edwards, and M.F. Ashby. A model of ductile fracture based on the nucleation and growth of voids. *Acta Metallurgica*, 29:1509–1522, 1981.

- [119] B.J. Lee and M.E. Mear. An evaluation of Gurson's theory of dilatational plasticity. *Journal of Engineering Materials and Technology*, 115:339–344, October 1993.
- [120] T. Lehmann. Some thermodynamical considerations on inelastic deformations including damage process. *Acta Mechanica*, 79:1–24, 1989.
- [121] T. Lehmann. Thermodynamical foundations of large inelastic deformations of solid bodies including damage. *International Journal of Plasticity*, 7:79–98, 1991.
- [122] J. Lemaitre. How to use Damage Mechanics. *Nuclear Engineering and Design*, 80:233–245, 1984.
- [123] J. Lemaitre. A continuous damage mechanics model for ductile fracture. *Journal of Materials and Technology*, 107:83–89, Jan 1985.
- [124] J. Lemaitre. Coupled elasto-plasticity and damage constitutive equations. *Computer Methods in Applied Mechanics and Engineering*, 51:31–49, 1985.
- [125] J. Lemaitre. Local approach of fracture. *Engineering Fracture Mechanics*, 25(5/6):523–537, 1986.
- [126] J. Lemaitre. *A Course on Damage Mechanics*. Springer-Verlag, Berlin, 1992.
- [127] J. Lemaitre and J.-L. Chaboche. Aspect phénoménologique de la rupture par endommagement. *Journal de Mécanique Appliquée*, 2(3):317–365, 1978.
- [128] J. Lemaitre and J.-L. Chaboche. *Mécanique des Matériaux Solides*. Dunod, Paris, 2<sup>nd</sup> edition, 1988.
- [129] J. Lemaitre and I. Doghri. Damage 90: a post processor for crack initiation. *Computer Methods in Applied Mechanics and Engineering*, 115:197–232, 1994.
- [130] J. Lemaitre and J. Dufailly. Damage measurements. *Engineering Fracture Mechanics*, 28(5/6):643–661, 1987.
- [131] J. Lemaitre, J. Dufailly, and R. Billardon. Évaluation de l'endommagement par mesures de microdureté. *C. R. Acad. Sc. Paris*, 304(12):601–604, 1987.

- [132] J. Lemaitre, F.A. Leckie, and D. Sherman. Crazeing of laminates. *European Journal of Mechanics, A/Solids*, 11(3):289–304, 1992.
- [133] J. Lemaitre, F.A. Leckie, and D. Sherman. Crazeing of laminates. *European Journal of Mechanics, A/Solids*, 11(3):289–304, 1992.
- [134] T.C. Lindley, G. Oates, and C.E. Richards. A critical appraisal of carbide cracking mechanisms in ferride/carbide aggregates. *Acta Metallurgica*, 18(11):1127–1136, 1970.
- [135] J. Liu and N. Jones. Experimental investigation of clamped beams struck transversely by a mass. *International Journal of Impact Engineering*, 6(4):303–335, 1987.
- [136] J. Liu and N. Jones. Dynamic response of a rigid plastic clamped beam struck by a mass at any point on the span. *International Journal of Solids and Structures*, 24(3):251–270, 1988.
- [137] J.H. Liu and N. Jones. Plastic failure of a clamped beam struck transversely by a mass. In M. Kleiber and J.A. König, editors, *Inelastic Solids and Structures*, pages 361–384. Pineridge Press, Swansea, UK, 1990.
- [138] V.A. Lubarda. An analysis of large strain damage elastoplasticity. *International Journal of Solids and Structures*, 31:2951, 1994.
- [139] V.A. Lubarda and D. Krajcinovic. Some fundamental issues in rate theory of damage–elastoplasticity. *International Journal of Plasticity*, 11(7):763–797, 1995.
- [140] J. Lubliner. *Plasticity Theory*. Macmillan Publishing Co., New York, 1990.
- [141] A.C.J. Luo, Y. Mou, and R.P.S. Han. A large anisotropic damage theory based on an incremental complementary energy equivalence model. *International Journal of Fracture*, 70:19–34, 1995.
- [142] Z.J. Luo, W.H. Ji, N.C. Guo, X.Y. Xu, Q.S. Xu, and Y.Y. Zhang. A ductile–damage model and its application to metal–forming processes. *Journal of Materials Processing Technology*, 30:31–43, 1992.

- [143] F. Ma and Z. Kuang. Elastic-plastic fracture analysis of finite bodies – II. Conditions of fracture initiation. *Engineering Fracture Mechanics*, 48(5):739–748, 1994.
- [144] A.C. Mackenzie, J.W. Hancock, and D.K. Brown. On the influence of state of stress on ductile failure initiation in high strength steels. *Engineering Fracture Mechanics*, 9:167–188, 1977.
- [145] P.E. Magnusen, E.M. Dubensky, and D.A. Koss. The effect of void arrays on void linking during ductile fracture. *Acta Metallurgica*, 36(6):1503–1509, 1988.
- [146] F.A. McClintock. A criterion for ductile fracture by the growth of holes. *Journal of Applied Mechanics*, 35(2):363–371, 1968.
- [147] S.B. Menkes and H.J. Opat. Broken beams – tearing and shear failure in explosively loaded clamped beams. *Experimental Mechanics*, pages 480–486, November 1973.
- [148] L.W. Meyer. Constitutive equation at high strain rates. In M.A. Meyers, L.E. Murr, and K.P. Staudhammer, editors, *Shock-wave and high-strain-rate phenomena in materials*, pages 49–68. Marcel Dekker, Inc., 1992.
- [149] M.A. Meyers. *Dynamic Behaviour of Materials*. John Wiley & Sons, Inc., New York, 1994.
- [150] Micro-Measurements Division. *Catalog 500. Part B- Strain gage technical data*.
- [151] J.P. Miles. Bifurcation in plastic flow under uniaxial tension. *Journal of the Mechanics and Physics of Solids*, 19:89–102, 1971.
- [152] S. Mingzhe. Measuring the damage factor of materials with the thin-walled cylinder torsion test and the low-cycle fatigue test. *Engineering Fracture Mechanics*, 44(2):267–273, 1993.
- [153] S. Murakami, M. Kawai, and H. Rong. Finite element analysis of creep crack growth by a local approach. *International Journal of Mechanical Sciences*, 30(7):491–502, 1988.



- [154] S. Murakami and M. Mizuno. Elaborated constitutive equations for structural analysis for creep, swelling and damage under radiation. *Nuclear Technology*, 95:219–227, August 1991.
- [155] S. Murakami and M. Mizuno. A constitutive equation of creep, swelling and damage under neutron irradiation applicable to multiaxial and variable states of stress. *International Journal of Solids and Structures*, 29(19):2319–2328, 1992.
- [156] P.M. Naghdi. A critical review of the state of finite plasticity. *Journal of Applied Mathematics and Physics, ZAMP*, 41:315–394, May 1990.
- [157] R. Narasimhan, A.J. Rosakis, and B. Moran. A three-dimensional numerical investigation of fracture initiation by ductile failure mechanisms in a 4340 steel. *International Journal of Fracture*, 56(1):1–24, 1992.
- [158] M.A. Nash and I.G. Cullis. Numerical modelling of fracture— a model for ductile fracture in triaxial states of stress. In J. Harding, editor, *Mechanical Properties at High Rates of Strain*, pages 307–314. The Institute of Physics, 1984.
- [159] A. Needleman. A numerical study of necking in circular cylindrical bars. *Journal of the Mechanics and Physics of Solids*, 20:111–127, 1972.
- [160] A. Needleman and A.S. Kushner. An analysis of void distribution effects on plastic flow in porous solids. *European Journal of Mechanics, A/Solids*, 9(3):193–206, 1990.
- [161] A. Needleman and V. Tvergaard. An analysis of ductile rupture in notched bars. *Journal of the Mechanics and Physics of Solids*, 32(6):461–490, 1984.
- [162] S. Nemat-Nasser and M. Hori. *Micromechanics: Overall Properties of Heterogeneous Materials*. North-Holland, 1993.
- [163] J.A. Nemes, J. Eftis, and P.W. Randles. Viscoplastic constitutive modelling of high strain-rate deformation, material damage, and spall fracture. *Journal of Applied Mechanics*, 57(2):282–291, 1990.

- [164] J.A. Nemes and E. Spécuel. Use of a rate-dependent continuum damage model to describe strain-softening in laminated composites. *Computers & Structures*, 58(6):1083–1092, 1996.
- [165] T. Nonaka. Some interaction effects in a problem of plastic beam dynamics. Part 1: Interaction analysis of a rigid, perfectly plastic beam. *Journal of Applied Mechanics*, pages 623–630, September 1967.
- [166] T. Nonaka. Some interaction effects in a problem of plastic beam dynamics. Part 2: Analysis of a structure as a system of one degree of freedom. *Journal of Applied Mechanics*, pages 631–636, September 1967.
- [167] D. Nouailhas. *Etude expérimentale de l'endommagement de plasticité ductile anisotrope*. PhD thesis, Laboratoire de Mécanique et Technologie, Université P.M. Curie - Cachan - France, 1980.
- [168] M. Ortiz and A. Molinari. Effect of strain hardening and rate sensitivity on the dynamic growth of a void in a plastic material. *Journal of Applied Mechanics*, 59:48–53, 1992.
- [169] A. Otsuka, K. Tohgo, and Y. Okamoto. Relationship between ductile crack initiation and void volume fraction. *Nuclear Engineering and Design*, 105:121–129, 1987.
- [170] J. Pan, M. Saje, and A. Needleman. Localization of deformation in rate sensitive porous plastic solids. *International Journal of Fracture*, 21:261–278, 1983.
- [171] N. Perrone and P. Bhadra. A simplified method to account for plastic rate sensitivity with large deformations. *Journal of Applied Mechanics*, 46:811–816, September 1979.
- [172] P. Perzyna. Internal state variable description of dynamic fracture of ductile solids. *International Journal of Solids and Structures*, 22(7):797–818, 1986.
- [173] K.K. Raju and G.V. Rao. The effect of localised axisymmetric damages on the buckling of circular plates. *Computers & Structures*, 58(3):651–654, 1996.
- [174] H. Rapp. Private communication.

- [175] J.R. Rice and D.M. Tracey. On the ductile enlargement of voids in triaxial stress fields. *Journal of the Mechanics and Physics of Solids*, 17:201–217, 1969.
- [176] E. Rizzi, I. Carol, and K. Willam. Localization analysis of elastic degradation with application to scalar damage. *Journal of Engineering Mechanics*, 121(4):541–554, April 1995.
- [177] K. Saanouni, J.L. Chaboche, and P.M. Lesne. On the creep crack-growth prediction by a non local damage formulation. *European Journal of Mechanics, A/Solids*, 8(6):437–459, 1989.
- [178] A. Seweryn and Z. Mróz. A non-local stress failure condition for structural elements under multiaxial loading. *Engineering Fracture Mechanics*, 51(6):955–973, 1995.
- [179] W.Q. Shen and N. Jones. A comment on the low speed impact of a clamped beam by a heavy striker. *Mech. Struct. & Mach.*, 19(4):527–549, 1991.
- [180] W.Q. Shen and N. Jones. A failure criterion for beams under impulsive loading. *International Journal of Impact Engineering*, 12(1):101–121, 1992.
- [181] W.Q. Shen and N. Jones. Dynamic plastic response and failure of a clamped beam struck transversely by a mass. *International Journal of Solids and Structures*, 30(12):1631–1648, 1993.
- [182] W.Q. Shen and N. Jones. Dynamic response and failure of fully clamped circular plates under impulsive loading. *International Journal of Impact Engineering*, 13(2):259–278, 1993.
- [183] Y.W. Shi, J.T. Barnby, and A.S. Nadkarni. Void growth at ductile crack initiation of a structural steel. *Engineering Fracture Mechanics*, 39(1):37–44, 1991.
- [184] J.G. Shin and D.G. Karr. Propagation of continuum damage in a nonlinear viscoelastic bar by finite difference method. In J.W. Ju, D. Krajcinovic, and H.L. Schreyer, editors, *Damage Mechanics in Engineering Materials*, volume AMD-109, MD-24, pages 237–249. ASME – Applied Mechanics Division, 1990.

- [185] D.A. Shockey, L. Seaman, K.C. Dao, and D.R. Curran. Kinetics of void development in fracturing A533B tensile bars. *Journal of Pressure Vessel Technology*, 102:14–21, February 1980.
- [186] J.C. Simo and J.W. Ju. Strain and stress-based continuum damage models– I. formulation. *International Journal of Solids and Structures*, 23(7):821–840, 1987.
- [187] J.C. Simo and J.W. Ju. Strain and stress-based continuum damage models– II. computational aspects. *International Journal of Solids and Structures*, 23(7):841–869, 1987.
- [188] L. Sun and Z. Huang. Dynamic void growth in rate-sensitive plastic solids. *International Journal of Plasticity*, 8(8):903–924, 1992.
- [189] W. Szczepiński. Mechanics of ductile fracture treated as a problem of the theory of plasticity. *International Journal of Plasticity*, 6:11–27, 1990.
- [190] S.E.F. Taher, M.H. Baluch, and A.H. Al-Gadhib. Towards a canonical elastoplastic damage model. *Engineering Fracture Mechanics*, 48(2):151–166, 1994.
- [191] W.H. Tai. Plastic damage and ductile fracture in mild steels. *Engineering Fracture Mechanics*, 37(4):853–880, 1990.
- [192] W.H. Tai and B.X. Yang. A new microvoid–damage model for ductile fracture. *Engineering Fracture Mechanics*, 25(3):377–384, 1986.
- [193] W.H. Tai and B.X. Yang. A new Damage Mechanics criterion for ductile fracture. *Engineering Fracture Mechanics*, 27(4):371–378, 1987.
- [194] C.Y. Tang and A. Plumtree. Damage mechanics applied to polymers. *Engineering Fracture Mechanics*, 49(4):499–508, 1994.
- [195] P.S. Theocaris. Failure criteria for isotropic bodies revisited. *Engineering Fracture Mechanics*, 51(2):239–264, 1995.
- [196] P.F. Thomason. *Ductile Fracture of Metals*. Pergamon Press, Oxford, 1990.
- [197] Y. Toi and J. Che. Computational Damage Mechanics models for brittle microcracking solids based on mesoscopic simulations. *Engineering Fracture Mechanics*, 48(4):483–498, 1994.

- [209] T. Wang. Further investigation of a new continuum damage mechanics criterion for ductile fracture: experimental verification and applications. *Engineering Fracture Mechanics*, 48(2):217–230, 1994.
- [210] T. Wang. A new ductile fracture theory and its applications. *Acta Mechanica Sinica*, 11(1):83–93, February 1995.
- [211] Z. Wang and M. Hou. A model of dynamic failure in ductile materials. *Acta Mechanica Solida Sinica (English edition)*, 5(2):193–202, Apr 1992.
- [212] Z.P. Wang and D.R. Hayhurst. The use of supercomputer modelling of high-temperature failure in pipe weldments to optimize weld and heat affected zone materials property selection. *Proc. R. Soc. Lond. A*, 446:127–148, 1994.
- [213] H.M. Wen, T.Y. Reddy, and S.R. Reid. Deformation and failure of clamped beams under low speed impact loading. *International Journal of Impact Engineering*, 16(3):435–454, 1995.
- [214] C.W. Woo and D.L. Li. A universal physically consistent definition of material damage. *International Journal of Solids and Structures*, 30(15):2097–2108, 1993.
- [215] S. Xia, S. Takezono, and K. Tao. Nonlocal elastic damage near crack tip. *International Journal of Fracture*, 62:87–95, 1993.
- [216] J. Yu and N. Jones. Numerical simulation for the failure of impact loaded steel beams. *To be published*.
- [217] J. Yu and N. Jones. Numerical simulation of a clamped beam under impact loading. *Computer & Structures*, 32(2):281–293, 1989.
- [218] J. Yu and N. Jones. Further experimental investigation on the failure of clamped beams under impact loads. *International Journal of Solids and Structures*, 27(9):1113–1137, 1991.
- [219] A. Zavaliangos and L. Anand. Thermo-elasto-viscoplasticity of isotropic porous metals. *Journal of the Mechanics and Physics of Solids*, 41(6):1087–1118, 1993.

- [220] F.J. Zerilli and R.W. Armstrong. Dislocation mechanics based constitutive relations for material dynamics calculations. *Journal of Applied Physics*, 61(5):1816, March 1987.
- [221] F.J. Zerilli and R.W. Armstrong. Description of tantalum deformation behaviour by dislocation mechanics based constitutive relations. *Journal of Applied Physics*, 68(4):1580-1591, August 1990.
- [222] L. Zhaoxia. Effective creep Poisson's ratio for damaged concrete. *International Journal of Fracture*, 66:189-196, 1994.
- [223] Y.Y. Zhu and S. Cescotto. A fully coupled elastoplastic damage modelling of contact-impact between two deformable bodies. In *Structures under Shock and Impact*, pages 113-132, 1992.
- [224] Y.Y. Zhu and S. Cescotto. A fully coupled elasto-visco-plastic damage theory for anisotropic materials. *International Journal of Solids and Structures*, 32(11):1607-1641, 1995.
- [225] Y.Y. Zhu, S. Cescotto, and A.-M. Habraken. A fully coupled elastoplastic damage theory based on the energy equivalence. In D.R.J. Owen, E. Onate, and E. Hinton, editors, *Computational Plasticity - Fundamentals and Applications*, pages 1455-1466. Pineridge Press, Swansea, UK, 1992.
- [226] H. Ziegler. *An Introduction to Thermomechanics*. North-Holland, 2<sup>nd</sup> edition, 1983.
- [227] H. Ziegler and C. Wehrli. The derivation of constitutive relations from the free energy and the dissipation function. In J.W. Hutchinson and T.Y. Wu, editors, *Advances in Applied Mechanics*, volume 25, pages 183-238. Academic Press, Inc., 1987.
- [228] J.A. Zukas. Numerical simulation of high rate behaviour. In C.A. Brebbia and V. Sánchez-Gálvez, editors, *Shock and Impact of Structures*, pages 1-26. Computational Mechanics Publications, Southampton, 1994.